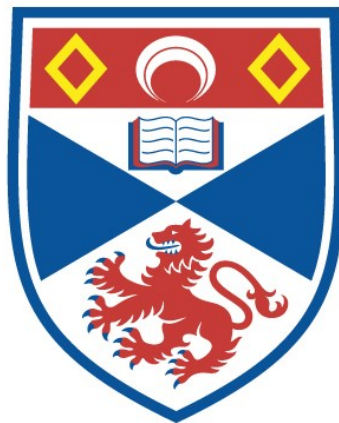


PHOTOPORATION AND OPTICAL MANIPULATION OF PLANT AND MAMMALIAN CELLS

Claire Amy Mitchell

A Thesis Submitted for the Degree of PhD
at the
University of St Andrews



2015

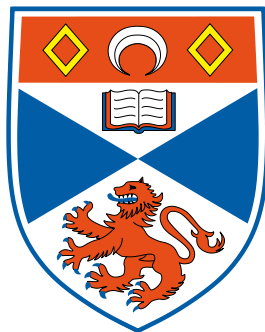
Full metadata for this item is available in
St Andrews Research Repository
at:
<http://research-repository.st-andrews.ac.uk/>

Please use this identifier to cite or link to this item:
<http://hdl.handle.net/10023/6328>

This item is protected by original copyright

PHOTOPORATION AND OPTICAL MANIPULATION OF PLANT
AND MAMMALIAN CELLS

Claire Amy Mitchell



A thesis submitted for the degree of Doctor of Philosophy at the
University of St Andrews

10th February 2015

Abstract

Optical cell manipulation allows precise and non-invasive exploration of mammalian cell function and physiology for medical applications. Plants, however, represent a vital component of the Earth's ecosystem and the knowledge gained from using optical tools to study plant cells can help to understand and manipulate useful agricultural and ecological traits. This thesis explores the potential of several biophotonic techniques in plant cells and tissue.

Laser-mediated introduction of nucleic acids and other membrane impermeable molecules into mammalian cells is an important biophotonic technique. Optical injection presents a tool to deliver dyes and drugs for diagnostics and therapy of single cells in a sterile and interactive manner. Using femtosecond laser pulses increases the tunability of multiphoton effects and confines the damage volume, providing sub-cellular precision and high viability. Extending current femtosecond photoporation knowledge to plant cells could have sociological and environmental benefits, but presents different challenges to mammalian cells.

The effects of varying optical and biological parameters on optical injection of a model plant cell line was investigated. A reconfigurable optical system was designed to allow easy switching between different spatial modes and pulse durations. Varying the medium osmolarity and optoinjectant size and type affected optoinjection efficacy, allowing optimisation of optical delivery of relevant biomolecules into plant cells.

Advanced optical microscopy techniques that allow imaging beyond the diffraction

limit have transformed biological studies. An ultimate goal is to merge several biophotonic techniques, creating a plant cell workstation. A step towards this was demonstrated by incorporating a fibre-based optical trap into a commercial super-resolution microscope for manipulation of cells and organelles under super-resolution. As proof-of-concept, the system was used to optically induce and quantify an immunosynapse. The capacity of the super-resolution microscope to resolve structure in plant organelles in aberrating plant tissue was critically evaluated.

Acknowledgements

I would like to thank my supervisors, Kishan, Frank, Alison and Lesley, for their invaluable advice and endless patience during my PhD.

Special thanks go to my family, Mum, Dad and Kylie, for their love, support and unfailing belief in my abilities, without which I wouldn't be where I am today. To my friends, who have shared my journey and supported me throughout, I can only say thank you. I would also like to thank my colleagues for their help and friendship, it would be impossible to list everyone individually but those who were directly connected to my research have been acknowledged at the end of relevant chapters.

This study has been made possible by funding from EPSRC UK and the James Hutton Institute.

Declaration

Candidate's declarations:

I, Claire Amy Mitchell, hereby certify that this thesis, which is approximately 37,000 words in length, has been written by me, and that it is the record of work carried out by me, or principally by myself in collaboration with others as acknowledged, and that it has not been submitted in any previous application for a higher degree. I was admitted as a research student in September 2010 and as a candidate for the degree of Doctor of Philosophy in September 2010; the higher study for which this is a record was carried out in the University of St Andrews between 2010 and 2014.

Date:.....

Signature of candidate:

Supervisor's declaration:

I hereby certify that the candidate has fulfilled the conditions of the Resolution and Regulations appropriate for the degree of Doctor of Philosophy in the University of St Andrews and that the candidate is qualified to submit this thesis in application for that degree.

Date:.....

Signature of supervisor:

Permission for publication:

In submitting this thesis to the University of St Andrews I understand that I am giving permission for it to be made available for use in accordance with the regulations of the University Library for the time being in force, subject to any copyright vested in the work not being affected thereby. I also understand that the title and the abstract will be published, and that a copy of the work may be made and supplied to any bona fide library or research worker, that my thesis will be electronically accessible for personal or research use unless exempt by award of an embargo as requested below, and that the library has the right to migrate my thesis into new electronic forms as required to ensure continued access to the thesis. I have obtained any third-party copyright permissions that may be required in order to allow such access and migration, or have requested the appropriate embargo below.

The following is an agreed request by candidate and supervisor regarding the publication of this thesis:

PRINTED COPY

Embargo on all or part of print copy for a period of 6 months on the following ground(s):

- Publication would preclude future publication

ELECTRONIC COPY

Embargo on all or part of electronic copy for a period of 6 months on the following ground(s):

- Publication would preclude future publication

Date:.....

Signature of candidate:

Signature of supervisor:

Abbreviations

1D	one dimensional
2D	two dimensional
3D	three dimensional
AM	acetoxymethyl
APC	antigen-presenting cell
BA	back aperture
<i>B. napus</i>	<i>Brassica napus</i>
BY-2	Bright Yellow 2
CCD	charge-coupled device
CHO	chinese hamster ovary
CL	condenser lens
CoM	centre of mass
CW	continuous wave
DL	diode laser
DM	dichroic mirror
DNA	deoxyribonucleic acid
DOF	depth of focus
DsRed	<i>Discosoma</i> red
dSTORM	direct STORM
EM-CCD	electron multiplying CCD

ER	endoplasmic reticulum
ET	exposure time
FEL	free electron laser
FITC	fluorescein isothiocyanate
fps	frames per second
FROG	frequency-resolved optical gating
fs	femtosecond
FWHM	full-width half-maximum
GDD	group delay dispersion
GFP	green fluorescent protein
GM	genetically modified/genetic modification
GRIN	gradient refractive index
GUS	β -glucuronidase
GVD	group velocity dispersion
HEK	human embryonic kidney
HOT	holographic optical tweezer
HWP	half-wave plate
IR	infrared
IS	immunological synapse
laser	light amplification by stimulated emission of radiation
MDU	MIIPS detection unit
MEM	modified Eagle's medium
MIIPS	multiphoton intrapulse interference phase scan
MIM	membrane-impermeable molecule
MO	morpholino
MPI	multiphoton ionisation
mRNA	messenger RNA
MTOC	microtubule-organising centre

MW	molecular weight
M & S	Murashige and Skoog
N	neuron
NA	numerical aperture
NIR	near infrared
ns	nanosecond
NUV	near ultraviolet
OTF	optical transfer function
P	power
PALM	photoactivated localisation microscopy
PB	photobleaching
PBS	polarising beam splitter
PD	plasmodesmata
PEG	polyethylene glycol
PG-FROG	polarisation gated FROG
PI	propidium iodide
PMT	photomultiplier tube
PRR	pulse repetition rate
ps	picosecond
PSD	power spectrum density
PSF	point spread function
PVX	potato virus X
PW	pulse width
QBB	quasi-Bessel beam
QPD	quadrant photodiode
RFP	red fluorescent protein
RNA	ribonucleic acid
SC	stem cell

SCT	single cell targeting
SEM	standard error of the mean
SHG	second harmonic generation
siRNA	small interfering RNA
SIM	stuctured illumination microscopy/microscope
SLM	spatial light modulator
SM	single mode
SMA	SubMiniature version A
SNR	signal-to-noise ratio
SPIDER	spectral phase interferometry for direct electric field reconstruction
SR	super-resolution
STED	stimulated emission by depletion
STORM	stochastic optical reconstruction microscopy
TCR	T cell receptor
TIRF	total internal reflection fluorescence
TL	transform-limited
TMV	tobacco mosaic virus
TOD	third-order dispersion
TRITC	tetramethylrhodamine isothiocyanate
UV	ultraviolet
YFP	yellow fluorescent protein

Publications

Peer-reviewed publications

- [1] Nylk, J., Kristensen, M. V. G., Mazilu, M., Thayil, A. K., Mitchell, C. A., Campbell, E. C., Powis, S. J., Gunn-Moore, F. J., Dholakia, K. “Characterization and application of a graded index microlens based fiber optical trap for biomedical microscopy”, (submitted)
- [2] Mitchell, C. A., Kalies, S., Cizmár, T., Heisterkamp, A., Torrance, L., Roberts, A. G., Gunn-Moore, F. J., Dholakia, K. “Femtosecond Optoinjection of Intact Tobacco BY-2 Cells Using a Reconfigurable Photoporation Platform”, PloS ONE, 8(11), e79235. doi:10.1371/journal.pone.0079235 (2013)

Conference proceedings

- [3] Mitchell, C. A., Kalies, S., Cizmár, T., Bellini, N., Kubasik-Thayil, A., Heisterkamp, A., Torrance, L., Roberts, A. G., Gunn-Moore, F. J., Dholakia, K. “Femtosecond optical injection of intact plant cells using a reconfigurable platform”, Proc. SPIE 8972, Frontiers in Ultrafast Optics: Biomedical, Scientific, and Industrial Applications XIV, 89720C, doi:10.1117/12.2037784 (2014)
- [4] Mitchell, C. A., Kalies, S., Cizmár, T., Heisterkamp, A., Torrance, L., Roberts, A. G., Gunn-Moore, F. J., Dholakia, K. “Femtosecond Photoporation of Intact BY-2 Suspension Cells”, EOSAM, Aberdeen (2012)

- [5] Mitchell, C. A., Kalies, S., Cizmár, T., Heisterkamp, A., Torrance, L., Roberts, A. G., Gunn-Moore, F. J., Dholakia, K. “Femtosecond optoinjection of intact tobacco BY-2 cells using a reconfigurable photoporation platform”, Scottish Microscopy Group Symposium, Edinburgh (2012)
- [6] Mitchell, C. A., Torrance, L., Roberts, A. G., Gunn-Moore, F. J., Dholakia, K. “Development of Optical Transfection techniques in plant and mammalian cells”, Biophotonics '11 Summer School, Sweden (2011)

Contents

Abstract	ii
Acknowledgements	iv
Declaration	v
Abbreviations	vii
Publications	xi
1 Introduction	1
1.1 Preface	1
1.1.1 Light for therapy, manipulation and imaging	1
1.1.2 Plants in biophotonics	2
1.2 Synopsis	3
2 Optical manipulation of mammalian cells	5
2.1 Introduction	5
2.2 Photoporation	5
2.2.1 Bypassing the cell membrane	6

2.2.2	Photoporation mechanisms	10
2.2.3	Femtosecond photoporation in mammalian cells	20
2.3	Optical trapping	25
2.3.1	Optical trapping theory	26
2.3.2	Trap calibration	30
2.3.3	Developments and applications	33
2.3.4	Optical trapping and fluorescence microscopy	35
2.4	Combining optical trapping and photoporation	38
2.5	Conclusions	38
3	Biophotonic methods for plant cells	40
3.1	Plant physiology	40
3.2	Genetic modification of plants	43
3.3	Current plant transformation protocols	45
3.4	Plant photoporation review	47
3.4.1	Nanosecond UV studies	47
3.4.2	Picosecond IR studies	51
3.4.3	Femtosecond NIR studies	52
3.4.4	CW studies	52
3.4.5	Optoporation	53
3.4.6	Osmolarity effects	53
3.4.7	Summary	55
3.5	Conclusions	57

4	Development of a reconfigurable photoporation system	58
4.1	Introduction	58
4.1.1	Gaussian beams	60
4.1.2	Bessel beams	62
4.1.3	Beam comparison	65
4.2	An optical system to select between Gaussian and Bessel beams	66
4.2.1	Laser parameters	66
4.2.2	Optical set-up	68
4.2.3	Beam characterisation	72
4.3	Optical system development for controlling pulse duration	73
4.3.1	Laser parameters	75
4.3.2	Optical set-up	76
4.3.3	Ultrashort Bessel beam generation	78
4.4	Discussion and conclusions	79
4.5	Chapter acknowledgements	82
5	Femtosecond photoporation of tobacco BY-2 cells	83
5.1	Introduction	83
5.2	Materials and methods	86
5.2.1	Photoporation of BY-2 cells	86
5.2.2	Propidium iodide optical injection	87
5.2.3	Measurement of plasmolysis	87
5.2.4	Optoinjection of calcein	88

5.2.5	Optoinjection of dextrans	88
5.2.6	Optoinjection of nucleic acids	89
5.3	Results	89
5.3.1	Bubble formation and optoinjection success	89
5.3.2	Determining the effect of changing optical parameters on optical injection	91
5.3.3	Effect of medium osmolarity on optoinjection efficiency	94
5.3.4	Exploration of optoinjection dynamics under hypertonic treatment	97
5.3.5	Effect of biomolecular size on cellular uptake	100
5.3.6	Delivery of oligonucleotides into cells	102
5.4	Attempting optical transformation	104
5.4.1	Testing common methods of transformation	104
5.4.2	Use of a nuclear targeting reagent	105
5.5	Discussion and conclusions	107
5.6	Chapter acknowledgements	114
6	Ultrashort broadband pulses for photoporation	115
6.1	Introduction	115
6.1.1	The role of pulse duration in biophotonic applications	116
6.1.2	Dispersion	117
6.1.3	Dispersion compensation	120
6.1.4	Pulse measurement	122
6.1.5	Complete measurement and control of ultrashort pulses	124
6.2	Materials and methods	125

6.2.1	Implementation of the MIIPS system	125
6.2.2	Determining the Chameleon pulse duration	126
6.2.3	Mammalian cell culture and optoinjection	128
6.2.4	Plant optoinjection protocol	128
6.3	Results	128
6.3.1	MIIPS implementation	128
6.3.2	Optical injection	130
6.4	Discussion and conclusions	134
6.5	Chapter acknowledgements	137
7	Optical trapping and super-resolution microscopy	138
7.1	Introduction	138
7.1.1	Super-resolution microscopy	140
7.2	Integration of optical trapping with a structured illumination microscope	143
7.2.1	Optical system	145
7.2.2	Trap calibration	145
7.2.3	Beam profile	150
7.2.4	Trapping and moving cells	150
7.3	Monitoring cell-cell interactions by optical trapping	152
7.3.1	The immunological synapse	152
7.3.2	Immunosynapse induction by optical trapping	153
7.4	Super-resolution imaging of plant cells	156
7.4.1	Previous SR imaging of plant cells	156

7.4.2	3D-SIM imaging of plant cells	157
7.5	Discussion and conclusions	160
7.6	Chapter acknowledgements	165
8	Conclusions and future work	166
8.1	Summary	166
8.2	Future work	168
8.3	Concluding remarks	171
A	Tissue culture	207
A.1	Plant cells	207
A.1.1	Liquid culture	207
A.1.2	Solid culture	208
A.1.3	Protoplast digest	208
A.2	Mammalian cells	209
A.2.1	Cell culture	209
A.2.2	Transfection protocol	209
B	The multiphoton intrapulse interference phase scan system	211
B.1	MIIPS optical set-up	211
B.2	MIIPS theory	211
C	Structured illumination microscopy	215
C.1	Principle of lateral resolution enhancement	216
C.1.1	Extension to 3D-SIM	217

C.2	Capturing a SIM image	219
C.2.1	Choice of sample	220
C.2.2	Sample preparation and mounting	220
C.2.3	Setting up for a SIM exposure	221
C.2.4	SIM exposure	222
C.2.5	Image reconstruction	223
D	Python code for determining the centre of mass	226

1 | Introduction

1.1 Preface

The application of light to biological systems is known as biophotonics. Using light it is possible to gently and non-invasively image and manipulate microscopic objects, such as biological cells, performing high-precision surgery and accurate biological measurements. The properties of light affect its interactions with matter. Changing the wavelength, intensity and spatial and temporal shape of incident light can elicit different effects in biological tissue; from sub-cellular ablation to photothermal therapy, creating a wide range of applications within this rapidly-expanding field.

1.1.1 Light for therapy, manipulation and imaging

Light is inherently multifunctional and can perform both therapeutic and diagnostic roles. Combining different light-based techniques into a multimodal tool can be a trivial task. Using different modalities it is possible to span a wide range of specimens, from whole organisms to single molecules.

Interactions of light with biological tissue are dependent on the incident light parameters. Careful selection of parameters can create specific and gentle, yet effective therapeutic effects. Light-based therapies invoke light for treatment of cancers and skin conditions, such as vitiligo, psoriasis and acne [1]. Many techniques employ light

for delivery of drugs into tissue and cells. At the cellular level, it is possible to use a tightly-focused laser to introduce drugs, dyes and nucleic acids into single cells and sub-cellular components, in a technique known as photoporation [2].

Optical imaging and sensing can provide important information in clinical and research fields. The development of optical imaging modalities such as optical coherence tomography [3], photoacoustic tomography [4] and diffuse optical imaging [5], have allowed imaging of previously optically inaccessible areas of the body with increased depth, contrast and resolution. The capacity to guide light along optical fibres also makes many optical imaging techniques applicable to non-invasive *in vivo* imaging in endoscopic arrangements. Incorporating spectroscopic techniques allows the remote determination of molecular composition, providing highly sensitive biosensors for diagnostics and non-invasive “optical biopsies” [6]. Moving to cell imaging, it is possible to track specific cellular proteins in real-time using optical microscopy techniques. In the past two decades, the achievable resolution has been squeezed beyond theoretical limits, allowing super-resolution imaging of single molecules [7].

The high precision of many biophotonic techniques is owed to the development of the laser. Laser light is temporally and spatially coherent, making it possible to focus down to sub-micrometre sizes, smaller than a cell. In this way, light has been used to activate neuron spiking (optogenetics [8]) and gene expression within cells with high spatial and temporal resolution, precisely controlling single cells within an organism or network. Light can also be used to gently move and manipulate individual cells and biomolecules, known as optical trapping [9], to investigate cell and biomolecule function.

1.1.2 Plants in biophotonics

The majority of biophotonics studies concentrate on mammalian cells. These cells can be highly representative of the *in vivo* environment of the human body and as such

provide a useful surrogate in medical research, a wide and important field. Investigation of plant biology, however, can be deemed to be an equally important, yet challenging, task. Harnessing light to create energy, plants are primary producers and provide a basis for feeding nearly every other organism on Earth. An understanding of plant physiology, genetics and breeding is needed for crop improvement. Artificial manipulation can provide advantages in targeted breeding approaches.

Using light as a tool for manipulating plant cells and tissues is hampered by cellular components absent in mammalian cell systems. A thick cellulosic cell wall introduces distortions into incident light that are magnified by absorptive and light-scattering plant tissue, reducing the transparency of the tissue and the depth to which light can penetrate. Overcoming these limitations requires careful choices of incident light parameters to minimise these effects and increase the effectiveness of biophotonic techniques in plant research.

1.2 Synopsis

This thesis will consider three biophotonic techniques and their potential applications in plant cell research. By structuring the light, spatially and temporally, it is possible to improve on standard techniques, making them more effective and increasing their usefulness and versatility.

Two of these biophotonic tools are introduced in Chapter 2: photoporation - the ability to inject membrane impermeable substances into cells using light - and optical trapping - using light to pick up microscopic objects and move them around. The motivation, mechanisms and uses of these methods are discussed in relation to mammalian cells initially. Chapter 3 then discusses the role of photoporation in plant cell research. The differences between plant and mammalian cells are highlighted and reasons for genetically modifying plant cells and common techniques used to do so are discussed. A comprehensive review of plant photoporation literature is then presented.

Chapters 4-6 are concerned with the development and optimisation of photoporation of a model plant cell suspension line. Chapter 4 discusses the design, construction and characterisation of a photoporation system optimised for plant photoporation. Chapter 5 presents the results of photoporating tobacco BY-2 cells when optical and biological parameters are varied. In particular, the spatial intensity is modified to produce an “optical syringe” and the effect on photoporation efficacy is monitored. Chapter 6 discusses the role of pulse duration in selected biophotonic techniques and investigates the effect of using broadband ultrashort pulses on plant and mammalian cell photoporation.

Chapter 7 demonstrates the characterisation of a novel fibre-based optical trap for integration onto various microscope systems, including fluorescence microscopy. A commercial structured illumination microscope (SIM) is used as a basis for the induction of immune cell interactions; using the optical trap to demonstrate its versatility. The microscope is then used to image plant cells at super resolution for comparison with other SIM studies in plant science.

Chapter 8 concludes on the results documented in the previous chapters and discusses ways in which the investigations performed in this thesis can be expanded upon and improved.

2 | Optical manipulation of mammalian cells

2.1 Introduction

Light can create sub-micrometre sized holes in a cell membrane, a technique known as photoporation. These transient pores allow the passage of membrane-impermeable molecules into cells for functional studies. Light is also able to exert picoNewton forces, enough to move microscopic objects such as cells, in an optical trap [10]. These laser-mediated manipulations allow precise control over biological systems.

This chapter describes and evaluates photoporation and optical trapping as tools that are part of a wider biophotonic toolbox. The background, mechanisms and theory behind these techniques are presented, along with reviews of the biological uses and key achievements.

2.2 Photoporation

Photoporation is a generic term that can be applied to any technique that uses light ("photo-" taken from the Greek for light) to make holes (or pores) in a cell membrane. A tightly-focused laser beam created by a high numerical aperture (NA, see Figure 2.1 for an aside on numerical aperture) objective applied to a single point on the cell mem-

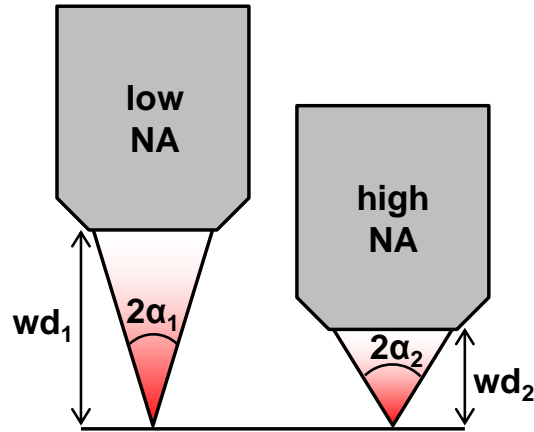


Figure 2.1 – Comparison of low and high numerical aperture (NA) objectives. The NA of a lens is $\sin\alpha$. A larger NA allows light to be collected from/illuminated at higher angles, reducing the size of the focused spot imaged/produced but increasing the divergence before and after the focal point. The highest NA objectives allow the highest possible resolution (both laterally and axially) but also tend to have short working distances (wd) and require oil as an immersion medium.

brane can transiently increase the permeability in a highly localised area (Figure 2.2). Membrane-impermeable molecules can then be taken up by the cell through the pore, this is termed optical injection (or optical transfection if nucleic acids are injected and expressed by the cell). Use of a mediator can allow light to create multiple pores in large numbers of cells at the same time, called optoporation or cellular laserfection [11]. A summary of the terminology used in this thesis is listed in Table 2.1.

2.2.1 Bypassing the cell membrane

Cells are the basic units of structure and function for all life; ranging from simple, single-celled organisms to complex bodies such as plants and animals. If we can understand the function, interactions and structure of single cells then we can begin to understand the mechanisms behind how complex organisms function.

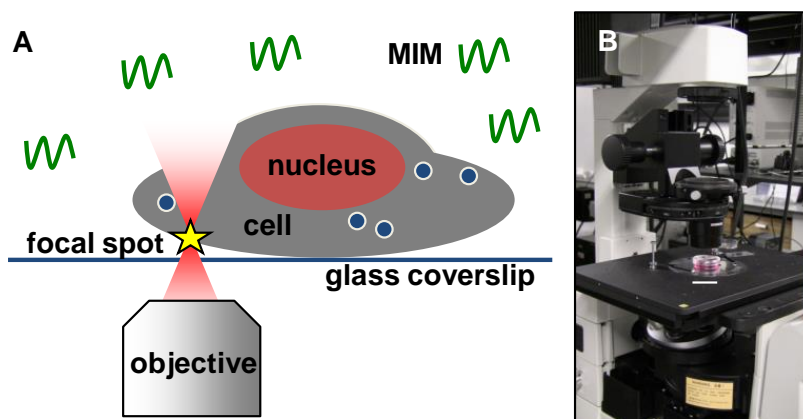


Figure 2.2 – Mammalian cell photoporation. The schematic (A - adapted from Mthunzi *et al.* [12]) depicts a cell adhered to a glass coverslip in medium containing the membrane-impermeable molecule (MIM) of choice. The objective is focused to align the focal point of the laser to the cell membrane. Induced multiphoton effects lead to a localised and transient increase in membrane permeability, allowing the MIM to diffuse into the cell. An inverted microscope set-up is usually used for photoporation, as in (B), which shows a glass-bottomed dish of mammalian cells in a Nikon microscope ready for photoporation experiments. Scale bar (white line) denotes 20 mm.

The delivery of functional molecules into living eukaryotic cells is a common research technique to study an organism's physiology. Desirable compounds for introduction into cells can include nucleic acids for gene function and protein expression studies [13], biosensors for monitoring response to stimuli as well as proteins, antibodies, dyes and drugs. However, the lipid bilayer of the cell membrane maintains the integrity of the cell and acts as a barrier to defend the cell against foreign molecules. Photoporation provides a protocol for molecular delivery into the cell that is more sterile and selective than its counterparts (discussed in Table 2.2), making it ideal for single cell analysis.

All cells are bounded by a phospholipid bilayer (Figure 2.3), separating the intracellular and extracellular environments and controlling transport of molecules into and out of the cell. These bilayers can also be found in many sub-cellular structures such as the Golgi apparatus, endoplasmic reticulum (ER), mitochondria and nuclear envelope.

Term	Description
Photoporation	Temporarily increasing the cell membrane permeability using light. A generic term.
Optoinjection	Laser-mediated injection of <i>membrane-impermeable molecules</i> into <i>single</i> cells.
Optical transfection	Laser-mediated injection of <i>nucleic acids</i> into <i>single</i> cells and the subsequent expression of the desired phenotype.
Optoporation	Delivering membrane-impermeable molecules and nucleic acids into <i>multiple</i> cells at once using light.

Table 2.1 – Explanation of photoporation terminology used in this thesis as defined in the literature [11].

Bilayers provide compartmentalisation, giving each organelle a distinct function, and aid the packaging of molecules for numerous uses such as exo- and endocytosis [14].

Phospholipids consist of a phosphate polar head and two non-polar, fatty acid tails. The bipolar nature of phospholipids causes them to spontaneously self-assemble into bilayers when in water, with the hydrophilic heads facing outwards to shield the hydrophobic tails from the water. The ends of the bilayers can then join to create a double membrane-bound vesicle, such as a cell. Along with phospholipids, the cell membrane also contains cholesterol and proteins. Cholesterol helps to maintain membrane fluidity at temperature extremes. Membrane proteins have many uses including transport of molecules across the membrane, receptor sites, cell-cell recognition, enzymes and cytoskeleton anchoring. These membrane constituents do not remain stationary but instead diffuse laterally within the plane of the membrane according to the fluid-mosaic model [15].

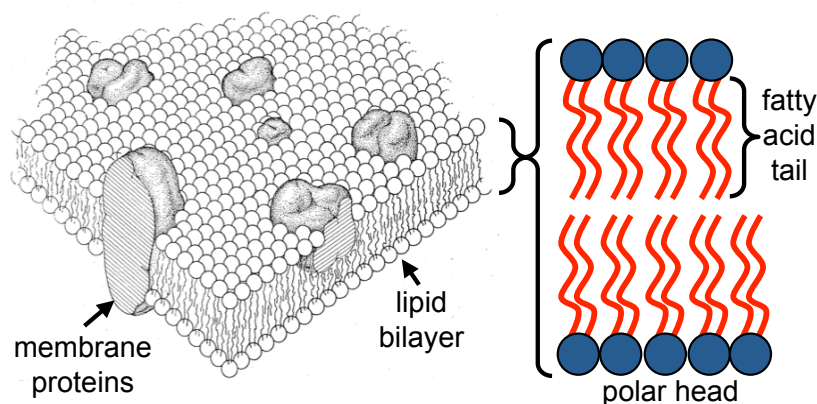


Figure 2.3 – The structure of the cell membrane showing the basic phospholipid bilayer and examples of integral and surface proteins, which have differing functions. Magnification of the bilayer shows the arrangement of the hydrophilic phosphate heads (blue circles) and the hydrophobic lipid tails (red lines). *From [15]. Reprinted with permission from AAAS.*

Cells employ a variety of mechanisms to transport molecules through the cell membrane. The phospholipid membrane is selectively permeable; very small molecules, such as polar water molecules, can diffuse across. Larger non-polar molecules can also easily pass through the hydrophobic region. Both ions and large polar molecules, into which category DNA (deoxyribonucleic acid) falls, cannot easily pass across the membrane, specialised proteins or externally applied effects are required for their transport.

Common research methods to bypass the membrane fall into two categories. High-throughput methods can target a large population of cells at once but lack selectivity whereas single-cell methods possess high efficiency of injection and sub-cellular precision but are slow and usually require highly skilled workers. A short summary of some of the most common transfection and injection methods are highlighted in Table 2.2. The ability of photoporation to maintain single-cell selectivity, while possessing the capability for high throughput, through the use of beam multiplexing and holography [16] or in conjunction with microfluidic systems [17, 18], makes it an accessible and useful tool in mammalian cell research. The mechanisms by which photoporation,

particularly pertaining to femtosecond lasers, can achieve such precision and efficiency are outlined in the next section.

Method	Description	SCT	Advantages	Disadvantages
Photoporation	Focused laser beam	Y	Moderate throughput, selective	Low penetration depth
Electroporation	Applied voltage	N	High throughput	Low cell viability
Viral vector	Engineered virus	N	High efficiency and viability	Slow to produce, biosafety issues
Chemical methods	Cationic polymers or lipoplexes	N	High throughput	Low cell viability
Microinjection	Microneedle	Y	High efficiency	Slow and highly technical
Single-cell electroporation	Glass pipette and microelectrode	Y	Selective	Slow

Table 2.2 – Summary of transfection/injection methods [19]. SCT = single cell targeting possible.

2.2.2 Photoporation mechanisms

It is possible to vary the damage mechanism by which pores are induced in a cell membrane by changing the laser parameters: primarily the irradiance, wavelength and pulse duration, although focal spot size and pulse repetition rate also influence photoporation.

Continuous wave (CW) lasers

For poration to occur, first absorption of the incident light must take place. In the case of CW and long pulse durations (μs and longer), linear absorption drives membrane poration [20]. The amount of absorption is dependent on the absorption coefficient of the tissue at the laser wavelength. Near-ultraviolet (NUV) lasers have been employed successfully for stable optical transfection because membrane constituents absorb at these wavelengths [21]. Absorption of cellular tissue, however, is not very high at NUV and visible wavelengths, leading to the use of highly absorptive dyes, such as Phenol-Red to enhance linear absorption. In the linear absorption regime, membrane permeabilisation is attributed to localised heating and a subsequent membrane phase change to increase fluidity (488 nm [22–24]) or oxidative stress (405 nm [25]). NUV and visible CW lasers are comparatively inexpensive and compact, making them ideal for adding a photoporation modality to any microscopy system.

Pulsed lasers

Using pulsed lasers, the higher field strengths created by the temporally-confined photons leads to high photon densities at the focal spot and allows multiphoton absorption. Multiphoton absorption (Figure 2.4) involves multiple photons being absorbed simultaneously to drive an atomic transition that a single low-energy photon could not. High densities of low energy, near-infrared (NIR) photons can be used to induce multiphoton effects. The multiphoton absorption rate is $\propto I^k$, where I is the incident intensity and k is the number of photons absorbed (therefore $\propto I$ in the case of linear absorption). Multiphoton effects therefore only become important at high intensities made possible with pulsed lasers.

Multiphoton absorption in biological tissue leads to plasma formation as molecules are excited (Figure 2.4). Biological tissue primarily consists of water so theoretical models of laser-tissue interactions are usually concerned with the excitation of water.

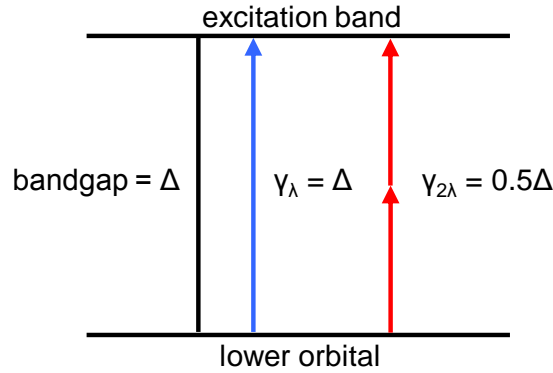


Figure 2.4 – Linear and multiphoton excitation of water. A bandgap of Δ requires the absorption of either a single photon of wavelength λ or multiple photons of longer wavelength ($2\lambda, 3\lambda \dots k\lambda$) to supply the requisite energy for ionisation to occur.

Water is treated as an amorphous semiconductor with a bandgap of $\Delta = 6.5$ eV [26]. When energy is absorbed, bound electrons are promoted into the conduction band and become “quasi-free” (the transition and the electron state are termed “ionisation” and “free” for simplified discussion in the literature and the following section).

The creation of free electrons in the focal spot by multiphoton ionisation (MPI) [27] creates a localised low-density plasma. Once these “seed” electrons have been created they can impact ionise further electrons, in a cascade effect (Figure 2.5). Electrons require a finite time to gain enough energy for cascade ionisation [20] so shorter pulses rely more on the seed electrons to create plasma-mediated effects. Longer pulses, however, have more time for cascade electrons to contribute to the plasma [28].

Optical breakdown of biological tissue occurs when a critical plasma density ($\rho_{crit} \geq 10^{21} \text{ cm}^{-3}$) is reached. For nanosecond pulses, damage effects are strongly delineated around the threshold irradiance, I_R . Below I_R no MPI and free electron generation can occur and above I_R very large free electron densities are produced as cascade ionisation dominates free electron generation (Figure 2.6A).

Reducing the pulse duration increases I_R (average power per unit area) but decreases

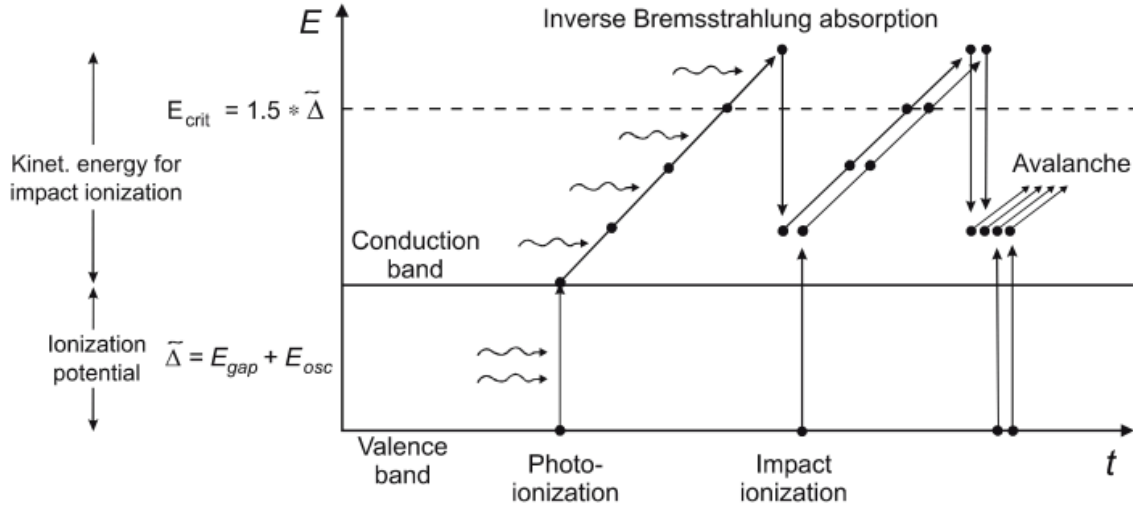


Figure 2.5 – Cascade ionisation schematic. Once an electron has been photoionised, it can gain energy by inverse Bremsstrahlung (absorbing photons in the presence of an ion). Once enough photons have been absorbed, the electron can impact ionise a molecule to free a second electron, both free electrons can continue to absorb photons and ionise further electrons in an avalanche process. *With kind permission from Springer Science+Business Media [20].*

the necessary radiant exposure threshold, Φ_{th} (pulse energy per unit area, $\Phi_{th} = \tau I_R$ where τ is the pulse duration) for optical breakdown [28]. As the time for effects to occur is shortened, damage mechanisms rely more on MPI than cascade ionisation, increasing the necessary irradiance. The overall pulse energy, however, decreases because at shorter pulse durations, the critical irradiance can be reached with smaller input pulse energies (Figure 2.7). When reducing the pulse duration to femtosecond length, the majority of electrons are generated by MPI. The free electron density has a smooth dependence on input irradiance, making it possible to finely tune the plasma density by changing the irradiance (Figure 2.6B) [20]. It is therefore possible to elicit cellular surgery without exceeding the breakdown threshold and associated damaging effects. At low irradiances, the primary poration mechanism is through photochemical effects such as the creation of reactive oxygen species, which are damaging to cells [20].

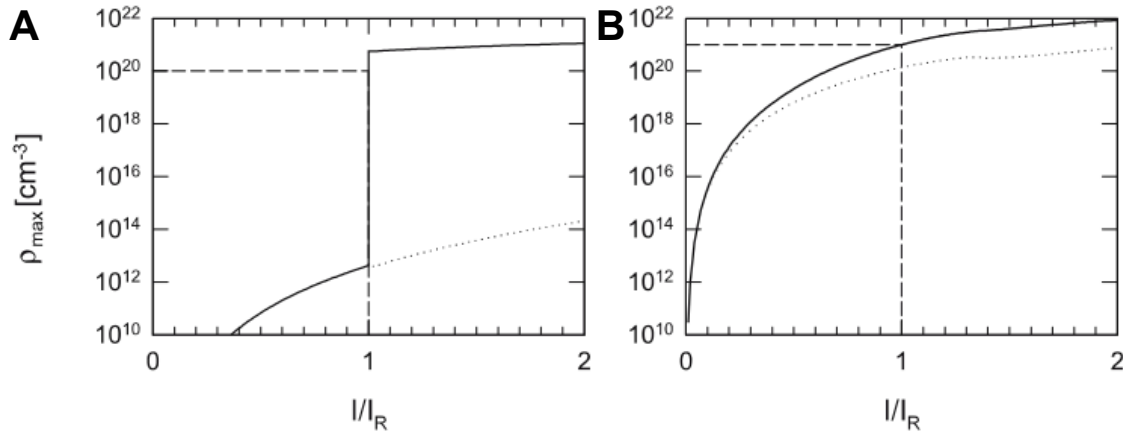


Figure 2.6 – Variation in the maximum free electron density created as the irradiance changes for nanosecond (A) and femtosecond (B) pulses. Dotted line represents the role of multiphoton ionisation only. Nanosecond pulses rely much more on cascade ionisation to create a high free electron density. Below the threshold for cascade ionisation very few free electrons are created, the density increases by nine orders of magnitude as the irradiance threshold is reached. Femtosecond pulses, however, have a much greater proportion of free electrons created by multiphoton ionisation, creating an electron density that varies smoothly with input irradiance. Picosecond pulses reflect a middle ground between the two. A representative ps graph would display a discontinuity as in (A) but with a higher electron density at $I < I_R$. *With kind permission from Springer Science+Business Media [20].*

The poration mechanism is also dependent upon the pulse repetition rate. There are two regimes that are usually used for laser nanosurgery studies: low energy pulses with high repetition rate (typically 80 MHz, the regime used in this thesis) and high, around threshold, energy pulses with kHz repetition rates. The first regime relies on the accumulation of chemical effects over multiple pulses for damage to occur. The irradiances used for optical transfection lie just below the level where thermal effects begin to occur. As the irradiance level is increased large bubbles, with lifetimes of a few seconds are seen caused by dissociation of biomolecules and leading to cell death [20]. In between these effects, small transient bubbles that allow optoinjection occur.

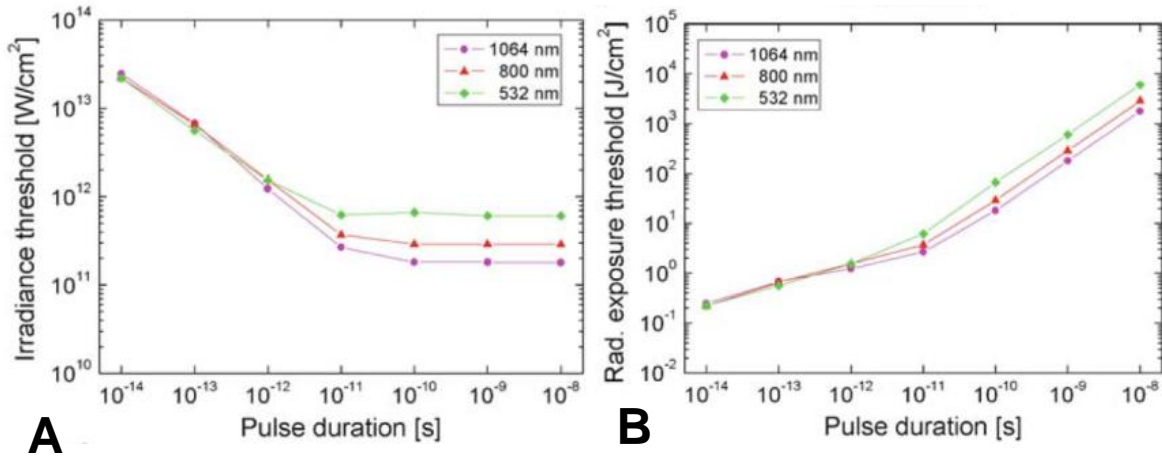


Figure 2.7 – Graphs depicting the change in threshold irradiance and threshold radiant exposure with pulse duration for different wavelengths. In (A), as the pulse duration decreases, less time is available for avalanche ionisation to take place so plasma formation is dominated by MPI, requiring a larger threshold irradiance to provide the necessary electrons. This increase plateaus after 10 ps because then only a threshold irradiance high enough to provide seed electrons for avalanche ionisation is required. The threshold radiant exposure (B), however, decreases with decreasing pulse duration because the threshold irradiance can be reached with smaller radiant thresholds. Recombination of free electrons and ions (reducing the plasma density) also matters less at shorter timescales. *With kind permission from Springer Science+Business Media [20].*

The mechanism behind these bubbles is not elucidated in the literature but is probably due to an interplay between chemical and thermal effects. The second regime (a few kHz), conversely, has long gaps between pulses so cumulative chemical effects cannot be relied upon and the energy must be raised to a point where thermomechanical effects are dominant [20]. This leads to the creation of more violent, less confined effects, although recent studies have optimised photoporation with kHz femtosecond lasers to achieve 30 % transfection efficiency [29].

Indirect and multiple cell targeting methods

CW and pico- and femtosecond photoporation create small areas of cellular injury in the cell membrane for localised delivery of exogenous molecules. This efficient and highly viable method provides many opportunities for single cell studies but is relatively low throughput compared to other traditional methods. It is, however, possible to use optical techniques to target large numbers of cells at once for high throughput molecular delivery while retaining some advantages of optical methods [30–32], such as easy integration into standard microscopes.

Nanosecond lasers provide limited precision in photoporation, owing to the production of high energy plasmas and propagating shockwaves at high pulse energies. By focusing a single nanosecond pulse 10 μm above a cell monolayer (Figure 2.8A), the laser energy is deposited faster than temperature diffusion can take place, leading to thermal confinement within the focal volume, invoking high tensile stresses [28]. This leads to stresswave propagation outside the focal volume causing mechanical damage and even large shockwaves at $I \gg I_R$, that can propagate over large distances spanning many cells [33]. The pressure generated by the shockwave itself is too low to induce membrane permeabilisation but the creation, expansion and subsequent collapse of a cavitation bubble exerts shear stresses capable of lysing cells at radii greater than a few cells' widths. Spreading out from the point of energy deposition, the maximum shear stress cells are subjected to decreases, reducing the extent of the cell injury incurred. Hellman *et al.* [30] identified four distinct regions of cellular injury under optical breakdown; lysis, necrosis, permeabilisation and unaffected (Figure 2.8B). The third region is crucial; where cells were subjected to shear stresses 8-16 kPa, cells were permeabilised but remained viable.

Further studies have investigated the effect of changing experimental parameters to reduce the number of lysed cells and optimise the number of permeabilised and viable cells. Compton *et al.* [34] reduced the pulse duration to the picosecond regime, reducing

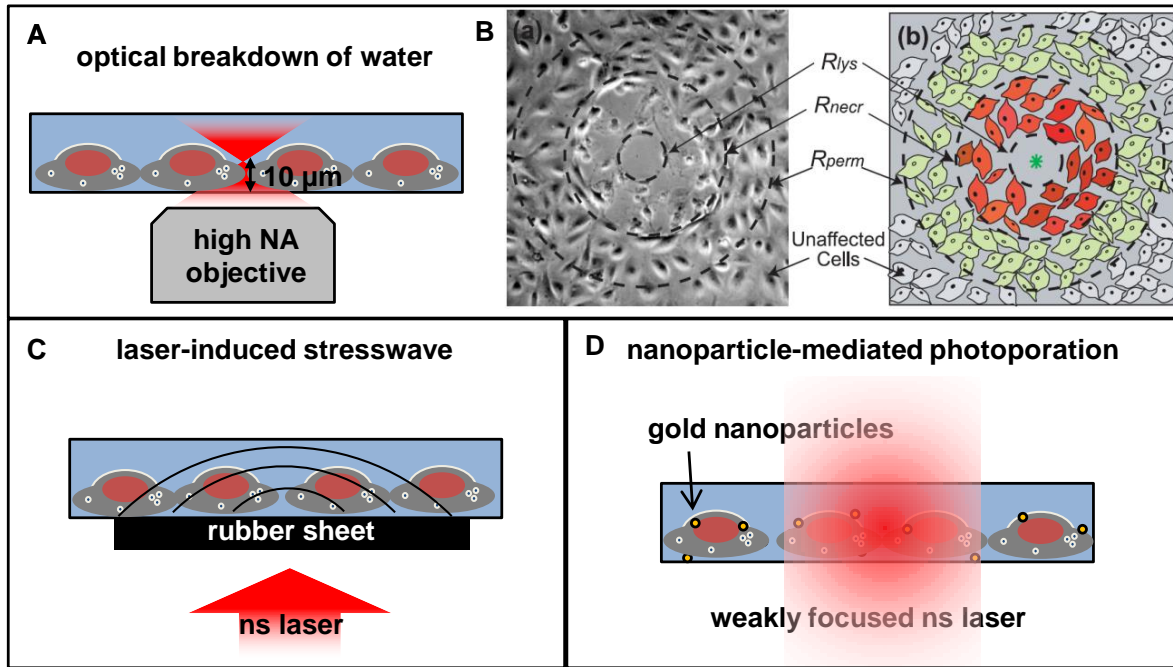


Figure 2.8 – Summary of the main indirect photoporation methods, using an intermediary agent to induce membrane permeabilisation. (A) A single tightly focused nanosecond pulse, using a high NA objective, just above a cell monolayer causes optical breakdown of the medium, leading to a cavitation bubble, exerting shear stress on the cells. As the shear stress experienced by the cells drops with distance from the point of irradiation, the damage incurred by the cells decreases too ((B) - (a) is a brightfield image and (b) is the corresponding schematic). In the centre, cells are lysed or killed. At large radii, cells are unaffected but in between these regions cells experience shear stress just large enough to permeabilise the membrane while retaining viability. [30] Copyright Wiley-VCH Verlag GmbH & Co. KGaA. Reproduced with permission. (C) When a rubber sheet adjacent to the cell chamber is irradiated by a nanosecond laser beam, a stresswave propagates into the chamber and permeabilises cells [31]. (D) Gold nanoparticles absorb photons from a weakly focused nanosecond laser beam and subsequent heating effects cause permeabilisation of the cell membrane [32].

the required pulse energy for optical breakdown and producing smaller damage regions. Arita *et al.* used a more complex, but effective, method by inducing optical breakdown in polystyrene [35] and gold [36] nanoparticles rather than the water itself. An optical

tweezer was used to lift the nanoparticle from the monolayer by a defined amount and a co-aligned nanosecond pulse initiated optical breakdown of the nanoparticle. The lower breakdown threshold for these materials compared to water or buffer requires pulse energies 1-2 orders of magnitude lower to induce optical breakdown and subsequent cavitation bubble formation. The size of the cavitation bubble is therefore reduced and it was possible to induce membrane permeability and transfection in up to 30 cells per nanoparticle without loss of viability.

Other optical techniques employ nanoparticles for membrane permeabilisation by exploiting absorptive effects. Generally, nanometre gold particles are adhered to cell membranes and irradiated by a weakly focused nanosecond pulsed laser (Figure 2.8D). Absorption of the light by nanoparticles leads to heating effects and, combined with plasmonic near-field enhancement creating low-density plasma effects surrounding the nanoparticle, induces permeabilisation of the cell membrane [32, 37, 38]. While the precise mechanism is not well understood and DNA transfection has not been consistently demonstrated, nanoparticles can be conjugated to a specific sub-population of cells, combining cell specificity with high throughput [39].

Terakawa *et al.* [31] also employ nanosecond pulses for indirect optical transfection, with a rubber sheet as a mediator. The irradiation of the rubber sheet, upon which a dish of cells can be placed, creates stresswaves that then propagate to permeabilise the cells (Figure 2.8C). Again, cavitation and shear stress are cited as the poration mechanisms. This technique has greater potential for deep *in vivo* photoporation than other methods due to the large propagation distance of the stresswave.

Both laser-induced shockwaves and laser-nanoparticle interactions have been employed to photoporate plant cells too, and will be discussed in a plant study context in Section 3.4. While high numbers of cells can be permeabilised at once when using indirect methods, high numbers of targeted cells can be lost or killed and injection and transfection efficiencies are typically low or inconsistent.

Comparison of photoporation techniques

Changing the laser parameters can dramatically affect the mechanism by which photoporation occurs. These can be broadly grouped into two groups, direct and indirect laser targeting.

The former group, where the laser is focused onto the cell membrane, causes localised damage to a small area on the cell membrane, inducing permeabilisation with sub-cellular precision. This group can be divided further by considering CW and pulsed lasers.

CW lasers are inexpensive and readily accessible, making them a useful entry-level tool for novices in photoporation. The damage region is confined to the area of linear absorption; the laser focal spot size is reduced due to the use of short wavelengths (NUV and visible). The necessity for sensitisers, however, introduces additional complexity and potentially toxic effects. Required irradiation times are also up to 250 times longer (up to 10 s) than typically used with femtosecond lasers (40 ms), substantially increasing the time taken to photoporate multiple cells.

The multiphoton nature of pulsed laser damage negates the need for sensitisers. Highly penetrating and minimally absorbed NIR pulsed lasers can be exploited for MPI of water, reducing the size of the damage region to the centre of the focal spot, a similar volume to NUV CW lasers. Femtosecond pulses allow fine, highly precise effects that are controlled by varying the input power. The, potentially prohibitive, high cost of femtosecond lasers can limit their accessibility. As technology improves, the expense of advanced lasers such as these will drop, widening the scope of femtosecond photoporation to many research applications. Indeed, many laboratories already possess suitable femtosecond lasers in multiphoton microscope systems.

Indirect methods use relatively inexpensive nanosecond lasers with a mediator to apply shear stress to cells by cavitation. Permeabilising multiple cells significantly increases throughput compared to direct methods, proving useful when large numbers of

a cell line are desired. While antibody conjugation of nanoparticles allows specificity to a single (immune) cell line, all single-cell selectivity, to perhaps investigate interactions between adjacent cells, is lost. The large numbers of cells lysed or detached using these indirect methods also makes them unsuitable for studies where few cells are available.

As a highly selective and minimally invasive photoporation tool, Chapters 5 and 6 of this thesis will be concerned with using femtosecond lasers for single-cell photoporation of plant and mammalian cells. The next section will concentrate on important biological and optical advances made in femtosecond photoporation of mammalian cells.

2.2.3 Femtosecond photoporation in mammalian cells

The damage mechanisms highlighted in Section 2.2.2 clearly identify femtosecond lasers as the single-cell photoporation tool of choice. The low pulse energies required and sub-cellular damage areas create highly precise and efficient injection and transfection (typically 40-60 %) while maintaining high viability (> 90 %). Femtosecond photoporation has proven a useful technique to target a variety of cell types and molecules.

Table 2.3 considers some important cell lines that have been successfully transfected or injected using femtosecond lasers. Many of these cell lines are hard to transfect by conventional methods. The mechanical (rather than biological) poration mechanism allows even recalcitrant cell types, such as stem cells, neurons, embryos and *in vivo* applications, to be efficiently transfected (Figure 2.9). The laser irradiation protocol varies between applications; multiple tightly-focused irradiation sites allow multiple points of entry for maximum delivery of exogenous molecules, which has proven effective for transfecting post-mitotic primary neurons [40–43]. For *in vivo* applications, lenses [44] or low NA (numerical aperture) objectives scanned over a region [45, 46] are used to target a wider area. While the efficacy of this technique is evident from increased expression of injected DNA, the mechanism of membrane permeabilisation is unknown,

Cell type	Laser			Shooting protocol					
	λ (nm)	PRR (MHz)	PW (fs)	NA	P (mW)	ET (ms)	Geometry	Eff. (%)	Ref.
Human salivary gland SC	800	75	16 (f)	1.25	5-7	50	1	80 (u)	[47]
Mouse embryonic SC	790	80	200	0.8	60		3x	25 (c)	[12]
PC12	800	75	12	0.4	20	100	1x	100 (i)	[48]
Embryonic rat cortical N.	800	75	200	0.8	42-77	20-60	4x4 grid	12	[40]
Primary rat hippocampal N.	80	80	100	0.8	30	1-5	8-16 pulses	70	[41–43]
Goldfish retina explants	NIR	80	100	0.5	20	10	array of holes	N/A	[49]
Mouse tibial muscle	780	76	200	0.5	20	2-10	95x95 μ m scan	N/A	[45, 46]
Zebrafish embryo	800	80	10	1.0	45-215	200	3-5x	87 (i)	[50, 51]
Various animal embryos	800	10 ⁻³	120	0.25	0.2	50	1	50 (c)	[52]
Sea worm embryo	800	80	180	0.8	65	30	3x triangle	55 (i)	[53]
Mouse tumour	1043	0.2	500	0.5 cm	520	80000	1	N/A	[44]

Table 2.3 – Summary of a selection of optical transfection and injection studies on important cell lines (SC = stem cell, N = neuron). Noted laser parameters are wavelength (λ), pulse repetition rate (PRR) and pulse width (PW, (f) means measured at the laser focus, all others are output PW). Shooting protocol features are numerical aperture (NA), power (P), exposure time (ET) and irradiation geometry used. The efficiency (Eff.) is determined differently for different studies, (u) is uncorrected for cell division, (c) is corrected and (i) denotes injection efficiency, N/A for either no efficiency noted or relative protein expression levels only.

particularly considering high NAs ($\gtrsim 0.9$) are required to minimise nonlinear propagation effects in the focal volume and maintain localised energy deposition [20].

Femtosecond photoporation has also been successfully employed to inject a variety of exogenous substances, for various different applications, listed below.

- **DNA:** important examples include the ChR2 plasmid for optogenetics [40, 49].
- **mRNA:** for differentiation of embryonic stem cells [12], eliciting region-dependent mRNA effects in neurons [41, 43] and for fate-manipulation of cells [52].
- **Morpholinos:** a highly stable synthetic oligonucleotide used in embryo gene expression studies [52].
- **Transcriptome:** multiple transfections of astrocyte transcriptome into a primary neuron induced an altered phenotype [42].
- **Nanoparticles:** quantum dots [54] and gold nanoparticles [55].
- **Sucrose:** for biopreservation applications [56]

Several advances in femtosecond photoporation have been directed at improving efficiency and increasing throughput. This can be achieved by spatial shaping of the focused laser light, combined with computer control of multiple laser beams. The small size of the multiphoton region of a tightly focused Gaussian laser beam has been previously discussed in Section 2.2.2. While this reduces collateral damage to the surrounding region, it also constrains the throughput of this technique; precise alignment of the multiphoton region with the cell membrane is required to induce photoporation (Figure 2.10A). Misalignment of the laser focus from the cell membrane by more than a few microns can adversely affect photoporation, reducing the photoporation efficiency significantly [58]. To increase the throughput of photoporation, it is important to relax this stringent and time-consuming alignment process.

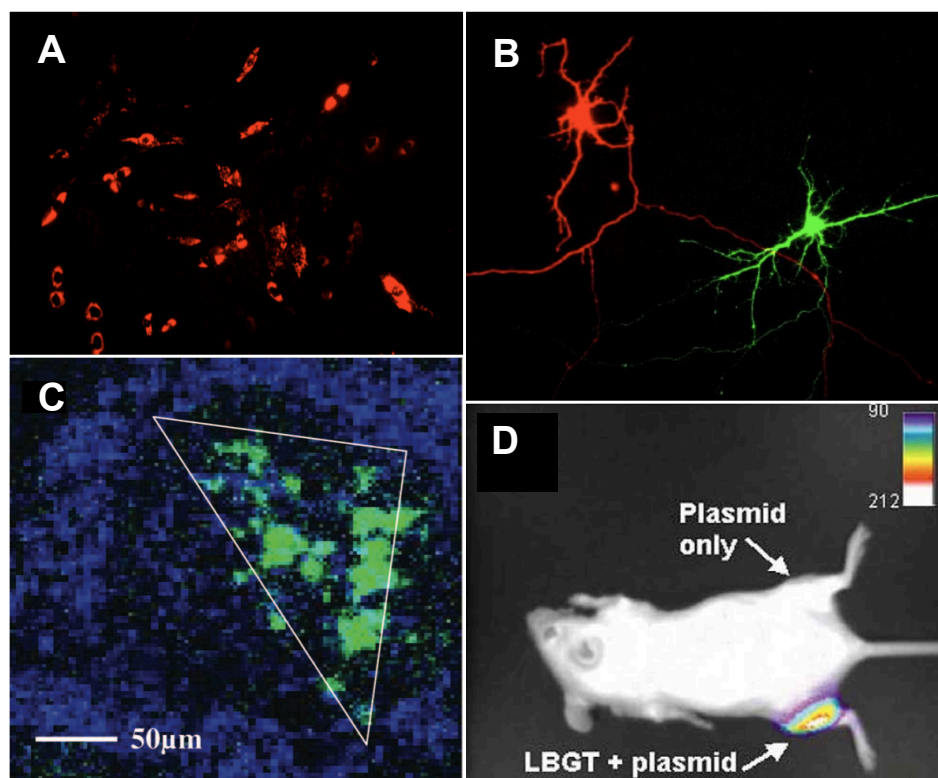


Figure 2.9 – Examples of optical transfection in mammalian cells. (A) Model CHO-K1 cells optically transfected with mitochondrially-tagged DsRed protein. [57] Copyright Wiley-VCH Verlag GmbH & Co. KGaA. Reproduced with permission. (B) Adjacent primary neurons optically transfected with different fluorescent proteins [40]. (C) Spatially selective expression of GFP only in a targeted area of cells in goldfish retina. Reprinted with permission from SPIE and the author [49]. (D) *in vivo* application, only the side where femtosecond laser irradiation was applied (LBGT + plasmid) shows expression of a bioluminescent protein. Reprinted by permission from Macmillan Publishers Ltd: *Molecular Therapy* [45], copyright (2003).

In 2008, exploration of optical transfection using a novel photoporation laser beam geometry paved the way for increased throughput of optical transfection and injection. A Bessel beam, which consists of a non-diffracting core surrounded by concentric rings, was used to optically transfect a model cell line. The long axial propagation of the central core, which extended over 100 μm , created a larger axial range over which

multiphoton effects that contribute to photoporation can occur. This “optical syringe” allowed efficient transfection over a much greater axial range (20 times) than a Gaussian beam of matched lateral diameter [58]. Combining Bessel beam photoporation with a microfluidic geometry (Figure 2.10B), to flow cells through the central core for a specific exposure time, has allowed throughput of up to 10 cells/s [18]. We will build upon this work in this thesis.

Another technique to increase the efficiency of photoporation is to apply a tightly-focused Gaussian beam at multiple irradiation sites, varying axial or transverse beam position [16]. Although this takes a greater amount of time to apply the multiple doses manually (a time delay between each dose is required to prevent accumulative effects between doses), the Gaussian beam is simpler to implement and more power efficient than the Bessel beam. It is therefore feasible to use a spatial light modulator (SLM) for automatic targeting and multiple dosing of each cell [59].

Both techniques provide a means to increase the efficiency of photoporation and provide different benefits, especially depending upon the available optomechanics and software control. A comparison of these two techniques in achieving efficient photoporation has not been performed previously but will be considered in Section 5.3.2. The basic irradiation protocol (a single Gaussian beam exposure) is compared to multiple Gaussian exposures and a single Bessel beam exposure. This is converse to the comparison performed in Tsampoula *et al.* where multiple doses of both the Gaussian and Bessel beams were applied to match total fluence [58]. This technique is potentially unnecessary for the Bessel beam where the membrane should be targeted with a single laser exposure.

The capacity for light to gently inject exogenous substances into cells has experienced significant uptake and development as a biophotonic tool in the past decade. Light is able to precisely and transiently injure a cell membrane (or other organelle in cellular surgery) while maintaining cell viability. In another capacity, it is possible to use a tightly-focused laser beam at vastly reduced irradiance levels to manipulate cells

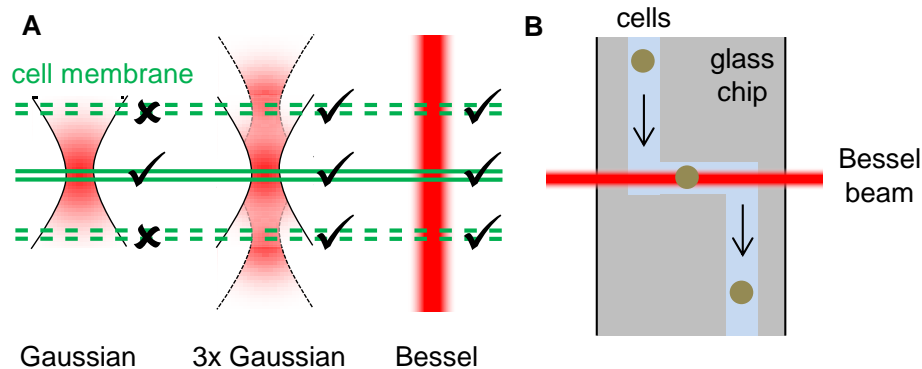


Figure 2.10 – The small axial extent of the multiphoton region of a tightly focused beam limits the axial range over which multiphoton effects can occur (A). If the cell membrane (green) is not aligned with the Gaussian beam focus then photoporation cannot occur. Application of multiple axially separated Gaussian doses can increase the possibility of targeting a misaligned membrane (dashed green). A Bessel beam acts like an “optical syringe” [60] to allow multiphoton effects to occur over much larger axial distances, relaxing the requirement for tight membrane focusing. The Bessel beam has proven useful in microfluidic applications (B) where it is possible to photoporate large numbers of cells in a short time by flowing them parallel to the central core (in red) [18].

in an entirely non-damaging way. Optical trapping is a biophotonic technique that has many important biological implications in moving cells, organelles, biomolecules and other objects. The next section concerns optical trapping as a highly sensitive tool to manipulate and quantify microscopic objects and forces.

2.3 Optical trapping

The ability of light, consisting of massless particles, to exert forces has been evident since the observation of comet tails in the sky. The comet dust tail points away from the Sun during its orbit, pushed by the radiation pressure from the Sun [61]. The huge flux of photons from massive objects such as stars has shaped the Universe we see around us, helping to drive galaxy formation and stellar evolution.

When moving from the astronomical to the microscopic scale, the forces involved drop significantly, as long as the objects being manipulated are equally small then optical manipulation is still possible. In 1970, Arthur Ashkin [62] demonstrated that it was possible to propel tiny particles ($1\text{--}2\ \mu\text{m}$) using focused beams of laser light and even hold a particle in place between two counter-propagating beams. Further development using tightly-focused beams made it possible to trap a particle using a single beam [63]. Use of a single beam simplifies the optical system required and makes optical trapping an easily-implemented biophotonic tool, realising what is now commonly termed optical tweezers. Crucially in biophotonics, optical traps can be used as highly-sensitive force transducers, capable of measuring picoNewton cellular forces with no detrimental laser damage of cells or biomolecules.

2.3.1 Optical trapping theory

To consider the forces acting on an optically-trapped particle using a single beam, two regimes are considered, the Mie and Rayleigh regime, dependent upon the particle size.

Mie regime

When the particle size is much greater than the wavelength of light, then a simple ray-optics approach is sufficient to describe optical trapping. As light passes through a particle, it will scatter in all directions. If homogeneous light impinges on one side of a particle then the scattered light will emerge isotropically on the other side. Each photon will change direction as it scatters from the particle but the dominating effect is from photons reflected backwards off the particle. Light carries momentum so a change in direction corresponds to a change in momentum. According to Newton's third law, the change in momentum of light will cause an equal and opposite force on the particle, pushing the particle in the direction of the light propagation [10]. This scattering force causes radiation pressure and is present in all optical traps. Homogeneous light has the

capacity to push a particle forwards; to trap a particle and manipulate it, there must be some variation in spatial intensity in the incident light, inducing a gradient force.

Considering a transparent particle with a higher refractive index than the medium, the light passing through the particle will be refracted. If the light passing through the particle is inhomogeneous in intensity then the change in momentum of light passing through will no longer be equal on either side of the particle (Figure 2.11A). The change in momentum of the higher intensity portion of the beam will be greater than the lower intensity portion, drawing the particle towards the former point by Newton's 3rd law. If the incident light is circularly symmetric with a central intensity peak (such as a Gaussian beam) then the force acting on the particle will always be towards the centre of the beam. The particle will then be held in the centre of the laser beam [10].

For weakly focused beams, the scattering force will hold the particle against a surface, allowing transverse movement only. If, however, the beam is tightly focused ($NA > 1.0$) then axial as well as transverse trapping can occur. Following the same ray optics principles, the gradient force acts towards the point of highest intensity axially too. This is termed an optical tweezer because the particle can now be picked up and moved in any required 3D direction [10].

The forces created by the passage of light rays of power P and incident angle θ in a medium of refractive index n_m through a spherical bead with reflection and transmission coefficients R and T respectively were calculated by Ashkin [64]:

$$F_S = \frac{n_m P}{c} \left[1 + R \cos 2\theta - \frac{T^2 (\cos(2\theta - 2r) + R \cos 2\theta)}{1 + R^2 + 2R \cos 2r} \right] \quad (2.1)$$

$$F_g = \frac{n_m P}{c} \left[R \sin 2\theta - \frac{T^2 (\sin(2\theta - 2r) + R \sin 2\theta)}{1 + R^2 + 2R \cos 2r} \right] \quad (2.2)$$

For trapping to occur, the gradient force F_g must be larger than the scattering force F_S . Increasing the incident angle relatively increases the gradient force, reinforcing the suggestion that higher NAs, contributing a greater number of high angle off-axis rays, create higher gradient forces and therefore greater trapping efficiency. The total force

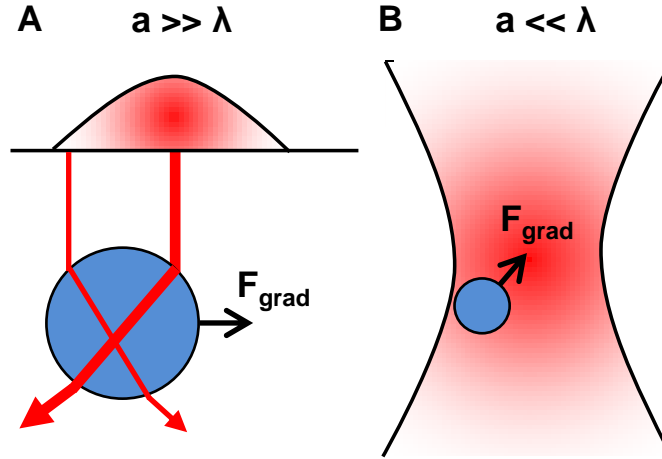


Figure 2.11 – Understanding optical trapping in two limits. The higher intensity in the centre of the applied beam causes the particle to be drawn towards the centre of the trap. When the particle size (a) is much larger than the wavelength of light (λ) then optical trapping can be understood using ray-optics (A). The change in momentum of light as it refracts through the off-centre particle is greater away from the point of highest intensity, the resulting change in momentum on the bead is therefore towards the trap centre. When $a \ll \lambda$, the bead is approximated to a point dipole. The force acting on it is then proportional to the intensity gradient when the refractive index of the bead is greater than that of the medium (B). Adapted from Dholakia *et al.* [61].

on the particle is therefore:

$$F_{trap} = \frac{Qn_m P}{c} \quad (2.3)$$

Where Q represents the Q value, a dimensionless measure of trapping efficiency. Theoretically $0 < Q < 2$ (from the transfer of photon momentum) but is experimentally < 0.3 [64].

Cells are generally $10\text{-}30\ \mu\text{m}$ in diameter and therefore fall into this regime. Cell trapping and trapping of $10\ \mu\text{m}$ beads using a novel optical fibre-based trap is demonstrated in Section 7.2, where the ray optics approximation is valid.

Rayleigh regime

When a dielectric particle is much smaller than the wavelength of light, it can be approximated as a point dipole. The forces acting on this dipole from the applied electric field is [63]:

$$F_S = \frac{In_m}{c} \frac{128\pi^5 r^6}{3\lambda^4} \left(\frac{m^2 - 1}{m^2 + 2} \right)^2 \quad (2.4)$$

$$F_g = \frac{n_m^3 r^3}{2} \left(\frac{m^2 - 1}{m^2 + 2} \right) \nabla E^2 \quad (2.5)$$

Where r is the size of the particle and $m = n_{\text{sphere}}/n_m$ and E is the amplitude of the electric field. Given that the intensity of the light, $I \propto E^2$, the gradient force is dependent on the gradient of the light intensity whereas the scattering force depends linearly on intensity. As long as the beam is focused tightly, increasing the intensity gradient, the particle will be drawn towards the point of highest intensity when $n_{\text{sphere}} > n_m$ (Figure 2.11B).

In between these two particle sizes is where most optical trapping occurs. The force analysis behind this parameter space (the Lorentz-Mie regime [61]) requires detailed numerical analysis for an accurate description of this regime where neither approximation discussed above is valid, though often researchers use the ray optics approach which gives reasonable agreement. Trapping of 1 and 2 μm beads, which fall into this regime, are performed for calibration purposes in Section 7.2.2.

Dual-beam traps

The trapping described above uses a single beam to trap particles, if instead two counter-propagating beams are used the particle is trapped between them. The trapping geometry usually employed is two opposing weakly focused beams, in this case the axial trapping is provided by gradient forces and the lateral trapping is provided by the scattering forces (Figure 2.12).

Dual-beam traps require precise alignment and potentially limiting geometry but

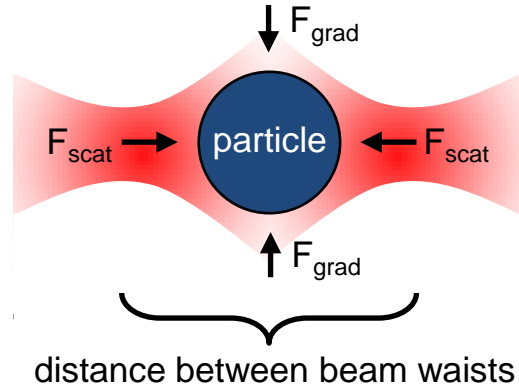


Figure 2.12 – Counter-propagating dual-beam traps employ scattering forces from two weakly-focused beams facing each other to hold a particle between them. The gradient force keeps the particle in the middle of the trapping region.

provide many advantages. The lower NAs used allow the use of longer working distance objectives or even optical fibres. The lack of a high intensity focal spot also reduces heating in the surrounding area. Using this trapping geometry, it is possible to trap larger objects than can be trapped with a single beam, including $100\ \mu\text{m}$ beads [65], embryos [53] and microorganisms [66].

Dual-beam traps are also used for cell-stretching experiments [9], where cell populations can be distinguished based on their deformability, and are useful for incorporation into microfluidic systems for high-throughput biophotonics experiments.

2.3.2 Trap calibration

The displacement, x , of a bead in a trap displays a Hookean proportionality to force, F , for small displacements $F = -\alpha x$ [67]. The trap stiffness, α , is typically on the order of tens of $\text{pN}\mu\text{m}^{-1}$. Calibrating an optical trap by determining this constant of proportionality allows precision force measurements to be performed, it also allows a trap to be compared to other optical traps. These are important points when testing a

novel trap type and important for later chapters, as in Section 7.2.2. There are many techniques for finding the trap stiffness that possess benefits and limitations.

Applying hydrodynamic drag by movement of the stage or optical trap can calibrate an optical trap (Figure 2.13). If small movements are made then α can be determined from the bead displacement [67].

$$\alpha = \frac{F_{drag}}{x} = \frac{\beta v_{fluid}}{x} \quad (2.6)$$

β is the Stokes' drag and v_{fluid} is the velocity of the fluid. Usually a piezo-driven stage is moved sinusoidally and the appropriate force variation applied to determine α . The dependence on β necessitates calculation of drag in the system, which is dependent on medium viscosity and the distance between the bead and the coverslip. When the bead is close to the coverslip, Faxen's correction must be applied, which corrects for a spherical body of diameter, r , moving at a distance, z , from a boundary in a viscous fluid (viscosity ν) [67]:

$$\beta = \frac{6\pi\nu r}{1 - \frac{9}{16} \left(\frac{r}{z}\right) + \frac{1}{8} \left(\frac{r}{z}\right)^3 - \frac{45}{256} \left(\frac{r}{z}\right)^4 - \frac{1}{16} \left(\frac{r}{z}\right)^5} \quad (2.7)$$

If the bead displacement is large then the linear proportionality between force and displacement is broken. While α is not measurable in this case, breaking this linearity allows the Q value to be determined. Increasing the stage or trap velocity to a point where $F_{trap} < F_{drag}$ will cause the bead to be lost from the trap. The velocity at which the trap was translated is then proportional to the Q value [68].

$$Q = \frac{\beta v_{fluid} c}{n_m P} \quad (2.8)$$

The escape method is useful when only a basic detector and stage are available to quantify the efficiency of a trap but, without knowledge of α , accurate force-displacement experiments are not feasible.

The optical trap acts as a harmonic potential well in which Brownian motion occurs.

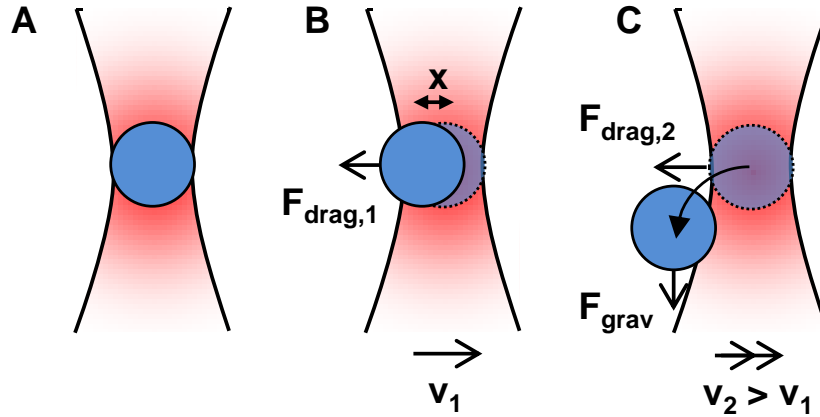


Figure 2.13 – Exerting hydrodynamic drag on an optically trapped bead can be used to calibrate an optical trap (A). Moving the optical trap or stage at a known velocity, v_1 exerts a drag force on the bead, causing it to be displaced a distance x , directly proportional to the force applied, from the centre of the trap (B), allowing determination of the trap stiffness. Applying a larger drag force (greater velocity v_2) breaks this proportionality and the bead will fall from the trap when the drag force exceeds the force exerted by the trap. The force at which the bead escapes can be used to determine the Q value.

If we track the position of a trapped bead, the nature of these fluctuations can determine the strength of the optical trap [10].

The power spectrum ($S_{xx}(f)$) of the bead's displacement follows a Lorentzian distribution [67].

$$S_{xx}(f) = \frac{k_B T}{\pi^2 \beta (f_0^2 + f^2)} \quad (2.9)$$

k_B is the Boltzmann constant, T is the temperature. The rolloff frequency, f_0 , can be determined from fitting this distribution to experimental data and is proportional to the trap stiffness following $\alpha = 2\pi\beta f_0$ (Figure 2.14D). Again, Faxen's correction (Equation 2.7) must be applied. Measurement of α by this method is independent of noise and misalignment in the optical system is evident in changes to the shape of the curve. A large bandwidth detector is, however, required to allow for Nyquist sampling of the roll-off frequency (at least $10f_0$ is suggested, usually kHz). A quadrant

photodiode (QPD) provides large bandwidths but also requires another calibration step to link signal to bead position (Figures 2.14A and B), a high-speed camera typically achieves lower bandwidths but position calibration is trivial.

A second method of determining α from the bead displacement considers the variance, which provides a drag-independent measure of α following equipartition [10].

$$\frac{1}{2}k_B T = \frac{1}{2}\alpha \langle x^2 \rangle \quad (2.10)$$

$\langle x^2 \rangle$ is equivalent to the variance (Figure 2.14C). Equipartition is a simple method to implement but requires an assumption of the temperature of the trap and the variance increases in the presence of drift or noise in the system, entangling these properties with α . There is no hard limit for the detector bandwidth, unlike the power spectrum method (although a low bandwidth detector does filter the movement and lead to a lower variance [10]).

The fibre-based optical trap developed in Section 7.2 possesses a relatively low NA that does not allow axial trapping. The equipartition method is independent of drag and is therefore highly suitable for calibrating this system. To avoid cumbersome position calibration with a QPD, a high speed camera is used to image bead displacement, simplifying displacement measurements but at the cost of potential noise and misalignment and reduced bandwidth filtering the movement.

2.3.3 Developments and applications

Many optical advances have improved the capacity of optical traps to manipulate and measure microscopic particles. Using acousto-optic deflectors, a single trap can be time-shared across multiple particles, creating optical landscapes for cell sorting [69] and tissue regeneration [70, 71]. The shape and polarisation of the trapping beam also affects trapping, providing the capacity to guide [72], sort [73] and spin [74] particles and increasing the types of particles that can be trapped (large metallic particles, for

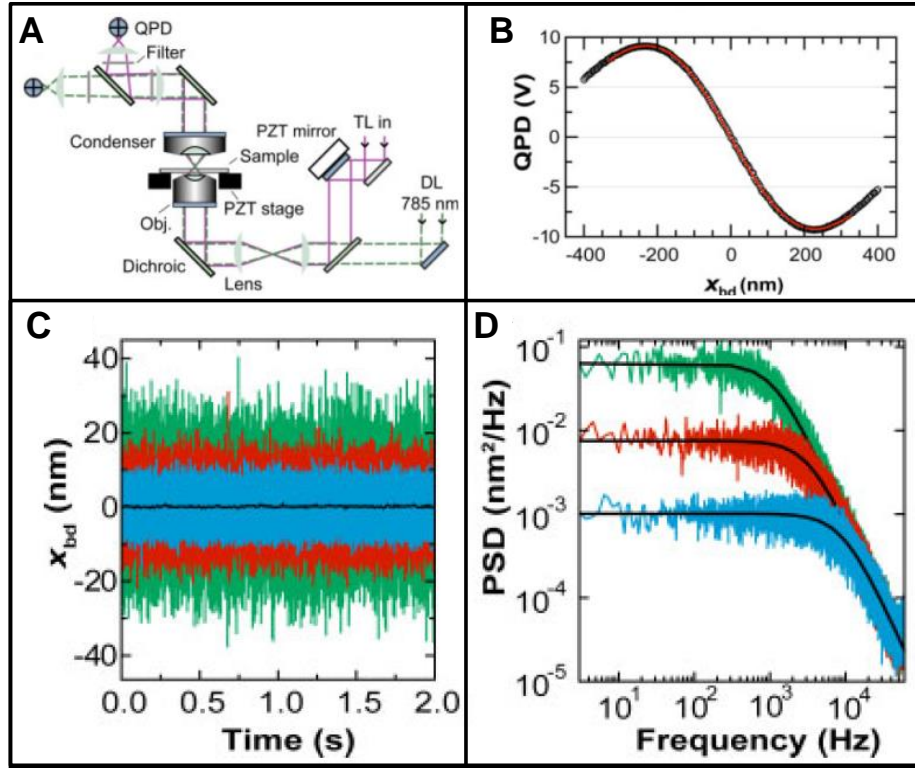


Figure 2.14 – Determination of trap stiffness from knowledge of bead Brownian motion. (A) A typical optical trapping set-up using forward scattering from a diode laser (DL) onto a QPD to measure the bead displacement. (B) Displacement to QPD signal calibration curve created by scanning a bead across the field of view and monitoring the QPD voltage. Bead displacement should lie within the linear region around $x_{bd} = 0$ for accurate monitoring of displacement for power spectrum or equipartition experiments. The variance of the bead motion in a trap can be used to determine α by the equipartition theorem. (C) shows the bead displacement for three different values of α (blue = $417 \text{ pN}\mu\text{m}^{-1}$, red = $130 \text{ pN}\mu\text{m}^{-1}$, green = $47 \text{ pN}\mu\text{m}^{-1}$). The black line shows the effect of reducing the bandwidth of the blue line from 120 to 100 Hz, filtering the bead movement. The rolloff (corner) frequency of the power spectrum density (PSD, D) of bead displacement is proportional to α , the same colour legend applies with black lines denoting fitted Lorentzian curves. *Reprinted by permission from John Wiley & Sons: Laser and Photonics Review [67].*

example [75]). SLMs [76] are routinely used to create dynamic traps [77], utilising multiple traps of differing beam types for complex manipulation of a variety of objects.

Optical trapping of micrometre objects has enhanced understanding in many fields, such as photonics, atomic and quantum physics, but the main beneficiary has been the biological sciences. Optical trapping has proven useful in a variety of biological contexts, from biochemistry up to blood flow in living animals [78]. A typical mammalian cell is 10-30 μm in size, easily trapped and manipulated using optical methods, allowing non-invasive and gentle studies of cellular mechanics. It is also possible to trap intracellularly [79], using either inserted particles or organelles, to quantify the cellular environment.

In the field of biochemistry, *in vitro* experiments involving the manipulation of biological structures, such as molecular motors and nucleic acids, have allowed precision measurements of biological processes involving nanoscale forces and distances. By monitoring the displacement of a particle in a calibrated trap, it is possible to accurately measure the strength of forces exerted on it. By conjugating biological molecules to optically trapped beads, the piconewton forces behind molecular reactions such as unzipping DNA [80] and molecular motors walking along cytoskeletal filaments can be measured.

2.3.4 Optical trapping and fluorescence microscopy

While a large majority of biological optical trapping studies are performed using only brightfield illumination to image the microscope field-of-view, much more information about cellular and biomolecular mechanics can be obtained by the use of fluorescent tags. Using fluorescence microscopy, cell function studies monitoring the movement of proteins under mechanical perturbation and advanced fluorescent techniques such as Förster resonance energy transfer (used to determine the proximity and conformation of certain biomolecules under optical tension in single molecule studies [67]) are possible. Epi-fluorescence is a standard microscopy technique that can easily be used

in combination with optical tweezers but, for some studies, higher spatial resolution is required, in the form of confocal, multiphoton or super-resolution microscopy techniques. The optical sectioning provided by these microscopy methods allow precise 3D localisation of regions of interest but require an increase in complexity in the combined optical system. Movement of the objective to capture a z -scan of an object also moves the trapping plane of the optical tweezer so it is only possible to capture a single plane of a trapped object. Several methodologies have been used to alleviate this problem, ranging from simple to highly complex.

For specialised applications, once the necessary optical manipulations have been performed, the trap can be turned off and imaging performed in any requisite plane. This technique has been employed for imaging cell-pathogen interactions [81] and virological synapses [82], events where once the initial connection has been induced, will proceed autonomously. In other applications, only a single plane is required for imaging so no movement of the objective is necessary, although this does not allow for any possible movement out of the plane that might occur during trapping and imaging.

To decouple the movement of the trapping and imaging planes when using the same objective, additional optics are required in the trapping or imaging beam path. This was first explored in Hoffman *et al* [83], who coupled a trapping laser into a confocal microscope. The trapping laser was directed in by means of a laser-coupled fibre and lens combination, the fibre was seated on a translation stage so that axial movement of the fibre changed the axial position of the trapping plane. The movement of the fibre was synchronised to the movement of the objective so the absolute height of the trapping plane remained the same, enabling trapping and 3D imaging of highly motile plant chloroplasts and axial displacement of granules in mammalian cells. Goksör *et al.* [84] employed an opposite technique; by keeping the objective height the same but moving a lens in the trapping beam path to change the height of the optical trap, it was possible to scan an object through the imaging plane. The dual-path trapping system (with different paths for confocal or multiphoton imaging) was based on a dual-trap

tweezer designed by Fallman *et al.* [85]. This system was also coupled into a STED (stimulated emission by depletion) microscope for super-resolution imaging of proteins on optically trapped DNA [86]. Both systems described above are highly complex, requiring precise software control and complex optical set-up respectively.

SLM-based optical tweezers can be used to change the height of an optical trap at the microscope focus. An SLM placed into the optical trapping beam path can shape the light into traps of varying axial positions. These dynamic traps have been used to create arrays of trapped yeast cells at different heights so each nuclei is in the same plane [87], increasing acquisition speed because only a single plane needs to be imaged to collect all the required nuclear information. They have also been used to create multiple dynamic traps for controlled rotation of immune cells, which were seen to rotate passively in a single trap, adversely affecting 3D imaging [88].

A third option, negating the use of expensive but highly reconfigurable HOTs, is to decouple the imaging and trapping beam paths completely. By bringing a trapping laser in to the opposite side of the sample to the imaging objective, by means of an objective or optical fibre, the trapping and imaging planes are independent of each other. Yevnin *et al.* [89] mounted a second objective above the trapping objective for confocal imaging of arrays of silica particles and yeast cells. Decoupling in this way also allows lower magnification imaging, if required, than that provided by the trapping objective, which requires high NA and therefore suffers from a restricted field of view.

Although low achievable NAs (< 1.0) limit their axial trapping efficiency, single beam optical fibre traps provide a simple-to-implement and easily configurable optical trap [90] that can be introduced to any inverted microscope and therefore combined with any number of imaging modalities. Surprisingly, the combination of an optical fibre trap with a fluorescence microscopy platform has yet to be reported, opening up an avenue for investigation in this thesis. The use of a fibre trap for epi-fluorescence imaging of immune cells is reported in Section 7.3, with the potential for combination with super-resolution imaging.

2.4 Combining optical trapping and photoporation

The influence of the two biophotonic techniques discussed in this chapter is undeniable, but only very rarely have they been combined, even though the microscope-based systems generally used for these experiments make adding extra modality in the form of optical tweezers or a photoporation beam a simple endeavour. A few studies have shown it is possible to optically tweeze a nanoparticle to the cell membrane and then use a femtosecond laser to transiently disrupt the membrane and allow passage of the particle into the cell. In this way, DNA coated particles for transfection [91] or potential biosensors [55] can be gently inserted into cells. A potentially more valuable protocol is employed in Brown *et al.* [60], where a tweeze-porate-tweeze system is designed. A cell is moved into a capillary and injected with molecules in the surrounding medium before being moved to an observation chamber. Different cells could therefore be sequentially dosed with different molecules and sorted for high-throughput drug testing or other single-cell assays.

2.5 Conclusions

The deployment of photoporation and optical tweezers has been beneficial in understanding biological function. It is impossible to cover all applications in a single chapter. Instead, highlights of the most interesting studies have been presented here, along with an understanding of the underlying theory, as an introduction to these topics. Plant cell applications of these techniques will be discussed in Chapter 3.

Using a laser to gently and precisely inject nucleic acids and other biologically important molecules into selected cells has enabled efficient transfection of hard-to-transfect cell lines such as primary neurons. The sub-micron size of the damage region created by a tightly-focused femtosecond laser confers high viability to the porated cells and allows molecules to be injected into specific sub-cellular locations not readily

achievable with other injection techniques. The effect of changing beam type (from Gaussian to Bessel) and irradiation geometry to increase photoporation efficiency has been discussed in this chapter. An optical system developed to directly compare these different protocols is presented in Section 4.2. Section 5.3.2 then applies this system to optimise plant photoporation.

With the microscopic forces created through optical trapping, precise measurements of biological interactions can be performed. Optical displacement of cells and organelles can non-invasively perturb tissue and intracellular environments in real time, enhancing our understanding of biological functions. Section 7.2.2 builds on previous studies to develop a fibre-based trap for cellular studies integrated onto a commercial fluorescence microscope.

3 | Biophotonic methods for plant cells

As a critical component of the food chain, understanding plant biology is crucial. Plant cells are, however, challenging to biophotonic applications owing to physiological differences to mammalian cell systems. The cell wall introduces aberrations and its constituents, along with the photosynthetic compound chlorophyll, make plant cells more absorptive at a broader range of wavelengths than mammalian cells. Turgor pressure within the cell also causes cytoplasmic extrusion upon breaching the cell membrane (or protoplast extrusion if the wall is breached but membrane stays intact).

This chapter will present the basic differences between plant and mammalian cells. A critique of genetic modification (GM) of plant cells is discussed, highlighting the beneficial uses of this contentious technique. The standard methods for creating GM plants are briefly covered, along with advantages and disadvantages, before a detailed review of the current plant photoporation literature is presented.

3.1 Plant physiology

There are numerous physiological differences between plants and animals, most of which can be traced to a tissue or cellular level. Although plant and mammalian cells are both

eukaryotic, they differ in form and function. A summary of the differences discussed in more detail below are presented in Figure 3.1A and B and Table 3.1.

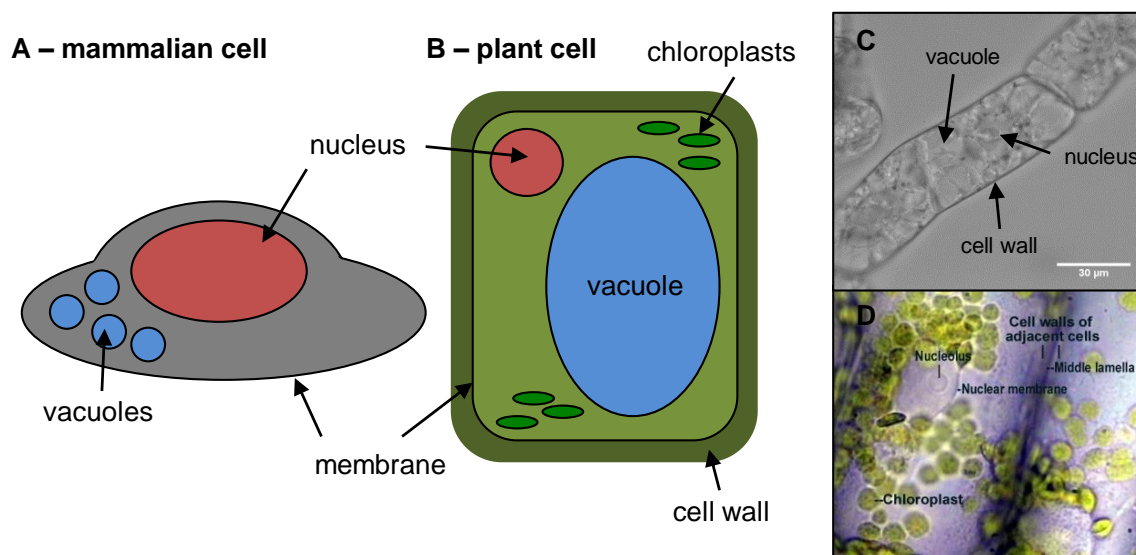


Figure 3.1 – (A) and (B) are simplified mammalian and plant cell diagrams respectively showing the main physiological differences between plant and mammalian cells, namely the presence of a cell wall, chloroplasts and a large central vacuole. Brightfield plant cell images of tobacco BY-2 cells (C) and Elodea leaf tissue (D) are shown with important visible organelles highlighted. The latter is taken from www.lima.ohio-state.edu [92].

The most prominent difference is the presence of a cell wall, composed primarily of polysaccharides such as cellulose (glucose molecules) [93]. Cellulose molecules are cross-linked by other polysaccharides (hemicelluloses) to form microfibrils, which twist to form cable-like macrofibrils [94]. Cellulose fibres made in this way can have a higher tensile strength than steel. The cell wall provides structure and rigidity to the organism and prevents rupture of the protoplast, the part of the cell bounded by the plasma membrane [95].

The plant cell plasma membrane is very similar to that of a mammalian cell, although there are differences that reflect the different functions of plant and animal cells. Crop plants are usually field-grown and so exposed to the elements. Therefore,

Cell physiology	Mammalian cells	Plant cells
Membrane sterols	Mainly cholesterol	Many different sterols
Membrane fluidity	Varies with temperature	Maintained with varying temperature
Cell wall	None	Rigid cellulose cell wall
Vacuoles	Small, numerous	Large, fewer, additional functionality
Plastids	None	Various, including chloroplasts for photosynthesis
Size	Tens of μm	Tens to hundreds of μm

Table 3.1 – Summary of some basic physiological differences between plant and mammalian cells.

they are subject to fluctuating temperature changes when compared to homeotherms (constant body temperature). These temperature changes can cause the mammalian plasma membrane to set to a gel at low temperatures, halting membrane activities, or become too fluid to maintain the permeability barrier at high temperatures. Plant cells, however, can change the composition of the membrane as the temperature changes, maintaining fluidity and function [95]. The plasma membrane throughout a plant is continuous with membranes of adjacent cells connected through pores in the cell walls, called plasmodesmata, allowing direct communication between cells [93].

A large proportion of the water in a turgid cell is contained within the vacuole. Vacuoles are very small in mammalian cells but make up as much as 90% of the volume of a mature plant cell [95]. A high concentration of solutes in the vacuole creates turgor pressure, driving water uptake into the cell. Active transport of solutes into the vacuole maintains the osmotic potential difference. The pressure exerted by the plasma membrane on the cell wall helps to support plant tissue and drives cell growth [93]. When

a plant cell is placed in a high concentration solution, water moves out of the cell into the solution. The turgor pressure decreases and the cell membrane detaches from the cell wall (plasmolysis).

Plastids are double membrane-bound organelles found only in plant and algae cells. Chloroplasts are plastids that manufacture sugars by photosynthesis and store them as starch grains [95]. Photosynthesis requires chlorophyll, which gives plants their green colour because chlorophyll absorbs all other colours in the visible spectrum and reflects green wavelengths. Many plastids emit broadband autofluorescence that can adversely affect fluorescence imaging of other plant organelles, particularly if fluorescent protein expression is low.

These physiological differences between plant and mammalian cells reflect the different functions and forms of these organisms. Some of these changes present new challenges when considering femtosecond photoporation of plant cells when compared to mammalian cells. The cell wall in particular adds many challenges. Not only is it an additional barrier for membrane-impermeable molecules to cross, it is also autofluorescent and counterbalances turgor pressure within the cell. Judicious choices of fluorophores and photoporation medium can aid in minimising these issues (the latter is addressed in Section 5.3.3). The difficulties in membrane targeting caused by large sizes of plant cells when compared to cultured mammalian cells is addressed in Section 5.3.2 by beam shaping. Manipulating light can increase photoporation efficiency, potentially increasing the possibility of obtaining genetic modification of plant cells, a difficult but necessary task.

3.2 Genetic modification of plants

Members of the plant kingdom are primary producers on which all food chains are based, taking in sunlight and converting it to usable energy by photosynthesis. In 2011, the World's population exceeded 7 billion [96]. It continues to grow and require nutrition.

The need for large tracts of arable land on which crops can be grown increases as we head towards a food deficit, requiring aggressive, environmentally-damaging farming techniques. GM crops can help to alleviate these problems by creating plants with greater nutritional content [97] and higher drought and disease resistance. Current plant breeding methods are slow, taking 10-15 years to develop new cultivars of cereals or potato. Targeted introduction of genes for desired traits by genetic modification techniques can speed up the introduction of improved crop plants.

There are a multitude of other uses for plant transformation, ranging from efficient renewable energy sources, through biomedical applications to novel examples such as bioluminescent plants for street-lighting [98]. Listed below are a few current avenues of GM research.

- **Agricultural:** Resistance to drought, disease, pathogens, herbicides, insects and insecticides are all important agricultural traits currently under research and, in some cases, in production in crops around the World. GM plants are also being developed to clean contaminated, and potentially toxic, soil [99].
- **Medical:** “Pharming” is the production of recombinant proteins in GM plants for low-cost production of biomolecules such as vaccines and other drugs [100, 101]. Additional micronutrients can be engineered into staple crops, the most famous example is Golden Rice, which produces beta-carotene for vitamin A deficient diets [97].
- **Renewable energy:** Algae are being engineered to produce hydrogen gas [101] and GM plants with reduced lignin content can provide more effective feedstock for biofuel production [102].

With many important applications, it is evident that efficient transformation methods are required to fully explore the benefits of plant transformation. Genetic modification of plant cells is a difficult task and often very low numbers of genetically modified plants

are recovered at the end of a long process (2-3 months [103]). This low efficiency is due to a lack of homologous recombination, making gene insertion occur at random sites in the genome [104] and plant, and difficulties in whole organism regeneration from transformed cells.

3.3 Current plant transformation protocols

There are several commonly-used methods for plant transformation. The most widely-used technique uses the organism *Agrobacterium tumefaciens* as a bacterial vector to transfer plasmid DNA to plant cells [105]. Wild-type *Agrobacterium* induces tumours in host plants by transfer of a section of DNA (known as T-DNA) from the tumour-inducing (Ti) plasmid. Virulence proteins act to coat and target the T-DNA to the host cell nucleus. T-DNA is transferred to the host cell where, with the assistance of recruited host proteins, it passes through the cytoplasm and nuclear pore complex to the nucleus. There the protective proteins are proteolysed to allow the T-DNA to integrate into the host cell genome. By deletion of the tumor-inducing gene and addition of a gene of interest, the Ti plasmid can become a useful vector for plant transformation [105]. Direct incorporation of the DNA to the plant genome allows stable and reproducible gene expression, highly desirable traits in GM [106].

Biolistics [107], a portmanteau of biology and ballistics, fires high velocity particles at plant tissue or cells. The particles, usually tungsten or gold, are coated in the desired plasmid that is active once inside the cell. This method does not require a biological vector to circumvent the thick cell wall. The host range is therefore not limited by biological factors, as with *Agrobacterium*, but large amounts of damage can occur within the tissue, and the achievable efficiency is low due to lack of targeting [106]. Yamashita *et al.* [108] showed that in 90 % of cases, the bombarded particle was required to enter the nucleus for transformation to occur. This is in contrast with mammalian cells where the particle is usually observed in the cytoplasm and is only in the nucleus in a few

cases [109]. Published efficiencies for *Agrobacterium* and bombardment methods are relatively low at 1-10 % [110] and 0.3 % [108] respectively.

Other transformation methods usually have more specific uses characterised by the protocol. The application of an electric field, known as electroporation, to protoplasts [111], cells [112] and even tissue [113] can cause an increase in cell wall and membrane permeabilisation for many cells but at the cost of decreased viability. Microinjection [114] is a very labour intensive method but can yield high transformation efficiencies. PEG fusion [115] uses polyethylene glycol to fuse protoplast membranes with liposomes containing the plasmid but the use of very fragile protoplasts presents regeneration problems [116].

The protocol used also determines whether stable or transient transformation is more likely to occur. Stable transformation is where the inserted gene is incorporated into the plant genome and can be passed onto progeny, making it necessary for plant GM [117]. In transient transformation the gene is only expressed for a few days before it is lost due to cell division, this is a useful technique in research [118]. *Agrobacterium* is most suited to stable transformation because the gene is inserted directly into the host genome. Other techniques, particularly those that inject naked DNA into the cell such as electroporation, are more suitable for transient transformation. Photoporation comes under the latter and is mainly used for transient transformation in mammalian cells, although it has been employed for stable transformation [21, 119].

When considering injection of other biomolecules such as dyes, drugs and proteins, common mammalian cell delivery techniques are not always effective in plant cells. Acetoxymethyl (AM) ester-conjugated dyes are cleaved by esterases in the apoplast, between the protoplast and cell wall, leading to insufficient or inhomogeneous loading [120]. Microinjection [121], electrophoretic injections [122], nanoparticles [123], cell penetrating peptides [124] and biolistic methods [125] have been employed successfully. The main problems with the current techniques for molecular delivery is that they are either slow or non-specific. This study will start to address these problems, among

others, by the use of a novel optical injection method. Photoporation of plant cells has been explored previously [126, and references therein] but is an under-developed technique in comparison to mammalian cell photoporation. The next section represents the first detailed and fully comprehensive review of plant photoporation literature.

3.4 Plant photoporation review

J. C. Sanford, inventor of biolistics for transformation, first identified lasers as a possible tool to inject exogenous DNA into plant cells in 1982 [127], five years prior to the publication of the first biolistics article [128]. He investigated the interactions of 532 nm, 100 ns laser pulses with Periwinkle pollen, finding it was possible to create large holes in dried pollen and initiate extrusion of cytosol in hydrated pollen. The application of Ficoll in the medium reduced the osmotic pressure of the pollen and reduced the severity of cytosolic expulsion.

Crucially, Sanford discovered it was possible to create holes in the pollen wall and membrane and, in the case of pollen tubes, the hole healed and cells remained viable (similar effects were seen in lily pollen in Broglia *et al.* [129]). It was not, however, possible to reduce the osmotic pressure enough to allow uptake of exogenous medium in this study without losing cell viability. Varied lasers and cell types have been employed since to further develop plant photoporation.

3.4.1 Nanosecond UV studies

Nanosecond (3-15 ns) UV (337-355 nm) lasers have proved ubiquitously popular in plant photoporation.

The research group of Weber, Monajembashi, Greulich and Wolfrum were prolific in the field of plant photoporation in the late 1980s and early 1990s. Their first study presented single UV nanosecond pulses for perforation of isolated chloroplasts, allowing

uptake of fluorescently-labelled DNA [130], proposing that they could then be reinserted into a cell. Plastid transformation presents an interesting challenge to crop engineers. Chloroplasts possess their own DNA (like mitochondria) and plants with transformed plastids run a significantly smaller risk of gene transfer to other organisms [131], making them a useful target for optical transformation studies. Further study showed that the photosynthetic qualities of algae (*Chlamydomonas reinhardtii*) were intact after chloroplast irradiation [132], suggesting that laser irradiation did not irreparably damage the cell.

The sub-cellular precision afforded by photoporation was exploited to progress this topic. DNA could be microinjected into a protoplast, and introduced into individual chloroplasts within the cell by laser irradiation. In this way, injection of fluorescent DNA [133] and functional DNA for stable plastid transformation with an efficiency of 2 % was demonstrated [134].

Turning to whole cells, Weber *et al.* also investigated photoporation of single cell suspensions of *Brassica napus*, otherwise known as rapeseed. This economically important plant is closely related to the *Arabidopsis* family, making it useful to be able to transfer the knowledge gained in this heavily-researched model organism into an agriculturally relevant crop [103]. The totipotent nature of the majority of plant cells [135] makes the choice of cell type to photoporate a theoretically arbitrary one, based on ease of laser application and research goal rather than dictating the possibility of regeneration into whole GM models (although some plant and cell types produce much greater regeneration frequencies in practice). Suspension cell cultures are therefore a sensible choice for optical injection studies, where access to the cell wall and membrane is enhanced and cells are homogeneous and easy to culture. However, the non-adherent nature of plant cells adds increased difficulty when performing follow-up observations.

Nevertheless, Weber *et al.* were able to inject osmotically treated (with 0.6 M sorbitol in Tris buffer [134]) *B. napus* suspension cells and microspores with both fluorescent (80 % with 40-60 % viability (30 % for pollen)) and functional DNA. Achieving transient

transformation efficiencies of 19-41 % [134] and stable transformation efficiencies of 8.5-20 % [133].

Laser irradiation of *B. napus* tissue was also investigated. Targeting cells within tissue can present challenges owing to the thicker cell walls and presence of surrounding cells. Single pulses were sufficient to induce cell damage in hypocotyl tissue [136]. Further studies investigated optical transformation of embryos, citing transformation efficiencies of 44 % [134, 137]. In an agriculturally-relevant study by another research group, *B. napus* cotyledon tissue was successfully transformed to stably express a sclerotia-resistant gene; sclerotia is a highly prevalent and devastating rapeseed pathogen [138].

The studies described above all used single nanosecond pulses focused onto the cell wall or membrane to induce poration. A potentially higher throughput method was employed by Guo *et al.* and Badr *et al.* Laser pulses were delivered to a sample on a motorised stage moving so that each pulse should target a single cell. This reduces the accuracy of targeting but significantly increases throughput. Using this technique, the first optical transformation of suspension cells of an important food source, rice (*Oryza sativa*) [139] was demonstrated, followed by wheat embryos, *Triticum aestivum* [140, 141]. Transfection efficiencies were low at 0.5 % of single rice cells and 0.5 % of embryos (the efficiency per targeted cell will be even lower). This is possibly exacerbated by the minimal targeting, Guo *et al.*, in particular, assumed that each laser pulse targets a separate cell, the number of cells targeted will be lower, leading to an increased efficiency.

When using UV nanosecond lasers, photoporation is attributed to components of the cell wall and cell membrane absorbing UV, leading to thermomechanical damage. The fluences used range from well below ($2 \times 10^5 \text{ Jm}^{-2}$ [139]) to well above ($5.2 \times 10^9 \text{ Jm}^{-2}$ [138]) the optical breakdown threshold of water [33], suggesting that for higher energies, large numbers of cells might be targeted at once by a shockwave.

Lowering the incident wavelength further reduces the irradiance threshold [33]. Deep-UV (193 nm) nanosecond lasers, corresponding to single-photon excitation of

water, allows very low fluences of $300\text{--}2000\text{ Jm}^{-2}$ [142, 143] to elicit cell injury. Both Kajiyama *et al.* [143] and Buer *et al.* [144] demonstrated deep-UV nanosecond lasers allow precise cell wall ablation while keeping the cell membrane intact (Figure 3.2).

In the case of Kajiyama *et al.* [143], a single pulse of variable spatial extent ablated a portion of the cell wall and allowed access for a microinjection needle, which has a high probability of breaking on the cell wall, into single cells in plant tissue of various species for injection of fluorophores and DNA. Buer *et al.* [144] used multiple pulses (10-100) to create a hole in the cell wall through which it was then possible to tweeze polymer beads and *Agrobacterium rhizogenes* into the apoplast, with applications for transformation without a plasmid purification step. Membrane permeabilisation at this wavelength is attributed to chemical bond breaking by Turovets *et al.* [142], who exposed multiple *Asparagus* suspension cells to a single nanosecond pulse, irradiating a metal plate with holes in it to split the beam up into many microbeams.

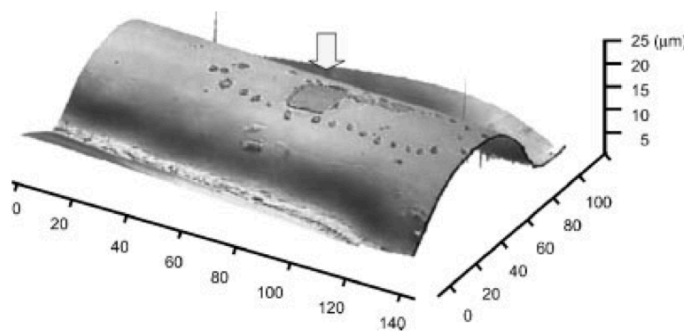


Figure 3.2 – Laser profiling of plant cell wall after application of a low intensity UV nanosecond laser beam. A $10 \times 10\text{ }\mu\text{m}$ depression in the cell wall has been created, allowing access to the protoplast for a microinjection needle. *Reprinted by permission from John Wiley & Sons: Biotechnology and Bioengineering [143].*

The Kajiyama group subsequently used the same laser system to introduce gold nanoparticles into *Torenia* tissue and tobacco guard cells. Mammalian nanoparticle laser transfection typically targets multiple cells, but this was done on an individual

cell basis, akin to optical transfection. Transfection efficiencies were 0.4 and 2 % for the different cell types respectively [145, 146].

3.4.2 Picosecond IR studies

The use of less damaging and more precise picosecond lasers has also been explored in plant cell photoporation. Schinkel *et al.* [147] used a tightly focused NIR laser beam (1064 nm, 17 ps) for protoplast photoporation. 1-10 pulses were applied tangentially to the cell membrane until a twitch was observed. Up to 73 % injection of propidium iodide was observed but only 2.5 % transformation.

Although investigative studies have shown that ns and ps laser irradiation create shockwaves that span many cells [33, 34], there is also evidence that it is possible to target single cells too. Krasieva *et al.* [148] were able to optoporate mammalian cells by focusing a single ns pulse onto the cell substrate; reducing the irradiation four times and instead focusing on the cell membrane allowed optical injection to take place too. Although the experimental practise has been demonstrated, the exact mechanism behind ps and ns optical injection is unsure. We can postulate that optical breakdown has not been initiated because the subsequent shockwave is highly damaging, the poration mechanism for ns and ps optical injection of mammalian cells and protoplasts is therefore likely to be photochemical or heating effects.

The absence of the cell wall in protoplasts helps to minimise the problems associated with the cell wall but also causes other issues. Protoplasts are highly fragile and osmotically sensitive, resulting in low yield of viable protoplasts long-term and low regeneration frequency.

3.4.3 Femtosecond NIR studies

Tirlapur *et al.* [149] first documented the use of a minimally invasive high repetition rate (80 MHz) femtosecond regime for plant photoporation. A single 40 ms exposure was sufficient to inject the fluorophore propidium iodide into central cells in *Arabidopsis* root meristem. The high penetration depth and limited damage zone of the femtosecond laser was useful in investigating symplastic connections in central root meristem cells, extending a previous microinjection-based study that could only access the epidermal layer [150].

Arabidopsis epidermal cells within plant stems were efficiently and quantitatively injected with high repetition rate 200 fs pulses in LeBlanc *et al.* [151]. Short exposure times (0.64 μ s) at comparatively high irradiances ($5 \times 10^{10} \text{ Jm}^{-2}$) were used to perforate epidermal stem cells and allow uptake of fluorescently-labelled dextrans. This study used a multiple targeting technique (seven exposures separated by 0.5 μ m and 30 s) to ensure accurate targeting of the membrane. This technique was slow but effective, allowing injection of up to 68 %, with cells remaining viable over long time-scales.

Despite their comparatively more damaging effects, higher energy single femtosecond pulses have been used successfully to transform lily pollen with 4.4 % efficiency [152]. mRNA transformation was also demonstrated but not quantified [153] (although the same figure is attributed to DNA transformation in [152]). Using genetically engineered pollen to fertilise plants can avoid tedious and difficult regeneration and sterile explant tissue culture [154]. Pollen also provides a quick viability test by observing germination post-irradiation.

3.4.4 CW studies

Although their low cost and availability make CW lasers a promising transformation tool, CW lasers have experienced minimal success in plant photoporation. Tirlapur *et*

al. initially tested a CW laser for their symplastic coupling study before turning to a femtosecond laser. The large damage region caused by linear absorption of the 488 nm confocal laser was detrimental when attempting to dye-load single cells deep in tissue, causing non-specific effects [149].

In an extension to the Schinkel *et al.* picosecond paper, highly efficient protoplast injection (83 %) was demonstrated using a 500 ms exposures from a 405 nm diode laser using brome cresol violet as a sensitiser. The transformation efficiency, however, was only half that when compared to a picosecond laser [155].

3.4.5 Optoporation

A few laser-based photoporation techniques have eschewed tightly-focused laser beams for multicell targeting methods.

Irradiating a rubber sheet to induce a stresswave for membrane permeabilisation in mammalian cells has been previously covered in Section 2.2.2. Tang *et al.* used this technique to introduce siRNA into a variety of callus types for gene silencing experiments [156].

Awazu *et al.* [157] used a defocused tunable free-electron laser (FEL) at far-IR wavelengths (approximately 6 μm) for injection and transformation of suspension cells by specific bond absorptions. Injection and transient transformation efficiencies were low (up to 3 and 0.3 % respectively) but many cells could be targeted with a single macropulse (FEL pulses are highly complex, consisting of bunches of 10 ps pulses).

3.4.6 Osmolarity effects

The majority of studies require a reduction in cell turgor pressure before optical injection can be achieved. Standard cell medium is hypotonic with respect to the intracellular environment and extrusion from the cell is observed upon photoporation.

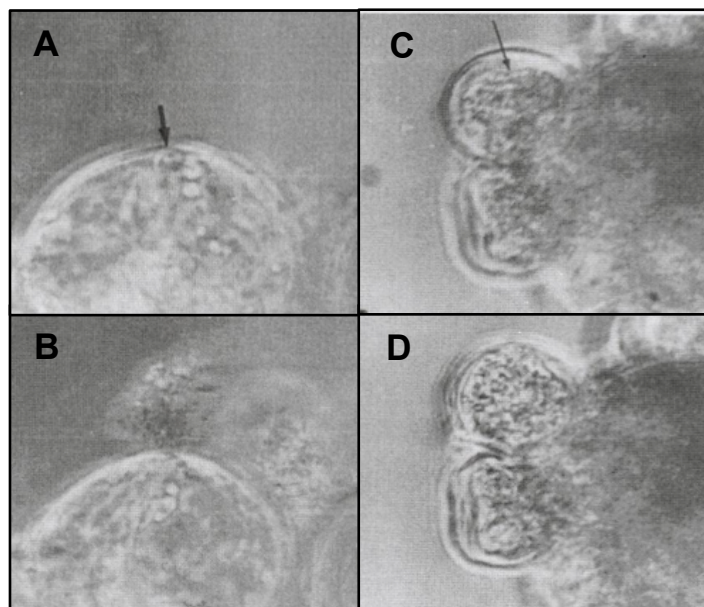


Figure 3.3 – Osmotic effects on photoporation of rice suspension cells. (A) A cell in hypotonic medium prior to laser irradiation. Upon photoporation, the cell extrudes cytosol (B). When pre-treated in hypertonic medium (C), the turgor pressure is reduced and the cell instead gains volume upon photoporation (D). *Reprinted by permission from John Wiley & Sons: Physiologia Plantarum [139].*

Hypertonic pre-treatment in high osmolarity medium reduces the turgor pressure in the cell. Studies observed a reduction in apoplast or cell volume upon application of the hypertonic treatment followed by an increase as the cell is photoporated and extracellular solution can flow back into the cell (Figure 3.3). Organic solutes (sorbitol [137, 138, 144], mannitol [140–142], sucrose, Ficoll [127] and dextrans [151]) are usually chosen as an osmoticum because they show high cell viability upon plasmolysis-deplasmolysis cycles [158]. CaCl_2 has also been used successfully [139], although in this case the osmotic gradient was increased by placing the cell back into normal medium just prior to photoporation so no CaCl_2 entered the protoplast. When investigating stomatal cells, Kajiyama *et al.* [146] found that viability was significantly higher when stomatal cells were closed prior to irradiation, closed guard cells show much lower turgor pressures than open cells. The optimum osmoticum and osmolarity (0.3–1 M has been used) for

maximum cell uptake and maximum viability will be dependent on cell type and should be optimised in preliminary experiments.

3.4.7 Summary

Using light for the injection of exogenous substances into plant cells is a technique that received attention a few decades ago. Between 1987-1991, ten papers were published on the subject, only two have been published in the last five years. With the advances made in scientific research in the last few decades it might be expected that researchers would be employing photoporation routinely but this is obviously not the case.

Table 3.2 shows the transformation efficiencies of various studies are typically low (0.3-5 %), apart from a few studies. Even the lowest stated efficiency is higher than that achieved with biolistic techniques but the need to target each cell individually reduces the throughput to a few thousand cells at most. It should be noted that the transformation efficiency can also be defined differently in different studies, considering transient or stable efficiency or even the number of regenerated fertile plants. Also, in the case of low transformation efficiencies, careful analysis of statistics is important to separate optically transformed cells from spontaneous transformation. Often, large numbers of cells are photoporated but the number of repetitions of an experiment is not noted, preventing rigorous statistical analysis.

To advance plant photoporation, progress should be two-fold.

1. Is it possible to increase the absolute efficiency of injection and transformation?
2. Is it possible to increase the throughput of plant photoporation?

For point one, it is notable that high-repetition rate femtosecond lasers have proven highly effective tools for photoporating mammalian cells, more effective than other laser types, but have only been minimally investigated for plant photoporation. Femtosecond lasers should be able to provide increased injection and transformation efficiencies in

Cell type	Gene	Laser	Transient eff. (%)	Stable eff. (%)	Ref.
Rice	GUS	UV ns	0.5	Y	[139]
Wheat embryos	GUS	UV ns	0.5	0.3	[140, 141]
<i>B. napus</i>	GUS/sclerotia resistance	UV ns	10-71	0.4-40	[133, 134, 137, 138]
Tobacco cells	hygromycin resistance	UV ns	Y	0.4	[159]
Tobacco BY-2	GFP	FEL	0.5	N	[157]
Lily pollen	Mito-RFP	kHz, fs, NIR	4.4	N	[152]
BY-2 protoplasts	peroxisomal YFP	ps, NIR	2	N	[147]

Table 3.2 – Summary of optical transformation in plant cells. Y means transformation was observed but no efficiency reported. N means no stable transformation achieved.

plant cells too. Other parameters can also be changed to increase the efficiency of photoporation in plant cells, namely medium osmolarity (Section 5.3.3) and pulse duration (Section 6.3.2) in this thesis.

Point two considers that, if the photoporation efficiency is low, a larger number of cells need to be targeted to output many photoporated cells. Section 2.2.3 already highlighted that it is possible to reduce time spent targeting the membrane and therefore increase throughput by beam-shaping, a Bessel beam to be precise. A Bessel beam could also provide better targeting of intracellular membranes such as chloroplast and nuclear membranes, which can be at varying heights within a deep plant cell, opening up the possibility for femtosecond organelle transformation. The effect of beam shaping on

plant photoporation has not previously been investigated and presents an interesting point for investigation in Section 5.3.2.

Chapters 5 and 6 in this thesis will consider the application of high repetition rate femtosecond lasers to plant cells for potentially efficient injection and transformation of plant cells. Irradiation methods previously employed to increase cell targeting to increase throughput will be tested, optimising the number of successfully photoporated cells obtained from an experiment. In this way, plant photoporation could become an effective and routine tool for plant cell and GM crop research.

3.5 Conclusions

This chapter has highlighted the relevance of studying plant biology as well as the challenges introduced by variations in cell structure and composition from the standard mammalian cell. The implications for sociological, environmental and biological benefits of genetically manipulating plant cells make the challenge a relevant and necessary one [160].

Photoporation has been employed to enhance our understanding of plant science. While not a routine technique currently in plant science laboratories, the benefits seen from proof-of-concept experiments demonstrate its potential. Plant cells present unique challenges to photonics experiments, some of which will be addressed through the use of spatial and temporal shaping of light in this thesis for enhanced optical manipulation of plant cells.

4 | Development of a reconfigurable photoporation system

Parts of this chapter are adapted from the article "Femtosecond Optoinjection of Intact Tobacco BY-2 Cells Using a Reconfigurable Photoporation Platform" [171] published in PLoS ONE.

4.1 Introduction

The efficacy of photoporation is dependent on the optical parameters used. The ability to quickly change beam shape, input irradiance (power and exposure time) and pulse duration allows easy and rigorous comparisons to be made among these variables for a full exploration of parameter space.

Section 2.2.3 highlighted a significant problem in femtosecond photoporation; the difficulty of aligning the small focal volume with the cell membrane. When considering photoporation of plant cells, this becomes even harder because the plant cell wall adjacent to the membrane can introduce aberrations. Plant cells are also relatively inhomogeneous and bulky when compared to typically flat mammalian cells, further increasing the difficulty in targeting the membrane. Using multiple, axially or laterally separated, exposures or using a different beam shape (a Bessel beam) have both previ-

ously been demonstrated to improve photoporation efficiency and could therefore assist in optimising photoporation of plant cells.

Pulse duration is another important parameter that can affect or enhance photoporation. With n-photon processes, such as femtosecond photoporation, the time-averaged intensity, $\langle S \rangle$, is dependent on the pulse duration according to $\langle S \rangle \propto E_p^n \tau_p^{1-n}$ [172]. For a two-photon process, by halving the pulse duration, τ_p , the pulse energy, E_p , can be reduced 1.4 times and the intensity is maintained. Reducing the input energy while maintaining the same multiphoton effects allows maximum viability of cells. Rudhall *et al.* [172] explored the effect of changing pulse duration on mammalian photoporation and found that using broadband ultrashort pulses (17 fs) allowed highly efficient optoinjection at much lower pulse energies and reduced exposure times.

While being able to change both spatial mode and pulse duration within an optical system is a useful technique in itself, an interesting proposition is raised at the prospect of being able to choose a broadband ultrashort pulsed Bessel beam. This system has not yet been tested in photoporation studies but combining the benefits of both a reduced constraint on axial position and higher efficiencies and increased viability with lower exposure times could greatly increase the achievable throughput.

A system was designed, and is outlined in this chapter, that could switch between two different beam types: a Gaussian and a Bessel beam, and two different lasers supplying different pulse durations at the microscope focus. In this way, it was possible to compare the effect of changing pulse duration and beam shape on plant cell optical injection and exploit the benefits of each variable as required.

This chapter considers the physical properties behind Gaussian and Bessel beams and the most rigorous ways to directly compare them for photoporation experiments. The design of an optical system is presented here, including descriptions of lasers used, designing and building of the optical system and subsequent characterisation of the generated beams to assess their suitability for the proposed experiments.

4.1.1 Gaussian beams

Gaussian beams are exact solutions to the paraxial wave equation [173]. The transverse intensity profile ($I(r, z)$) follows a Gaussian function (Figure 4.1).

$$I(r, z) = I_0 \left(\frac{\omega_0}{\omega(z)} \right)^2 e^{-\frac{2r^2}{\omega(z)^2}} \quad (4.1)$$

I_0 is the maximum intensity, $\omega(z)$ is the beam radius at an axial position z , ω_0 is the minimum beam radius and r is the radial position from the centre of the beam. Simple Gaussian beams are used widely in photonic studies owing to their useful properties; as the beam propagates or passes through simple optics, such as a lens, a Gaussian distribution is maintained, although the parameters vary [173]. Gaussian beams can be focused to very small spot sizes, making them useful in inducing multiphoton effects.

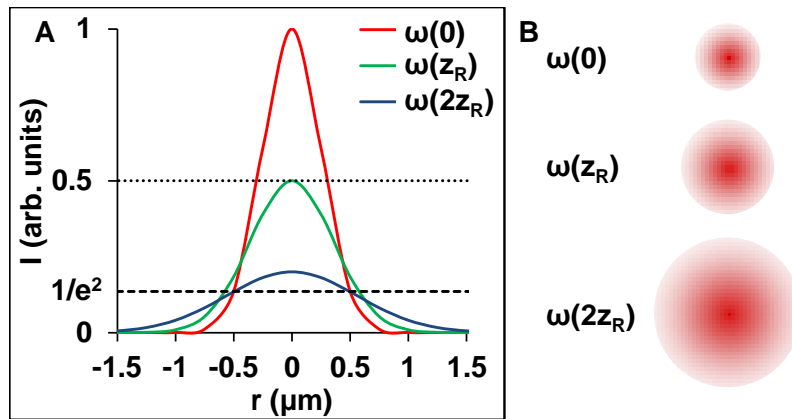


Figure 4.1 – Transverse behaviour of a focused Gaussian beam. (A) 1D transverse intensity profile for a Gaussian beam plotted at three values of z ($z = 0$ (red), $z = z_R$ (green), $z = 2z_R$ (blue)). The transverse intensity at $z = 0$ has a $1/e^2$ diameter of $1 \mu\text{m}$, the full-width half-maximum ($I = 0.5$) has also been plotted. As z increases, the diameter increases (to 1.4 and $2.2 \mu\text{m}$ respectively) as the beam diverges and the central intensity drops accordingly (0.5 and 0.2 of maximum respectively). (B) 2D transverse profiles of the diverging beam at each axial position. Intensities are not to scale for clarity.

When a collimated Gaussian beam is directed through a lens, the beam spot size

reaches a minimum at the focal point. This is ideal for the creation of multiphoton effects because the small focal volume creates a high photon density. This point of minimum radius is termed the beam waist, ω_0 (Figure 4.2), and is measured at the point at which the intensity drops to $1/e^2$ the maximum value. Outside of this focused spot, the beam diverges according to (Figures 4.1 and 4.2).

$$\omega(z) = \omega_0 \sqrt{1 + \left(\frac{z}{z_R}\right)^2} \quad (4.2)$$

Where z_R is the Rayleigh range, the point at which the area of the beam is twice that of the beam waist.

$$\omega(\pm z_R) = \sqrt{2}\omega_0 \quad (4.3)$$

The Rayleigh range is defined by.

$$z_R = \frac{\pi\omega_0^2}{\lambda} \quad (4.4)$$

λ is the wavelength of the laser light. The more tightly the beam is focused (smaller ω_0), the smaller the Rayleigh range and therefore the greater the beam divergence around that point (beam area reaches twice that of the beam waist in a shorter axial distance) [173]. The axial range in which multiphoton events can be initiated is therefore reduced.

Gaussian beams possess many beneficial characteristics for use in biophotonic systems, they can be easily multiplexed for beam splitting and recombination. Gaussian beams are also highly power efficient with 50 % of the power carried by the beam located within the full-width half-maximum (FWHM) [173]. The incident laser power required to deliver the same intensity dose at the cell membrane is therefore reduced compared to less efficient beam shapes, increasing the cell viability. The ability to focus to a small beam waist creates axial confinement too, leading to high photon densities only within a highly confined volume. While this allows high axial precision, greatly beneficial in many biophotonics modalities such as multiphoton imaging, it also requires precise alignment of the focal volume with the desired target, such as a cell membrane.

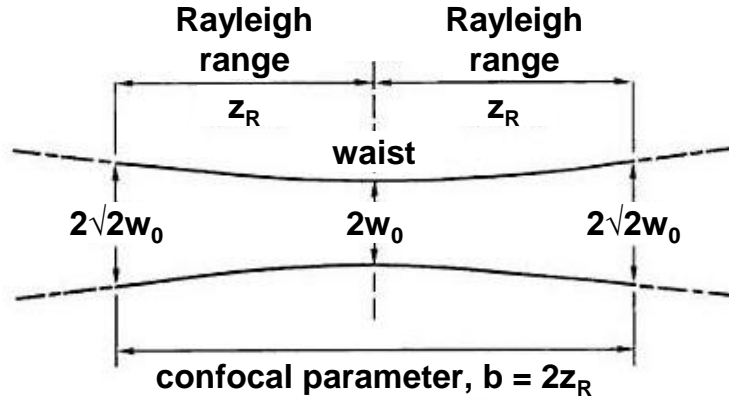


Figure 4.2 – Axial behaviour of a Gaussian beam focused to a beam waist of diameter $2w_0$. The beam diameter increases either side of the beam waist. At distance z_R from the beam waist, known as the Rayleigh range, the beam diameter is $\sqrt{2}$ times larger than at the waist. The total axial distance between $w(\pm z_R)$ is termed the confocal parameter, b . Figure adapted from Siegman [173].

4.1.2 Bessel beams

Bessel beams, in contrast to Gaussian beams, are “non-diffracting” and can theoretically propagate along an infinite length without diverging. They are propagation-invariant solutions to the Helmholtz equation. The transverse electric field of a Bessel beam follows a Bessel function [73].

$$E(r, \phi, z) = A_0 e^{ik_z z} J_0(k_r, r) \quad (4.5)$$

E is the electric field amplitude, J_0 is the zeroth-order Bessel function of the first kind and k_z and k_r are the longitudinal and radial wave-vector components respectively. The transverse intensity is then:

$$I(r, \phi) = |E(r, \phi, z)|^2 = |A_0|^2 J_0^2(k_r, r) \quad (4.6)$$

The transverse intensity profile of a Bessel beam consists of concentric rings around a central spot, as shown in Figure 4.3B. This transverse intensity profile does not depend

on z , and as such does not vary with propagation, leading to a theoretically infinite axial length.

A Bessel beam can be considered as a set of plane waves propagating on a cone [73]. In the far field therefore, it becomes a ring (evident in Figure 4.3A). Conversely, the Fourier transform of a ring is a Bessel beam. An illuminated annulus and lens combination was used to experimentally reproduce the first Bessel beam [174]. A true Bessel beam could propagate infinitely and therefore require an infinite amount of power. In practice, only a quasi-Bessel beam (QBB), non-diffracting over a large, but finite, distance, is achievable. Conical lenses called axicons [175] or holograms are commonly used today to create Bessel beams. For this system, an axicon is used to produce the Bessel beam owing to its high power efficiency when compared to holograms, SLMs or annuli.

Figure 4.3A demonstrates how a QBB is generated from an axicon. When a beam is incident upon an axicon, light either side of the cone tip are refracted inwards. At the point of overlap, interference of the k-vectors creates a Bessel beam [176].

The choice of input beam waist and axicon opening angle, γ , control the parameters of the generated QBB. The size of the central core (central core radius = r_0) and the propagation distance, Z_{max} (the point at which the on-axis intensity drops to 32.27 % of the maximum), vary according to [73]:

$$r_0 = \frac{2.405}{k_r} = \frac{2.405\lambda}{2\pi \sin \theta} \quad (4.7)$$

$$Z_{max} \approx \frac{\omega_0}{\theta} \quad (4.8)$$

$\theta = (n-1)\gamma$ where n is the axicon refractive index. The choice of axicon is crucial, a low opening angle will increase Z_{max} but will also increase r_0 , reducing photon density. The beam waist affects Z_{max} and the number of concentric rings in the QBB. The power in the Bessel beam is shared out equally between the rings so it is important to choose the correct parameters to maximise axial propagation while limiting the number of rings and core size.

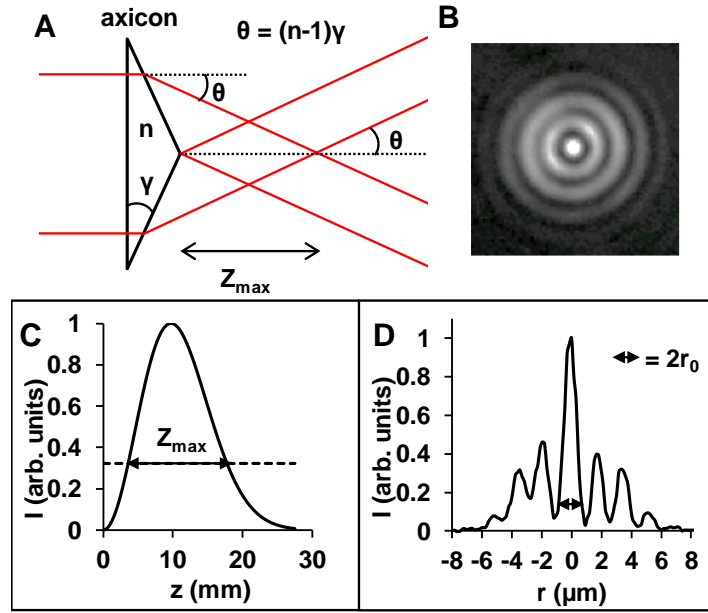


Figure 4.3 – An axicon-generated Bessel beam. (A) Ray diagram of light incident on an axicon of opening angle γ . Light exits the axicon at an angle θ to the axis. The Bessel beam (of axial propagation Z_{max}) is created in the overlap of light emerging from either side of the cone tip. (B) A 2D transverse intensity profile of an axicon-generated Bessel beam at the point of highest axial intensity, showing a central core surrounded by concentric rings. (C) Calculated intensity profile of a Bessel beam created from a $1.2 \mu\text{m}$ diameter beam incident on a 5° axicon, $Z_{max} = 13 \text{ mm}$. (D) Transverse intensity profile of B, highlighting the central core diameter, $2r_0$.

The spread of Bessel beam power among the rings makes them less power efficient than Gaussian beams; only the central spot possesses high enough photon density to allow multiphoton effects. Bessel beams also suffer from difficult alignment, outlined in Section 4.2. The long axial propagation, however, makes Bessel beams an important tool for enhancing photoporation by reducing the stringent membrane alignment requirements. Bessel beams can also self-reconstruct if obstructed [177], a property that has proven useful in optical manipulation [178], imaging [179, 180] and photoporation studies [18, 58]. The longer depth of focus and beam reconstruction abilities were pos-

tulated to aid in plant cell photoporation. The reconfigurable beam system designed provided a way to quickly switch between the two beam shapes and thus utilise the properties of either beam when required.

4.1.3 Beam comparison

When attempting to compare two different beam types, the comparison made should be as fair as possible. By matching the Gaussian beam waist to the Bessel beam's central core radius we ensure that the intensity applied at the image plane is kept the same, we can then consider the depth of focus (DOF) for each beam. For a given beam waist diameter, $2\omega_0$, the depth of focus can be defined as twice the Rayleigh range (Equation 4.4) [73]. One Rayleigh range from the beam waist, the area of the beam has expanded to twice that at the beam waist and the intensity has therefore halved because the total power contained within the beam is the same.

In the case of an axicon-generated Bessel beam, the propagation length can be tuned independently of the central core radius (r_0), which is only dependent on beam wavelength and axicon opening angle (γ). The on-axis intensity of the Bessel beam varies according to $z^2 e^{(-2z^2/z_{max}^2)}$ (Figure 4.3C) [176]. The central core size stays the same but the total power carried in the core changes as the number of rings increases along the direction of propagation. The axial propagation length is usually defined as the point at which the intensity drops to 32.27 % of its maximum [73]. Given the definition of the DOF for the Gaussian beam, we can define the Bessel beam DOF to be the point at which the intensity drops to 50 % of the maximum instead, which is determined experimentally.

4.2 An optical system to select between Gaussian and Bessel beams

4.2.1 Laser parameters

A high-power, turn-key Chameleon Ultra II laser (Coherent Inc., USA) was used for the optical system described below. The Ti:sapphire laser was tuned to a central wavelength of 800 ± 2 nm, 4 W maximum average output power, 140 fs output pulse duration and 80 MHz pulse repetition rate.

Beam profile

A tomographic beam profiler (Melles-Griot, USA) was used to analyse the beam cross-section (Figure 4.4). The beam profiler works using a knife-edge method. A rotating disc with an aperture with a knife-edge allows light from a certain portion of the beam to fall upon a detector. The amount of light falling upon the detector can then be found at each position of the knife-edge across the beam and from this the beam shape can be reconstructed. An accurate 3D image of the beam can be achieved using tomographic techniques, which require at least three knife-edged apertures aligned at different angles to the beam. The $1/e^2$ beam diameter along the major and minor axes were 1186 ± 3 μm and 1143 ± 3 μm respectively.

M^2 measurements

The M^2 value is a measure of how close a given laser beam is to an ideal Gaussian beam. Theoretically, a laser should focus down to a diffraction-limited spot size. The M^2 value defines a lower limit to which that particular beam can be focused, which will be larger than the diffraction-limit allows and therefore needs to be taken into account when designing and building a system. The M^2 value here was measured by focusing the

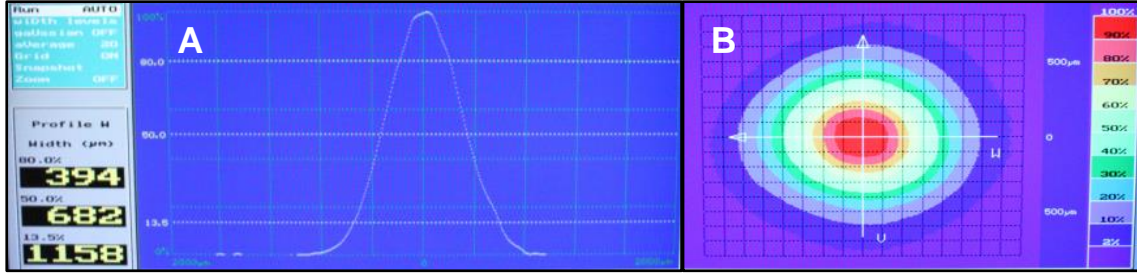


Figure 4.4 – Example screen captures from the tomographic beam profiler displaying (A) the Gaussian-like beam profile in the x (w) direction and a 2D intensity plot (B).

laser using a lens and taking tomographic beam profile measurements of the changing beam diameter, taking data inside and outside the Rayleigh range.

This data was then analysed using least-squares optimisation (see below) to find M^2 using [181].

$$\omega^2 = \omega_0^2 + [M^2(\frac{\lambda}{\pi\omega_0})(x - x_0)]^2 \quad (4.9)$$

For the x direction, M^2 was 1.02, which is within the manufacturer's specified value of <1.1 . The y direction was 0.993 but, considering the M^2 value cannot be less than one, this was assumed to be 1 for the fit shown in Figure 4.5, indicating a measurement error of approximately 0.7 %.

Least-squares optimisation

Least-squares optimisation was performed using the Solver function in Microsoft Excel. The sum of the least-squares, S , is minimised.

$$S = \sum (f(x) - f_t(x))^2 \quad (4.10)$$

Where x is the independent variable (e.g. x in the above case), $f(x)$ is the measured variable (ω), $f_t(x)$ is the theoretical variable, calculated from a known equation, with parameters initially estimated. The estimated parameters are then varied to minimise

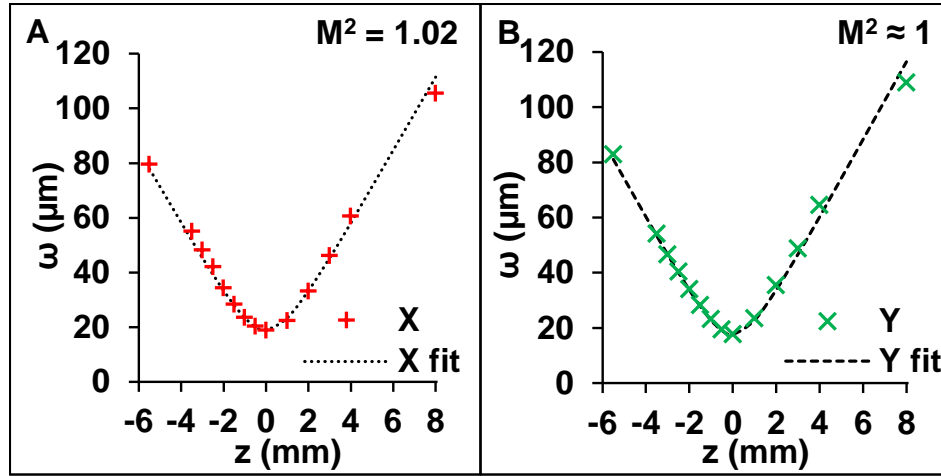


Figure 4.5 – Orthogonal M^2 values for the Chameleon laser. Dotted and dashed line denotes the least squares fit to measured x (red) and y (green) data.

S. As long as initial estimates were accurate enough, optimal minimisation was achieved with a single iteration.

For example, to find the M^2 value using Equation 4.9, ω is measured for a range of x values. For each known x value, a theoretical value of ω is calculated based on (initially) estimated values of ω_0 , M^2 and x_0 (λ is already known from the laser parameters). The difference between the measured and theoretical values of ω is found and squared to ensure it is positive. The squared differences are then summed to find S , which is minimised by optimising ω_0 , M^2 and x_0 . This gives an estimate of the M^2 value of the laser (ω_0 and x_0 are dependent on the lens chosen and are therefore non-requisite values).

4.2.2 Optical set-up

A laser system was designed that used flip mirrors to switch between different paths and enable selection of the Gaussian beam or Bessel beam. A rotating half-wave plate and polarising beam splitter (Thorlabs, Germany) were inserted just after the laser for

varying power and a shutter (capable of producing millisecond exposure times, Newport, USA) to control irradiation times for photoporation.

The optics required for generation of Bessel and Gaussian beams at the same objective focus was considered to design a system. A moderately high-NA (60x, 0.8 NA, Nikon, UK) air objective is used for Gaussian beam photoporation. This creates a minimal focal spot at the focal plane of the microscope without immersion oil, which is toxic and undesirable for live-cell studies.

The objective was just underfilled, creating a focused spot at the microscope focus. A system of telescopes were used for this task, a 4x telescope to magnify the diameter of the beam and a 1x telescope to relay the beam from the bench into the microscope. This final telescope and the objective were used as the final optical elements in the Bessel beam set-up too, all other optics were mounted at bench level for safety. A flip mirror was placed before the 1x telescope in the Gaussian beam path and used to couple in the Bessel beam.

A Bessel beam is generated directly after the axicon tip [176]. This beam will generally be too large for photoporation so needs to be demagnified using telescopes. A lens between the axicon and 1x telescope and objective was required to translate the Bessel beam to the objective focal plane, outlined in Figure 4.6. The choice of incident beam waist, axicon angle and lens was vital to determining the parameters of the Bessel beam at the focal point.

The beam diameter was not varied before passing through a 5° axicon (Comar Optics, UK). A QBB of central spot size $r_0 = 7 \mu\text{m}$ and propagation distance $Z_{max} = 13 \text{ mm}$ was formed according to Equations 4.7 and 4.8.

A 50 mm lens was used to relay the Bessel beam to the 1x telescope and objective, giving 15 times total demagnification. The Bessel beam parameters are then changed according to:

$$r'_0 = \frac{r_0}{x} \quad (4.11)$$

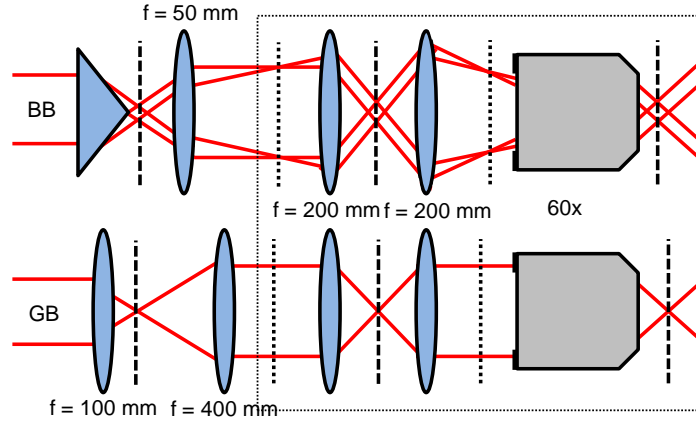


Figure 4.6 – Schematic of Bessel beam and Gaussian beam optics. The Bessel beam (BB) is generated by an axicon and then demagnified using two telescopes (50 and 200 mm lenses and 200 mm lens and 60x objective, 15 times demagnification overall) to create a Bessel beam at the focal plane of the objective. A collimated Gaussian beam is magnified to just underfill the objective using two sets of lenses, a 4x and 1x telescope. Dotted and dashed lines represent conjugate planes. Box represents optics that are shared by both beams.

$$Z'_{max} = \frac{Z_{max}}{x^2} \quad (4.12)$$

Where x is the demagnifying power of the telescope. This produces a Bessel beam with a theoretical central spot radius of 468 nm and propagation distance 59 μ m in air. Using this system of optics, a Bessel beam with a theoretical central core diameter less than 1 μ m and propagation distance of tens of μ ms could be formed. A useful compromise between small focal spot and long propagation length while limiting the number of rings (and therefore reduced power in central spot) was therefore found. A schematic of the optical system is seen in Figure 4.7.

Co-alignment of different beams onto the same focal plane requires careful alignment of the system. The Bessel beam was aligned first through the system and the reflection from a coverslip imaged onto a CCD camera (Clara, Andor, UK). Alignment was optimal when the Bessel beam imaged at the focus was evenly illuminated and

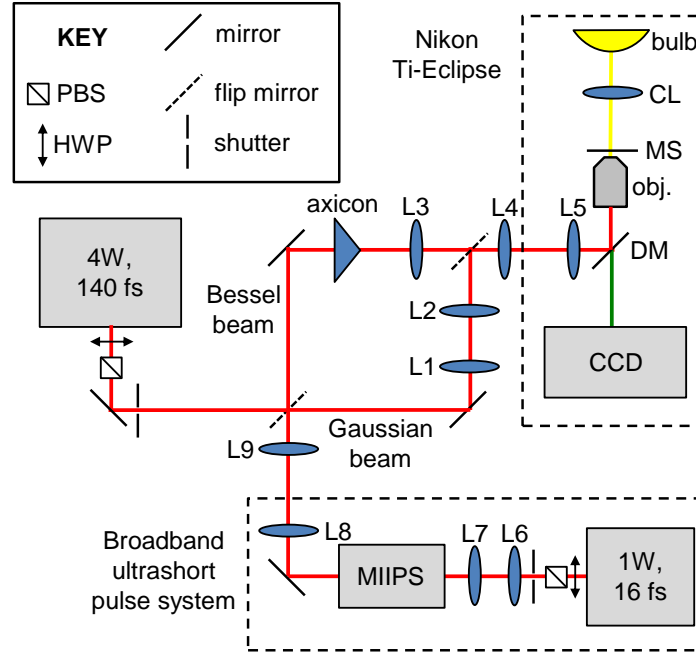


Figure 4.7 – Schematic diagram of the reconfigurable laser system used for the plant photoporation experiments. Output from the 140 fs laser was passed through a rotating half-wave plate (HWP) and polarising beam splitter (PBS) combination for power variation, a shutter was used to allow millisecond exposure times. The beam was directed into either of two arms using a flip mirror (dashed lines). A Bessel beam was generated using an axicon and a Gaussian beam spot was created using a system of telescopes. The beam paths were relayed into a commercial inverted microscope where all imaging was performed. Brightfield illumination consisted of a bulb and condenser lens (CL) imaged through the microscope objective (obj.) and dichroic mirror (DM) onto a CCD camera. The 16 fs laser was passed through a HWP, PBS and shutter, magnified and directed into the MIIPS. The MIIPS compensated for introduced dispersion and achieved transform-limited pulses at the microscope focus. The output beam was demagnified and flip mirrors were used to couple it into the optical system. For comparing spatial modes, $L1 = 100$ mm, $L2 = 400$ mm, for comparing pulse duration, $L1 = 150$ mm, $L2 = 300$ mm and lens positions were changed accordingly. $L3 = 50$ mm, $L4 = 200$ mm, $L5 = 200$ mm, $L6 = 100$ mm, $L7 = 200$ mm, $L8 = 200$ mm, $L9 = 150$ mm.

the central core propagated perpendicularly to the microscope stage (no lateral movement was seen when the objective was translated up and down). Perpendicular and centred alignment of the incident beam through the tip of the axicon ensured optimum alignment [182]. If this was done then the ring imaged in the far-field would be evenly illuminated. Changing the axial position of the axicon varied the axial position of the Bessel beam, the point of highest intensity was matched to the focal plane.

Once the Bessel beam alignment was optimised, the Gaussian beam was co-aligned. Mirrors in the Gaussian beam arm prior to coupling into the 1x telescope varied the lateral position and perpendicularity of the beam. Slight underfilling of the objective yielded an Airy disc at the focal plane. Defocusing the objective revealed rings, symmetrical illumination of these rings indicated optimal alignment [183]. Movement of the 100 mm lens varied the axial position of the focal spot to ensure matching of the beam focal planes.

4.2.3 Beam characterisation

Beam characterisation ensures optimum alignment of the optical system. If the beam characteristics closely match the calculated values then the system is optimised for photoporation experiments.

Gaussian beam

Gaussian beam characterisation was performed by imaging the focal spot onto a glass-bottomed dish, the reflected image was then directed to a CCD. Least squares optimisation was used to fit a Gaussian curve and the beam waist was determined from the fitted standard deviation. Uncertainties in the beam waist measurement were determined by re-focusing the objective onto the dish several times (usually $n = 3$) and taking the standard deviation of the multiple measurements. A calibration for converting pixels into distance was obtained by imaging a graticule at the focus.

The Gaussian beam waist was $2\omega_0 = 1.0 \pm 0.1 \mu\text{m}$, giving a confocal range (DOF) of $2z_R = 2.0 \pm 0.2 \mu\text{m}$ according to Equation 4.4.

Bessel beam

Axial scans through the Bessel beam were performed by moving the objective with respect to the coverslip. Plotting the central spot intensity for each successive image then revealed the propagation distance of the beam by taking the distance between the points where the intensity falls below the desired cut-off.

The experimental Bessel beam profile is shown in Figures 4.3B and D showing the characteristic rings around the central spot. The measured Bessel beam parameters are plotted in Figure 4.8. The spot size is very large initially but quickly reduces to a constant radius. The average spot size, excluding the first $5 \mu\text{m}$, was $2r_0 = 1.0 \pm 0.2 \mu\text{m}$, in very good agreement with the Gaussian beam spot size. The $1/e^2$ axial propagation, Z_{max} , was $34 \pm 2 \mu\text{m}$, nearly half the theoretical length. The DOF, as defined in Section 4.1.3, was $26 \pm 2 \mu\text{m}$, 13 times longer than the Gaussian beam. Plant photoporation using this system to compare the effect of changing the axial propagation of the irradiating beam is discussed in Section 5.3.2.

4.3 Optical system development for controlling pulse duration

Varying the pulse duration has previously been shown to affect photoporation behaviour in mammalian cells [172] and was employed here to investigate the effect on plant cells too. To allow different pulse durations at the microscope focus, a second laser capable of producing 16 fs pulses was coupled into the optical system. To compensate for the large dispersion inevitably introduced by the optical system and the detrimental effect on pulse width, a system that can both measure and compensate ultrashort

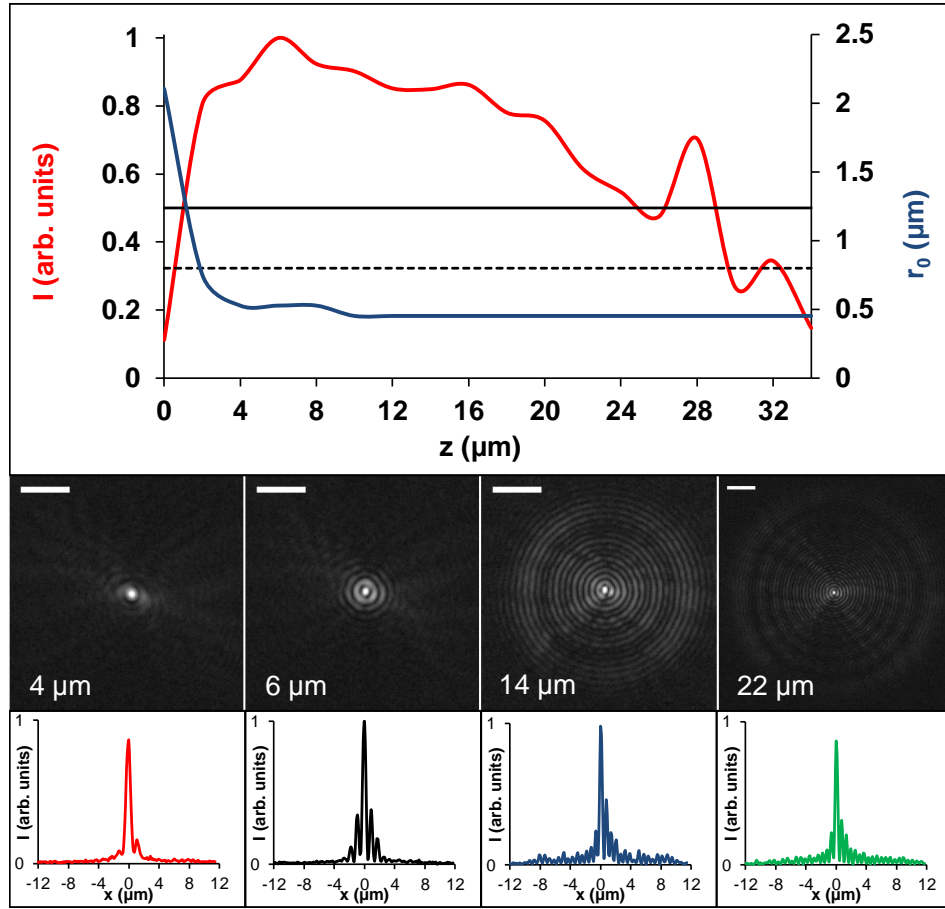


Figure 4.8 – Measured parameters of the axicon-generated Bessel beam at the microscope focus. The intensity (red) peaks at 7 μm and displays some oscillations, particularly at greater distances from the objective. Black solid and dotted lines show the 50 % and 32.27 % limits used to define the DOF and Z_{max} respectively. r_0 (blue) starts off large and rapidly decreases to an approximately constant value for the length of the Bessel beam. Images show the variation of the transverse QBB with increasing axial distance, from 4 to 22 μm . Plots below represent the respective transverse intensity profiles. Scale bars represent 5 μm .

pulses, known as MIIPS (multiphoton intrapulse interference phase scan) was inserted between the laser and the optical system. Further details on the MIIPS can be found in Appendix B.

4.3.1 Laser parameters

The 75 MHz laser (Swift 10, KM Labs, USA) used for this study possessed moveable prisms in the laser cavity, moving them could change the output parameters of the laser. Larger bandwidths could produce pulse durations of 10-12 fs but severely reduced the output power to less than 600 mW. The transmission efficiency of the MIIPS was 28 % so using larger bandwidths significantly affected the power available at the microscope focus. Maximising the power to greater than 1 W reduced the bandwidth to 30-35 nm (approximately 25 fs pulse duration). For the experiments performed in Section 6.3.2, the prism positions were selected as a compromise between large bandwidth and high output power, which were 58 nm (16 fs) and 900-1020 mW respectively. Using these laser parameters, it was possible to compensate and retain 22 fs at the microscope focus using the MIIPS. Changing the prisms varied the central wavelength slightly but it was typically between 780 and 800 nm.

Beam spot size

The beam spot size was $1510 \pm 10 \mu\text{m}$ by $1365 \pm 10 \mu\text{m}$. The beam possessed a higher aspect ratio and less Gaussian shape than the 140 fs laser, making accurate measurements difficult.

M^2 measurements

M^2 values were measured as described in Section 4.2.1 and are displayed in Figure 4.9. The beam diameters showed a greater deviation from the theoretical curve, which could be due to difficulty in the tomographic beam profiler fitting a Gaussian profile to the beam (which might not be Gaussian). The M^2 values, however, are still low with 1.22 and approximately 1 (calculated to be 0.973, indicating less than 3 % uncertainty) in orthogonal directions.

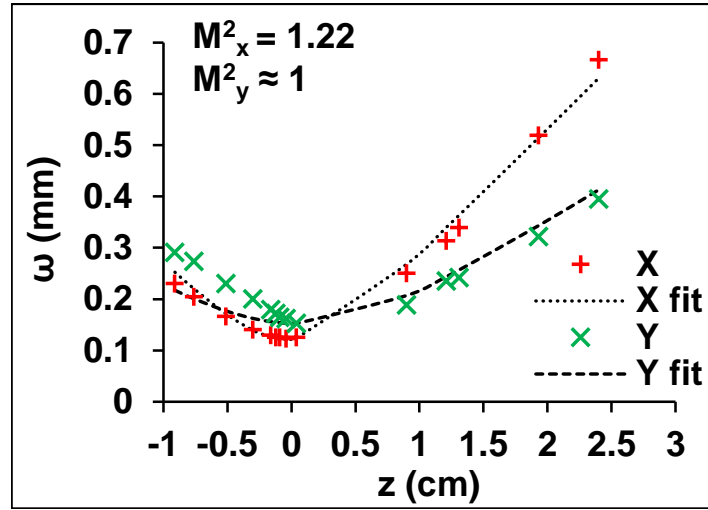


Figure 4.9 – Orthogonal M^2 values for the Swift laser. Plotting x (red) and y (green) values on the same axes highlights the contrasting beam qualities in either direction. Dotted (x) and dashed (y) lines display least squares fits of the measured curves. The y -direction shows a poor fit to theoretical values owing to a large deviation prior to the focal plane, possibly due to a less Gaussian beam shape (compared to the 140 fs laser).

4.3.2 Optical set-up

The 16 fs laser was initially passed through a combination of a rotating half wave plate and polarising beam splitter for power adjustment. The laser beam was then magnified twice before entry into the MIIPS to allow adequate optical resolution on the SLM.

After passing through the MIIPS, the beam was magnified by 0.75 before being coupled into the reconfigurable optical system described above by means of a flip mirror, as shown in Figure 4.7.

Considerations for Gaussian beam comparisons

To quantitatively compare the effects elicited by using the different lasers, it was necessary to match the focal spot sizes. The large bandwidth of the 16 fs laser (up to 90

Laser	<i>x</i>-axis (μm)	<i>y</i>-axis (μm)	Average (μm)	Area (μm^2)
16 fs	0.77(2)	1.03(4)	0.90(5)	0.62(3)
140 fs	0.91(1)	1.02(2)	0.97(2)	0.73(2)

Table 4.1 – Comparison of different pulse duration laser beam waists at the microscope focus. *x* and *y*-axis data were measured by Gaussian fits of camera images of the beams. Average and area were calculated from the measured data. Brackets denote uncertainty in the final digit.

nm) compared to the 140 fs laser (6.35 nm) causes a larger diffraction-limited spot due to chromatic aberrations, limiting the minimum spot size (the larger M^2 value in one direction should also be taken into account).

Beam waist matching was achieved by measuring the size of the diffraction-limited spot from the 16 fs laser and then changing the size of the 140 fs laser at the objective BA (back aperture) to create a similar spot size. This was achieved with a 2x magnifying telescope in place of the 4x telescope used in the above system, creating a 140 fs laser spot size of $0.97 \pm 0.02 \mu\text{m}$ at the focus. Both laser beams pass through the same telescope optics before entering the objective so the 16 fs laser beam size needed further adjustment prior to the entering the optical system to create the diffraction-limited spot at the focal plane. Minimal overfilling of the objective BA created a close-to diffraction-limited spot with minimal power losses. The 16 fs laser was magnified 0.75x before entering the reconfigurable photoporation set-up, leading to a focal beam waist of $0.90 \pm 0.05 \mu\text{m}$, slightly smaller than the 140 fs laser beam waist. Measured focal spot parameters are listed in Table 4.1 and comparative transverse intensity profiles are displayed in Figure 4.10. Photoporation of plant and mammalian cells using this optical system is described in Section 6.3

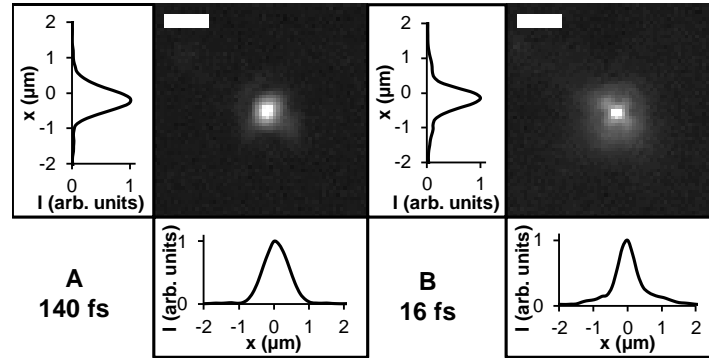


Figure 4.10 – Intensity profiles for focal spots produced by 140 fs (A) and 16 fs (B) lasers at the microscope focus. Corresponding orthogonal 1D intensity profiles are displayed by black lines. The 140 fs laser shows a less distorted profile but a slightly larger spot size than the 16 fs laser. Scale bars represent $2 \mu\text{m}$.

4.3.3 Ultrashort Bessel beam generation

It was possible to create and compensate an axicon-generated Bessel beam at the microscope focus using the 16 fs laser and MIIPS system. The Bessel beam (Figure 4.11) had a slightly smaller propagation length than the longer pulse duration Bessel beam ($\text{DOF} = 18 \pm 2 \mu\text{m}$, $Z_{\text{max}} = 26 \pm 2 \mu\text{m}$) and a larger central spot. The central spot diameter ($1.8 \pm 0.4 \mu\text{m}$) shows large variations, possibly due to noisy background making it difficult to find the point at which the intensity drops to below 13.5 %. The FWHM was also plotted, which was less affected by noise and was calculated as $0.9 \pm 0.1 \mu\text{m}$ - implying $2r_0 = 1.6 \pm 0.3 \mu\text{m}$. The transverse intensity profiles of both the ultrashort and longer pulse duration Bessel beams were plotted at the point of highest intensity (Figure 4.11D). The spot sizes at this point appear similar but the intensity of the ultrashort rings is much lower than for the longer pulse duration Bessel beam.

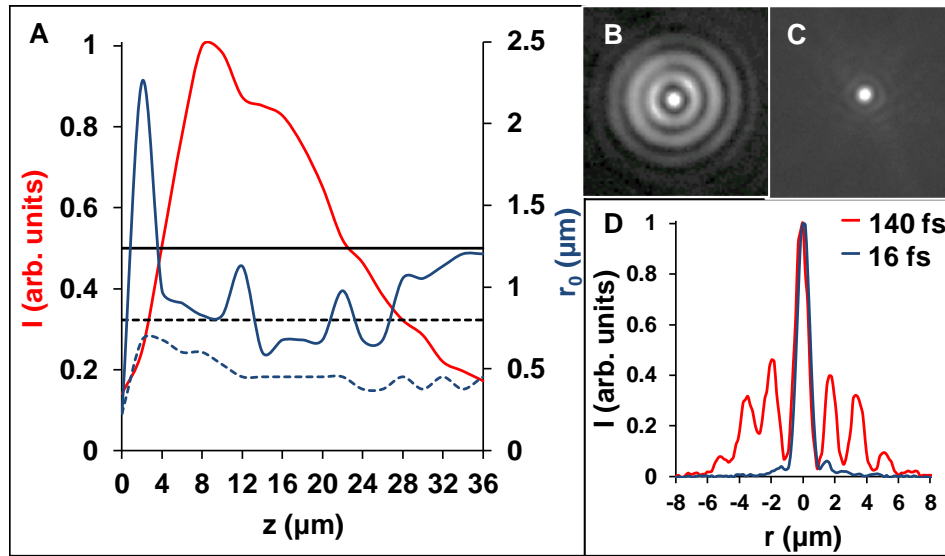


Figure 4.11 – Bessel beam created using ultrashort pulses. The 16 fs laser was directed into the optical system and compensated using the MIIPS at the microscope focus. The Bessel beam created (A) shows a slightly reduced propagation length (on-axis intensity displayed in red) compared to Figure 4.8. The central core radius (blue) is very noisy so the FWHM was also plotted (dashed blue). The transverse intensity, plotted in D, shows decreased fringe visibility at shorter pulse duration (C - blue) when compared to the longer pulse duration Bessel beam (B - red).

4.4 Discussion and conclusions

An optical system was designed to allow changing spatial modes and pulse duration at the microscope focus. These parameters have previously been shown to enhance photoporation in mammalian cells and so this system was built to test these benefits in plant cells.

The long axial propagation of Bessel beams reduce the requirement for precise axial focusing on the mammalian cell membrane but are highly power inefficient and difficult to align and manipulate, in contrast to Gaussian beams. A system that can switch between beams can then exploit the benefits of either beam as required. Flip mirrors were

employed to switch between an axicon-generated Bessel beam and close-to-diffraction-limited Gaussian beam.

The measured Gaussian beam was smaller than the theoretical diffraction limited spot size of $1.22 \mu\text{m}$. This discrepancy is probably due to the using the same NA objective for imaging. A more accurate measurement technique might be to either use a second objective of higher NA in transmission mode or to use a knife-edge measurement technique. The former measurement technique would require accurate mounting of a second objective above the microscope stage. The latter is not suitable for Bessel beam characterisation, making it impossible to provide a fair comparison between the two beams using this method.

The measured Bessel beam showed a central spot size close to that of the theoretical value (936 nm) but the axial propagation was greatly reduced. This reduction in propagation distance is probably caused by an imperfect axicon tip [184]. It is impossible to manufacture an axicon with a perfectly conical tip, the tip will always be rounded-off slightly. The large initial central spot size and oscillations in the on-axis intensity are artefacts of the imperfect tip. Using demagnifying telescopes after the axicon, as was necessary in this system, enhances intensity oscillations, further decreasing the axial propagation. It is possible to introduce a spatial filter in the Fourier plane of the axicon (where the beam takes the form of ring) to reduce the effect of an imperfect tip [184] but this was found to reduce the power prohibitively. Non-optimal positioning of telescope lenses after the axicon can also reduce the propagation distance but tend to lead to decreasing spot size with axial distance too, implying this is probably not the case in this system, where the spot size stays constant.

To create a system that can also vary pulse duration at the microscope focus, two lasers were coupled into the system: a high-powered, 140 fs, turn-key system and a laser capable of producing sub-12 fs pulses combined with a pulse dispersion system to achieve transform-limited pulses at the microscope focus. To compare these two different pulse durations quantitatively it was necessary to match the spot sizes at

the focus. The lasers had different initial spot sizes, aspect ratios, M^2 values, and bandwidths, making it necessary to fill the objective BA by different amounts to yield similar focal spot sizes.

The greater difference in orthogonal M^2 values for the Swift created a larger aspect ratio focal spot than the Chameleon. To compare spot sizes between the two lasers, the average beam waist and focal spot area were found. The average spot sizes varied by less than 10 % and were just within the measured uncertainties of each other. The difference in area was larger than the difference in average spot size but still under 20 %. Use of a CCD to image the spot sizes is not the most accurate method, as described above, and at large bandwidths the sensitivity of the camera to different wavelengths might have an effect on the measured values.

Grunwald *et al.* [185] found that ultrashort-pulsed (< 30 fs) Bessel beams displayed different behaviour to CW Bessel beams, some observed properties are also seen in the ultrashort Bessel beam created in this chapter. Pulse duration is inversely proportional to laser bandwidth. Short pulses contain more wavelengths and this translates to spatial variation when an ultrashort pulse is incident on an angularly dispersive element, such as an axicon (dispersion of ultrashort pulses is discussed in more detail in Section 6.1.2) [186]. This spatiotemporal coupling, when the spatial and time coordinates are interdependent, decreases the contrast and intensity of the Bessel beam rings. Fischer *et al.* [187] showed that Bessel beams using ultrashort pulses exhibited fringe extinction beyond a certain radius as superpositions of different spectral components occur. Decreased ring intensity at low pulse duration was visible in Figure 4.11D.

An increase in ring spatial frequency was possibly in evidence, although the decreased intensity makes this difficult to discern. The Bessel beam produced here also showed slightly reduced axial propagation but this could also be due to a difference in beam waist incident on the axicon. The spatial frequency change and decrease in axial length observed here is interesting. Grunwald *et al.* attributed the effect to reduced contributions from other axicons within an array when the distance exceeds the

coherence length. The same observation here for a single axicon suggests another possible source of these effects. A nearly two-fold increase in beam spot size was observed here, contrary to Grunwald *et al.*, this could be due to different camera sensitivities or difficulty in extracting the central spot radius from the noisy data.

This chapter has designed and constructed a system to switch between different optical configurations and change optical parameters, such as spatial mode, pulse duration and power at the microscope focus, while keeping important parameters, such as the transverse area of induced multiphoton effects, the same. These optical parameters have all previously been proven to affect photoporation in mammalian cells but have yet to be tested in plant cells. The next two chapters will describe the use of this optical system to investigate photoporation in plant cells.

4.5 Chapter acknowledgements

Preliminary design of the reconfigurable system was aided by Tomas Cizmar. Building of the system was performed with help from Anisha Kubasik-Thayil. Bessel beam plots were produced using a MATLAB code written by Helen Rendall.

5 | Femtosecond photoporation of tobacco BY-2 cells

Parts of this chapter are adapted from the article “Femtosecond Optoinjection of Intact Tobacco BY-2 Cells Using a Reconfigurable Photoporation Platform” [171] published in PLoS ONE.

5.1 Introduction

The current literature concerning plant photoporation has been outlined in Section 3.4. A large variety of plant types and laser parameters have been employed but there is still much room for further investigation. The majority of the literature displays very low efficiency of injection or transformation, not more than a few percent, which suggests that not all parameters have been fully optimised to achieve efficient injection into plant cells. This chapter varies optical and biological parameters to optimise and investigate the delivery of membrane impermeable molecules into a model suspension plant cell line, tobacco BY-2 cells (*Nicotiana tabacum* L., cv Bright Yellow 2 (BY-2) [188]).

The majority of plant photoporation studies employ nanosecond (ns) ablation with a UV excimer laser [130, 132–134, 137, 139–141] for injection and transformation studies. The shorter the pulse duration applied to the cell, the less collateral damage occurs when irradiating the cell [20], which is reflected in the transformation efficiency. For ns

irradiation in mammalian cells, the achieved transformation efficiency is between 0.6-10 %, much lower than the 40-60 % that can typically be achieved when using femtosecond pulses (although the laser wavelength used also changes, from 355 nm to 800 nm so the accompanied changes in absorption and penetration depth should also be taken into consideration). Although only a few plant photoporation studies have been concerned with using femtosecond lasers [149, 151, 152], the injection efficiencies achieved were much higher (up to 68 %) than those cited in ns studies (a few percent), which lends promise to femtosecond lasers as efficient plant photoporation tools.

The relatively small pool of femtosecond plant photoporation papers have varied in aim and experimental protocol. Jeoung *et al.* [152] studied perforation of lily pollen grains with a 1 kHz repetition rate laser, inducing poration by a different damage mechanism to the other two studies (and this thesis) using 80 MHz repetition rates, making direct comparison difficult. Tirlapur *et al.* [149] used photoporation as a tool to investigate symplastic connections within *Arabidopsis* root meristem unachievable by other methods. This demonstrated a unique trait of photoporation, but included very little experimental detail on the photoporation protocol and important variables such as viability and efficiency.

The most similar study to the one presented in this chapter was that of LeBlanc *et al.* [151], which investigated the injection of dextrans into *Arabidopsis* epidermal cells from plant stems. While it is useful to explore single cell photoporation in higher plant tissue, it cannot be considered particularly representative of the plant cell system due to the individual cells' specialised states. The tobacco BY-2 cells used in this chapter were chosen for their homogeneity and predictability, which makes them a widely accepted representative model system [189–191]. LeBlanc *et al.* [151] also use a slow injection protocol using seven separate irradiation doses 0.5 μm and 30 seconds apart to maximise the probability of targeting the membrane. A Bessel beam, as outlined in Section 2.2.3, can increase the chance of targeting the membrane with a single irradiation dose, significantly reducing the time taken to target a single cell.

Bessel beam photoporation of plant cells is therefore investigated in this chapter as a possible method to increase throughput.

Nearly every photoporation study concentrating on intact plant cells describes the use of a change in the external osmotic pressure to facilitate entry of extracellular medium into the cell. Standard plant culture medium is hypotonic with respect to the cell interior so the creation of a pore in the membrane initiates an outward flux of cytosol as the osmotic pressure is equalised. Hypertonic treatment of the cell causes plasmolysis, creating a “temporary protoplast” as the membrane is pulled away from the cell wall and laser access to the cell membrane is enhanced [112]. A breach of the cell membrane will then cause uptake of extracellular medium by the cell.

Ferrando *et al.* [158] showed that subjecting plant cells to high osmolarities during plasmolysis-deplasmolysis cycles can cause high cell death rates. Guo *et al.* [139] reported a transformation efficiency of only 0.5 %. The reasons for the low transformation efficiency were not elucidated and could be due to frequent cell death induced by the large osmotic change in medium applied for the poration of cells in this study. Media that are only weakly hypertonic, however, reduce the void area produced [158] and therefore decrease the maximum possible medium uptake by the plasmolysed cells. By incrementally changing osmolarity and studying the effects on both cell death and medium uptake, it would be possible to optimise photoporation in plant cells.

In this chapter, the optimal parameters that determine femtosecond optical injection of intact plant cells were evaluated and described. An experimental set-up, described in Section 4.2, allowing reconfiguration between a Gaussian and a Bessel beam at the focus by switching optical components, was used to vary optical parameters. Comparisons between the two optical geometries were conducted on tobacco cells in culture to determine the effect of beam geometry on plant cell optoinjection and subsequent viability.

Identifying a strategy to investigate photoporation of plant cells, first we employed the fluorophore propidium iodide (PI) as a binary measure of optical injection success

to efficiently optimise photoporation, comparing different powers, beam shapes and medium osmolarity. We then injected different fluorophores to glean more information about the injection process, such as calcein to monitor the dynamics of injection and different-sized fluorescent dextrans to determine the effect of molecular size. Weber *et al.* successfully photoporated fluorescently-labelled DNA into plant cells [136] as a precursor to achieving optical transformation [137]. We therefore investigated photoporation of fluorescent oligonucleotides before discussing applications to optical transformation of plant cells.

5.2 Materials and methods

5.2.1 Photoporation of BY-2 cells

BY-2 culture is described in Section A.1 [188]. Prior to the experiment, cells were collected by centrifugation of 1 ml of a 3-5 day-old culture at 500 g for 2 min. The standard culture medium was aspirated and replaced with 500 μl of medium containing varying sucrose concentrations (from 0.09-0.69 M sucrose) depending on the experimental condition. The cells were then left at room temperature for 30 minutes to allow plasmolysis to occur. 100 μl of this solution was plated on a 10 mm glass-bottom dish (World Precision Instruments, USA) with an optical thickness of 0.17 mm. The dish of cells was placed onto the stage of the inverted microscope into which the optical system described in the previous chapter is coupled. A 60x objective was used for imaging and delivering laser irradiation to the imaged cell. The cell membrane of individual cells was then targeted with 40 ms laser doses: a single shot with the Gaussian beam, a single shot with the Bessel beam or three 2 μm axially separated shots with the Gaussian beam (one shot focused on the membrane, the other two 2 μm above and 2 μm below the membrane) using the optical system described in Section 4.2.2 [171]. Axial separation was performed manually using a calibrated stage.

The osmolarity of each solution was measured using a freezing-point osmometer (Type 15, Löser, Germany) with each solution measurement performed in triplicate.

5.2.2 Propidium iodide optical injection

Just prior to laser irradiation, propidium iodide (PI) was added [147, 149] to a final concentration of 1.5 μM (Life Technologies, USA). The working concentration was empirically determined so that cell death was minimised after 1 hour in solution. PI was added post-incubation to reduce contact time with cells and therefore maximise cell viability.

Determination of optoinjection success was performed 2-3 minutes after photoporation using epi-fluorescence imaging with a cooled CCD camera (Clara, Andor, UK) and a TRITC filter cube (Nikon UK). Successful, viable optoinjection manifested as a low-level fluorescence over the protoplast interior. Extracellular fluorescence was indicative of optoejection having occurred. Unsuccessful photoporation would display either no fluorescence or only localised autofluorescence, which could be identified by scanning the imaging plane over the entire cell volume; autofluorescence was only present at the site of laser irradiation. Photoporated yet non-viable cells, were identified by a strong PI fluorescence in the cell nucleus.

5.2.3 Measurement of plasmolysis

The degree of plasmolysis induced at different solution osmolarities was determined by two methods. First, cells were incubated in osmotic solutions as described above. Then, for each medium osmolarity, 20 cells were selected at random and the CCD was used to image a cross-section in brightfield. To measure the void space, both cell and protoplast were outlined manually in ImageJ to measure their areas. The number of cells that displayed plasmolysis for each experiment was also noted.

5.2.4 Optoinjection of calcein

A 30 μM working concentration of calcein (Life Technologies) was added just prior to irradiation. Calcein uptake was monitored using the 488 nm laser attached to a confocal imaging head (C1, Nikon UK); a cross-sectional image of the cell in the plane of laser irradiation was taken every 5 seconds for 6 minutes. Analysis of the images was performed using ImageJ [192]. The normalised fluorescence within the whole cell relative to the background was established. No photobleaching was observed for these imaging parameters.

Confocal imaging did not reliably observe bubbles, which generally lasted for less than 5 seconds. It was therefore impossible to screen the cells for bubble formation (assumed to be the catalyst for optoinjection) during irradiation. Post-experiment determination of optoinjection success was performed by using a 3σ threshold on the fluorescent data: if the maximum fluorescence reached was greater than three times the standard deviation of a control cell in the same field of view then the cell was assumed to be optoinjected. Curve-fitting was performed by least squares optimisation of a saturation curve of the form $I(t) = I_{max}(1 - e^{-\frac{\ln 2}{t_{1/2}}t})$ [193] relating relative fluorescence intensity ($I(t)$) and time (t), where I_{max} is the maximum relative fluorescence intensity and $t_{1/2}$ is the time taken to reach $\frac{1}{2}I_{max}$.

5.2.5 Optoinjection of dextrans

Fluorescein-conjugated dextrans of sizes 3-70 kDa (Sigma-Aldrich Co., USA) were added to make a working concentration of 10 μM . For intact cells, dextrans were added prior to incubation to help draw the dextran through the cell wall and maximise dextran concentration in the apoplast [194].

Enzymatic digestion of the cell walls of intact cells to make protoplasts was per-

formed as described in Section A.1.3 and experiments were performed within 24 hours. Dextran was added prior to the experiment, no incubation was required.

Single cross-sectional images of porated cells were taken before and 3 minutes after irradiation using the confocal system described in the previous section. No imaging during irradiation was required so real-time brightfield imaging could be used to photoporate cells and protoplasts. Observation of a bubble upon laser irradiation was used as a marker for successful optoinjection. Normalised cellular fluorescence relative to the background was measured using ImageJ.

5.2.6 Optoinjection of nucleic acids

Fluorescein-conjugated morpholinos (MOs) (GeneTools, LLC, USA) and DY-547 labelled synthetic siRNA (Thermo-Scientific, USA) were added to cells at concentrations of 30 μM and 2 μM respectively. MOs were imaged using the 488 nm confocal laser line with emission detected using a green-sensitive photomultiplier tube (PMT) and siRNA was imaged using the 534 nm laser line with a red-sensitive PMT for emission detection. Protoplast isolation, photoporation protocol and image analysis were performed as described in the previous section.

5.3 Results

5.3.1 Bubble formation and optoinjection success

Successful optoinjection by both beam geometries of the BY-2 cells was always preceded by the creation of a gas bubble at the cell surface as seen in Figure 5.1B. These bubbles are caused by multiphoton absorption leading to photoionisation within the focal volume. If the density of free electrons created exceeds the optical breakdown threshold of the irradiated material then a cavitation bubble will be produced [195], disturbing

the cell membrane and transiently increasing its permeability. By increasing the laser fluence, long-lasting gas bubbles, of the order of a few seconds, with larger diameters ($\geq 5 \mu\text{m}$) could be created; however, these forms of bubbles were observed to be followed by cell death as damage to the membrane is permanent [17]. The transient nature of the bubble at low laser intensities is shown in Figure 5.1C, which was taken 3 minutes after a laser dose and shows no lasting visible damage to the area of irradiation.

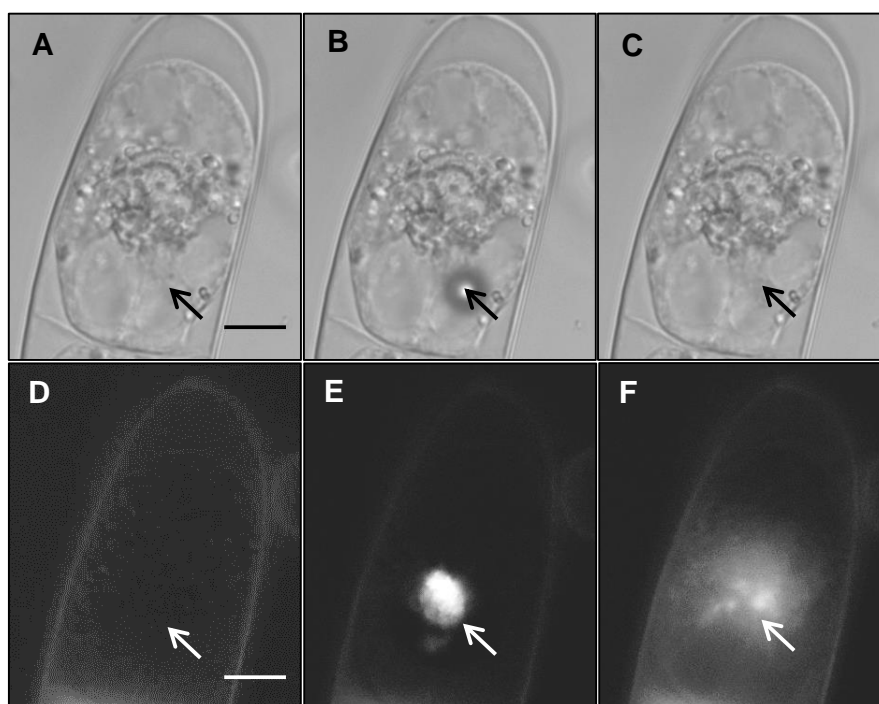


Figure 5.1 – Optical injection of PI into a plasmolysed BY-2 cell, plasmolysis was achieved by incubation in standard culture medium made hypertonic by the addition of 0.488 M sucrose (solution osmolarity = 699 mOsm/L). Shown in brightfield (A-C) and fluorescence (D-F). (A) Before shooting, (B) transient bubble created on cell membrane during laser dose, (C) no visible laser damage left post-irradiation. (D) Pre-irradiation showing faint PI staining of the cell wall. (E) Laser induced transient auto-fluorescence at the point of irradiation. (F) Permanent increase in cytosolic fluorescence as PI enters the cell. Arrows indicate site of laser irradiation. Scale bars denote $10 \mu\text{m}$.

5.3.2 Determining the effect of changing optical parameters on optical injection

The effect of the beam geometry on successful photoporation was determined by irradiating the cells with either a Gaussian beam or a Bessel beam. From the literature and preliminary experiments, it was evident that osmotic pre-treatment of the cells would be required to allow uptake into the cell protoplast. The initial experimental conditions used standard culture medium made hypertonic by the addition of 0.29 M sucrose (osmolarity of 320 mOsm/L) as the surrounding medium to induce plasmolysis of cells. Sucrose was chosen as an osmoticum due to the high viability it allows during plasmolysis-deplasmolysis cycles when compared to inorganic solutes [194].

The diameter of the central spot of the Bessel beam was matched to the beam waist of the focused Gaussian beam ($2r_0 \approx 2\omega_0 \approx 1 \mu\text{m}$). The axial extent ($26 \mu\text{m}$) was approximately 13 times longer than the confocal range of the Gaussian beam ($b = 2z_R = 2 \mu\text{m}$). Two different modes of laser irradiation were employed using the Gaussian beam; either a single dose or three doses separated by approximately $2 \mu\text{m}$ axially and 1 second temporally. The latter is intended to increase the chance of targeting the cell membrane while avoiding any accumulative effect from multiple exposures [16]. In mammalian cells, $1 \mu\text{m}$ separation is used but the larger size and shape of the plant cells led to a decision to increase this separation to a more useful distance. A single shot was applied with the Bessel beam. In this way we could compare the two methods previously utilised to increase the chance of targeting the cell membrane alongside the standard single Gaussian dose. The laser intensity applied to the cell was also varied because it has previously been shown that the laser fluence affects the efficiency of optoinjection [196].

PI was chosen as the optoinjection fluorophore for this part of the experiment since the lack of background fluorescence makes small uptake volumes easy to image. PI is membrane-impermeable unless the cell membrane is compromised and it is used as

a standard proof-of-concept photoporation fluorophore [49, 53, 172]. Upon entry into a photoporated cell, PI intercalates with nucleic acids present in the cytosol causing enhanced fluorescence, which is seen experimentally in the cytoplasm. Optoinjection of PI into the cell can be seen in the fluorescent images from Figure 5.1. Prior to laser irradiation, no background fluorescence is seen except a weak staining of the plant cell wall (Figure 5.1D) caused by PI binding to pectins in the cell wall [197]. Upon irradiation, a broadband autofluorescence was induced at the laser focus, as shown in Figure 5.1E. This effect was either transient or permanent depending upon laser intensity, with permanent autofluorescence indicating cell death. If photoporation was successful, entry of PI into cells occurred and cytosolic fluorescence was observed (Figure 5.1F).

The application of each of the three laser irradiation patterns displayed increasing efficiency of optoinjection (O) as the intensity within the central spot (where all multiphoton effects are assumed to occur) increased (Figures 5.2A,B,C). Three doses with the Gaussian beam (Figure 5.2B) displayed the highest efficiency, achieving up to 61 ± 5 %. Viability (V) was severely compromised in this regime, never rising above 65 %. Single shots with the Gaussian beam (Figure 5.2A) showed the lowest efficiencies overall, (maximum efficiency of 32 ± 7 %) but with greater viability than with three doses. The Bessel beam (Figure 5.2C) displayed the highest viabilities at the majority of intensities and provided intermediate efficiencies, reaching a maximum at 51 ± 6 %. To compare quantitatively the beam geometries, we considered which irradiation pattern would produce the highest proportion of cells that are both optoinjected and viable (defined as N). To determine N , the product of the optical injection efficiency and viability was calculated at each central beam spot intensity (Figure 5.2D). The percentage of the power in the central spot of the Bessel beam was 6.5 %. As the area of the central spot is smaller than the surrounding concentric rings, only the central spot has a high enough intensity to create multiphoton interactions and therefore contribute to photoporation [20]. At low laser intensities, N is small due to the low optoinjection

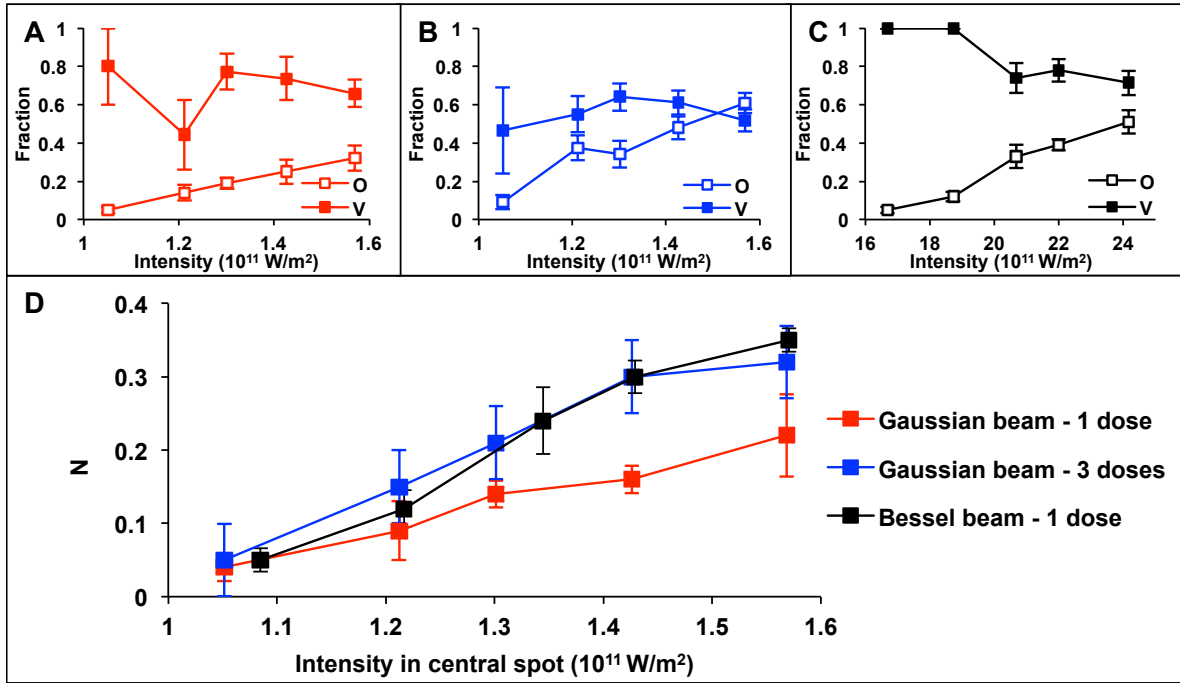


Figure 5.2 – Optoinjection efficiency (O) and viability (V) of BY-2 cells. Cells were plasmolysed prior to optical injection by incubation in cell culture medium with 0.29 M sucrose (osmolarity = 320 mOsm/L). Cells were then irradiated with different laser powers using (A) a single 40 ms laser exposure or (B) three 40 ms laser exposures with the Gaussian beam or (C) a single 40 ms laser exposure with the Bessel beam. For both beam geometries the optoinjection efficiency (represented by open squares) increases with power at the focal plane while viability (solid squares) usually decreases. (D) shows N (the proportion of cells being both viable and optoinjected) for varying central spot intensities. N increases as the intensity increases. The Bessel beam (black) shows a higher value for N than the Gaussian beam (red) when considering a single shot. When comparing with three axially separated shots of the Gaussian beam (blue), N is comparable to the Bessel beam. Each data point represents the mean for $n = 5$ with 20 cells per experiment. Error bars represent the standard error of the mean (SEM).

efficiency even though the viability of the optoinjected cells can be up to 100 %. As the intensity of the laser increases, so does N as O begins to increase with only a slight reduction in viability. Figure 5.2D shows that at higher intensities, the single shot

Gaussian provides the lowest values of N . For all intensities explored in this study, the Bessel beam and three shots with the Gaussian beam display comparable values for N ; the higher efficiencies achieved when using the Gaussian beam are counteracted by the subsequent decrease in viability.

5.3.3 Effect of medium osmolarity on optoinjection efficiency

Having established that the Bessel Beam geometry was the optimal configuration for time-efficient optoinjection of dyes into tobacco BY-2 cells, the role of the extracellular medium on optoinjection efficiency was investigated in more depth. Prior to laser irradiation in the presence of PI, cells were incubated in media using differing sucrose concentrations to vary the osmolarity, starting with the standard hypotonic medium used for culturing (total osmolarity of 171 ± 2 mOsm/L). Experiments were performed using a single 40 ms dose from the Bessel beam with a power of 1.6 W at the focal plane to maximise photoporation efficiency.

At each of the five osmolarities tested, cells were photoporated and studied for either injection or ejection of cytosol from the protoplast (Fig 5.3A). Cells were also screened for viability as described in the previous section. At low osmolarity (lower than 320 ± 2 mOsm/L) the primary effect observed was ejection of cytosolic medium into the extracellular environment after laser treatment (Figure 5.3B,C). Extracellular PI then binds to solutes ejected from the cell to cause an increase in fluorescence around the exterior of the cell (Fig 5.3C). Conversely, at osmolarities greater than 320 ± 2 mOsm/L, the dominant effect was intake of extracellular medium (injection, Fig 5.3A). In contrast to optoejection, optoinjection was characterised by fluorescence within the protoplast (Fig 5.1F). The increase in injection frequency, however, was counteracted by an increase in the occurrence of cell death in optoinjected cells. Figure 5.3A shows that in media with an osmolarity of 320 ± 2 mOsm/L, optoinjection and optoejection both occur in about 10 % of cells.

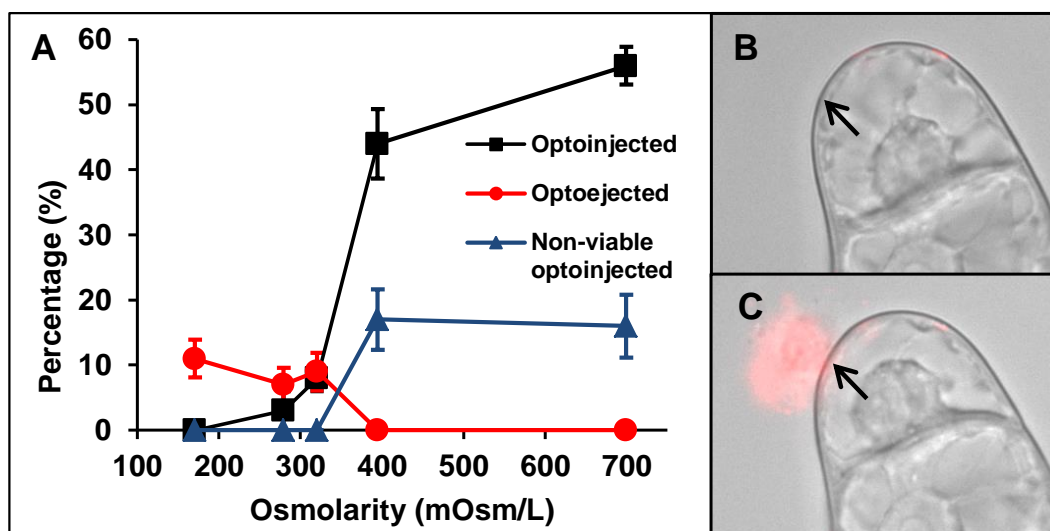


Figure 5.3 – Optoinjection efficiency differs depending upon the osmolarity of the surrounding medium. As we increase the osmolarity (A), the efficiency of optoinjection (black squares) increases from zero to 50 % as the surrounding medium changes from hypertonic to hypotonic. Conversely, the optoejection efficiency (red circles) falls from around 10 % to 0 % above 320 ± 2 mOsm/L. As the molarity of the solution increases, cell death (blue triangles) increases. At 320 mOsm/L the optoinjection and ejection efficiency are approximately equal. Each data point shows the mean for $n = 3$ with 20 cells per experiment; error bars represent SEM. (B) and (C) show brightfield and fluorescence overlays of a cell prior to (B) and 2 minutes after (C) laser irradiation in standard culture medium in the presence of PI. Photoporation causes cytosol extrusion, the ejected cytosol is stained by PI and fluorescence is seen outside the cell.

To relate these photoporation effects seen to plasmolysis changes within the cell, the degree of plasmolysis at the different solution osmolarities was measured by the two methods usually employed [198]: measuring the void space and counting the number of plasmolysed cells. The void space fraction was determined by manually outlining both the whole cell and cell protoplast and dividing the area of the latter by the former. A cell was determined to be plasmolysed by observation; if the protoplast was visibly pulled away from the cell wall then it was counted as plasmolysed.

By looking at the void space as a fraction of the whole cell (Figure 5.4A), a general

increasing trend is observed as the osmolarity of the surrounding solution is increased. This trend begins slowly at 171-279 mOsm/L, is steepest around 279-395 mOsm/L and then starts to level off again after 395 mOsm/L. The number of plasmolysed cells seen in each solution also shows an increase with osmolarity. Much sharper growth between 171-320 mOsm/L is followed by a saturation point at 399 mOsm/L, beyond which all observed cells were plasmolysed. Examples of cells in low, medium and highly osmotic solutions are shown in Figures 5.4B-D respectively.

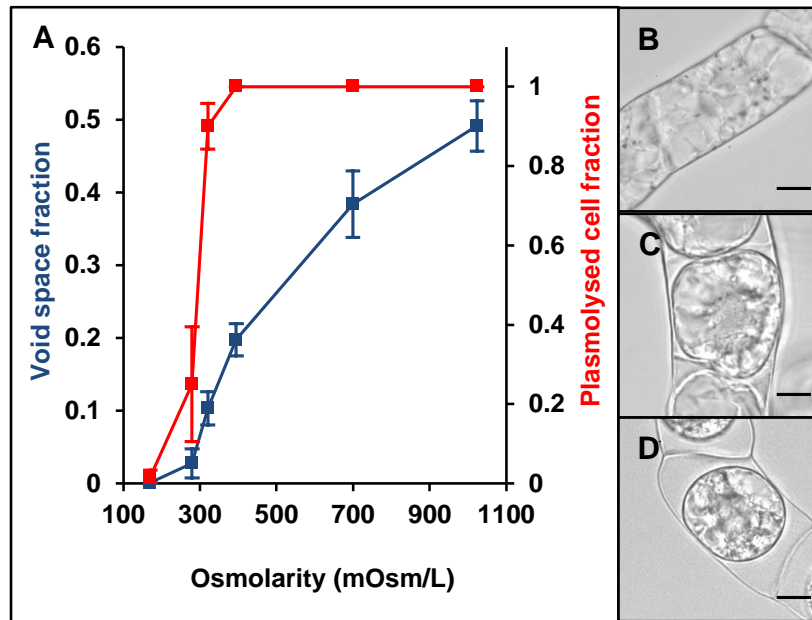


Figure 5.4 – The osmotic effect on plasmolysis of BY-2 cells (A). Both the void space (blue) and fraction of plasmolysed cells (red) increases with the osmolarity of the surrounding medium but the red line shows a much steeper incline around the point of incipient plasmolysis (50 %). Error bars denote the SEM for $n=3$ experiments with 20 cells counted in each. (B-D) show example cells in standard culture medium (171 ± 2 mOsm/L), very weakly hypotonic (320 ± 2 mOsm/L) and strongly hypotonic (699 ± 4 mOsm/L) solutions respectively. The resulting plasmolysis occurs slightly in (C) but seen very strongly in (D) as the membrane pulls away from the cell wall in the highly osmotic solution. Scale bars denote 10 μm .

5.3.4 Exploration of optoinjection dynamics under hypertonic treatment

Next we explored the dynamics of optoinjection in more detail. By determining the rate and volume of uptake of an optoinjected molecule, we can begin to understand the dynamics of pore formation and closing [49], crucial to optimising optical injection for use as a potential research tool. Calcein was used to monitor the continuous uptake of extracellular medium during photoporation of intact cells in media of differing hypertonic osmolarities (395 ± 6 , 699 ± 4 and 1024 ± 11 mOsm/L; abbreviated to 0.4, 0.7 and 1 Osm/L in the following section). These measurements allowed us to establish the time-scales over which optoinjection occurs and also the volume of extracellular medium that is taken up and how these change with extracellular osmolarity. The small size and inert nature of calcein makes it an ideal fluorophore for monitoring cellular uptake, moreover there is no time delay (as occurs with PI) in visibility of the fluorescence inside the cell. As described above, three axially separated shots using the Gaussian beam at 70 mW at the focal plane were used for optoinjection, taking advantage of the power-efficiency of the Gaussian beam. This allowed other experiments using the same laser to take place simultaneously because the Gaussian beam required only 6 % of the power required for the Bessel beam.

The increase in intracellular fluorescence was observed using a confocal microscope to eliminate background fluorescence. Unlike PI, calcein possesses high levels of fluorescence even when not bound to a target. Calcein cannot pass through the cell membrane so the interiors of viable, non-porated cells will be dark. When using epi-fluorescence, the optical sectioning is very low so light will be collected from above and below a cell. When using a fluorophore like calcein, fluorescence emitted from the calcein surrounding a cell will be collected when attempting to image a cell, this will increase the level of background observed for a cell which should appear dark. Using confocal microscopy, light is collected only from a thin section so the contrast between a dark cell and highly

fluorescent solution is increased. The contrast could be further enhanced by using more stringent optical sectioning techniques such as structured illumination, standing wave or 4pi microscopy [7] but confocal microscopy could be easily performed using an attachment to the current microscope, making it ideal for the following experiments.

For each solution osmolarity a least squares fit was performed in order to determine the asymptotic value for the maximum fluorescence (the value reached if we could observe at later time-scales, given by I_{max}). This strategy avoids selection of spurious maxima and gives an accurate estimate of the late time behaviour. The asymptotic value of the maximum fluorescence reached has a direct correspondence to the volume of extracellular medium taken up by the cell as a fraction of the cell volume. Using these fitted curves also allows us to establish the time taken to reach 50 % of that value ($t_{1/2}$), which gives an indication of the rate of medium uptake.

It can be seen from Figure 5.5A that for each solution, the average fluorescence increases relative to the background and shows a sharp increase in the first few minutes followed by a trend towards a horizontal asymptote. The curve is similar to that seen by LeBlanc *et al.* [151]. The 1.0 Osm/L curve decreases once a maximum point is reached, which could indicate the onset of cell death caused by the large physiological changes discussed in the previous section. Data for the first 200 seconds only are used to perform the fit for the 1.0 Osm/L curve and thereafter extrapolated to accurately fit the initial rapid increase. This allows more appropriate values for I_{max} and $t_{1/2}$ to be determined that are independent of the observed decrease.

In Table 5.1, the asymptotic maximum fluorescence for the different molarity solutions is compared. As the molarity increases, I_{max} also increases, more than doubling between 0.4 and 1.0 Osm/L. From inspection of the time taken to reach half of the maximum fluorescence ($t_{1/2}$, Table 5.1), we can gain an insight into the rate at which calcein is taken up by the cell. Each of the curves appears close to saturation after three minutes (Figure 5.5A) but Table 5.1 shows that higher molarity solutions induce

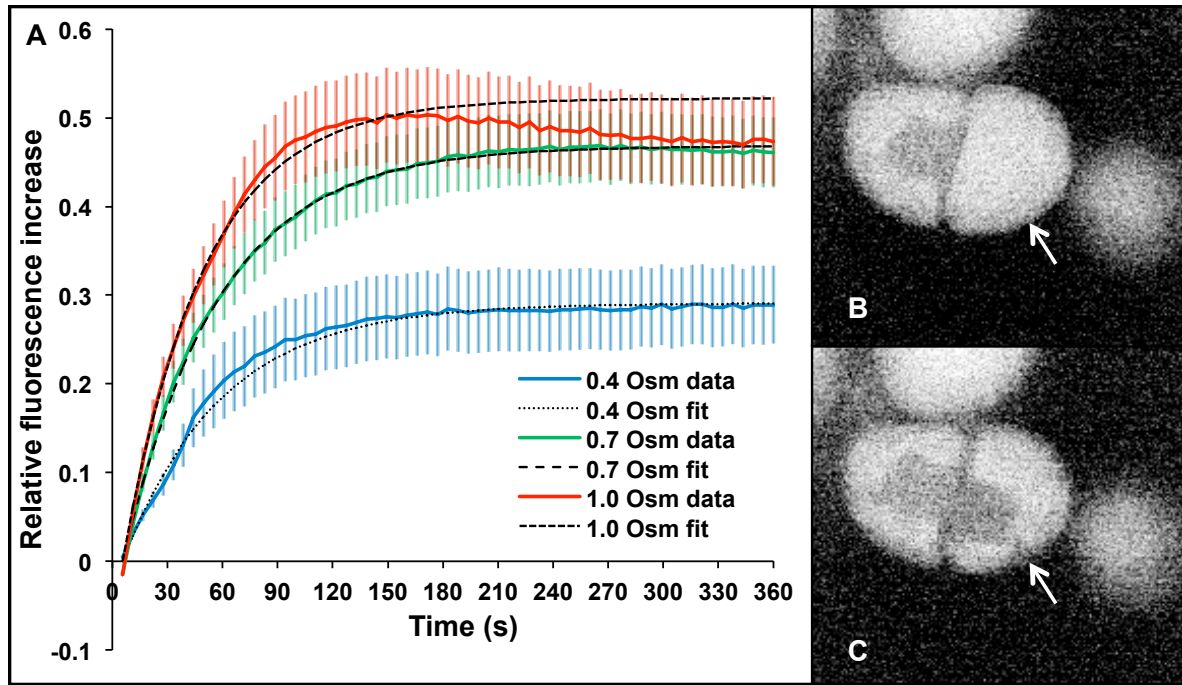


Figure 5.5 – Uptake of calcein during photoporation in hypertonic medium. Solid lines in (A) show the mean increase in intracellular fluorescence relative to background for $n = 20$ cells with error bars representing 0.5 SEM for clarity. Each curve shows a sharp increase in fluorescence in the first few minutes after photoporation, which plateaus after around 3 minutes. The higher molarity solutions show a quicker increase in calcein uptake and reach a higher level of maximum fluorescence than the lower molarity solutions. Dashed lines denote fitted saturation curves. (B) and (C) show a cell (arrowed), in negative contrast for clarity, before and 60 seconds after photoporation in 0.4 Osm/L medium containing calcein. The nucleus, indistinguishable from the rest of the unporated cell in B, becomes filled with calcein along with a cytosolic strand (just visible at arrow tip) but none enters the large vacuole surrounding it.

a greater uptake rate. The variation of $t_{1/2}$ with osmolarity is less pronounced than for I_{max} , with a decrease of less than 20 % occurring between 0.4 and 1.0 Osm/L.

An example of calcein optoinjection before and after photoporation is shown in Figures 5.5B and C. The confocal image is shown in negative to better highlight the entry of the calcein (dark) into the cell (light). Prior to photoporation, the protoplast

Osmolarity (Osm/L)	I_{\max}	$t_{1/2}$ (s)
0.4	0.291(7)	37(1)
0.7	0.468(3)	36.3(3)
1.0	0.521(9)	30.8(5)

Table 5.1 – As the osmolarity increases, the asymptotic maximum fluorescence value, which the saturation curve tends towards, increases. The time taken to reach 50 % of the maximum fluorescence decreases as the molarity of the solution increases. The increased pressure difference caused by higher molarity solutions induces more and quicker uptake of medium to balance it. Brackets denote the error in the final digit; uncertainties were calculated from the R-squared value of the fitted curves.

interior is free of calcein and surrounded by strong background fluorescence. After photoporation, the nucleus and a thin cytosolic strand are filled with calcein as they turn dark. The arrow highlights where a cytosolic strand has become filled with calcein. Although the cell was not porated at this point, the cytoplasmic streaming that occurs in plant cells allows movement of molecules throughout the cell also causes movement of the injected fluorophore, causing it to spread throughout the cytoplasm.

5.3.5 Effect of biomolecular size on cellular uptake

Although biomolecules with a molecular weight of less than 1 kDa are useful for investigating and optimising the optical injection process, biologically-relevant compounds are usually much larger than this, with proteins and DNA reaching up to hundreds of kDa in weight. The presence of the cell wall might therefore present a problem in the delivery of these molecules. To investigate this, fluorescently-labelled dextrans of varying sizes were optoinjected into both intact BY-2 cells and BY-2 protoplasts. Dextrans are non-ionic polysaccharides available in specific weights that are frequently used in membrane exclusion studies. Cells were optoinjected using the same irradiation param-

eters as the preceding experiment. Confocal images were taken prior to irradiation and 3 minutes afterwards to monitor how cellular uptake changes with optoinjectant size.

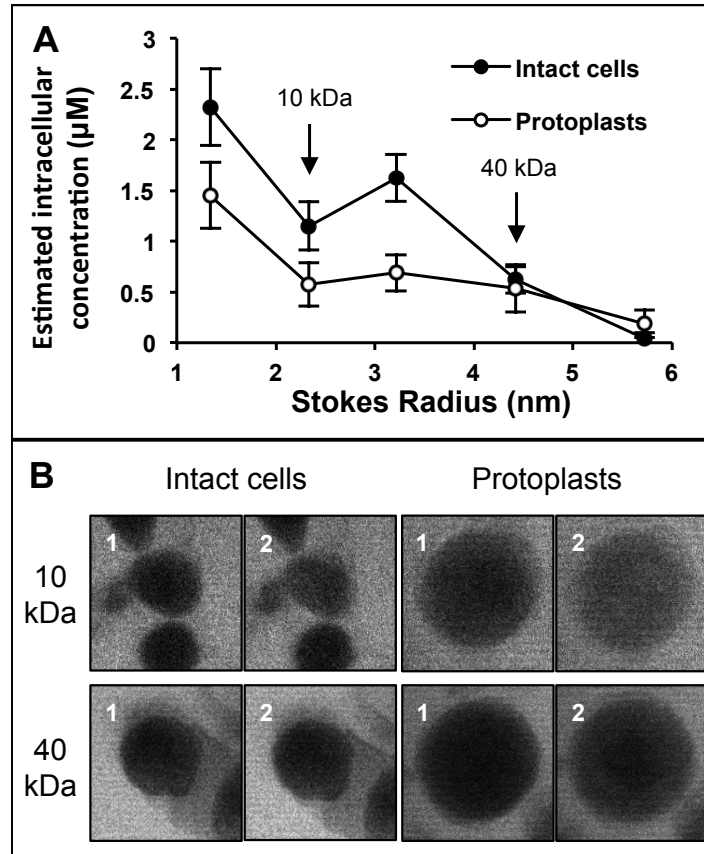


Figure 5.6 – Effect of molecule size on cellular uptake. As the Stokes radius increases, the amount of dextran taken up by the cell decreases (A). The protoplasts take up fewer dextrans than the intact cells for Stokes radii smaller than 5 nm. Beyond 5 nm, the cellular uptake by the intact cells decreases to practically zero and more is taken up by the protoplasts. Data points shown are for $n = 30$ cells with error bars representing the SEM. (B) Representative images (those depicting uptake most comparable to the average uptake) of intact cells and protoplasts before (1) and 3 mins after (2) photoporation in the presence of small and large dextrans. The larger dextrans show less (though still visible) entry into the cell than the smaller dextrans.

The effect of dextran size on cell uptake can be seen in Figure 5.6. The Stokes radius (or hydrodynamic radius, R_H) is calculated from the molecular weight (MW)

using the empirical formula $R_H[nm] = 0.81(MW[kDa])^{0.46}$ [199, 200]. Both intact cells and protoplasts display decreased cellular uptake as the Stokes radius increases. For Stokes radii equal to and smaller than 4.42 nm (corresponding to 40 kDa dextrans), the protoplasts show less cellular uptake than the intact cells. At 3.2 nm (20 kDa), the cellular uptake for intact cells is three times greater than for protoplasts. At 5.71 nm (70 kDa), the cellular uptake is severely reduced in both cell types, although four times more dextrans are taken up by the protoplasts than the intact cells.

5.3.6 Delivery of oligonucleotides into cells

The availability of dextrans in a variety of sizes make them a useful molecule for studying uptake into cells but they have limited use in plant biology. The successful intracellular delivery of a biologically important molecule, such as an oligonucleotide, could help to elucidate the viability of femtosecond photoporation as a relevant plant biotechnology tool.

The size exclusion limit of the cell wall allows small oligonucleotides, such as siRNA, into the apoplast, making them a suitable target for intracellular delivery. Fluorescent siRNA has previously been used as a marker for cellular uptake into BY-2 cells using nanoparticles [123] and therefore was used in this study to identify successful uptake into both photoporated plant cells and protoplasts. The injection of fluorescently-labelled morpholinos, highly RNase resistant synthetic oligonucleotides that are popular in gene expression studies in embryos but relatively underused in plant studies [201], was also investigated. The photoporation and imaging protocol used for this study was the same as described in the previous section.

The degree of intracellular uptake of both siRNA and MOs can be seen in Figure 5.7A in red and green respectively. All datasets showed some severe outliers (greater than 3 times the interquartile range [202]). Positive outliers showed cellular uptake up to 1, equivalent to the background. These were assumed to be caused by cell death

and were removed from the study. Some negative values are expected due to statistical noise (some cells displaying no uptake might show a very slight decrease) but large negative values were assumed to be caused by environmental changes during the study and therefore undesirable. The number of severe outliers was never more than 4 out of 30 cells. Data before removal of severe outliers were plotted using dotted (siRNA) or dashed (MOs) for comparison to the cleaned-up data.

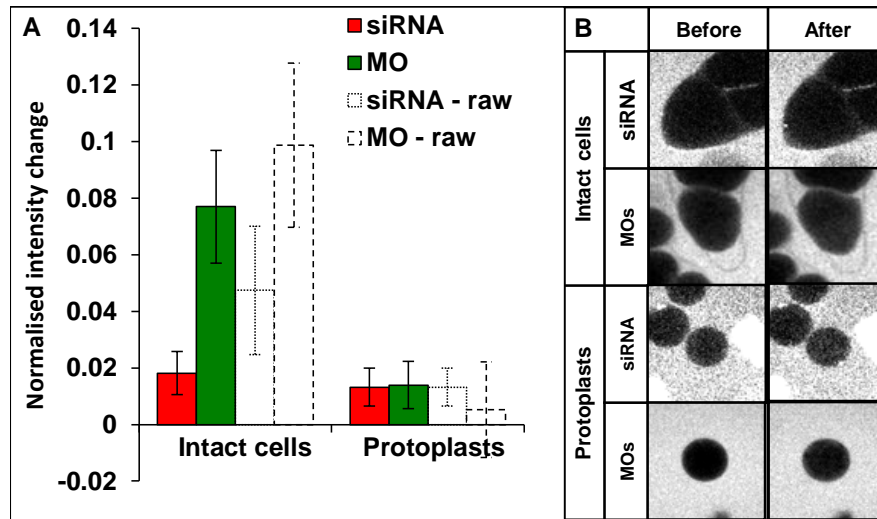


Figure 5.7 – Delivery of synthetic oligonucleotides into plant cells. The fraction of extracellular oligos taken up by the cell varies depending on cell state and oligo type (A). Injection of MOs (green) into intact cells shows four times higher uptake than siRNA (red). Injection of both oligo types into protoplasts displayed similar effects. Dotted and dashed lines show data for siRNA and MO injection respectively with severe outliers included. The data show the average intracellular fluorescence normalised to the background level for $n = 30$ with error bars denoting SEM. (B) Example cross-sections of cells before and 3 minutes after irradiation in the presence of an oligo. Before irradiation the cell is black as no oligo has entered. After irradiation the irradiated cell (centre) increases in intensity as fluorescent oligo enters the cell. siRNA adheres to the plant cell wall (bottom left of intact cell) and accumulates in cell debris (middle right of protoplast). This is unlike the MOs, where the cell wall (intact cell) and cell debris (just seen, bottom) are free from fluorescence.

The greatest degree of cellular uptake was seen when injecting morpholinos into intact plant cells ($7.7 \pm 2 \%$). The uptake of siRNA was approximately 4 times lower than this ($1.8 \pm 0.7 \%$) but was similar to the uptake of both molecules in protoplasts. Figure 5.7B shows example cells before and after laser irradiation. Cells that displayed an intracellular increase of around 10 % were chosen to enable visualisation of the molecular uptake. siRNA and MOs localised differently in both cell types. While both molecules were able to access the apoplast, siRNA accumulated both at the cell wall and in cell debris (seen in intact and protoplast examples respectively) whereas MOs showed no cell wall affiliation and were also excluded from cell debris and dead cells (just seen at the bottom of the protoplasts).

5.4 Attempting optical transformation

One of the projected goals of this study was to obtain femtosecond optical transformation of single plant cells. Optical transformation of tobacco BY-2 cells was not observed at any point during this project and attempts were made to elucidate the reason behind this. This chapter has demonstrated the optical system was capable of injecting extracellular substances into plant cells and its suitability for mammalian cell optical transfection is demonstrated in Section A.2.2. Here, the functionality of the DNA and the addition of a nuclear-delivery reagent was tested to determine any problems with the specific constructs or if a lack of nuclear targeting caused these issues.

5.4.1 Testing common methods of transformation

Common plant transformation techniques were employed to test the suitability of the DNA (and mRNA) for plant cell transformation. Three different nucleic acids were used in experiments, all using various fluorescent proteins as the gene of interest.

- The pRTL2 vector contains a modified 35S transcriptional promoter from the

cauliflower mosaic virus, the 5' non-translated region sequence from tobacco etch virus, a multiple cloning site, and the 35S transcriptional terminator or polyadenylation sequence [203]. Both GFP and RFP reporters were used in two different plasmids.

- 30B. Δ CP: A hybrid vector containing a GFP gene of interest based on TMV strains U1 and U5. A derivative of 30B in which the U5 derived sequences have been replaced with the 3' untranslated region of strain U1 [204]. The DNA plasmid encodes for an RNA virus. A single plasmid entering the nucleus is enough to initiate the replication process and cause large amounts of fluorescence expression.
- PVX and TMV viral mRNA constructs expressing mCherry and GFP respectively. mRNA does not require delivery to the nucleus for protein expression.

Agrobacterium, biolistics and rub inoculation all showed positive results when used to transform tobacco leaves (Figures 5.8C,D and E). This ruled out the possibility of a lack of optical transformation due to the viral DNA being non-infectious in the cell line, or not being of transformation quality.

Transformation of protoplasts was also successfully tested using electroporation of viral DNA and PEG transformation of viral mRNA [115] (Figure 5.9, made using *in vitro* transcription). The protoplasts and purified nucleic acids were therefore amenable to transformation, suggesting another reason for the lack of transformation (spontaneous or otherwise) seen during this study.

5.4.2 Use of a nuclear targeting reagent

For DNA transformation to occur, the injected DNA must pass through the nuclear membrane to enter the nucleus. Praveen *et al.* [57] demonstrated that it was possible to conjugate DNA with a nuclear-localising signal molecule (Nupherin-neuron, Biomol Research Labs, Inc., USA) prior to optical transfection to enhance delivery to the

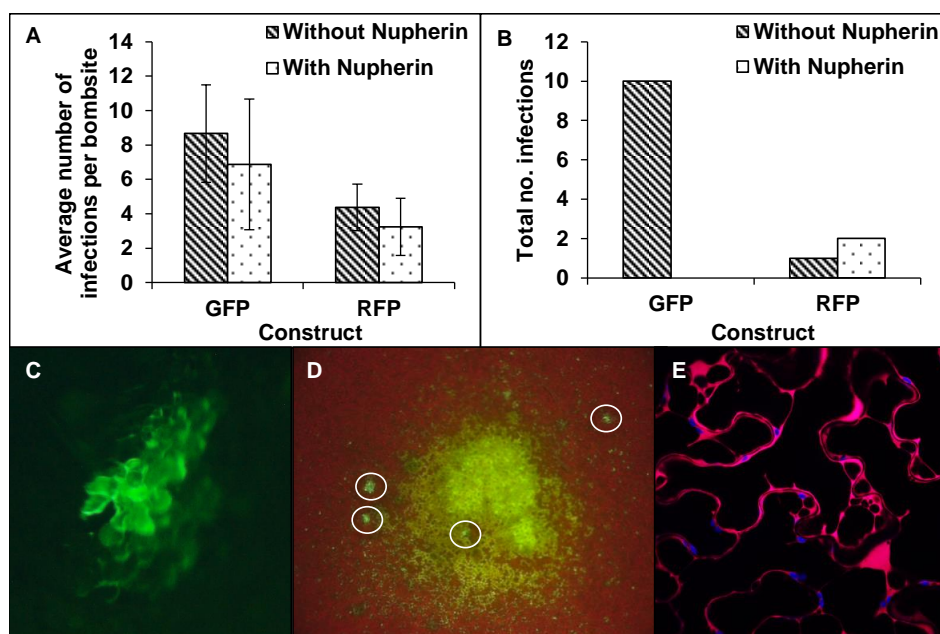


Figure 5.8 – Effect of Nupherin on plant transformation by biolistics (A) and rub inoculation (B). The addition of Nupherin showed no apparent increase in transformation efficiency. (C) GFP-transformed cell using rub inoculation. (D) Four separate infections at a single bombsite from biolistics. (E) Confocal image of GFP-transformed epidermal cells (magenta), chloroplasts are shown in blue.

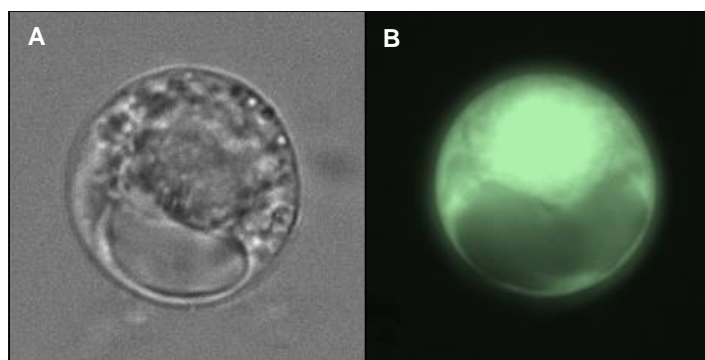


Figure 5.9 – Brightfield (A) and fluorescence (B) image of GFP-expression in a tobacco BY-2 protoplast 12 hours after PEG transformation of TMV-mRNA.

nucleus and increase transfection efficiency, enhancing transfection in slowly dividing, and even post-mitotic, cells. The addition of Nupherin was tested in other mechanical

transformation techniques (rub inoculation and particle bombardment) to see if it was effective in plant cells.

The addition of Nupherin was not seen to enhance the transformation efficiency by either rub inoculation or biolistics (Figure 5.8), suggesting that the nuclear localisation sequences exploited by Nupherin are not present in plant cells. Future experiments could help determine if other nuclear-targeting agents, such as histones [205] or *Agrobacterium* virulence proteins [206, 207] that have been previously been shown to increase transformation efficiency, could increase the opportunity for optical transformation.

5.5 Discussion and conclusions

This study has demonstrated the potential for femtosecond lasers for the optical delivery of membrane impermeable molecules into intact plant suspension cells. By varying the optical and biological parameters, the optoinjection efficiency and dynamics vary greatly.

By increasing laser intensity, the optoinjection efficiency was maximised for both beams because a larger disruption to the cell membrane occurred. The more severe the disruption to the membrane, the more likely that the cell will be non-viable post-irradiation as the membrane permeability may become permanently compromised. The maximum optoinjection efficiency achieved with either beam was over 10-fold higher than reported for FEL laser photoporation of intact BY-2 cells [157] and similar to when using a femtosecond Gaussian beam in *Arabidopsis* epidermal stem cells [151]. The fluence per dose applied ($4\text{--}6.4 \times 10^9 \text{ Jm}^{-2}$) was around ten times smaller than the fluence per dose applied by LeBlanc *et al.* ($5\text{--}5.8 \times 10^{10} \text{ Jm}^{-2}$, [151]). This variation could be due to the increased effects of aberrations when targeting through tissue and absorption when irradiating cells that contain thicker cell walls and chloroplasts, requiring more energy for successful photoporation. The $> 40 \%$ viability of successfully

optoinjected cells was high when compared to other molecule delivery techniques such as bombardment (1-2 % [208]).

When considering the application of a single dose, using the Bessel beam over the Gaussian beam provided a higher efficiency of optoinjection, producing nearly 50 % more viable optoinjected cells, shown in Figure 5.2D. This could lead to an increase in throughput in plant cell optoinjection as the total number of cells that require targeting to achieve a certain number of usable cells is reduced. The most time-consuming part of the optoinjection process is aligning the membrane with the focal plane of the focused Gaussian beam. With plant cells this is made even more challenging as (along with the difficulty of the cell wall) plant cells are much larger, barrel-shaped, non-adherent and relatively less homogeneous in morphology than mammalian cells. The long propagation invariance of the Bessel beam makes it easier to target the membrane without the necessity for precise focusing beforehand, reflected in the higher optoinjection efficiencies achieved. The time spent focusing is then reduced and the number of cells that can be photoporated in a given time is increased.

Figure 5.2D shows that it is possible to increase the efficiency of Gaussian beam photoporation to match that of the Bessel beam by using multiple doses. This photoporation protocol, however, increases the time taken to target cells due to the extra time required to apply the doses and manually align the stage above and below the focal point, making the cell throughput using the Bessel beam at least three times higher than with the Gaussian beam. The power required for injection, however, is 15 times lower with the Gaussian beam, making it a useful compromise in power-poor systems.

Using the Bessel beam, approximately 300 cells could be irradiated per hour, which is three times higher than an automated protoplast microinjection system [209]. This frequency could be further increased with the inclusion of automated cell targeting [59], raster-scanning [16] or microfluidic technology [17, 18]. The long axial propagation of the Bessel beam and the self-healing properties may also prove useful when considering other plant cell types that might possess different cell wall thickness and composition.

A higher power may be required to counteract any aberrations introduced to the beam by passing through the cell wall. Another option to bypass a thicker cell wall could be to employ wavefront shaping [210] to correct for aberrations introduced by the cell wall.

External osmotic pressure was critical to be able to inject cells with the compound of interest. At low osmolarities, the cell is fully turgid and the cell membrane is pushed against the cell wall by osmotic pressure (Figure 5.4B). Therefore, breaching the membrane allows cytosol to flow from the cell, reducing the pressure within the cell and ultimately rendering it non-viable. At higher osmolarities the opposite effect occurs, with the difference in pressure caused by the osmotic gradient that draws material into the cell. Higher osmolarity media induce larger voids between the cell membrane and cell wall (Figure 5.4D), which are then partially refilled as medium enters the cell upon photoporation. Higher osmolarities, however, also caused increased cell death as the amplitude of physical changes induced in the cell was increased. A compromise between greater uptake and higher levels of cell death needs to be made. Low cell viability following photoporation in high osmolarity media has also been seen in mammalian cells [56].

The crossover between optoejection and injection occurring at 320 ± 2 mOsm/L could represent the approximate internal molarity of the average BY-2 cell. Figure 5.4A shows the point of incipient plasmolysis (taken to be where 50 % of cells are plasmolysed [56]) occurs between 279 and 320 mOsm/L. Incipient plasmolysis is the point at which the cell membrane just starts to pull away from the cell wall, the surrounding medium will therefore be isotonic. This is also supported by looking at the void fraction, which increases the quickest around 279 and 395 mOsm/L. It appears that the fraction of cells plasmolysed is a more sensitive measure of the cell osmolarity whereas determining the void space better represents the plasmolysis effects at higher osmolarities, where the first method saturates. The primary mechanism of molecule delivery at an isotonic osmolarity will be via diffusion, akin to mammalian cell optical injection [16].

Complementary effects were seen when temporally monitoring cell uptake for differing osmolarities. The increased I_{max} at higher osmolarities is due to the larger osmolarity gradient between the intra- and extracellular medium producing a greater plasmolysing effect that creates a large pressure differential across the cell membrane. This is also supported by the larger void space at higher osmolarities, as measured in Figure 5.4A. A greater volume of the highly osmotic solution must be taken up by the cell to balance the pressure, hence we see a greater uptake of calcein. The reduced $t_{1/2}$ is also caused by the larger pressure differential induced by higher osmolarity solutions creating a higher inward flux of extracellular medium in accordance with mass conservation laws and has been observed in mammalian cells too [56].

The changes in cellular fluorescence upon photoporation initially seem problematic because the time taken for the fluorescence signal to saturate could identify the time taken for the membrane to reseal [49]. Membrane resealing should occur over short time scales to maximise cell viability post-photoporation. An increase in fluorescence followed by saturation after approximately 200 s was also seen by LeBlanc *et al.* [151], who monitored photoporation of cascade blue dextran into *Arabidopsis* tissue. This large time delay until saturation was attributed to movement outside the volume monitored and could account for the effects seen here too.

This study also evaluated the effect of changing the biomolecule to be optoinjected. While PI and calcein freely diffused into the cell upon photoporation, using dextrans of increasing MW adversely affected the amount of dextran that could enter the cell. Increasing the Stokes radius of the molecule decreases the diffusion coefficient, decreasing the likelihood of molecules entering the cell during the transient pore opening; this effect was seen in both intact cells and isolated protoplasts. Intact cells showed higher intracellular concentrations of dextrans at low MW than isolated protoplasts. This is most likely due to the osmotic pressure present in the plasmolysed intact cells actively drawing more extracellular medium into the cell upon photoporation. Isolated protoplasts rely solely on diffusion to optically inject the dextrans because they were porated in a

close-to-isotonic solution to maximise viability (hypertonic solutions induce protoplast shrinkage and hypotonic solutions cause protoplast bursting) [147].

For higher MW dextrans the cell wall begins to affect the number of molecules that can be porated into the intact cell protoplast. Even before photoporation has taken place, as the size of the dextran added to the medium increases, the fluorescence within the apoplast decreases until at 70 kDa almost no fluorescence is seen in the apoplast, this will limit the dextran concentration next to the cell membrane and therefore the number of molecules that can be photoporated into the intact cell protoplast. Attempts to directly target the cell wall saw no increase in fluorescence in the apoplast, implying that photoporation only affects the cell membrane. The reduction in cellular fluorescence beyond 40 kDa suggests that the exclusion size of the cell wall for dextrans is between 4.42 and 5.71 nm (although partial exclusion occurs at lower Stokes radii). This limit supports previous experiments that put the dextran cell wall exclusion size at between 4.6 and 5.5 nm [211]. This limit may be representative only for polysaccharides and other similar molecules though because cell wall permeability has been shown to vary for differing molecule types e.g., globular proteins and ionic DNA [158].

The isolated protoplast data suggest that it could be possible to use photoporation to inject molecules larger than 70 kDa past the plant cell membrane, although with very low intracellular concentrations achievable. For injecting larger molecules, isolated protoplasts might prove to be a more useful receiver vessel, although the number of molecules entering the protoplasts will still be low and protoplasts have limited use in research due to the difficulty in regeneration from them. For comparison, in animal embryonic cells dextrans of up to 500 kDa have been optoinjected [53].

Delivery of small fluorescent oligonucleotides into both intact cells and protoplasts was also demonstrated, paving the way for possible gene silencing experiments. A large difference in the capacity of intact BY-2 cells to uptake siRNA and morpholinos was seen. This is possibly due to the difference in charges between the two molecules; siRNA is negatively charged whereas MOs are neutral [212]. Whilst the cell wall has

an overall negative charge that should repel the siRNA, proteins within the cell wall are positively charged, which could cause an attraction, or perhaps the presence of an intermediate ion. Charge difference, however, would not account for the similarity seen in the protoplast uptake for both oligos, given the negative charge on the plasma membrane.

Differing sizes between the molecules could also account for some differences seen in the oligo studies. MOs are around 8.9 kDa in size whereas the siRNA weight is not explicitly known but can be calculated to be approximately 14-17 kDa. This is, however, less than twice the size of the MOs and could not account for a four-fold reduction in uptake alone.

The working concentrations and degree of nucleotide labelling also differ between the oligos. The working concentration of the siRNA (the manufacturer's maximum recommended concentration) is 15 times less than the working concentration of the MOs (taken from a similar study [213]). If the density of fluorophore labelling is similar for both oligos then this could significantly increase the SNR (signal-to-noise ratio) for the siRNA data. The data suggest that morpholinos are the most suitable oligonucleotide for injecting into intact cells for gene expression studies. Even though the larger size, lower concentration and possible nuclease activity could reduce cellular delivery of siRNA in this study, the protoplasts still display comparable uptake of both siRNA and MOs. siRNA might therefore be considered the most suitable oligo for delivery into protoplasts.

Despite the positive steps taken towards optical transformation of plant cells in this chapter, optical transformation was not observed during this study. Reasons for this were found to not be due to poor quality DNA or cells and protoplasts, because these were successfully transformed by other methods. Possible barriers to optical transformation are considered below:

- **The cell wall could limit DNA entry into the apoplast.** Investigation of

uptake of fluorescently-labelled DNA could identify this as a problem but this does not explain the lack of transformation in protoplasts too.

- **Minimal entry of DNA into cells or improper localisation once inside.** Fluorescently-labelled DNA injection could help elucidate on this possibility. It should be noted, however, that mRNA, which does not require nuclear translocation, was tested without success too.
- **Limited long-term viability.** The experimental protocol used in this chapter did not allow long-term viability to be monitored. Results from other studies [151] suggest that long-term viability is acceptable but slight modifications in protocol could cause different results. Long-term viability monitoring would be possible for cells in tissue.

The reasons behind the lack of transformation are probably a mixture of the issues identified above combined with other problems not yet realised. Also, some methods used to aid understanding have their own problems, for instance mRNA does not require translocation to the nucleus to be expressed but is much more easily degraded than DNA, possibly preventing transformation by other means. Experiments in tissue and investigating injection of fluorescently-labelled DNA are suitable starting points to investigate this further.

The size of the oligonucleotides for injection might also affect their delivery into the cell and movement to the nucleus, hampering transfection. A comparison of sizes of both successful and proposed optoinjectants is listed in Table 5.2. The successfully injected biomolecules were at least 200 times smaller than the desired mRNA and DNA sizes. This suggests that the molecular size might prevent successful transfection. In mammalian cells, however, this has not been the case. Sea-worm embryos were only able to be injected with up to 500 kDa dextrans [53] but, in other studies, it was possible to transfect chick [52] and zebrafish [50] embryos with up to 5500 bp plasmid DNA. This

may be due to the different mechanisms involved in transfection and optical injection, discussed later in Section 6.4.

Biomolecule	Size (bp)	Size (kDa)
Dextran	NA	2-70
MO	NA	8.9
siRNA	20-25	14-17
mRNA	6400 (ss)	2000
plasmid DNA	4600	3000

Table 5.2 – Comparison of sizes of biomolecules for injection into plant cells. ss = single-stranded.

In conclusion, when compared to the current molecule delivery methods, optoinjection can provide increased cell throughput (which reduces the time required to inject large numbers of cells) while still maintaining high efficiency and single-cell selectivity. The Bessel beam was shown to provide a more effective optoinjection method than with Gaussian irradiation, although the Gaussian beam is more power-efficient and simpler to implement. The delivery of a wide variety of fluorophores was facilitated by the application of an osmotic gradient. Optical transformation was not achieved owing to a number of possible reasons; further experiments could help elucidate these issues.

5.6 Chapter acknowledgements

Preliminary data for Figure 5.2 and data for Figure 5.3 were taken with Stefan Kalies. Plasmids were kindly provided by the James Hutton Institute. Biolistics, rub inoculation and *Agrobacterium* studies were performed with Alison Roberts, Vinciane Tillemans and Sean Chapman. We thank Dr. Neil Hazon for use of his osmometer.

6 | Ultrashort broadband pulses for photoporation

6.1 Introduction

Ultrashort pulsed lasers are an invaluable tool in biophotonics. Pulse duration is inversely proportional to peak power [214], allowing shorter pulses to initiate important multiphoton processes at lower incident average energies, reducing collateral damage and maximising cell viability. Shorter pulses (< 30 fs), however, also suffer significantly from dispersion when passing through an optical system, limiting their usefulness unless complex dispersion compensation systems are employed.

The previous chapter investigated many optical parameters in the context of plant photoporation. A parameter that was not covered, however, was the role of pulse duration. As discussed in Section 2.2.3, the high precision and increased injection efficiencies provided by femtosecond pulses (when compared to more destructive nanosecond or picosecond pulses) have made them an unrivalled method for gentle, single-cell photoporation [2]. Primarily, pulses on the order of hundreds of femtoseconds long are used. These longer pulses do not broaden as much passing through optical systems (although they can exceed 1.5 ps in length after passing through highly dispersive medium such as optical fibres [215]), negating the need for expensive and complicated dispersion com-

pensation systems, but also do not possess the extremely high peak powers of < 30 fs pulses.

This chapter discusses some important characteristics of ultrashort pulses. A technique that can measure and compensate pulses known as MIIPS is used to create 22 fs pulses at the microscope focus for optical injection of mammalian cells and, for the first time, plant cells. 22 fs photoporation behaviour is compared against the high-powered and simple, longer pulse duration laser employed in Chapter 5.

6.1.1 The role of pulse duration in biophotonic applications

Multiphoton microscopy exploits multiphoton processes to enable higher penetration and optical sectioning of biological tissue. Typically, a NIR ultrashort-pulsed laser is focused into the sample. At the microscope focus, photon density reaches a critical value and multiphoton absorption can occur, causing fluorescent emission only within a limited focal volume. As the pulse duration is decreased, the peak power of the incident pulses increases, causing higher photon densities and increased fluorescence emission. Decreasing the incident pulse duration from 500 to 20 fs can increase the two-photon fluorescence emission intensity 15-fold, potentially decreasing the required exposure times to obtain an image and increasing penetration depth [216].

Bringing pulse durations into the sub-30 fs regime allows better than diffraction-limited precision in cellular laser surgery. Uchugonova *et al.* [217] investigated nuclear dissection using pulse durations ranging from 3 ps to 12 fs. Not only did surgery with 12 fs pulses require reduced incident energy to elicit an effect, the lines etched into the nucleus using these broadband ultrashort pulses could be less than 100 nm in diameter. This precision can only be afforded by very short pulse durations.

The high precision demonstrated in cellular surgery also has implications for optical injection and transfection of mammalian cells. Lower incident energies and more tightly confined damage volumes can increase the cellular viability post-irradiation. The tech-

nical difficulties of fully exploiting the useful properties of sub-30 fs pulses have limited their use in photoporation to a handful of papers. Uchugonova *et al.* [47] were able to efficiently transfect human stem cells with powers of 5-7 mW using 12 fs pulses, much lower than 70 mW typically used with the 100-200 fs lasers usually employed for femtosecond optical transfection [183]. The number of cells targeted was low, however, preventing rigorous statistical analysis.

A more detailed study of optical injection of mammalian cells for varying pulse durations (from 17-140 fs) was performed in Rudhall *et al.* The fixed nature of the dispersion compensation employed in Uchugonova *et al.* [47] (using chirped mirrors) prevented detailed investigation of photoporation at different pulse durations. Rudhall *et al.* [172] used the MIIPS system (employed in this chapter) combined with optical flats to controllably stretch and compensate pulses from an ultrashort pulsed laser and investigated optical injection under a variety of laser parameters including pulse duration, pulse energy and number of pulses. Decreasing the pulse duration was found to increase the achieved optical injection efficiency and reduce the required number of pulses applied (irradiation time) to initiate injection. Also, saturation of multiphoton effects were observed at very short pulse durations and higher pulse energies, leading to linear photon absorption dominating the observed behaviour in these conditions and breaking the linear dependence on pulse duration.

6.1.2 Dispersion

The minimum possible size of a laser pulse is inversely proportional to the laser bandwidth [218]. CW lasers will typically have bandwidths ranging from kHz to GHz but broadband ultrashort pulses can have THz bandwidths. The large number of frequencies required to form these short pulses make frequency-dependent effects, such as dispersion, particularly problematic.

The classic example of dispersion is the formation of a rainbow after white light

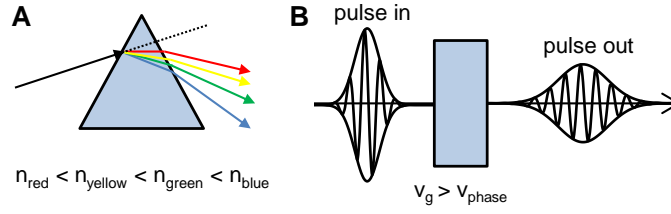


Figure 6.1 – Dispersion of light. (A) Angular dispersion of white light incident on a prism. The refractive index is dependent on frequency, causing each frequency to refract at a different angle, resulting in a frequency-separated output. (B) Temporal dispersion in normally dispersive medium ($v_g > v_{\text{phase}}$). The input pulse is temporally broadened as different frequencies travel at different speeds through the medium when the group velocity is frequency-dependent. The peak power decreases correspondingly as the pulse energy is spread over longer time.

passes through a prism. This angular dispersion is caused by a frequency-dependent refractive index of the material the light passes through, $n(\omega)$, where ω is the angular frequency. The refraction angle then varies for each wavelength according to Snell's law (Figure 6.1A).

Dispersion can also cause temporal broadening in a laser pulse [219]. The spectral phase, $\phi(\omega)$, of a pulse as it passes through a dispersive medium varies as the spectral phase of the medium is added to it. We can perform a Taylor expansion around ω_0 , the central frequency [220]:

$$\begin{aligned} \phi(\omega) = \phi^{(0)}(\omega_0) + \phi^{(1)}(\omega_0)(\omega - \omega_0) + \frac{1}{2}\phi^{(2)}(\omega_0)(\omega - \omega_0)^2 + \frac{1}{6}\phi^{(3)}(\omega_0)(\omega - \omega_0)^3 + \\ \frac{1}{24}\phi^{(4)}(\omega_0)(\omega - \omega_0)^4 + \dots + \frac{1}{n!}\phi^{(n)}(\omega_0)(\omega - \omega_0)^n \end{aligned} \quad (6.1)$$

where $\phi^{(n)}(\omega_0) = \frac{d^n \phi(\omega_0)}{d\omega^n}$, where the spectral phase at ω_0 is denoted by $\phi(\omega_0)$. Each of the derivatives of $\phi(\omega)$ correspond to a different order of dispersion.

If:

$$\phi(\omega) = n(\omega)kL = k(\omega)L \quad (6.2)$$

Where k is the k-vector and L is the length of the dispersive medium. Then the first

term is a global phase [220].

$$\phi(\omega_0) \propto k(\omega_0) = \frac{\omega_0 n(\omega_0)}{c_0} = \frac{\omega_0}{v_{phase}(\omega_0)} \quad (6.3)$$

v_{phase} defines the speed at which the light travels through the medium where c_0 is the vacuum speed.

The second term:

$$\phi^{(1)}(\omega_0) = \frac{dk}{d\omega} L = \frac{1}{v_g(\omega_0)} L \quad (6.4)$$

adds a delay to the pulse and defines the group velocity, v_g , the speed at which the wave packet propagates, considered to be the speed at which information is carried by the light [220]. When $v_g > v_{phase}$ then dispersion is positive.

The group velocity can also be frequency dependent. For very large broadband pulses, higher frequencies travel slower than lower ones, leading to a temporally broadened pulse (Figure 6.1B). The pulse is now positively chirped as the frequency increases with time [220]. Chirp is introduced in the third term:

$$\phi^{(2)}(\omega_0) = \frac{d}{d\omega} \left[\frac{1}{v_g} \right] L = k^{(2)} L \quad (6.5)$$

The variation of group velocity with frequency is known as the group velocity dispersion (GVD, $k^{(2)}(\omega)$) [219]. This is measured in units of $\text{fs}^2\text{cm}^{-1}$ and varies between different media. The GDD (group delay dispersion, $\phi^{(2)}$) is the total GVD encountered by the pulse as it traverses a medium of length L . The larger the GDD a pulse encounters, the more it will spread and become longer in time.

As shorter and shorter pulses are considered, the higher-order dispersion components must also be considered. The effect of third order dispersion (TOD) is to add satellite pulses to one side of a pulse, depending on the polarity of TOD. If the pulse is very short (< 10 fs) then even fourth, fifth and sixth-order dispersion terms must be considered to add phase distortion to the pulse [220]. The shape of an ultrashort pulse after passing through highly dispersive medium can become very complex and measuring the pulse or employing dispersion compensation can become highly complicated.

6.1.3 Dispersion compensation

The dispersion of ultrashort pulses passing through any medium is unavoidable and can be detrimental to studies utilising multiphoton effects because the peak power reduces rapidly as the pulse broadens. The shorter the initial pulse, τ_{in} , the more it is affected by dispersion. Figure 6.2 displays the effect of increasing GDD in an optical system on the output pulse duration, τ_{out} , calculated according to:

$$\tau_{out} = \tau_{in} \sqrt{1 + \frac{16 \ln(2)^2 \phi^{(2)2}}{\tau_{in}^4}} \quad (6.6)$$

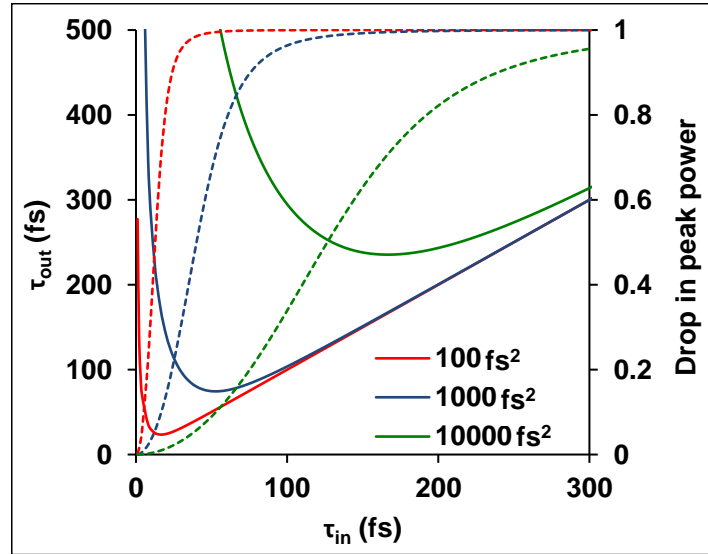


Figure 6.2 – Effect of GDD on an input pulse, τ_{in} , on output pulse duration, τ_{out} . The solid lines (denoting τ_{out}) tend towards infinity as τ_{in} tends towards zero. There exists a minimum, after which τ_{out} tends towards τ_{in} and the effect of dispersion becomes less for larger pulses. Increasing GDD (100 fs² - red, 1000 fs² - blue, 10000 fs² - green) changes the shape of the curve, introducing more temporal broadening at the same τ_{in} . Dotted lines denote the output peak power compared to the input peak power.

For a particular GDD applied, there exists a minimum output pulse duration, after which τ_{out} tends towards τ_{in} . Before the minimum, τ_{out} becomes infinitely large as τ_{in} tends towards zero. As the GDD applied increases, this minimum occurs at higher input

pulse durations, increasing τ_{in} required to achieve minimal broadening. At low GDD, when $\tau_{in} = 100$ fs little dispersion is introduced but at GDD of 10000 fs^2 , even 300 fs pulses broaden as they traverse the medium. An input pulse of 12 fs would broaden to 26 fs, 231 fs and 2.3 ps respectively as the GDD increases, reaching more than 100 times the size of the input pulse.

This increase in pulse duration has a detrimental effect on the resultant peak power of a pulse, the total energy remains the same but the pulse broadens, reducing the peak power. An input pulse of 12 fs would have its peak power reduced to 46 %, 5 % and 0.5 % of the initial peak power after passing through the selected GDD respectively.

To retain the pulse duration, and therefore peak power, of a pulse after passing through an optical system, it is possible to pre-compensate for dispersion before the pulse enters the optical system. For example, pre-applying a negative chirp to a pulse equivalent to the GDD of the optical system would cancel out the chirp and would achieve transform-limited pulses at the desired point.

A set of prisms can act as a pulse compressor because angular dispersion leads to negative GDD [221]. A positively chirped pulse has wavelengths separated in time, as each wavelength will take a different path through the prism, they can then line up again in time, but spatially separated. A set of four prisms (or two prisms and a mirror) at the correct angles and distances can recombine all the wavelengths spatially at the output, creating a transform-limited pulse (Figure 6.3).

A similar alignment of gratings can also apply negative GDD [222]. The amount of negative GDD created is larger with gratings than with prisms but the losses can be higher. Whilst both gratings and prisms can apply negative GDD, they both apply TOD too. A grating compressor applies a large positive TOD whilst prisms apply negative TOD. When designed correctly, it is possible to use both compressor types together to cancel out TOD and GDD [223].

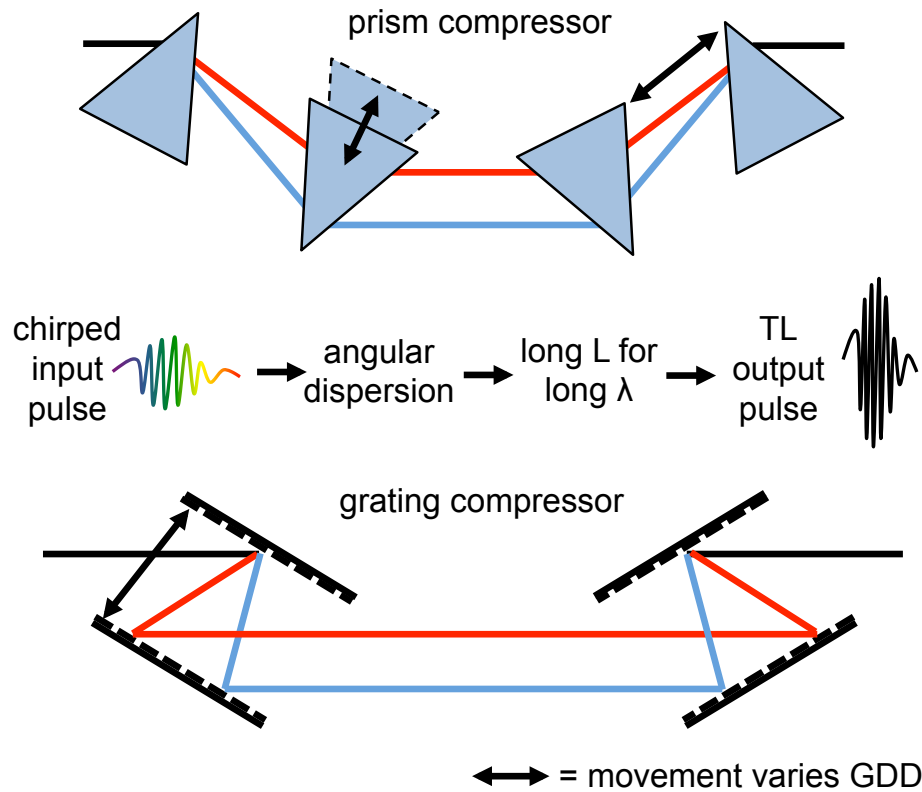


Figure 6.3 – Using sequences of prisms and or gratings for pulse compression. The angular dispersion introduced upon hitting a prism or grating causes different wavelengths to travel different pathlengths. In the case of prisms, more glass is traversed by more red wavelengths and in grating compressors, more distance is covered. The longer wavelengths (in front in a positively chirped pulse) take longer to pass through the system than the shorter wavelengths. All wavelengths are recombined at the final optical component with all wavelengths in phase, creating a pulse compressed in time. Moving prisms parallel to the beam path or changing the separation of prisms/gratings changes the amount of negative GDD introduced.

6.1.4 Pulse measurement

The shorter an event becomes in time, the quicker a detector must be to accurately measure it. Once pulses entered the femtosecond regime, they became shorter than any

other known event and therefore difficult to measure. The only possible event that can be used to measure the pulse is the pulse itself.

The most basic method employed is autocorrelation [220]. This is performed by creating a replica pulse using a Michelson interferometer set-up, the delay between the pulses can then be varied, causing a different amount of overlap between pulses, leading to a variation in measured signal with delay. The signal obtained is a characteristic autocorrelation trace. The pulse width can be extracted from the shape of the envelope but a pulse shape (e.g. Gaussian, sech^2) must be assumed so it is not possible to extract accurate information for a complex pulse.

Complete characterisation of a pulse using an altered replica of the test pulse as the reference pulse has been developed with two methods: FROG and SPIDER.

For frequency-resolved optical gating (FROG), the pulse is interfered with a gated version of itself. This can be performed by overlapping pulses into a second harmonic generation (SHG) crystal (nonlinear signal is only created when the pulses overlap, creating optical gating) and measuring the SHG spectrum with a spectrometer (SHG-FROG). The phase from the resulting 2D-spectrogram of SHG at each time delay can be extracted using iterative methods [220]. SHG-FROG is simple but contains time ambiguities (negative and positive chirp appear the same) [220, 224]. Polarisation gated FROG (PG-FROG) uses fused quartz (a 3rd order non-linear medium) to induce birefringence when the gated pulse is incident and changes the polarisation of the probe pulse, which can be detected with an analyser. Spectrograms created by PG-FROG are intuitive (orders of dispersion can be identified by eye) and non-ambiguous [224].

In SPIDER (spectral phase interferometry for direct electric field reconstruction), spectral interferometry is performed with a time-delayed and spectrally shifted replica pulse. Spectral shear is applied by sum frequency mixing the replica pulse with a highly chirped pulse (acting as a quasi-monochromatic pulse whose frequency changes slightly over time), each delayed replica is shifted in frequency by a different amount [220].

6.1.5 Complete measurement and control of ultrashort pulses

The complications of compensating and measuring ultrashort pulses have been highlighted in the above sections. The insertion of an SLM between two gratings can control the spectral phase of a pulse for complex pulse shaping [225]. If the phase applied by the SLM is the negative of that applied by the optical system, then the SLM can be used to compensate a dispersed pulse. MIIPS uses an SLM pulse shaper configuration to apply a reference phase and extract the spectral phase (characterising the pulse), which can then be used to perform subsequent pulse compression [226].

Detailed theory and optical set-up of a MIIPS system can be found in Appendix B. MIIPS provides a simple single-beam method to characterise and compensate for introduced dispersion. It should be noted, however, that it suffers from some limitations when the GDD and/or higher-order dispersion in a system is very high. To apply a large phase ($\phi < -2\pi, \phi > 2\pi$), phase-wrapping on the SLM must occur. Crosstalk between pixels can introduce phase and amplitude distortions into the pulse at the boundaries where the phase crosses $\pm\pi$ [227]. The MIIPS algorithm considers the second-order derivative of the spectral phase, this works well for minimal higher-order dispersion but is less accurate for highly distorted pulses, reducing the accuracy of measurement and compensation. Additional pre-compensation using prisms or use of slower genetic algorithms can be used for compression of very highly distorted pulses (large GDD and large higher-order dispersion respectively), possibly combined with an external FROG or SPIDER pulse measurement system for accurate pulse characterisation [227].

This chapter will evaluate MIIPS as a tool for measuring and compensating broadband ultrashort pulses within a reconfigurable system, containing more optics than a simple Gaussian photoporation system and therefore harder to accurately compensate. Photoporation of mammalian cells is then investigated to compare against previously obtained results [172] and assess the suitability and reliability of the optical system and compensation to reproduce similar results. This is then applied to tobacco BY-2 cells,

the first time that broadband ultrashort pulses have been tested in a plant cell line. An comparison of photoporating plant and mammalian cells, photoporated with the same optical system, is then drawn from the obtained data.

6.2 Materials and methods

6.2.1 Implementation of the MIIPS system

The MIIPS system corrects for dispersion by measuring a non-linear optical response and the effect on this response when changing the phase of individual pixels (wavelengths) on the SLM. A MIIPS detection unit (MDU) is placed at the focal point where the dispersion-compensated pulses are required. The MDU consists of an SHG crystal and a mirror, which directs light onto a fibre spectrometer, allowing the measurement of IR or SHG signal at the microscope focus (Figure 6.4).

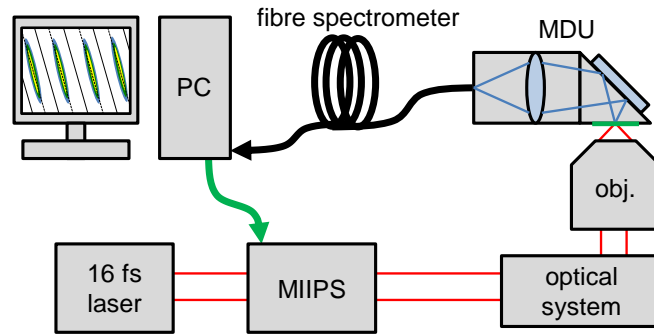


Figure 6.4 – Schematic of MIIPS operation. The laser (red) passes through the MIIPS before entering the optical system (described in Section 4.3.2). Upon passing through the microscope objective (obj.), the laser is tightly focused. The MDU is placed so the SHG crystal (green) is aligned with the microscope focus. The SHG light (blue) is then focused onto a fibre spectrometer. The SHG spectrum is fed into a PC, which monitors the change in SHG intensity as the phase on the SLM in the MIIPS is varied.

The MIIPS runs multiple iterations to converge on the shortest possible pulse du-

ration. The process is exponentially fast and was often able to compensate down to within 3 % of the transform-limited (TL) pulse duration ($\tau/\tau_{TL} = 1.03$, where τ is the measured pulse duration and τ_{TL} is the predicted transform-limited pulse duration), which, depending on the input pulse, could be under 13 fs. The software could be run in either ‘coarse’ or ‘fine’ mode. Only three iterations were performed in ‘coarse’ mode and took approximately one minute to run. The more accurate ‘fine’ mode performed six iterations and took approximately six minutes to run. The alignment and set-up of the software of the MIIPS took up to ten minutes between runs, making it more time-efficient to run fewer iterations of the more accurate ‘fine’ mode.

6.2.2 Determining the Chameleon pulse duration

For direct comparison with the 22 fs pulse laser, it was necessary to determine the pulse duration of the longer pulse duration laser at the microscope focus. This was calculated given the pulse duration of the laser at its output, estimating the amount of GDD within the optical system from manufacturer’s specifications. As seen in Table 6.1, the total estimated GDD for the system was 31938 fs². The largest contributors to the system GDD were the dielectric mirrors, whose GDD depended on incident polarisation, and the thick polarising beam splitters (PBS) and objective. Dielectric mirrors were used despite their high GDD owing to their higher reflectivity (better than 99 %) than silver mirrors (around 96 %) to minimise losses in the system. Mirrors that possess both high reflectivity and low-GDD are available but are very expensive.

Once the GDD has been estimated, the pulse duration at the microscope can be determined from τ_{in} . The manufacturer’s specifications list the output pulse duration as < 140 fs, leading to a pulse duration at the focus of 647 fs using Equation 6.6. An autocorrelator (FR103-PD, Femtochrome, USA) was also used to corroborate the manufacturer’s specification; placed after a single half wave plate and polarising beam splitter to allow a variation in power incident on the sensitive autocorrelator (introducing 3975 fs² of GDD). The pulse duration measured at this point was 200 ± 20

Optical component	Number	Information	GDD (fs ²)	Source
PBS	2	25.4 mm SF1	7951	Thorlabs (w)
Mirror (s)	3	S-polarisation	23700	Thorlabs (pc)
Mirror (p)	2	P-polarisation	-2400	Thorlabs (pc)
200 mm lens	2	8 mm BK7	714.4	Thorlabs (w)
150 mm lens	1	7.5 mm BK7	339.3	Thorlabs (w)
300 mm lens	1	6 mm BK7	267.9	Thorlabs (w)
Dichroic mirror	1	Max. value	20	Semrock (w)
Objective	1	Estimated	1350	[228]

Table 6.1 – Determination of GDD of optical components in the system encountered by the long pulse duration laser. w = website, pc = personal communication. All GVD values for materials were taken from [229]. Total GDD is 31938 fs².

fs, implying an original pulse duration of approximately 192 fs, much larger than the specified pulse duration.

This pulse duration is larger than the transform-limited pulse duration (148 fs assuming Gaussian pulses), requiring an adjustment to Equation 6.6 to include chirp:

$$\tau_{out} = \tau_{in} \sqrt{\left(1 + C_0 \frac{4\ln(2)\phi}{\tau_{in}^2}\right)^2 + \frac{16\ln(2)^2\phi^2}{\tau_{in}^4}} \quad (6.7)$$

Taken from Cannone *et al.* [230], where the chirp coefficient C_0 can be determined from the bandwidth and output pulse duration using $\Delta_\nu \tau_{in} = 0.315\sqrt{1 + C_0^2}$, assuming Gaussian pulses. Using Equation 6.7 with an input pulse duration of 192 fs, the pulse duration at the focal plane becomes 734 fs.

6.2.3 Mammalian cell culture and optoinjection

Chinese hamster ovary (CHO-K1) cells were cultured as described in Section A.2.1. Cells were plated onto glass-bottomed dishes (World Precision Instruments, USA) 24 hours prior to optoinjection experiments. Just prior to optoinjection, cells were washed twice in 1 ml OptiMEM (Life Technologies, USA) before the addition of 300 μ l OptiMEM with 3 μ M PI, using PI as a marker for successful optoinjection. Cells were then placed on the Nikon microscope system described before and exposed to a single 40 ms dose of laser radiation and observed under mercury arc lamp illumination using a TRITC filter. If optoinjection was successful then fluorescence within the cytoplasm is observed 2-3 minutes after irradiation. After photoporation, medium was replaced with 2 ml normal MEM (minimum essential medium). Viability 1.5 hours post-shooting was determined by staining for 20 minutes with 300 μ l of 2 μ M calcein-AM (Life Technologies, USA) in Hank's Balanced Salt Solution (Sigma-Aldrich Co., USA).

6.2.4 Plant optoinjection protocol

Plant culture and PI optoinjection was performed as described in Section 5.2.

6.3 Results

6.3.1 MIIPS implementation

The results of an example MIIPS compensation for the Gaussian beam at the microscope focus are shown in Figure 6.5. The IR spectrum (A) after compensation varies minimally, reducing in bandwidth slightly. The SLM possesses some dead pixels, which appear as dips in the spectrum. The presence of these dips will affect the compensation slightly but the total number of non-working pixels (approximately 20) is small

compared to the total number of pixels on the SLM (640) so the reduction in efficacy is minimal.

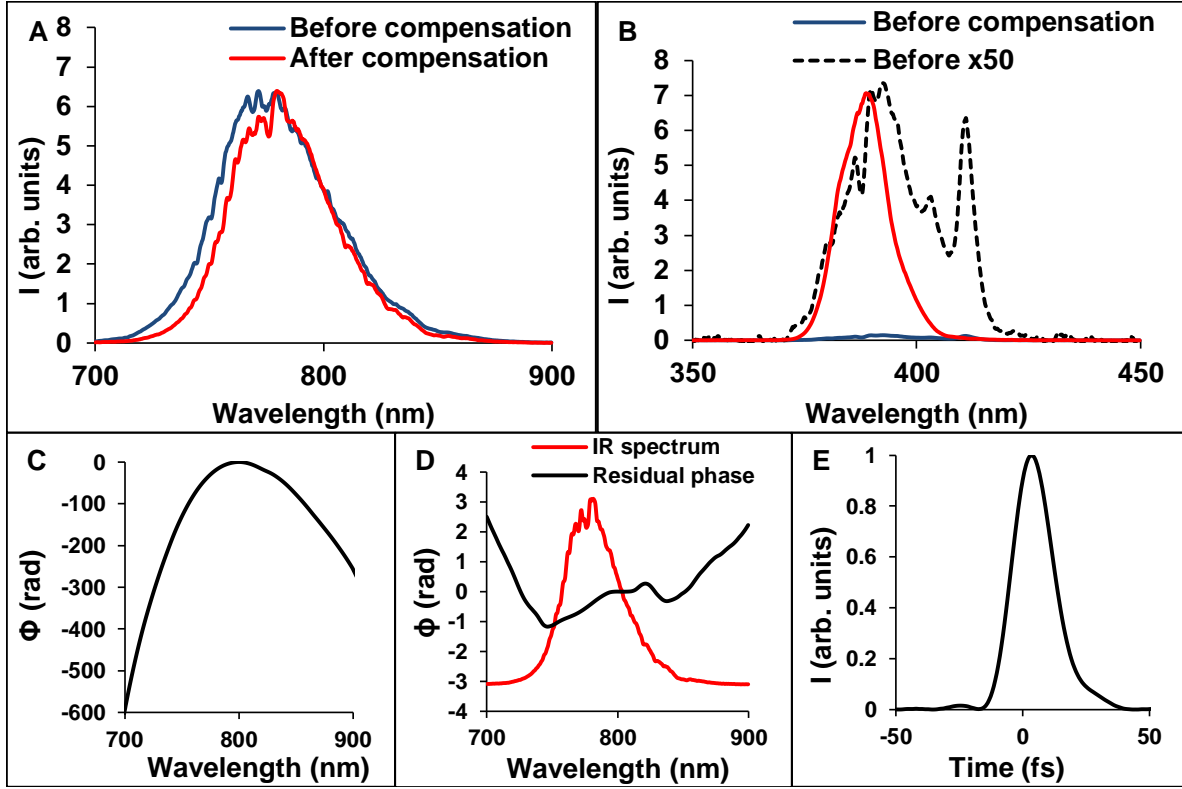


Figure 6.5 – Typical results from a MIIPS compensation. (A) Minimal change in fundamental spectrum before (blue) and after (red) compensation. (B) Dramatic increase in SHG spectrum intensity from before (blue and dotted black) to after (red) compensation. The black dotted line shows the SHG spectrum before compensation multiplied 50 times to highlight the substructure. (C) Spectral phase applied by SLM, the negative of the phase introduced by the system. (D) Residual phase after compensation. (E) Temporal profile of the pulse after compensation.

The SHG spectrum (B) changes dramatically in shape and intensity as the compensation is measured and applied. Prior to compensation the SHG spectrum shows structure caused by higher order dispersion introduced by the optical system. After the compensatory phase is applied, the intensity increases 50-fold and the spectrum now

shows a smoother, single Gaussian-like peak as the higher-order phase distortions are reduced.

The phase applied by the MIIPS to achieve compensation is shown in Figure 6.5C. The maximum phase applied is 600 radians over the whole spectrum (or 130 radians over the FWHM), requiring significant phase-wrapping on the SLM because the maximum phase that can be applied is $\pm 2\pi$. The residual phase after compensation (D) was minimised to less than 2.5 radians over the whole spectrum and less than 1.15 radians over the FWHM. The temporal pulse shape (Figure 6.5E) shows a smooth structure without any significant distortions. The pulse duration is 18.475 fs in this example compensation, giving $\tau/\tau_{TL} = 1.084$.

6.3.2 Optical injection

Mammalian cell optoinjection

Preliminary comparative experiments were performed on mammalian cells, namely CHO-K1 cells, a model cell line that has been thoroughly investigated for optical injection studies. Cells were targeted on the membrane with a single 40 ms laser dose with a focused Gaussian beam of either 22 fs or 734 fs in the presence of PI using the optical system described in Section 4.3.2. Successful optical injection of a cell was confirmed by imaging cellular fluorescence five minutes post-irradiation using a cooled CCD (Figure 6.6B). Cell viability was confirmed by staining with calcein-AM 90 minutes after optical injection, viable cells contain esterases that cleaves calcein from the AM group and causes it to fluoresce (Figure 6.6C).

Photoporation was performed at three different laser powers for each pulse duration. The back aperture powers used were empirically determined to maximise injection efficiency while not reducing viability significantly. At low powers, the injection efficiency is low, although the viability might be high. Above a certain applied power, the viability decreases very quickly so increasing the power beyond this will not maximise the

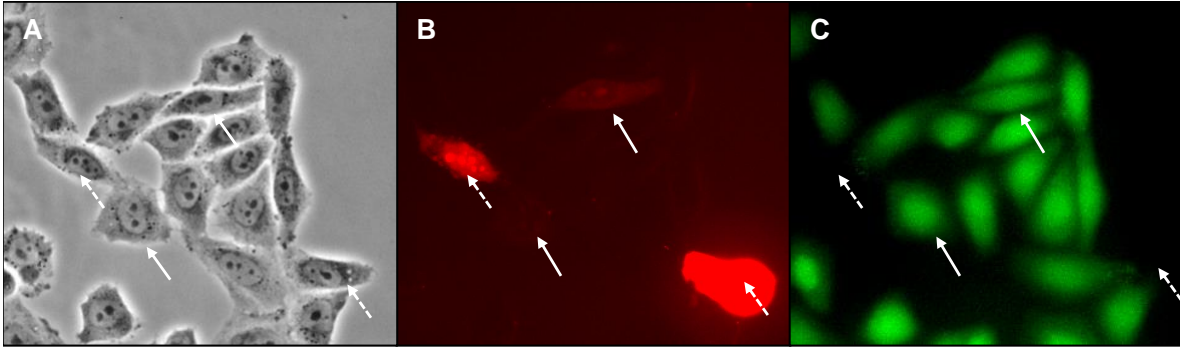


Figure 6.6 – Example optoinjection of PI into CHO-K1 cells in brightfield (A) and fluorescence (B) 5 minutes after laser irradiation. Successfully injected cells show fluorescence in the nucleus after targeting with the laser. Calcein-AM stains the viable cells 90 minutes after injection (C). Injected cells are highlighted with arrows. Injected and viable cells (solid arrows) display lower PI fluorescence than cells that subsequently die (dashed arrows).

number of viable optically injected cells any further. The range of powers applied (11 mW for 734 fs and 14 mW for 22 fs) was similar.

As the power is increased, the optical injection efficiency increased whilst the viability decreased (Figure 6.7A and B). When using 734 fs pulses, the viability and efficiency showed a large decrease at 102 mW where the low efficiency probably caused statistical effects. When few cells are successfully injected (10 %, 3 per dish when 30 cells are irradiated) then if one cell dies the viability is reduced significantly (66 %).

Comparatively, for 22 fs pulses (Figure 6.7B), the viability was never less than 50 %. Even though the powers required to inject mammalian cells were smaller for 22 fs than for 734 fs (approximately 50-56 % smaller), the fraction of viable injected cells were significantly higher. This behaviour is confirmed in Figure 6.7C, which shows a comparison of the fraction of viable optically injected cells (the product of viability and efficiency, N , defined in Section 5.3.2) obtained at different powers and pulse durations. The average N for 734 fs was 7 ± 2 % and for 22 fs was 29 ± 4 % ($p = 0.001$); over four times higher.

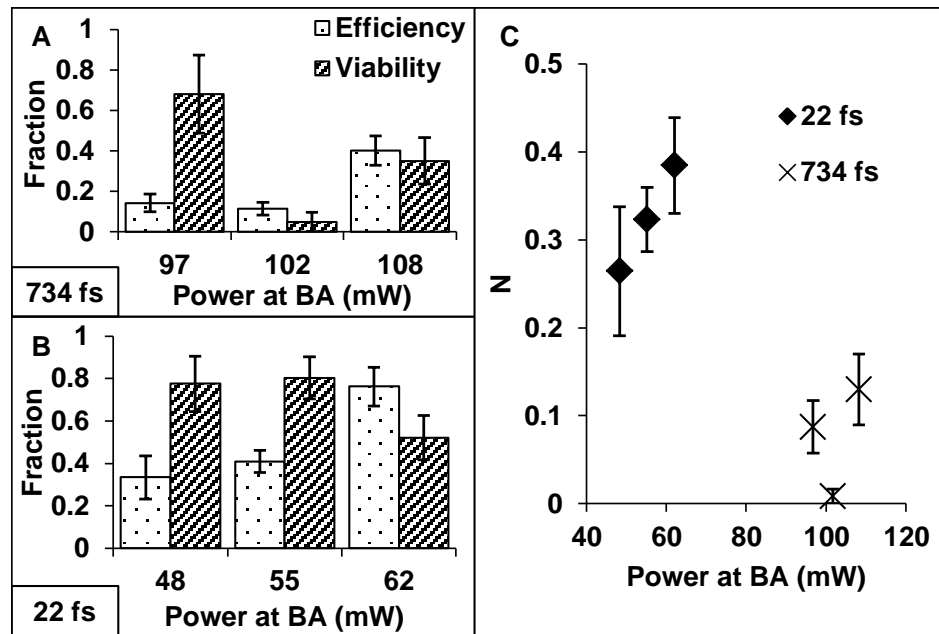


Figure 6.7 – Optical injection of mammalian cells with 734 fs pulses (A) and 22 fs pulses (B). The viability and injection efficiency were both higher overall when using 22 fs pulses, even though lower input powers were used. The fraction of cells that were both injected and viable (N) is shown in (C) to compare the different pulse durations. Results are for $n = 3$ with 30 cells dosed per dish. Errors bars denote the SEM.

Plant cell optoinjection

Whilst the effect of changing pulse duration on optical injection in mammalian cells has been well investigated [172], in plant cell injection, only pulse durations on the order of hundreds of femtoseconds have been employed. To investigate if similar highly precise effects can be elicited in plant cells too, the same laser system was employed to photoporate tobacco BY-2 cells. Three axially-separated 40 ms laser doses (as described in Section 5.2.1) with a focused Gaussian beam of either 22 fs or 734 fs were employed for plant optical injection.

Overall, the same trend for increasing efficiency and decreasing viability as the incident power is increased is observed for both 734 fs and 22 fs pulse durations (Figure 6.8A and B respectively). Looking at injection with the same back aperture powers but dif-

ferent pulse durations (Figure 6.8D), N is significantly different at 78 mW, 20 times lower and 12 times lower for approximately 68 mW. Using the 734 fs laser, the highest efficiencies were achieved ($47 \pm 3 \%$) but with very low viabilities ($40 \pm 3 \%$) whereas viability with the 22 fs laser was always greater than 80 %.

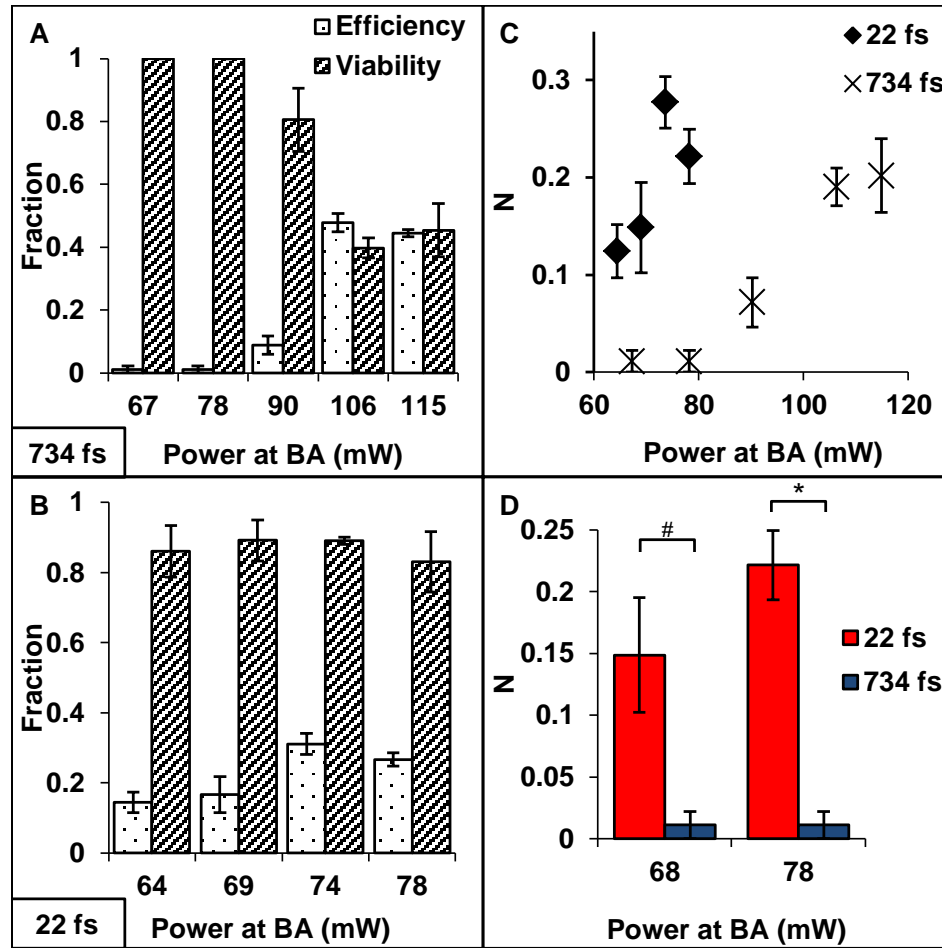


Figure 6.8 – Optical injection results for plant cells. Optical injection and viability fractions for 734 fs (A) and 22 fs (B). Comparison of viable and optically injected cells is shown in (C). Higher efficiencies are achievable with the lower pulse duration but results show a less dramatic variation than for the mammalian cells. (D) Direct comparison of for similar BA powers (# - $p = 0.084$, * - $p = 0.006$, both Student's t-test). Results are for 30 cells per dish with $n = 3$. Error bars denote the SEM.

6.4 Discussion and conclusions

This chapter has demonstrated the use of broadband ultrashort pulses, combined with a pulse dispersion compensation system to achieve 22 fs pulses at the microscope focus, for optical injection studies of both plant and mammalian cells, comparing with a longer pulse duration laser (734 fs at the microscope focus).

The MIIPS could accurately measure and compensate pulses after passing through a complex optical system involving highly dispersive optics such as polarising beam splitters, dielectric mirrors and high NA objectives, achieving 22 fs pulses at the microscope focus. The highly dispersive nature of the system was indicated by the large phase applied by the SLM to compensate for this system (Figure 6.5C). The inverted quadratic shape of the applied spectral phase indicates the dominant phase distortion introduced by the optical system is positive chirp, with a small amount of TOD (cubic curve). The residual phase distortions after compensation were more than four times larger than the residual phase distortions measured in Xu *et al.* [231], which is consistent with the system in this chapter being more complex than the simplified systems tested in that study, and therefore difficult to compensate effectively.

The uncompensated pulse duration of the longer pulse duration laser was calculated to be more than 30 times larger than the 22 fs pulses. Incorporation of a pulse measurement set-up into the optical system would further increase the complexity but could also help to avoid making assumptions about the temporal broadening (Gaussian pulses and application of only second-order dispersion), making the comparisons drawn between different pulse durations more accurate.

When optically injecting mammalian cells with different pulse durations, the effects seen corresponded well with those in Rudhall *et al.* [172]. For shorter pulses, the power required to inject the mammalian cells efficiently was reduced by a factor of two, even though the efficiencies obtained were higher. Larger pulse durations tended to show lower efficiencies of injection than shorter pulse durations. The range of pulse energies

considered are similar to those in Rudhall *et al.* [172] where pulse energies of 0.26-1.8 nJ were applied, compared to pulse energies of 0.6-0.78 nJ for 22 fs pulses and 1.21-1.35 nJ for 734 fs pulses used in this chapter.

The pulse energies employed for this chapter were nine times higher than those used in Uchugonova *et al.* [47] to achieve transfection of stem cells (66-92 pJ). It is, however, difficult to compare this study directly because optical transfection works by different mechanisms. Optical injection and transfection often concentrate on injecting biomolecules with different properties. Small molecules generally require a single site of irradiation (as performed here with mammalian cells) using a higher power, whereas nucleic acid transfection can be achieved with multiple spatially-separated sites using low powers [183]. These differences reflect the possible different mechanisms by which the membrane is porated and the biomolecule is taken up, although the precise differences are not well understood. It should also be noted that the extremely low pulse energies required in Uchugonova *et al.* have not been replicated elsewhere in the literature.

This chapter also applied broadband ultrashort pulses to plant cells for the first time. Similar effects of reducing pulse durations providing higher efficiencies and viabilities were in effect but not as pronounced. By reducing the pulse duration from 734 fs to 22 fs, the fraction of viable optically injected cells was increased by more than an order of magnitude for the same input powers (68 and 78 mW). The 1.45 times decrease in power required for optoinjection of plant cells for 22 fs was less than for mammalian cells, possibly testament to the ease with which mammalian cells can be targeted or an effect of the cell wall spatially and temporally aberrating the beam. That plant cells required higher powers than mammalian cells to inject using 22 fs pulses is probably due to the aberrating effect of the plant cell wall on the laser because the chemical composition of the plant and mammalian cell membranes is very similar. Spatial aberrations are more likely to affect the photoporation efficiency than temporal aberrations; a 22 fs pulse would only stretch by 0.01 fs upon passing through 0.1 μm of cellulose ($\text{GVD} = 59.7 \text{ fs}^2/\text{mm}$ [232]) according to Equation 6.6.

The increasing efficiency and reduced levels of cell death experienced for both plant and mammalian cells when using shorter pulse durations are expected from previous theoretical and experimental studies [20, 172]. The shorter pulse durations allow for fine-tuning of the low-density plasma formation, minimising collateral damage and producing very precise multiphoton effects.

The higher powers required to photoporate the plant cells used the maximum possible output power of the 22 fs laser once passed through the optical system. It would therefore not be possible to stretch the pulse because the peak power would be reduced even further. It was not possible to initiate photoporation using the Swift without compensation applied. In this uncompensated case, the pulse duration would be approximately 4 ps using Equation 6.6, more than five times longer than the Chameleon and therefore greater input powers than used in this study would be required to initiate photoporation. This power deficiency confirms the necessity for using another laser (with four times higher output power) for the longer pulse duration comparison experiments. Using two different lasers rather than changing the pulse duration at the focus of the same laser could introduce some discrepancies between photoporation effects caused by small variations in beam spot size and central wavelength, which needs to be taken into account.

The comparatively alignment-free structure of the Bessel beam when compared to the Gaussian beam makes it an interesting proposition for broadband ultrashort photoporation. Using the MIIPS system, it was possible to compensate a Bessel beam system down to 18 fs ($\tau/\tau_{TL} < 1.03$) at the microscope focus, the intensity profile of which is discussed in Section 4.3.3. The power available at the BA was only 120 mW and not sufficient to induce photoporation of either plant or mammalian cells, even when the length of the Bessel beam was reduced to 12 μm by reducing the size of the incident beam waist on the axicon (intensity profile of this short beam not shown). Using different dispersion compensation techniques such as gratings or chirped mirrors might provide the necessary high transmission but at the cost of reduced efficiency in compensation.

Applying an amplitude modulation to the MIIPS during a phase-scan to create a gated effect [227] could increase the effectiveness of the compensation by correcting more fully for higher order dispersion and increasing the efficiency of multiphoton interactions at the focal point.

In conclusion, this chapter has demonstrated that by reducing the pulse duration incident on the cell membrane, multiphoton effects could be precisely controlled, minimising cell death and maximising the number of viable, injected cells obtained. This effect was confirmed for mammalian cells and shown to be present for plant cells too, where the strength of this effect is smaller but still significant, possibly due to laser-cell wall interactions not affecting mammalian cell photoporation. A higher achievable power at the focus for the 22 fs pulses could extend this study in two ways - by allowing a range of very short pulse durations at the point of photoporation for a more thorough study akin to Rudhall *et al.* [172] in plant cells, or by allowing investigation of ultrashort Bessel beam photoporation, possibly receiving the benefits of highly precise multiphoton effects but achievable over a larger axial range.

6.5 Chapter acknowledgements

The author implemented the MIIPS system with assistance and advice from Nicola Bellini. Autocorrelation measurements were taken with assistance from Alison McDonald.

7 | Optical trapping and super-resolution microscopy

7.1 Introduction

In this chapter we turn away from plant photoporation to concentrate on different biophotonic techniques. Optical trapping provides precise and non-invasive manipulation of cells and other microscopic objects. When combined with functional fluorescence imaging, many opportunities for interesting studies arise: single-molecule studies [86, 233], understanding cell-cell interactions [81, 82, 234], cell tomography [88, 235–237] or manipulating an object for optimal imaging [238, 239]. Developing novel ways to effectively combine these optical techniques is therefore imperative.

As previously highlighted in Section 2.3.4, one of the major barriers to combining optical trapping and fluorescence microscopy is decoupling the trapping and imaging planes. If the imaging objective is also used to introduce the trapping laser, additional optics are required to decouple these planes. This increases the system complexity and can introduce aberrations into the optical system. We therefore concentrate on trapping from the opposite side to imaging. This method also allowed free rein to choose optimal wavelengths for both trapping and fluorescence individually, avoiding photobleaching and leakage of trapping light by judicious choices of filters [240].

To this end, this chapter describes the use of a novel optical fibre-based trap that is

fully compatible with any inverted fluorescence microscope. Optical fibre traps possess many benefits over free-space trapping systems but usually require complex and precise fabrication techniques to create high intensity gradients. By using a high-NA GRIN (gradient refractive index) lens micro-objective (0.8) to focus the light from an off-the-shelf optical fibre, it is possible to reduce the complexity of fabrication while retaining optical fibre advantages. These advantages include eye safety, input angle tolerance (allowing bi-directional imaging [241]) and alignment-free integration into different systems.

Super-resolution (SR) microscopy uses advanced fluorescence imaging to see beyond the diffraction limit. By spatially and temporally varying fluorescence emission and detection, it is possible to gain access to higher spatial frequency information, where interesting biological phenomena and structures lie. SR microscopy, however, places stringent limits on the incorporation of other optical modalities. This chapter will be primarily concerned with structured illumination microscopy (SIM) as a SR technique, a microscope available in the laboratory that is quick and easy to use and works with standard fluorophores. SIM projects a sinusoidal excitation pattern and detects spatial fringes in emission. Optical aberrations can therefore affect imaging and severely reduce the achievable resolution, making additional optics within the imaging path highly undesirable. SIM also possesses SR axial sectioning capabilities, making decoupling imaging and trapping planes important for 3D SR imaging of optically trapped objects. SR microscopy is swiftly becoming more standard practice, necessitating the development of suitable optical traps.

This chapter will initially review super-resolution imaging. The development of a novel GRIN lens optical trap for fluorescence microscopy of cell-cell interactions is then discussed and used to induce an immunological synapse under epi-fluorescence. We then turn back to plant cells, testing a commercial SIM microscope for its suitability for imaging plant cells.

7.1.1 Super-resolution microscopy

To form an image, light diffracted from the sample must be captured by the imaging lens (Figure 7.1). The angle of the diffracted light from a periodic structure is proportional to the spatial frequency of the structure. There exists a spatial frequency, above which the emerging angle of the diffracted light is too large to enter the lens and an image can no longer be formed. We can decompose any sample we wish to image into multiple overlapping spatial frequencies so this limit holds true for all samples using standard linear microscope systems and defines the Abbe limit [242]:

$$d_{min} = \frac{\lambda}{2NA} \quad (7.1)$$

where d_{min} is the smallest distance between two points before they can no longer be distinguished [243]. We can also imagine a point source emitter as containing all spatial frequencies and so define the same limit for fluorescence microscopy, which this chapter will be primarily concerned with. To exceed Abbe's limit, we must find a way to access higher spatial frequency information within the sample.

Many techniques can be employed to go beyond this fundamental limit, although they increase the optical system complexity and acquisition time. The advances in biological imaging made using these microscopy methods, however, have proven invaluable.

Before the development of optical SR, electron microscopy was the only routinely used sub-diffraction imaging technique. Electron microscopy provides very high resolution of structures but no functional information and require detrimental sample fixation and prohibitively expensive equipment [7]. Functional imaging of electron microscopy samples is possible using immunogold labeling. Antibody-tagged gold nanoparticles bind to the protein of interest and increase contrast in the vicinity. The penetration of the nanoparticles into fixed tissue is low, however, allowing labelling of superficial layers only and the distance between the target and tag is close to the size of the tag itself [244]. These problems can be minimised by using optical microscopy imaging of genetically-encoded fluorescently-tagged proteins instead. Although optical microscopy

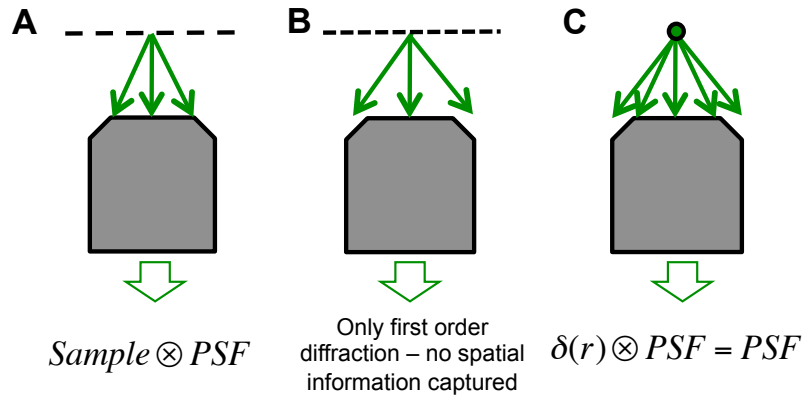


Figure 7.1 – The Abbe limit defines the smallest spatial frequency that can be captured by an imaging system. A low spatial frequency causes low-angled diffraction, which enters the objective and combines at the imaging plane (A). The image formed is then the sample convolved with the point spread function (PSF) of the imaging system, discussed further in Figure 7.2. If the spatial frequency is high, the diffraction angle will be too great for the imaging lens to capture the higher diffraction orders. Only the zeroth-order will pass through the imaging system, resulting in no spatial information, only a constant term (B). If we instead consider a point source emitter (fluorescence) then the Abbe limit still holds because there is still a loss of information as higher-angled emission cannot pass through the objective. Rather than seeing a perfect point source at the imaging plane, we can instead see the PSF of the imaging system (C). Imaging a point source is a useful way of measuring the PSF of a system. Figure adapted from [243].

can only reach resolutions 10^3 times worse than electron microscopy, it can also provide invaluable real-time, 3D, functional information about a sample.

By spatially varying the illumination, it is possible to extend the achievable resolution two-fold. Confocal microscopy tightly focuses an excitation laser onto the specimen and passes emitted fluorescence through a pinhole in the confocal image plane before collection at a PMT; the pinhole rejects out-of-focus light and creates optical sectioning. The laser focus is then scanned across the sample to build up an image. The confocal PSF (point-spread function - see Figure 7.2) of the system is then a convolution of the emission and detection PSF, creating a smaller PSF than a standard epi-fluorescence

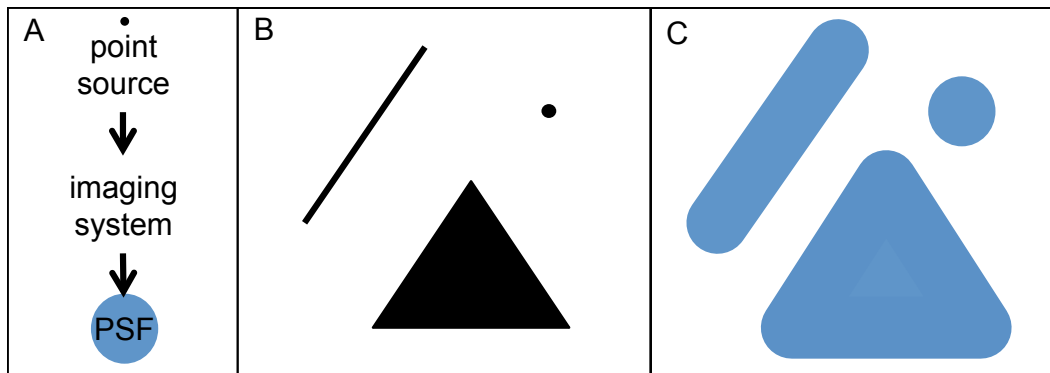


Figure 7.2 – The point-spread function (PSF) is the image of a point source at the sample plane obtained from an imaging system (A). The PSF can be thought of as a paintbrush that paints all points in a sample passing to the sample plane with the PSF shape, a convolution that creates a lower resolution approximation of the image. If we consider a sample distribution (B), then the image obtained from our imaging system in (A) would be (C). A typical PSF is an airy disc.

microscope. The theoretical lateral resolution of a confocal microscope is twice the Abbe limit but cannot be reached in practice because the pinhole should be infinitely small [245]. Confocal imaging can be extended to SR by using a CCD detector rather than a PMT [246], providing extra information about the sample. Structured illumination microscopy (SIM) uses a spatially varying illumination to bring higher resolution information in the sample into the passband of the objective [247]. A thorough description of the theory behind SIM imaging can be found in Appendix C.2. SIM is a wide-field technique that requires ≥ 9 exposures per image to achieve up to 2 times the lateral resolution limit with increased axial sectioning at rates of approximately 1 Hz.

By breaking the linear dependence of excitation and emission, it is possible to extend beyond the theoretical limit. STED (stimulated emission depletion) microscopy was the first SR technique proposed, using dual illumination to exploit non-linear properties of fluorophores [248]. The STED beam possesses a central point of zero intensity (usually a Laguerre-Gaussian beam). The wavelength of the STED beam is chosen to induce stimulated emission (red-shifted photons that are filtered out) in sample fluorophores.

A second beam induces normal fluorescence emission only in the point where the beams do not overlap (usually 10-70 nm in extent), the other fluorophores are depleted [249]. The necessity for point-scanning limits STED acquisition speed. Single-molecule localisation techniques, such as PALM and STORM [250, 251], rely on switching on and off individual fluorophores in a field of view. Low-intensity illumination causes a subset of molecules in the field of view to emit. If the PSFs of each fluorophore lit up at any one time do not overlap then each can be localised individually. An image is reconstructed using the knowledge of all the fluorophore positions, many images are taken to collect information from all present fluorophores. Non-linear SR techniques can achieve up to 20 nm resolution but require slow acquisition times and specialised fluorophores.

Owing to accessibility to standard fluorophores and relatively fast acquisition times, combined with modest resolution increase, SIM has been successfully used for many biological scenarios. A commercial SIM (N-SIM, Nikon, UK) is therefore used as a platform to test the suitability of our fibre-based optical trap for combination with fluorescence imaging.

7.2 Integration of optical trapping with a structured illumination microscope

An optical fibre attached to a high-NA (0.8) gradient refractive index (GRIN) lens micro-objective was employed for optical trapping experiments. The continuously-varying refractive index within a GRIN lens causes the light entering to move along a curved trajectory and thus can be focused without the curved facets of conventional lenses [252] (Figure 7.3A). GRIN lenses are favoured for endoscope imaging because they can be made small both axially and radially while maintaining large NAs.

The optics required for fibre coupling is bench-mounted away from the SIM to ensure stability of the coupling beam. The GRIN lens can then be brought into the microscope

and mounted above the stage in an upright format for trapping purposes. This does not interfere with the imaging set-up and, by use of a removable mount, can be easily switched out when not in use.

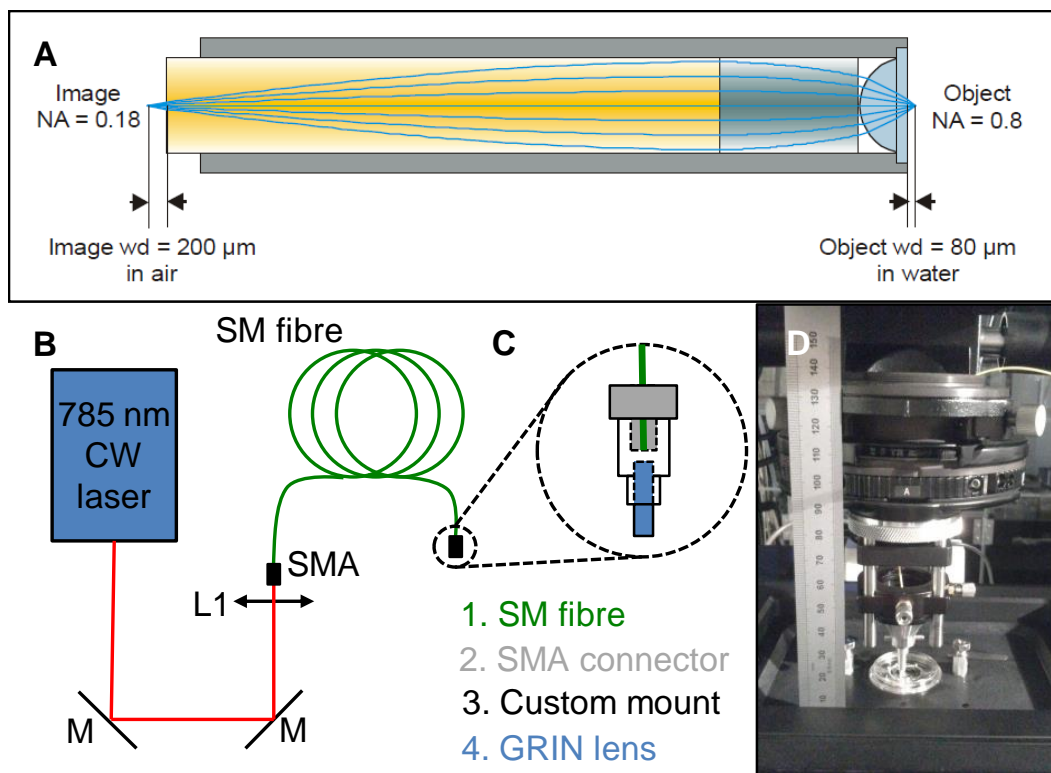


Figure 7.3 – Schematic of GRIN lens microobjective and optical system coupling light into the fibre and from the fibre to the GRIN lens. (A) The curved path of light passing through the micro-objective. *Reproduced with kind permission from GRINtech. [253].* (B) The laser light (red) was coupled into a SM fibre (green) using steering mirrors (M) and an aspheric lens (L1). The SM fibre had SMA connectors at either end. (C) Close-up view of the GRIN lens assembly. A custom mount was used that screwed into the SMA connector and allow the end of the fibre to lie close to the back of the GRIN lens. (D) Mount connected to the condenser lens by optomechanics, the fibre can be seen in yellow.

7.2.1 Optical system

A 785 nm continuous wave laser (TA100, Tui Optics, USA) with output power up to 300 mW and beam diameter 2-4 mm was coupled into a single mode (SM) fibre (Thorlabs, USA) using an aspheric lens (Thorlabs, USA) with a NA close to that of the fibre (Figure 7.3B). The efficiency of coupling was up to 21 %. The other end of the fibre was screwed into a custom mount into which the GRIN lens micro-objective (GT-MO-080-018-488, GRINtech, Germany) could be fastened. The working distance of the GRIN lens is 200 μm so the mount was designed to separate the end of the fibre and the GRIN lens by this amount (Figure 7.3C). The GRIN lens was optimised for 488 nm incident light but was found to focus well with 785 nm, the transmission of 785 nm light through the GRIN lens was 95 %.

A custom mount for the GRIN lens assembly was used to attach it to the microscope. The condenser lens mount was chosen as the anchor because it provides coarse axial and lateral movement and the mount was easily removable from the SIM when standard imaging was required. Optomechanics providing finer axial and lateral resolution (Thorlabs, USA) were used to connect the GRIN lens assembly to the condenser lens mount. A white light source was jointly coupled into the same fibre by a band-pass dichroic mirror (Semrock, USA) to create scatter from trapped particles to enable tracking of non-fluorescent beads.

7.2.2 Trap calibration

The motives and methods of calibrating optical traps were outlined in Section 2.3.2. Owing to a moderate NA preventing axial trapping and use of a high-speed camera rather than QPD for position detection, the GRIN lens trap was calibrated by the equipartition method, using Equation 2.10.

Videos of trapped beads at varying powers were taken using a high speed camera

(piA640-210gm, Basler AG, Germany). Three different sizes of fluorescent polymer beads and 5 μm silica beads were trapped and imaged. Five separate videos of 3000 frames each at 400 fps were taken for each data point. The average and standard deviation of the five videos provided the value and uncertainty in α for each power and bead size. If any obvious noise occurred during an exposure, the current exposure was discarded and a new one taken.

A custom Python program (Appendix D) was written to determine the centre of mass (CoM) of the bead in each frame. α could then be determined from the standard deviation of the bead's displacement for the duration of the video. Fluorescent beads were thresholded prior to CoM determination. The 2 μm beads showed very noisy fluorescence due to the low exposure times required to achieve high frame rates and that contributed to an increased standard deviation of displacement. The 10 μm beads were inhomogeneous in fluorescence and rotated in the trap (shown in Figure 7.4), thresholding reduced these effects with the added benefit of suppressing any possible background fluctuations too. The level of thresholding was determined empirically to best represent the whole bead while not allowing any background noise past the filter. Figure 7.5 shows an example bead's displacement.

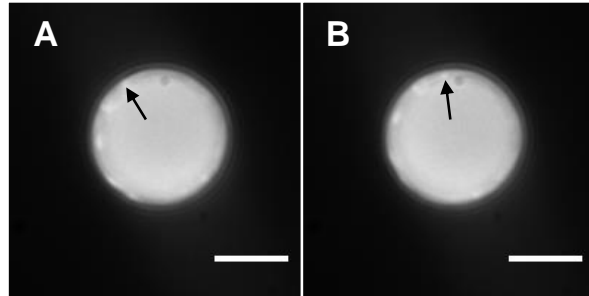


Figure 7.4 – Rotation of a 10 μm bead when optically trapped. The bead is inhomogeneously fluorescent and fluorescent spots on the edge of the bead are observed to move around the circumference between times $t = 0$ (A) and $t = 7.5$ s (B).

The trap stiffness for fluorescent polymer beads was proportional to trap power

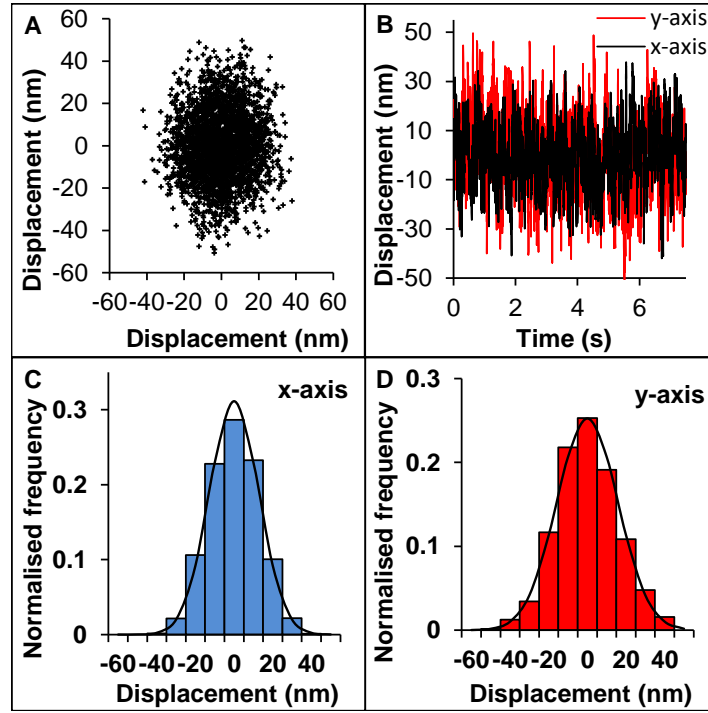


Figure 7.5 – Position of a single bead trapped for 7.5 seconds. Images were collected every 2.5 ms and the centre of mass (CoM) of the bead was determined for each frame. (A) Lateral position of the bead’s CoM during a single exposure of 3000 frames. (B) The x (black) and y (red) CoM changing with time. (C) and (D) are histograms of the bead’s position from the average (set to 0 nm) and overlaid Gaussian curves with variance equal to that calculated from the data. Data are for a 10 μm bead at 60 mW.

(Figure 7.6). α for smaller beads was also generally smaller than for larger beads with $\alpha = 1.46 \text{ pN}\mu\text{m}^{-1}$ at $33 \pm 1 \text{ mW}$ for a 1 μm bead and $11 \text{ pN}\mu\text{m}^{-1}$ for a 10 μm bead.

The 2 μm data, however, show some very different effects that vary from the trends seen in the 1 μm and 10 μm data. All the data showed different α values for the x - and y -axes, this is expected because the laser M^2 value will be different in orthogonal directions, this affects the focusing capabilities of the laser in either direction and therefore the trap stiffness of the trap. The x - and y -axes for the 1 and 10 μm beads do not vary very much; the y -axis being no more than 1.4 times that of the x -axis (apart from the 60 mW data points for the 10 μm beads, which could be due to a noise floor). The

2 μm data, however, show the x -axis to be around three times stiffer than the y -axis, with α_y levelling off at 20 mW.

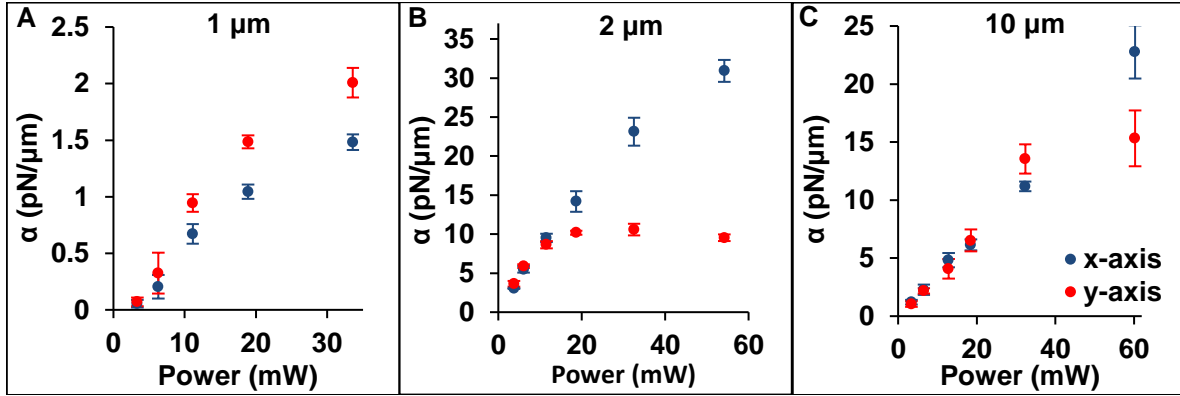


Figure 7.6 – Trap stiffness measurements at varying powers for fluorescent polymer beads of different sizes ((A) - 1 μm , (B) - 2 μm and (C) - 10 μm) in the x (blue) and y (red) directions. Generally α increased as the power increased. α for the 10 μm beads was approximately 10 times greater than for the 1 μm beads. The 2 μm beads show anomalous behaviour compared to the other two, with the appearance of a large noise floor in the y -axis. Data represent 5 videos of 3000 frames each per point. Error bars show the standard deviation.

Fluorescent beads could absorb and re-emit the trapping beam at different wavelengths, which could introduce non-linear effects into the optical trapping and affect determination of α . Fluorescent beads were used to quickly obtain data using the fluorescent capabilities of the microscope but it was necessary to trap non-fluorescent beads too to measure α without any possible introduced fluorescence effects.

To observe non-fluorescent beads, a white light source was coupled into the optical fibre to illuminate the beads from the top. Light scattered from the beads was collected by the imaging objective and passed to the high-speed camera. The illumination obtained using this method was quite inhomogeneous and many image processing steps were required to obtain an easily trackable representation of the bead. Figures 7.7A-D show the image processing steps taken before the CoM was determined. Firstly, adaptive thresholding was applied to correct the inhomogeneous illumination. This left a

dark ring that was the basis for tracking. The image was inverted, dilated and the centre ring was filled to create a bright spot in the centre. The image was then closed to remove the unwanted bright areas surrounding the central bright spot. This bright spot was used to track a CoM for the bead.

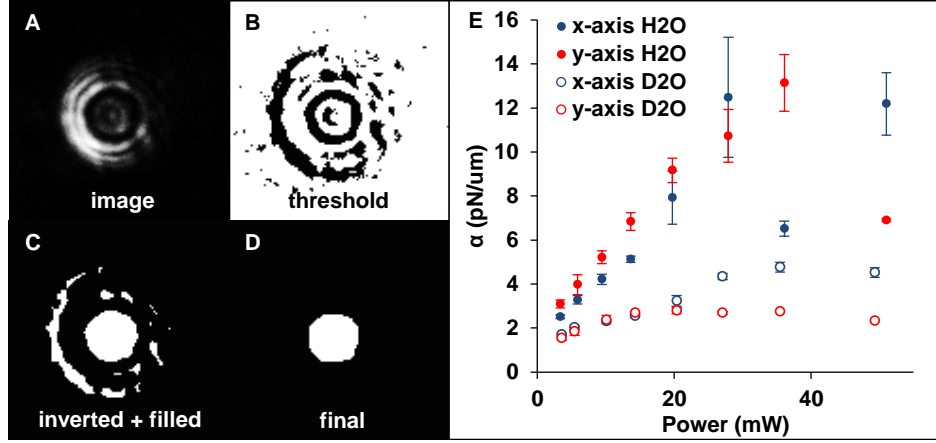


Figure 7.7 – Trap stiffness determination for non-fluorescent silica beads images using scattering from a brightfield source. (A-D) Example of the image processing steps to allow the extraction of the centre of mass of the bead from the image. (A) - initial image, (B) - after adaptive thresholding, (C) - after inversion and flood fill of the centre ring, (D) - final image after clean-up by closing. (E) Trap stiffness values extracted from the images in both H_2O (closed circles) and D_2O (open circles) in the x (blue) and y axes (red). Data represent 5 videos of 3000 frames per point. Error bars show the standard deviation.

Figure 7.7E shows α for 5 μm silica beads in both H_2O and 80 % heavy water, D_2O . The absorption coefficient of H_2O at 785 nm is at least three times higher than for D_2O [254] so there will be more absorption of the laser light by the surrounding medium occurring and subsequent increases in temperature. The equipartition calculation used here assumed room temperature (293 K) but if absorption is occurring then this assumption is no longer valid. The trap stiffness in H_2O was therefore compared to that in D_2O to test the effect of absorption. Silica beads were used for this calibration because polymer beads are less dense than D_2O and do not sink to the bottom for easy

trapping. The beads in H_2O show higher α values than beads in D_2O , peaking at 13.1 and $4.8 \text{ pN}\mu\text{m}^{-1}$ respectively.

7.2.3 Beam profile

Images of the beam profile were captured using the N-SIM TRITC filter to block out most of the laser light and avoid saturating the camera. 25 slices were taken every $0.5 \mu\text{m}$ either side from the point of highest intensity to capture a $25 \mu\text{m}$ stack.

Figure 7.8 shows a slice through the stack at the point of highest intensity (A) and orthogonal projections (B(i) and C(i)) through the centre of the focus. The focal spot was 1.1 by $1.2 \mu\text{m}$ in diameter from Gaussian fits. The axial views (B(i) and C(i)) of the beam show a significant skew to the beam. This skew has been exaggerated by the aspect ratio of these views, with the z -scale being eight times shorter than the lateral direction, the actual angle of skew is around 10 % from perpendicular. To properly view the axial beam profile, intensity values were plotted from lines drawn at the correct angle along the beam (B(ii) and C(ii)). The measured confocal parameter ($b = 2z_R$) is $3.2 \mu\text{m}$.

7.2.4 Trapping and moving cells

Optical trapping of murine hybridoma T cells (B3Zs) was performed in optically-flat glass-bottomed dishes (World Precision Instruments, USA) with a 10 mm diameter well to minimise reagent use. Trapping was intermittent with some cells completely immovable, some seemingly anchored to a specific point (they could be moved by an amount but not beyond a certain point) and some picked up and moved relatively easily. The longer the cells were in the dish, the more they appeared to settle down and become stuck and untrappable. The application of both Sigmacote and 1 % bovine serum albumin in phosphate buffered saline (all Sigma-Aldrich Co., USA) increased the frequency of trappable cells by providing a hydrophobic surface. Using a substrate

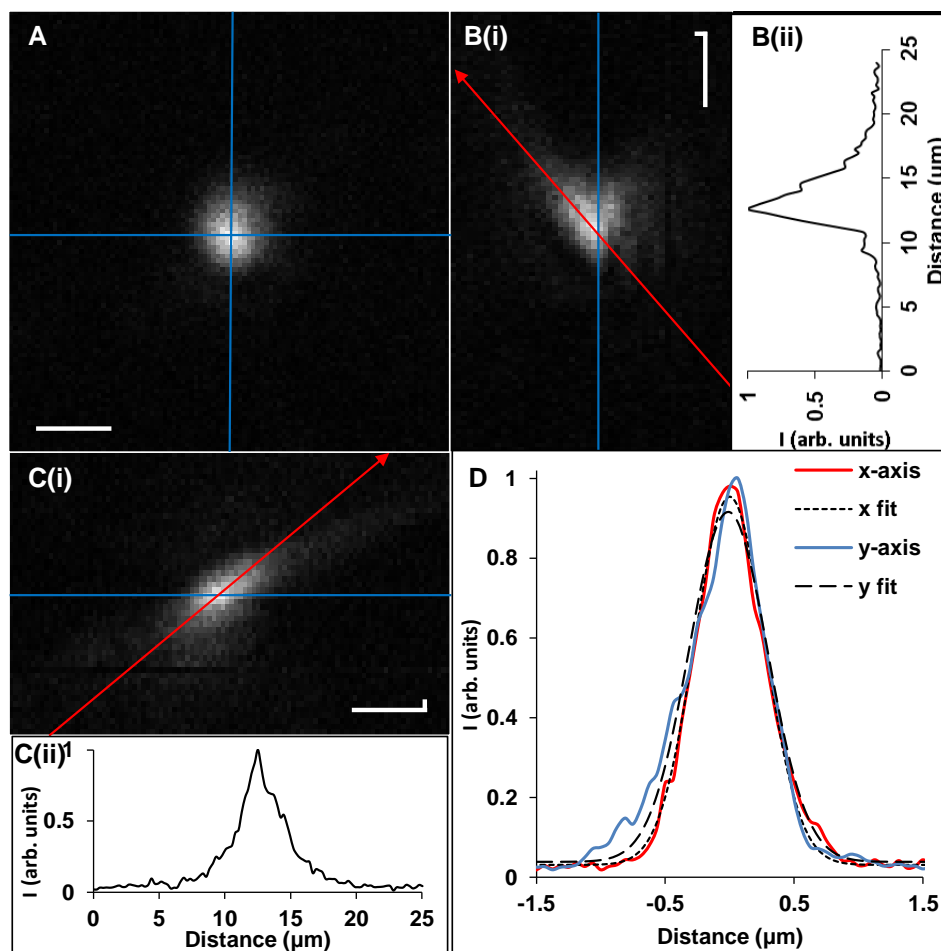


Figure 7.8 – Beam profile produced by the GRIN lens. (A) Focal spot of the GRIN lens, with (B(i)) and (C(i)) showing orthogonal views through the beam. White lines depict the slice positions. Red lines represent the line from which the (ii) intensity graphs are taken. (D) Lateral intensity of the focal spot in the x and y directions, with the Gaussian fits overlaid. Scale bars denote 1 μm .

to decrease adhesion caused cells to move more in undesirable ways too; moving a cell towards another cell on 1 % bovine serum albumin caused the other cell to move away as momentum was exchanged. Once a cell was trapped, optical trapping could be achieved with as little as a few mW of power.

7.3 Monitoring cell-cell interactions by optical trapping

With optical trapping of cells demonstrated, the next important step was to demonstrate manipulation of biological events during fluorescence imaging. Here, we turned to the induction of immunological synapses, an important immune event within the body that mediates immune function.

7.3.1 The immunological synapse

Regulation of the body's immune response is through cell-cell interactions. Antigen-presenting cells (APCs) capture antigens from their environment, process them, and present them on their membranes in a readable format for T cells. T cells will junction to an APC and act depending on the familiarity of the presented antigens. If a pathogen is detected then the T cell can turn cytotoxic and kill the cell or secrete cytokines to recruit pathogen-killing cells to the area [255].

The junction between a T cell and an APC is known as an immunological synapse (IS). A synapse is initiated when a T cell receptor (TCR) is stimulated by an epitope (fraction of the captured antigen) and major histocompatibility complex molecule pair on an APC membrane in the presence of a co-factor [255]. During a synapse, the T cell will polarise. Actin within the cell remodels to form a ring at the periphery of the synapse to stabilise the synapse. The microtubule organisation centre (MTOC) remodels close to the IS, which brings the Golgi and cytotoxic granules (in the case of Natural Killer cells) proximal to the IS to allow for polarised secretions of cytokines or granules [256]. ISs also mediate exchanges of proteins, nucleic acids [257] and vesicles (which also polarise to the IS [258]) and are thought to regulate gene expression within the immune system, making the IS much more multifunctional than previously thought.

A typical IS experiment uses a population of synapsing cells; by scanning the field of view, it is possible to infer temporal information from the proportion of synapses at each stage. Not only is this process laborious, it also has poor temporal resolution. The manipulation of individual cells to induce ISs allows us to follow the synapse from induction to termination. Micro-manipulators have been used for IS induction and subsequent force measurement [259] but this is slow (only 3-5 cells were used for each experiment) and requires experienced users. Ease-of-use and the potential for automation and computer control makes optical tweezers an attractive method for IS induction. Indeed, optical tweezers have been used for a variety of cell manipulation experiments [81, 82, 260].

SR imaging of actin and lytic granules at Natural Killer cell ISs has been well investigated using fixed cells [261, 262] with both STED and SIM. The majority of these studies involved imaging fixed cells synapsing with an antigen-coated substrate or lipid bilayer, while this brings the IS close to the imaging interface for better optical imaging, it does not adequately represent a synapse in 3D space in an *in vivo* setting.

The mechanisms behind the MTOC and endosomal remodelling to the IS is poorly understood, developing a protocol to induce ISs at will and perform live-cell imaging, using an integrated optical trap and SR microscopy, would greatly advance our knowledge of this important process.

7.3.2 Immunosynapse induction by optical trapping

One of the markers for the start of an immunological synapse is an increase in calcium in the T cell. This is an almost instantaneous effect, which makes it a useful marker for the onset of an IS, remodelling is a more subtle and slower effect (at least ten minutes), which might be difficult to observe during an experiment. A calcium fluorophore, Fluo-4 (Life Technologies, USA), which increases in fluorescence when it binds to calcium, was used to detect changes in cytosolic calcium. An optical trap was employed to induce

a single bead-cell IS and the calcium response was monitored. 3 μm polymer beads (Spherotech, USA) were conjugated with mouse antibodies (eBioscience, USA): anti-CD3 bypasses the TCR and directly activates the B3Zs, and anti-CD28 is a co-factor to ensure sustained synapse induction (unlike in Wei *et al.* [234] and Tam *et al.* [81] where beads coated in anti-CD3 only are used) [255, 263].

The antibody conjugated beads adhered to the coated-glass surface. It was therefore easier to move the cell towards the bead than the bead towards the cell. The imaging and trapping planes were co-aligned so the cells were in focus when trapped, improving imaging of the cells when trapped. Epi-fluorescence images using the FITC filter were taken every 50 ms for 160 s using a 20x objective. Region of interest intensities were measured at each time point using ImageJ and background corrected. Photobleaching correction was performed by fitting an exponential curve by least squares optimisation to the normalised control cell signal and dividing the normalised activated response by the fitted curve.

An optical trap-induced immunosynapse and subsequent calcium increase is shown in Figure 7.9. (A) shows a bright cell (B3Z) with a polymer bead attached to it to the left of the field of view and a dark cell (right) that is yet to be activated (low fluorescence), with a bead present not currently visible. The dark cell was brought towards a bead adhered to the bottom of the dish using the optical trap (B). The bead becomes visible as the cells begins to increase in fluorescence intensity (C). Between 10 and 160 seconds, the fluorescence increases six-fold, signalling the creation of an immunosynapse as the T cell is activated (D). No increase in calcium levels were seen when trapping cells in the absence of beads.

While it was possible to demonstrate cell trapping and the induction of an immunosynapse with the trapping system described above, the next step of incorporating super-resolution imaging to formation of an IS was not achieved during this study. The adhesion of cells and beads to the dish made trapping and moving difficult. Coating the dishes made cells tend to move away from each other even when placed close together,

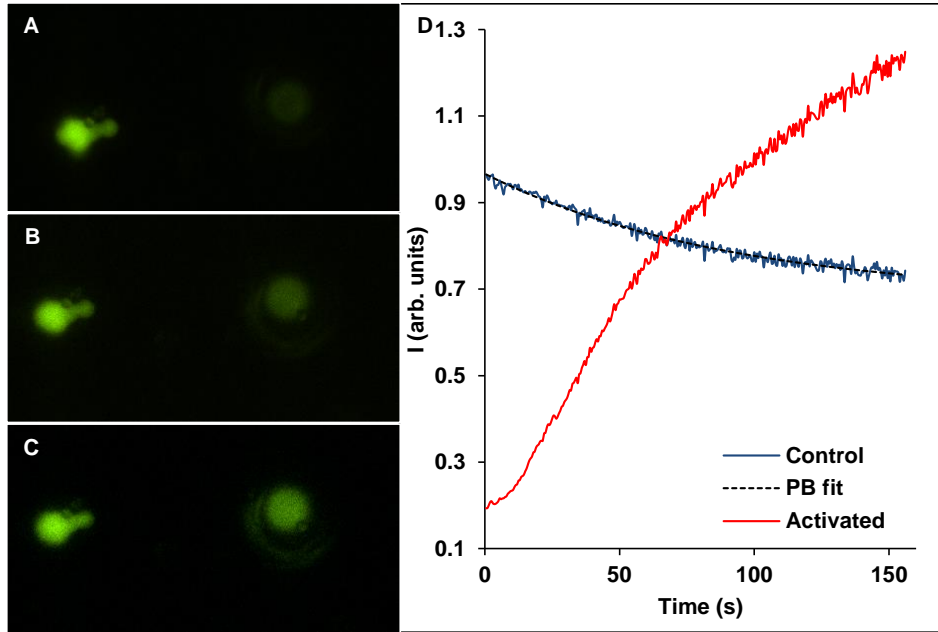


Figure 7.9 – Use of an optical trap to induce an IS by moving a Fluo-4 loaded B3Z towards an anti-CD3 anti-CD28 coated bead. (A) Unactivated T cell (right) prior to synapse formation with an antibody coated bead. (B) Slight increase in fluorescence as an IS is initiated. (C) Larger increase as the synapse matures. (D) Increase in fluorescence of the activated cell (red), where every point plotted represents the average of ten measured points. The activated cell's fluorescence was corrected for photobleaching by dividing by the PB line (dashed) fit to the control cell (blue).

as performed in McNerney *et al.* [82]. Adherent target test cells (HeLa) displayed invisible protrusions, preventing close contact with the trapped suspension cell. When adding antibody-coated beads to a dish of cells, no tubulin, mitochondrial or endosomal remodelling was observed. The stains [264] and beads [265] used should be sufficient to induce remodelling so the reason behind this behaviour is currently unknown. More experiments with other cell types and different incubation protocols would perhaps extricate the reasons behind this failure to polarise.

7.4 Super-resolution imaging of plant cells

With the novel optical trapping and fluorescence imaging system demonstrated to work with mammalian cells, attention was then turned back to plant cells. The highly inhomogeneous nature of plant tissue makes it a challenging imaging target. The presence of high refractive index thick cell walls and low refractive index intercellular airspace introduces many aberrations in light passing through plant tissue [266, 267]. Lignin within the cell wall and chlorophyll both produce auto-fluorescent signals, leading to a broadband autofluorescence that dominates most standard imaging wavelengths [268]. Liu *et al.* [269] demonstrated that the cell wall can cause distortions in confocal imaging and lead to spurious effects such as the appearance of fluorescent doublets when only one spot is present. Super-resolution techniques rely on aberration-free imaging to achieve the best possible resolution so this could have deleterious consequences for SR imaging of plant cells.

7.4.1 Previous SR imaging of plant cells

Fitzgibbon *et al.* [270] first applied super-resolution imaging to plant cells, using 3D-SIM to image the various plasmodesmata throughout a tobacco leaf. Plasmodesmata (PDs) are connections between plant cells; pores through the cell walls that consist of plasma membrane bounding a cytoplasmic cavity. Desmotubules pass through the PD and connect ER between cells [271]. PDs are around 50 nm in diameter and up to 1-2 μm in length, making it difficult to resolve any structure with standard confocal microscopy; electron microscopy is routinely used to image PDs. PDs are relatively static and their dimensions make them a useful target for SIM, with the relatively modest extension in resolution (compared to other SR techniques) providing enough to resolve sub-PD localisation. PDs can either occur as single or branched pores, with some having many pores connecting to a single, large central cavity.

3D-SIM has proven able to resolve plasmodesmatal structure unavailable to conventional widefield and confocal microscopy [270, 271], making it possible to distinguish between the central cavity and pore necks and identifying highly-branched structures. The axial sectioning provided by SIM also aided in optically resolving the complex and branched nature of mature PDs.

The enhanced resolution and optical sectioning provided by 3D-SIM has been exploited in a number of other plant studies, imaging the structure of viral replication complexes [272, 273], identifying different configurations of synaptonemal complexes [274] and following microtubule dynamics [275].

As long as the sample type, fluorophores used and imaging modalities are chosen correctly, plants are not inaccessible to SR imaging. Conflicting information has been cited in different studies, for instance Liesche *et al.* [276] chose not to use STED because the depletion laser is absorbed strongly by chlorophyll, making STED difficult in green tissue but Kleine-Vehn *et al.* [277] employs STED effectively. The SNR also dramatically affects whether a technique can be used e.g., Liesche *et al.* [276] imaged microfibrils (within the highly autofluorescent cell wall) and found the SNR too high to utilise SIM effectively (finding dSTORM more effective) but successful imaging of PDs and microtubules have been achieved using this SR technique.

7.4.2 3D-SIM imaging of plant cells

To evaluate the N-SIM to image plant cells, plant tissue was imaged for comparison to published data. A detailed description of N-SIM imaging protocol can be found in Appendix C.2.

Figures 7.10 and 7.11 are SIM images taken from epidermal peels of fixed tobacco leaves expressing a GFP-tagged protein that targets the ER running through the PD. Figure 7.10 is a transverse view between two epidermal cells (bottom left and top right), with PD connecting the two. The white lines indicate the approximate curve of the

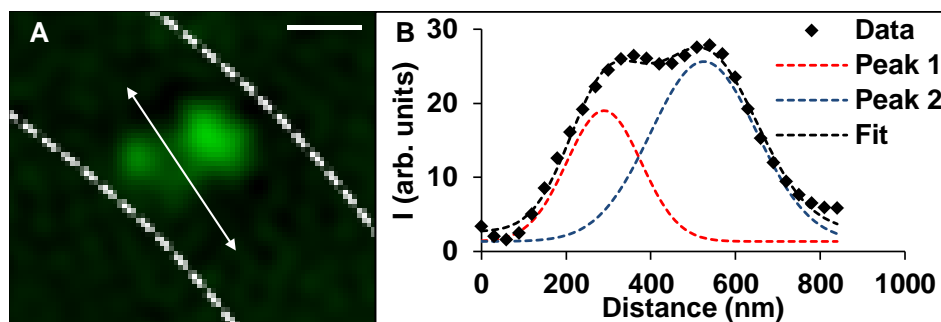


Figure 7.10 – N-SIM image of plasmodesmata (PD) in a fixed epidermal peel from a tobacco leaf (A). The dashed lines follow the curve of the cell walls of both adjoining epidermal cells. The pore shows two strands of ER membrane in the cavity between the walls, indicating the presence of two adjacent pores. An intensity profile (black diamonds) was taken along the arrow position and plotted in (B). Two Gaussian peaks (red and blue dashed lines, black dashed line denotes addition of two peaks) were fitted to the data to determine the FWHM and separation of the peaks. Scale bar denotes 1 μm .

cell walls, but are offset to avoid covering important information. The PD displays two sections of fluorescence, caused by ER membrane accumulating just outside the PD. Between these two areas two lines of fluorescence are seen. These are strands of ER passing through the pore (or more likely two adjacent pores) and are only 20 nm in diameter [278]. The N-SIM can resolve these into two separate strands. Fitting two Gaussian curves allows us to place the FWHM of the ER to be 206 nm and 293 nm. The distance between the peaks is approximately 150 nm.

Figure 7.11 shows an *en face* stack of a collection of pores, known as a pitfield, and illustrates the highly complex nature of some PDs. Pitfields are dense regions of pores connecting the epidermal cells to the mesophyll layer [271] and offer another imaging angle for PDs. Using structured illumination can help to increase the achievable lateral and axial resolution to resolve more structure within these highly complicated arrangements of interconnecting pores. Orthogonal projections of the stack are displayed here, with yellow lines indicating the displayed sections. The interleaving nature of the pores can be easily seen here, in particular, the white arrows show a pore that (from bottom

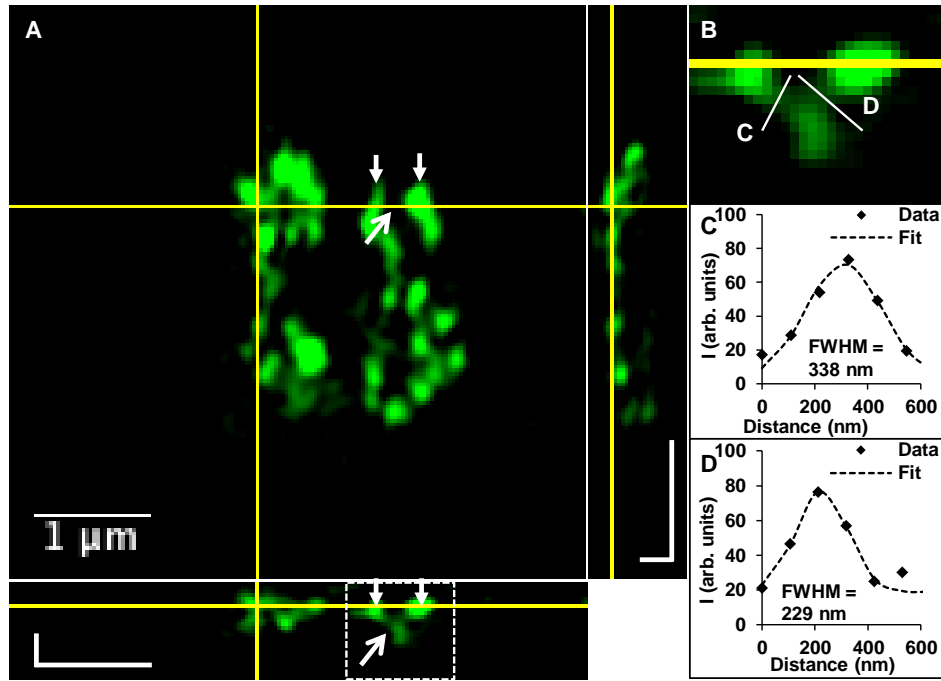


Figure 7.11 – Orthogonal views taken from a SIM stack of a GFP-labelled pitfield connecting the epidermal layer to the mesophyll layer (A). The solid arrowheads highlight the two pores on the epidermal side, which join at a branching point (open arrowhead) to form a single pore at the mesophyll side, akin to what has been seen previously [270]. All scale bars denote $1\ \mu\text{m}$. The white dashed box is shown enlarged in (B) with white lines denoting the positions where intensity profiles in (C) and (D) were taken (black diamonds). Gaussian fits were performed (dashed lines) to determine the achievable axial resolution.

to top of the stack) starts out as a single pore (open arrowhead) and branches out into two (closed arrowheads). The point at which the yellow lines cross also shows significant structure and PD connections that would be lost under confocal microscopy.

The axial resolution was determined by taking line profiles of the branched pore. Gaussian fits of the pore necks were taken. The FWHM of the necks were determined to be 339 and 229 nm respectively.

7.5 Discussion and conclusions

This chapter has demonstrated the development of a commercial microscope-friendly optical trap using a fibre-fed GRIN lens used to induce immunological synapses at will, with the eventual aim to image MTOC remodelling at super-resolution. The capacity of a commercial structured illumination microscope to readily obtain images beyond the diffraction limit even in a notoriously challenging sample like whole plant tissue was also evaluated.

To pave the way towards developing an optical trap integrated with structured illumination microscopy for all-optical manipulation and SR imaging of biological samples, an optical fibre-based trap using a high-NA GRIN lens, the first of its kind, was incorporated onto the N-SIM and characterised. The restrictions of working within a highly specialised system were somewhat circumvented by the use of an easily removable, upright trap but still imposed some strict limitations on the achievable quality of the optical trap.

The optical trap was characterised by measuring the trap stiffness and beam parameters. By observing the trap stiffness measurements for fluorescent beads, the 10 μm beads showed higher α values than 1 μm beads. The Brownian motion for a smaller bead will be larger, reducing α as r_{max} increases. The trap stiffness was overall proportional to laser power P at these beads sizes following:

$$\alpha = \frac{Qn}{r_{max}c}P \propto P \quad (7.2)$$

Derived by substituting $F_{trap} = \alpha r_{max}$ into Equation 2.3 where r_{max} is the maximum bead displacement [279].

The 2 μm beads displayed unexpected behaviour that could be attributed to the axial position of the trap, which was altered slightly for each bead size so that the trapping was optimised. Whilst the bead was checked for movement between each exposure to ensure it had not adhered to the surface, the bead or position on the

coverslip could affect the trapping; something causing the bead to stick in one place would artificially increase the trap stiffness to the high levels seen in the x -axis. The saturation observed in the y -axis data is caused by a noise floor, when movement of the system is greater than the displacement caused by the Brownian motion in the trap and could be due to the upright configuration introducing vibrations.

When using D_2O to minimise laser absorption, (Figure 7.7) the data show up to 6.5 times higher trap stiffness for H_2O than D_2O , the opposite effect to what is expected. If the temperature was higher than assumed due to absorption by H_2O then we should see a lower trap stiffness than with D_2O as the bead moved around more due to thermal fluctuations. This disparity could be due to the same issues suggested for the 2 μm polymer beads. Both media show unreliable behaviour at powers > 30 mW, possibly due to a noise floor at this point or unreliable bead tracking at smaller displacements.

The trap stiffness varies depending on input power, bead size and bead type. The measured data was compared with other literature using optical fibre-based traps in Table 7.1. To correct for the different powers used in each study, the trap stiffness per unit power, k_{trap} , was determined from the trap stiffness and input power. The GRIN k_{trap} was determined by lines of best fit. For data showing a strong noise floor (y -axis 2 μm and 5 μm data) only points up to the saturation point were fitted.

The measured trap stiffness per unit power varies over an order of magnitude from 60 to 633 $pN\mu m^{-1}W^{-1}$. For the published literature, k_{trap} covers 35-220 $pN\mu m^{-1}W^{-1}$, generally lower than the GRIN lens values, implying the GRIN trap is an efficient fibre trap. There is no evident proportionality between NA and k_{trap} , which is expected as the gradient forces increase for a tighter focus, or between bead size and k_{trap} but, given the differences in trap creation, environment and calibration of the traps a fully quantitative review is not sensible. Comparing with standard objective-based optical traps of a similar NA (~ 0.8), the trap stiffness per unit power ranges from 100-600 $pN\mu m^{-1}W^{-1}$ [279, 282, 283].

No consistent z -trapping was observed for this optical trap. This is probably due

Reference	NA	Bead size (μm)	k_{trap} ($pN\mu\text{m}^{-1}W^{-1}$)	Axial trapping
[280]	N/A	2	220	Y
[281]	1.15	10	97	N
[281]	1.15	7	35	N
GRIN	0.8	10	330(50)	N
GRIN	0.8	5	433(6)	N
GRIN	0.8	2	633(6)	N
GRIN	0.8	1	60(10)	N

Table 7.1 – Review of typical trap stiffness per unit power, k_{trap} , for fibre-based optical traps for comparison with the GRIN lens trap stiffness. Brackets denote the uncertainty in the measurement.

to the low NA of the GRIN lens, when compared with usual NAs employed for axial trapping of ≥ 1.0 . At low NA, the gradient force cannot counteract the scattering forces. Given the nature of the cell trapping being performed with this system, the lack of axial trapping does not affect the experiments performed using the trap.

The produced trapping beam spot size (Figure 7.8) was 5 % less than a diffraction-limited spot ($1.2 \mu\text{m}$). This small discrepancy is probably due to the use of a camera for measurement, a knife-edge measurement would be a more accurate method. The skew to the beam is caused by difficulty in aligning the GRIN lens orthogonally to the microscope stage. A tip/tilt mount was tested to aid this matter but was found to affect the stability of the mount. The predicted confocal range is $2.8 \mu\text{m}$, slightly smaller than the measured value.

Using an optical trap integrated onto the N-SIM allowed the formation and monitoring of an immunosynapse in real time (within 3 minutes). Using a fluorescent calcium indicator, it was possible to monitor the induction of a T cell-bead IS by optical trap-

ping. The strong calcium increase indicates the formation of an IS but no remodelling was seen after activation. The use of multiple traps or a higher gradient force could help to induce an immunosynapse and follow the remodelling, in super-resolution, of a sustained synapse by allowing 3D manipulation of multiple cells, providing more degrees of freedom to investigate. Wright *et al.* [284] optically trapped T cells and brought them proximal to dendritic cells to measure interaction forces. Although trapping was performed in brightfield so no functional fluorescence imaging was possible, an interesting point was the use of overlapping Laguerre-Gaussian modes for trapping to prevent cell roll and therefore increase the manipulation precision. This might be possible with the GRIN lens trap if the SM fibre was swapped for a low mode fibre [285].

The N-SIM was able to demonstrate an increase in resolution over standard epi-fluorescence imaging in plant tissue. Using the N-SIM in fixed tobacco leaves to image PDs, it was possible to distinguish between two desmotubules of 200-300 nm width that were 150 nm apart (Figure 7.10). The experimental resolution for structured illumination at 520 nm emission is 110 nm [7] so the images obtained were close to this limit and smaller than the confocal resolution limit of 182 nm. Fitzgibbon *et al.* measured the width of ER in sieve plate pores to be 103 ± 3 nm [270], less than half the width of the ER observed here. This disparity might be due to the width of the ER changing in different parts of the leaf. The actual size of the desmotubules has been measured to be 10-15 nm under electron microscopy. The resolution obtained using the N-SIM was enough to distinguish between adjacent pores that would have been classified as a single pore under normal epi-fluorescence or confocal microscopy.

The optical sectioning provided by the SIM also allowed imaging of the complex nature of a pitfield (Figure 7.11) that would be unachievable with confocal or epi-fluorescence (confocal axial resolution = 545 nm and SIM axial resolution = 280 nm [7] for GFP). The axial resolution limit measured here was 229 nm, this is slightly smaller than the theoretical limit but this is because the line profiles were not parallel to the axial direction. PDs proved a perfect imaging target for the multiple exposures

required for SIM imaging through their stationary behaviour over long time-scales. The widefield, rather than point-scanning, image formation used by the SIM means that even low-fluorescence objects, such as the PDs imaged here, can be imaged with high SNR.

Whilst the images displayed here clearly demonstrate the super-resolution capabilities of the N-SIM, further imaging would be useful to cement and expand on this result. Low SNR can lead to imaging artefacts (seen in the background of Figure 7.10) that can be reduced by choosing suitable reconstruction parameters or look-up tables. Reducing the noise by altering the strength of the apodizing filter in post-processing also removes possible interesting high frequency information. Secondary labelling by fluorescent proteins (live samples) or antibodies (fixed samples) of a different colour targeting the same protein or a complementary one could help to strengthen the conclusions drawn in this chapter.

The PDs imaged in this chapter were within fixed samples. Fitzgibbon *et al.* [286] developed a high-throughput imaging technique using a complex PD-targeting protein and showed that it was possible to image PD development in detached leaves in a specialised chamber for up to 24 hours. Extending this technique to follow the development of PD formation from simple to complex pores, or from single pores to twinned pores in super-resolution in real time could provide useful insights into this poorly-understood mechanism.

The benefits and limitations of the N-SIM for imaging plant cells and as a basis for a trapping and super-resolution workstation are presented in this chapter. It was possible to obtain truly super-resolution images of challenging plant tissue samples with similar results to what had been previously observed on a different SIM system [270]. An optical trap was developed for inducing immunological synapses between a T cell and an antibody conjugated bead [81, 234] with the aim to combine with super-resolution imaging. It would be interesting to adapt the trap for trapping and imaging plant cells, either intracellularly or with whole protoplasts, requiring a dual beam system owing

to their large size. The adoption of other SR microscopy techniques in this system might also prove beneficial due to the higher resolutions possible, although for live cell trapping and imaging, a technique such as STED might only prove fast enough in very small areas [287]. Incorporating a femtosecond laser beam via the GRIN lens (using a hollow-core fibre to reduce dispersion) could provide both trapping and photoporation modalities, further enhancing the functionality of the system and its benefit in both plant and mammalian cell research.

7.6 Chapter acknowledgements

Plants were provided by Vinciane Tillemans, Alison Roberts and Jens Tilsner. Plant imaging was performed with Elaine Campbell and Jens Tilsner. The optical trap was designed by Anisha Kubasik-Thayil and built with Jonathan Nylk. Fluo-4 stained cells were provided by Elaine Campbell. Immunosynapse experiments were performed with Elaine Campbell.

8 | Conclusions and future work

8.1 Summary

This thesis has demonstrated some powerful optical techniques that can be used to investigate and manipulate plant and mammalian cell biology. The novel aspects of this thesis are listed below:

- Femtosecond optical injection of plant cell suspension culture (Chapters 5 and 6).
- Application of spatial beam shaping to enhance plant cell photoporation (Section 5.3.2).
- Optical injection of morpholinos into plant cells (Section 5.3.6).
- Application of broadband ultrashort pulses to enhance plant cell photoporation (Section 6.3.2).
- Development and characterisation of a GRIN lens optical trap (Section 7.2).

This thesis began by introducing photoporation as an effective tool for the investigation of mammalian cells, using light to introduce membrane-impermeable molecules into mammalian cells. Optical trapping for sterile and non-invasive cell manipulation was also introduced. The next step was to place biophotonics techniques into the context of plant cell science, highlighting possible benefits, challenges and previous achievements.

The next three chapters were concerned with the development of femtosecond photoporation of plant cells. The design and characterisation of a highly reconfigurable optical system was outlined in the fourth chapter. The system could change laser spatial mode, incident power and pulse duration by using moveable optics, including flip mirrors and half-wave plate and polarising beam splitter combinations, to compare the effects of varying these optical parameters and utilising the benefits of each parameter as required. The spatial mode at the laser focus could be changed to either a Gaussian or Bessel beam. The central core size of the Bessel beam was the same as the Gaussian spot size but the axial extent was 13 times longer to allow multiphoton effects to take place over a larger axial distance, reducing the requirement for precise alignment on the cell membrane during photoporation. Two different femtosecond lasers were coupled in to allow for changing pulse duration at the microscope focus: a high powered but long pulse duration laser and an ultrashort broadband laser combined with a pulse dispersion compensation system, the system could provide either 3 W, 734 fs pulses or 70 mW, 22 fs pulses with the same Gaussian spot size for direct comparison. An ultrashort broadband Bessel beam was also created at the focal point and characterised.

The fifth chapter then utilised this system to investigate photoporation of tobacco BY-2 cells. A small cavitation bubble was observed upon irradiation that initiated optical injection into the cells. By varying the incident power, it was possible to increase the percentage of cells that were successfully injected with propidium iodide but reduced the number of viable cells. Using a single 40 ms dose from the Bessel beam was equivalent to using three axially separated shots using the tightly-focused Gaussian beam, but the reduced time taken to perform the injection leads to an increased throughput of injected cells in a given time. Osmolarity of the external medium affected, and in some cases prohibited, optical injection. A slightly hypertonic solution was optimal to introduce extracellular substances whilst reducing cell death, although the amount of substance taken in by the cell is reduced. When injecting different substances, the size of the injected molecule adversely affected injection efficiency, with dextran molecules

larger than 70 kDa unable to pass through the cell wall. Synthetic oligonucleotides were successfully introduced into cells and protoplasts; the smaller, neutral-charged morpholinos were injected more easily than the larger, negatively charged siRNA.

The sixth chapter investigated the role of changing pulse duration in photoporation of plant and mammalian cells by comparing the standard laser with a broadband ultra-short pulse emitting laser. A pulse compensation system, the MIIPS, was required to achieve close-to transform-limited 22 fs pulses at the focus by measuring the spectral phase and applying the inverse phase to the pulse. In both plant and mammalian cells, the shorter pulse duration was found to achieve significantly more efficient optical injection with increased viability. This effect was more significant for adherent mammalian cells than for plant cells, possessing a thick cell wall.

The final results chapter considered two other important biophotonic techniques and demonstrated steps towards integrating them into a workstation. An optical fibre-based trap using a GRIN lens to focus the output beam was integrated onto a commercial SIM microscope for potential trapping under super-resolution. As a proof-of-concept, the trap was characterised and used to induce an immunological synapse between a bead and a T cell using the epi-fluorescence attachment on the SIM, showing its suitability for use on commercial microscopes. The SIM was used to image plasmodesmata of tobacco epidermal leaves, demonstrating better resolution than standard epi-fluorescence imaging and resolution beyond the diffraction limit for these respective cell components.

8.2 Future work

The work presented within this thesis has demonstrated some interesting developments in biophotonic applications to plant cells but has also highlighted avenues for future work. The short-term goals for each section of this thesis are discussed below, followed by a longer-term view of future prospects.

The next steps for each chapter would involve:

- **Chapter 4:** Incorporation of a mirror galvanometer for multi-site Bessel beam targeting.
- **Chapter 5:** Injection of fluorescent DNA to enhance understanding of DNA localisation upon photoporation into plant cells.
- **Chapter 6:** Introduction of a more power-efficient dispersion compensation system for broadband ultrashort Bessel beam photoporation.
- **Chapter 7:** Development of an aspheric lens system to introduce multiple traps for highly reconfigurable dynamic trapping.

In the long-term, the optical system designed was power efficient and simple to implement through the use of an axicon for Bessel beam generation. An SLM, although power inefficient, could increase the reconfigurability of the system, allowing multiplexing of both the Gaussian [16] and Bessel beam [288] for multiple irradiation sites or even experimenting with other beam types, such as super-resolution beam spots [289]. It would also be possible to engineer the Bessel beam, varying the propagation distance and intensity as well as the number of rings [290], potentially creating a more efficient Bessel beam with a larger percentage of power carried in the central spot.

The obvious milestone when considering photoporating plant cells is to achieve transformation of injected nucleic acids. The uptake of morpholinos, which are smaller than DNA, suggests that the next step would be to demonstrate gene knockdown using functional morpholinos. Not only is gene knockdown a useful technique in its own right, it would also provide a stepping stone towards stable DNA transformation - the ultimate goal. Attempts to optically transform BY-2 cells and protoplasts proved unsuccessful and the steps taken to understand the reasons behind this can be found in Section 5.4. Once demonstrated, femtosecond optical transfection of plant cells could prove a powerful tool in the genetic modification toolbox, providing selective and

highly viable means of transforming single cells, from which entire organisms could be regenerated.

When considering optical injection, there are many molecules that are desirable, but difficult, to deliver intracellularly into plant cells, such as RNA probes, calcium indicators and actin dyes among many others. Demonstrating the versatility of this technique by applying it to other cell types, such as in tissue and pollen grains would also enhance the functionality of optical injection of plant cells, both of these cell types provide easier viability monitoring than suspension cells. Further investigation of the cell-laser interaction is also required, investigation of cell response to femtosecond laser irradiation using calcium or reactive oxygen species dyes has been explored in mammalian cells to great effect [291] and can help understand optimal environmental conditions for photoporation.

Optoporation could be used to target large numbers of plant cells at a time by shockwave or plasmonic effects. Laser-induced stresswaves have already proven useful for gene silencing studies in suspension plant cell cultures so the shockwave created by focusing a nanosecond laser onto a cell substrate [30] or an optically trapped nanoparticle [35] might also be used effectively. This technique has the benefit of applying different shear stresses at different distances from the focal spot, effectively testing a range of different parameters at once. The lack of single cell selectivity and usually lower injection efficiencies prevented the exploration of these techniques in the thesis.

Throughout this thesis, the cell wall interaction with molecules has suggested that it is not breached by the laser but other studies using different laser parameters show definite cell wall damage. Cell wall staining by calcofluor white could help identify any cell wall damage induced by the femtosecond laser. A combination of nanosecond irradiation for cell wall ablation combined with femtosecond irradiation for membrane poration could increase the size of molecules that can be injected into intact cells.

When investigating the role of pulse duration, the ability to incrementally change the pulse duration using the MIIPS while monitoring the effect on photoporation could

provide interesting insight into the interaction of the plant cell with ultrashort pulses, for full comparison with Rudhall *et al.* [172]. This would require more power at the sample plane, which would also allow for broadband ultrashort Bessel beam photoporation - an interesting development for both plant and mammalian cells, potentially providing highly efficient and minimally damaging photoporation. Other pulse compression techniques might provide greater power efficiency, but at the loss of precise control over pulse duration and shape provided by the MIIPS system.

The final chapter explored several threads, all of which have many possible enhancements and developments. Given the success of SIM imaging of plant cells, an interesting development would be to enhance the multi-modality of the system to create a biophotonics workstation for imaging, manipulation and cell surgery of plant cells. This was started with the integration of an optical trap but the design was not optimal for plant cell experiments. Plant cells are large so a dual-focus trap could help in manipulating protoplasts and other single cells. Incorporation of a femtosecond laser beam could allow photoporation, cellular surgery and optical trapping with a single beam for a simple yet multifunctional system. Photoporation under super-resolution imaging with suitable membrane and molecule dyes could also help to elucidate photoporation mechanisms.

8.3 Concluding remarks

The incidences of applications of biophotonics to plant sciences is small but growing. The development of newer and more sophisticated optical techniques can help to mediate the problems posed by these challenging cells and tissues. Temporal and spatial beam shaping has been employed here to enhance the optical injection and imaging of plant cells with potential applications in genetic modification and plant cell research.

Bibliography

- [1] K. Svanberg, N. Bendsoe, J. Axelsson, S. Andersson-Engels, and S. Svanberg. “Photodynamic therapy: superficial and interstitial illumination”. *Journal of Biomedical Optics* **15**:4 (2010), 041502.
- [2] D. J. Stevenson, F. J. Gunn-Moore, P. Campbell, and K. Dholakia. “Single cell optical transfection”. *Journal of the Royal Society Interface* **7**:47 (June 2010), 863–871.
- [3] W. Drexler and J. G. Fujimoto. “State-of-the-art retinal optical coherence tomography”. *Progress in Retinal and Eye Research* **27**:1 (Jan. 2008), 45–88.
- [4] L. V. Wang. “Multiscale photoacoustic microscopy and computed tomography”. *Nature Photonics* **3**:9 (Aug. 2009), 503–509.
- [5] D. Jakubowski, F. Bevilacqua, S. Merritt, A. Cerussi, and B. J. Tromberg. “Quantitative Absorption and Scattering Spectra in Thick Tissues Using Broad-band Diffuse Optical Spectroscopy”. In: *Biomedical Optical Imaging*. Ed. by J. G. Fujimoto and D. L. Farkas. Oxford University Press, 2009, 352–377.
- [6] T. D. Wang and J. Van Dam. “Optical Biopsy: A New Frontier in Endoscopic Detection and Diagnosis”. *Clinical Gastroenterology and Hepatology* **2**:9 (2004), 744–753.
- [7] L. Schermelleh, R. Heintzmann, and H. Leonhardt. “A guide to super-resolution fluorescence microscopy”. *The Journal of Cell Biology* **190**:2 (July 2010), 165–175.

- [8] K. Deisseroth. “Optogenetics”. *Nature Methods* **8**:1 (2011), 26–29.
- [9] D. J. Stevenson, F. J. Gunn-Moore, and K. Dholakia. “Light forces the pace: optical manipulation for biophotonics”. *Journal of Biomedical Optics* **15**:4 (2010), 041503.
- [10] K. C. Neuman and S. M. Block. “Optical trapping”. *The Review of Scientific Instruments* **75**:9 (Sept. 2004), 2787–2809.
- [11] D. J. Stevenson, F. J. Gunn-Moore, P. Campbell, and K. Dholakia. “Transfection by optical injection”. In: *The Handbook of Photonics for Medical Science*. CRC Press, 2010. Chap. 3, 87–117.
- [12] P. Mthunzi, K. Dholakia, and F. J. Gunn-Moore. “Phototransfection of mammalian cells using femtosecond laser pulses: optimization and applicability to stem cell differentiation”. *Journal of Biomedical Optics* **15**:4 (2011), 041507.
- [13] S. Mehier-Humbert and R. H. Guy. “Physical methods for gene transfer: improving the kinetics of gene delivery into cells”. *Advanced Drug Delivery Reviews* **57**:5 (Apr. 2005), 733–53.
- [14] N. A. Campbell. *Biology*. 4th ed. The Benjamin/Cummings Publishing Company, 1996, 140–159.
- [15] S. J. Singer and G. L. Nicolson. “The fluid mosaic model of the structure of cell membranes”. *Science* **175**:4023 (Mar. 1972), 720–731.
- [16] M. Antkowiak, M. L. Torres-Mapa, F. J. Gunn-Moore, and K. Dholakia. “Application of dynamic diffractive optics for enhanced femtosecond laser based cell transfection”. *Journal of Biophotonics* **3**:10-11 (Oct. 2010), 696–705.
- [17] R. F. Marchington, Y. Arita, X. Tsampoula, F. J. Gunn-Moore, and K. Dholakia. “Optical injection of mammalian cells using a microfluidic platform”. *Biomedical Optics Express* **1**:2 (Jan. 2010), 527–536.

- [18] H. A. Rendall, R. F. Marchington, B. B. Praveen, G. Bergmann, Y. Arita, A. Heisterkamp, F. J. Gunn-Moore, and K. Dholakia. “High-throughput optical injection of mammalian cells using a Bessel light beam”. *Lab on a Chip* **12**:22 (Nov. 2012), 4816–4820.
- [19] L. Bonetta. “The inside scoop for evaluating gene delivery methods”. *Nature Methods* **2**:11 (2005), 875–883.
- [20] A. Vogel, J. Noack, G. Hüttman, and G. Paltauf. “Mechanisms of femtosecond laser nanosurgery of cells and tissues”. *Applied Physics B* **81**:8 (Nov. 2005), 1015–1047.
- [21] L. Paterson, B. Agate, M. Comrie, R. Ferguson, T. Lake, J. Morris, A. Caruthers, C. T. A. Brown, W. Sibbett, P. Bryant, F. J. Gunn-Moore, A. Riches, and K. Dholakia. “Photoporation and cell transfection using a violet diode laser”. *Optics Express* **13**:2 (Jan. 2005), 595–600.
- [22] G. Palumbo, M. Caruso, E. Crescenzi, M. F. Tecce, G. Roberti, and A. Colasanti. “Targeted gene transfer in eucaryotic cells by dye-assisted laser optoporation”. *Journal of Photochemistry and Photobiology B: Biology* **36**:1 (Oct. 1996), 41–46.
- [23] H. Schneckenburger, A. Hendinger, R. Sailer, W. S. L. Strauss, and M. Schmitt. “Laser-assisted optoporation of single cells”. *Journal of Biomedical Optics* **7**:3 (July 2002), 410–16.
- [24] A. V. Nikolskaya, V. P. Nikolski, and I. R. Efimov. “Gene printer: laser-scanning targeted transfection of cultured cardiac neonatal rat cells”. *Cell Communication & Adhesion* **13**:4 (2006), 217–222.
- [25] M. L. Torres-Mapa, L. Angus, M. Ploschner, K. Dholakia, and F. J. Gunn-Moore. “Transient transfection of mammalian cells using a violet diode laser”. *Journal of Biomedical Optics* **15**:4 (2010), 041506.
- [26] C. A. Sacchi. “Laser-induced electric breakdown in water”. *Journal of the Optical Society of America B* **8**:2 (Feb. 1991), 337–345.

- [27] L. V. Keldysh. “Ionization in the field of a strong electromagnetic wave”. *Soviet Physics JETP* **20**:5 (1965), 1307–1314.
- [28] P. A. Quinto-Su and V. Venugopalan. “Mechanisms of laser cellular microsurgery”. In: *Laser Manipulation of Cells and Tissues*. Ed. by M. Berns and K. Greulich. Vol. 82. Elsevier Inc., Jan. 2007, 113–151.
- [29] A. A. Davis, M. J. Farrar, N. Nishimura, M. M. Jin, and C. B. Schaffer. “Optoporation and genetic manipulation of cells using femtosecond laser pulses”. *Biophysical Journal* **105**:4 (Aug. 2013), 862–871.
- [30] A. N. Hellman, K. R. Rau, H. H. Yoon, and V. Venugopalan. “Biophysical response to pulsed laser microbeam-induced cell lysis and molecular delivery”. *Journal of Biophotonics* **1**:1 (2008), 24–35.
- [31] M. Terakawa, M. Ogura, S. Sato, H. Wakisaka, H. Ashida, M. Uenoyama, Y. Masaki, and M. Obara. “Gene transfer into mammalian cells by use of a nanosecond pulsed laser-induced stress wave”. *Optics Letters* **29**:11 (2004), 1227–1229.
- [32] C. Yao, R. Rahmanzadeh, E. Endl, Z. Zhang, J. Gerdes, and G. Hüttmann. “Elevation of plasma membrane permeability by laser irradiation of selectively bound nanoparticles”. *Journal of Biomedical Optics* **10**:6 (2005), 064012.
- [33] V. Venugopalan, A. Guerra III, K. Nahen, and A. Vogel. “Role of Laser-Induced Plasma Formation in Pulsed Cellular Microsurgery and Micromanipulation”. *Physical Review Letters* **88**:7 (2002), 078103.
- [34] J. L. Compton, A. N. Hellman, and V. Venugopalan. “Hydrodynamic Determinants of Cell Necrosis and Molecular Delivery Produced by Pulsed Laser Microbeam Irradiation of Adherent Cells”. *Biophysical Journal* **105**:9 (Nov. 2013), 2221–2231.
- [35] Y. Arita, M. L. Torres-Mapa, W. M. Lee, T. Čižmár, P. Campbell, F. J. Gunn-Moore, and K. Dholakia. “Spatially optimized gene transfection by laser-induced

- breakdown of optically trapped nanoparticles”. *Applied Physics Letters* **98**:9 (2011), 093702.
- [36] Y. Arita, M. Ploschner, M. Antkowiak, F. J. Gunn-Moore, and K. Dholakia. “Laser-induced breakdown of an optically trapped gold nanoparticle for single cell transfection”. *Optics Letters* **38**:17 (2013), 3402–3405.
- [37] D. Heinemann, M. Schomaker, S. Kalies, M. Schieck, R. Carlson, H. M. Escobar, T. Ripken, H. Meyer, and A. Heisterkamp. “Gold nanoparticle mediated laser transfection for efficient siRNA mediated gene knock down”. *PLoS ONE* **8**:3 (Jan. 2013), e58604.
- [38] S. Kalies, T. Birr, D. Heinemann, M. Schomaker, T. Ripken, A. Heisterkamp, and H. Meyer. “Enhancement of extracellular molecule uptake in plasmonic laser perforation”. *Journal of Biophotonics* **7**:7 (Jan. 2013), 474–482.
- [39] E. Y. Lukianova-Hleb, D. S. Wagner, M. K. Brenner, and D. O. Lapotko. “Cell-specific transmembrane injection of molecular cargo with gold nanoparticle-generated transient plasmonic nanobubbles”. *Biomaterials* **33**:21 (July 2012), 5441–5450.
- [40] M. Antkowiak, M. L. Torres-Mapa, E. C. Witts, G. B. Miles, K. Dholakia, and F. J. Gunn-Moore. “Fast targeted gene transfection and optogenetic modification of single neurons using femtosecond laser irradiation”. *Scientific Reports* **3**:3281 (Jan. 2013), 1–8.
- [41] L. E. Barrett, J.-Y. Sul, H. Takano, E. J. V. Bockstaele, P. G. Haydon, and J. H. Eberwine. “Region-directed phototransfection reveals the functional significance of a dendritically synthesized transcription factor”. *Nature Methods* **3**:6 (2006), 455–460.
- [42] J.-Y. Sul, C.-w. K. Wu, F. Zeng, J. Jochems, M. T. Lee, T. K. Kim, T. Peritz, P. Buckley, D. J. Cappelleri, M. Maronski, M. Kim, V. Kumar, D. Meaney, J. Kim, and J. Eberwine. “Transcriptome transfer produces a predictable cellular

- phenotype". *Proceedings of the National Academy of Sciences of the United States of America* **106**:18 (May 2009), 7624–7629.
- [43] A. Sharma, L. M. Callahan, J.-Y. Sul, T. K. Kim, L. Barrett, M. Kim, J. M. Powers, H. Federoff, and J. Eberwine. "A neurotoxic phosphoform of Elk-1 associates with inclusions from multiple neurodegenerative diseases". *PLoS ONE* **5**:2 (Jan. 2010), e9002.
- [44] S.-W. D. Tsen, C.-Y. Wu, A. Meneshian, S. I. Pai, C.-F. Hung, and T.-C. Wu. "Femtosecond laser treatment enhances DNA transfection efficiency in vivo". *Journal of Biomedical Science* **16**:36 (Jan. 2009), 1–7.
- [45] E. Zeira, A. Manevitch, A. Khatchatourians, O. Pappo, E. Hyam, M. Darash-Yahana, E. Tavor, A. Honigman, A. Lewis, and E. Galun. "Femtosecond infrared laser - an efficient and safe in vivo gene delivery system for prolonged expression". *Molecular Therapy* **8**:2 (Aug. 2003), 342–350.
- [46] E. Zeira, A. Manevitch, Z. Manevitch, E. Kedar, M. Gropp, N. Daudi, R. Barsuk, M. Harati, H. Yotvat, P. J. Troilo, T. G. Griffiths II, S. J. Pacchione, D. F. Roden, Z. Niu, O. Nussbaum, G. Zamir, O. Papo, I. Hemo, A. Lewis, and E. Galun. "Femtosecond laser: a new intradermal DNA delivery method for efficient, long-term gene expression and genetic immunization". *FASEB journal* **21**:13 (Nov. 2007), 3522–3533.
- [47] A. Uchugonova, K. König, R. Bueckle, A. Iseman, and G. Tempea. "Targeted transfection of stem cells with sub-20 femtosecond laser pulses". *Optics Express* **16**:13 (2008), 9357–9364.
- [48] M. Lei, H. Xu, H. Yang, and B. Yao. "Femtosecond laser-assisted microinjection into living neurons". *Journal of Neuroscience Methods* **174**:2 (2008), 215–218.
- [49] L. Gu and S. K. Mohanty. "Targeted microinjection into cells and retina using optoporation". *Journal of Biomedical Optics* **16**:12 (2011), 128003.

-
- [50] V. Kohli, V. Robles, M. L. Cancela, J. P. Acker, A. J. Waskiewicz, and A. Y. Elezzabi. “An Alternative Method for Delivering Exogenous Material Into Developing Zebrafish Embryos”. *Biotechnology and Bioengineering* **98**:6 (2007), 1230–1241.
- [51] V. Kohli and A. Y. Elezzabi. “Laser surgery of zebrafish (*Danio rerio*) embryos using femtosecond laser pulses: optimal parameters for exogenous material delivery, and the laser’s effect on short- and long-term development”. *BMC Biotechnology* **8**:7 (Jan. 2008), 1–20.
- [52] Y. Hosokawa, H. Ochi, T. Iino, A. Hiraoka, and M. Tanaka. “Photoporation of Biomolecules into Single Cells in Living Vertebrate Embryos Induced by a Femtosecond Laser Amplifier”. *PLoS ONE* **6**:11 (Nov. 2011), e27677.
- [53] M. L. Torres-Mapa, M. Antkowiak, H. Cizmarova, D. E. K. Ferrier, K. Dholakia, and F. J. Gunn-Moore. “Integrated holographic system for all-optical manipulation of developing embryos”. *Biomedical Optics Express* **2**:6 (June 2011), 1564–1575.
- [54] J. Umanzor-Alvarez, E. C. Wade, A. Gifford, K. Nontapot, A. Cruz-Reese, T. Gotoh, J. C. Sible, and G. A. Khodaparast. “Near-infrared laser delivery of nanoparticles to developing embryos: a study of efficacy and viability”. *Biotechnology Journal* **6**:5 (May 2011), 519–524.
- [55] C. McDougall, D. J. Stevenson, C. T. A. Brown, F. J. Gunn-Moore, and K. Dholakia. “Targeted optical injection of gold nanoparticles into single mammalian cells”. *Journal of Biophotonics* **2**:12 (2009), 736–743.
- [56] V. Kohli, J. P. Acker, and A. Y. Elezzabi. “Reversible permeabilization using high-intensity femtosecond laser pulses: Applications to biopreservation”. *Biotechnology and Bioengineering* **92**:7 (Dec. 2005), 889–899.

- [57] B. B. Praveen, D. J. Stevenson, M. Antkowiak, K. Dholakia, and F. J. Gunn-Moore. “Enhancement and optimization of plasmid expression in femtosecond optical transfection”. *Journal of Biophotonics* **4**:4 (Jan. 2011), 229–235.
- [58] X. Tsampoula, V. Garcés-Chávez, M. Comrie, D. J. Stevenson, B. Agate, C. T. A. Brown, F. J. Gunn-Moore, and K. Dholakia. “Femtosecond cellular transfection using a nondiffracting light beam”. *Applied Physics Letters* **91**:5 (2007), 053902.
- [59] D. J. Cappelleri, A. Halasz, J.-Y. Sul, T. K. Kim, J. Eberwine, and V. Kumar. “Towards A Fully Automated High-Throughput Phototransfection System”. *JALA* **15**:4 (Aug. 2010), 329–341.
- [60] C. T. A. Brown, D. J. Stevenson, X. Tsampoula, C. McDougall, A. A. Lagatsky, W. Sibbett, F. J. Gunn-Moore, and K. Dholakia. “Enhanced operation of femtosecond lasers and applications in cell transfection”. *Journal of Biophotonics* **1**:3 (Aug. 2008), 183–199.
- [61] K. Dholakia, P. Reece, and M. Gu. “Optical micromanipulation”. *Chemical Society Reviews* **37** (Jan. 2008), 42–55.
- [62] A. Ashkin. “Acceleration and trapping of particles by radiation pressure”. *Physical Review Letters* **24**:4 (1970), 156–159.
- [63] A. Ashkin, J. M. Dziedzic, J. E. Bjorkholm, and S. Chu. “Observation of a single-beam gradient force trap for dielectric particles”. *Optics Letters* **11**:5 (1986), 288–290.
- [64] A. Ashkin. “Forces of a single-beam gradient laser trap on a dielectric sphere in the ray optics regime”. *Biophysical Journal* **61**:2 (1992), 569–582.
- [65] P. R. T. Jess, V. Garcés-Chávez, D. Smith, M. Mazilu, L. Paterson, A. Riches, C. S. Herrington, W. Sibbett, and K. Dholakia. “Dual beam fibre trap for Raman micro-spectroscopy of single cells”. *Optics Express* **14**:12 (June 2006), 5779–5791.

- [66] G. Thalhammer, R. Steiger, S. Bernet, and M. Ritsch-Marte. “Optical macro-tweezers: trapping of highly motile micro-organisms”. *Journal of Optics* **13**:4 (Apr. 2011), 044024.
- [67] T. T. Perkins. “Optical traps for single molecule biophysics: A primer”. *Laser & Photonics Review* **3**:1-2 (Feb. 2009), 203–220.
- [68] H. Felgner, O. Müller, and M. Schliwa. “Calibration of light forces in optical tweezers”. *Applied Optics* **34**:6 (1995), 977–982.
- [69] M. P. MacDonald, G. C. Spalding, and K. Dholakia. “Microfluidic sorting in an optical lattice”. *Nature* **426**:6965 (2003), 421–424.
- [70] P. Jordan, J. Leach, M. Padgett, P. Blackburn, N. Isaacs, M. Goksör, D. Hanstorp, A. Wright, J. Girkin, and J. Cooper. “Creating permanent 3D arrangements of isolated cells using holographic optical tweezers”. *Lab on a Chip* **5**:11 (2005), 1224–1228.
- [71] U. Mirsaidov, J. Scrimgeour, W. Timp, K. Beck, M. Mir, P. Matsudaira, and G. Timp. “Live cell lithography: using optical tweezers to create synthetic tissue”. *Lab on a Chip* **8**:12 (2008), 2174–2181.
- [72] J. Arlt, V. Garcés-Chávez, W. Sibbett, and K. Dholakia. “Optical micromanipulation using a Bessel light beam”. *Optics Communications* **197**:4-6 (2001), 239–245.
- [73] D. McGloin and K. Dholakia. “Bessel beams: Diffraction in a new light”. *Contemporary Physics* **46**:1 (Jan. 2005), 15–28.
- [74] M. E. J. Friese, T. A. Nieminen, N. R. Heckenberg, and H. Rubinsztein-Dunlop. “Optical alignment and spinning of laser-trapped microscopic particles”. *Nature* **395**:6691 (1998), 348–350.

- [75] A. T. O’Neil and M. J. Padgett. “Three-dimensional optical confinement of micron-sized metal particles and the decoupling of the spin and orbital angular momentum within an optical spanner”. *Optics Communications* **185**:1-3 (2000), 139–143.
- [76] G. Lazarev, A. Hermerschmidt, S. Kruger, and S. Osten. “LCOS Spatial Light Modulators: Trends and Applications”. In: *Optical Imaging and Metrology: Advanced Technologies*. 2012, 1–30.
- [77] J. E. Curtis, B. A. Koss, and D. G. Grier. “Dynamic holographic optical tweezers”. *Optics Communications* **207**:1-6 (2002), 169–175.
- [78] M.-C. Zhong, X.-B. Wei, J.-H. Zhou, Z.-Q. Wang, and Y.-M. Li. “Trapping red blood cells in living animals using optical tweezers”. *Nature Communications* **4**:1768 (2013), 1–7.
- [79] A. Ashkin and J. M. Dziedzic. “Internal cell manipulation using infrared laser traps”. *Proceedings of the National Academy of Sciences of the United States of America* **86**:20 (Oct. 1989), 7914–7918.
- [80] U. Bockelmann, P. Thomen, B. Essevaz-Roulet, V. Viasnoff, and F. Heslot. “Unzipping DNA with Optical Tweezers: High Sequence Sensitivity and Force Flips”. *Biophysical Journal* **82**:3 (2002), 1537–1553.
- [81] J. M. Tam, C. E. Castro, R. J. W. Heath, M. L. Cardenas, R. J. Xavier, M. J. Lang, and J. M. Vyas. “Control and manipulation of pathogens with an optical trap for live cell imaging of intercellular interactions”. *PLoS ONE* **5**:12 (Jan. 2010), e15215.
- [82] G. P. McNerney, W. Hübner, B. K. Chen, and T. Huser. “Manipulating CD4+ T cells by optical tweezers for the initiation of cell-cell transfer of HIV-1”. *Journal of Biophotonics* **3**:4 (Apr. 2010), 216–223.

- [83] A. Hoffmann, G. Meyer zu Hörste, G. Pilarczyk, S. Monajembashi, V. Uhl, and K. O. Greulich. “Optical tweezers for confocal microscopy”. *Applied Physics B* **71**:5 (2000), 747–753.
- [84] M. Goksör, J. Enger, and D. Hanstorp. “Optical manipulation in combination with multiphoton microscopy for single-cell studies”. *Applied Optics* **43**:25 (2004), 4831–4837.
- [85] E. Fällman and O. Axner. “Design for fully steerable dual-trap optical tweezers”. *Applied Optics* **36**:10 (Apr. 1997), 2107–2113.
- [86] I. Heller, G. Sitters, O. D. Broekmans, G. Farge, C. Menges, W. Wende, S. W. Hell, E. J. G. Peterman, and G. J. L. Wuite. “STED nanoscopy combined with optical tweezers reveals protein dynamics on densely covered DNA”. *Nature Methods* **10**:9 (2013), 910–916.
- [87] E. Eriksson, D. Engström, J. Scrimgeour, and M. Goksör. “Automated focusing of nuclei for time lapse experiments on single cells using holographic optical tweezers”. *Optics Express* **17**:7 (2009), 5585–5594.
- [88] D. Wolfson, M. Steck, M. Persson, G. McNerney, A. Popovich, M. Goksör, and T. Huser. “Rapid 3D fluorescence imaging of individual optically trapped living immune cells”. *Journal of Biophotonics* (Jan. 2014), 1–9.
- [89] M. Yevnin, D. Kasimov, Y. Gluckman, Y. Ebenstein, and Y. Roichman. “Independent and simultaneous three-dimensional optical trapping and imaging”. *Biomedical Optics Express* **4**:10 (Jan. 2013), 2087–2094.
- [90] C. Liberale, P. Minzioni, F. Bragheri, F. De Angelis, E. Di Fabrizio, and I. Cristiani. “Miniaturized all-fibre probe for three-dimensional optical trapping and manipulation”. *Nature Photonics* **1**:12 (Nov. 2007), 723–727.
- [91] M. Waleed, S.-U. Hwang, J.-D. Kim, I. Shabbir, S.-M. Shin, and Y.-G. Lee. “Single-cell optoporation and transfection using femtosecond laser and optical tweezers”. *Biomedical Optics Express* **4**:9 (Aug. 2013), 1533–1548.

-
- [92] *Organelles in live cells*. July 2014. URL: www.lima.ohio-state.edu/biology/archive/organel.html.
- [93] H Lodish, A Berk, and S. Zipursky. “The Dynamic Plant Cell Wall”. In: *Molecular Cell Biology*. 4th ed. New York: W. H. Freeman, 2000. Chap. 22.5.
- [94] P. H. Raven, R. F. Evert, and S. E. Eichhorn. *Biology of Plants*. 5th ed. Worth Publishers, 1992, 14–73.
- [95] B. B. Buchanan, W. Gruissem, and R. L. Jones. *Biochemistry and Molecular Biology of Plants*. American Society of Plant Physiologists, 2000.
- [96] *Worldometers.info*. July 2014. URL: www.worldometers.info/world-population/.
- [97] J. E. Mayer, W. H. Pfeiffer, and P. Beyer. “Biofortified crops to alleviate micronutrient malnutrition”. *Current Opinion in Plant Biology* **11**:2 (Apr. 2008), 166–170.
- [98] A. Krichevsky, B. Meyers, A. Vainstein, P. Maliga, and V. Citovsky. “Autoluminescent plants”. *PLoS ONE* **5**:11 (Jan. 2010), e15461.
- [99] P. Kotrba, J. Najmanova, T. Macek, T. Ruml, and M. Mackova. “Genetically modified plants in phytoremediation of heavy metal and metalloid soil and sediment pollution”. *Biotechnology Advances* **27**:6 (2009), 799–810.
- [100] J. K.-C. Ma, P. M. W. Drake, and P. Christou. “The production of recombinant pharmaceutical proteins in plants”. *Nature Reviews. Genetics* **4**:10 (Oct. 2003), 794–805.
- [101] P. G. Lemaux. “Genetically Engineered Plants and Foods: A Scientist’s Analysis of the Issues (Part I)”. *Annual Review of Plant Biology* **59**:1 (Jan. 2008), 771–812.
- [102] M. C. Chang. “Harnessing energy from plant biomass”. *Current Opinion in Chemical Biology* **11**:6 (Dec. 2007), 677–684.
- [103] P. L. Bhalla and M. B. Singh. “Agrobacterium-mediated transformation of *Brassica napus* and *Brassica oleracea*”. *Nature Protocols* **3**:2 (2008), 181–189.

-
- [104] M. Hanin and J. Paszkowski. “Plant genome modification by homologous recombination”. *Current Opinion in Plant Biology* **6**:2 (Apr. 2003), 157–162.
- [105] T. Tzfira and V. Citovsky. “Agrobacterium-mediated genetic transformation of plants: biology and biotechnology”. *Current Opinion in Biotechnology* **17**:2 (Apr. 2006), 147–154.
- [106] S. Dai, P. Zheng, P. Marmey, S. Zhang, W. Tian, S. Chen, R. N. Beachy, and C. Fauquet. “Comparative analysis of transgenic rice plants obtained by Agrobacterium-mediated transformation and particle bombardment”. *Molecular Breeding* **7**:1 (2001), 25–33.
- [107] J. C. Sanford, T. M. Klein, E. D. Wolf, and N. Allen. “Delivery of substances into cells and tissues using a particle bombardment process”. *Particulate Science and Technology* **5**:1 (1987), 27–37.
- [108] T. Yamashita, A. Iida, and H. Morikawa. “Evidence That More than 90% of beta-Glucuronidase-Expressing Cells after Particle Bombardment Directly Receive the Foreign Gene in their Nucleus”. *Plant Physiology* **97**:2 (Oct. 1991), 829–831.
- [109] M. Uchida, X. W. Li, P. Mertens, and H. O. Alpar. “Transfection by particle bombardment: Delivery of plasmid DNA into mammalian cells using gene gun”. *Biochimica et Biophysica Acta* **1790**:8 (Aug. 2009), 754–764.
- [110] G. An. “High efficiency transformation of cultured tobacco cells”. *Plant Physiology* **79**:2 (Oct. 1985), 568–570.
- [111] J. A. Saunders, C. H. Lin, B. H. Hou, J. Cheng, N. Tsengwa, J. J. Lin, C. R. Smith, M. S. McIntosh, and S. Van Wert. “Rapid Optimization of Electroporation Conditions for Plant Cells, Protoplasts, and Pollen”. *Molecular Biotechnology* **3**:3 (1995), 181–190.
- [112] F.-S. Wu and T.-Y. Feng. “Delivery of plasmid DNA into intact plant cells by electroporation of plasmolyzed cells”. *Plant Cell Reports* **18**:5 (Jan. 1999), 381–386.

- [113] K. D'Halluin, E. Bonne, M. Bossut, M. De Beuckeleer, and J. Leemans. "Transgenic maize plants by tissue electroporation". *The Plant Cell* **4**:12 (Dec. 1992), 1495–1505.
- [114] H. Matsuoka, Y. Yamada, K. Matsuoka, and M. Saito. "High Throughput Microinjection Technology for the Single-Cell Analysis of BY-2 in Vivo". In: *Tobacco BY-2 Cells: From Cellular Dynamics to Omics*. Ed. by T Nagata, K Matsuoka, and D Inzé. Vol. 58. Springer-Verlag Berlin Heidelberg, 2006, 339–346.
- [115] D. R. Gallie, W. J. Lucas, and V. Walbot. "Visualizing mRNA expression in plant protoplasts: factors influencing efficient mRNA uptake and translation". *The Plant Cell* **1**:3 (Mar. 1989), 301–311.
- [116] C. A. Newell. "Plant transformation technology. Developments and applications". *Molecular Biotechnology* **16**:1 (Sept. 2000), 53–65.
- [117] H. D. Jones and C. A. Sparks. "Stable Transformation of Plants". In: *Methods in Molecular Biology, Plant Genomics*. Ed. by J. Gustafson, P. Langridge, and D. J. Somers. vol. 513. Vol. 513. Methods in Molecular Biology. Totowa, NJ: Humana Press, 2009. Chap. 7, 111–130.
- [118] H. D. Jones, A. Doherty, and C. A. Sparks. "Transient transformation of plants". In: *Methods in Molecular Biology, Plant Genomics*. Ed. by J. Gustafson, P. Langridge, and D. J. Somers. vol. 513. Vol. 513. Methods in Molecular Biology. Totowa, NJ: Humana Press, 2009. Chap. 8, 131–152.
- [119] S.-I. Kurata, M. Tsukakoshi, T. Kasuya, and Y. Ikawa. "The laser method for efficient introduction of foreign DNA into cultured cells". *Experimental Cell Research* **162**:2 (1986), 372–378.
- [120] W.-H. Zhang, Z. Rengel, and J. Kuo. "Determination of intracellular Ca^{2+} in cells of intact wheat roots: loading of acetoxymethyl ester of Fluo-3 under low temperature". *The Plant Journal* **15**:1 (1998), 147–151.

- [121] A. O. Noueiry, W. J. Lucas, and R. L. Gilbertson. “Two proteins of a plant DNA virus coordinate nuclear and plasmodesmal transport”. *Cell* **76**:5 (Mar. 1994), 925–932.
- [122] D. T. Clarkson, C. Brownlee, and S. M. Ayling. “Cytoplasmic calcium measurements in intact higher plant cells: results from fluorescence ratio imaging of fura-2”. *Journal of Cell Science* **91**:1 (1988), 71–80.
- [123] A. T. Silva, A. Nguyen, C. Ye, J. Verchot, and J. H. Moon. “Conjugated polymer nanoparticles for effective siRNA delivery to tobacco BY-2 protoplasts”. *BMC Plant Biology* **10**:291 (Jan. 2010), 1–14.
- [124] M. Chang, J. C. Chou, and H. J. Lee. “Cellular Internalization of Fluorescent Proteins via Arginine-rich Intracellular Delivery Peptide in Plant Cells”. *Plant Cell Physiology* **46**:3 (2005), 482–488.
- [125] J. H. F. Bothwell, C. Brownlee, A. M. Hetherington, C. K.-Y. Ng, G. L. Wheeler, and M. R. McAinsh. “Biolistic delivery of Ca²⁺ dyes into plant and algal cells”. *The Plant Journal* **46**:2 (Apr. 2006), 327–335.
- [126] F. Hoffmann. “Laser microbeams for the manipulation of plant cells and subcellular structures”. *Plant Science* **113**:1 (Jan. 1996), 1–11.
- [127] J. C. Sanford. “Pollen studies using a laser microbeam”. *Pollen: Biology and Implications for Plant Breeding*. (1983). Ed. by E. O. D.L. Mulcahy, 107–115.
- [128] T. M. Klein, E. D. Wolf, R. Wu, and J. C. Sanford. “High-velocity microprojectiles for delivering nucleic acids into living cells”. *Nature* **327**:6117 (1987), 70–73.
- [129] M Broglia. “Lasers in Plant Genetic-Engineering”. In: *Basic and Applied Histochemistry*. Vol. 32. 3. 1988, 342.
- [130] G Weber, S Monajembashi, K. O. Greulich, and J Wolfrum. “Uptake Of DNA In chloroplasts Of Brassica-napus (L) by means of a microfocused laser-beam”. In: *European Journal of Cell Biology*. Vol. 43. 1987, 63.

- [131] S. Ruf, D. Karcher, and R. Bock. “Determining the transgene containment level provided by chloroplast transformation”. *Proceedings of the National Academy of Sciences of the United States of America* **104**:17 (2007), 6998–7002.
- [132] G. Weber, S. Monajembashi, K. O. Greulich, and J. Wolfrum. “Uptake of DNA in chloroplasts of *Brassica napus* (L.) facilitated by a UV-laser microbeam”. *European Journal of Cell Biology* **49**:1 (1989), 73–79.
- [133] G. Weber, S. Monajembashi, J. Wolfrum, and K. O. Greulich. “A laser microbeam as a tool to introduce genes into cells and organelles of higher plants”. *Berichte der Bunsengesellschaft für Physikalische Chemie* **93**:3 (1989), 252–254.
- [134] G. Weber, S. Monajembashi, K. O. Greulich, and J. Wolfrum. “Genetic changes induced in higher plants by a UV laser microbeam”. *Israel Journal of Botany* **40**:2 (1991), 115–122.
- [135] K. D. Birnbaum and A. Sanchez Alvarado. “Slicing across Kingdoms: Regeneration in Plants and Animals”. *Cell* **132**:4 (2008), 697–710.
- [136] G. Weber, S. Monajembashi, K. O. Greulich, and J. Wolfrum. “Microperforation of Plant Tissue with a UV Laser Microbeam and Injection of DNA into Cells”. *Naturwissenschaften* **75**:1 (1988), 1–2.
- [137] G. Weber, S. Monajembashi, J. Wolfrum, and K. O. Greulich. “Genetic changes induced in higher plant cells by a laser microbeam”. *Physiologia Plantarum* **79**:1 (May 1990), 190–193.
- [138] Z. Chen, L. Wang, H. Lan, L. Zhang, B. Dang, and Y. Tian. “Obtaining new sclerotia-resistant lines of rape by genetic engineering”. In: *Proceedings of the 10th International Rapeseed Congress*. 1999, 1–4.
- [139] Y. Guo, H. Liang, and M. W. Berns. “Laser-mediated gene transfer in rice”. *Physiologia Plantarum* **93**:1 (1995), 19–24.

- [140] Y. Badr, A. Bahieldin, M. A. Aziz, M. A. Yehia, A. A. El-Magd, and M. A. Madkour. “A modified protocol for laser-mediated gene transfer in wheat”. *Arab Journal of Biotechnology* **7**:2 (2004), 299–304.
- [141] Y. A. Badr, M. A. Kereim, M. A. Yehia, O. O. Fouad, and A. Bahieldin. “Production of fertile transgenic wheat plants by laser micropuncture”. *Photochemical & Photobiological Sciences* **4**:10 (Oct. 2005), 803–807.
- [142] I. Turovets, A. Lewis, D. Palanker, H. Gilo, A. Vilenz, J. C. Broder, and S. Lewis. “Permeabilizing Millions of Cells with Single Pulses of an Excimer Laser”. *Biotechniques* **15**:6 (1993), 2–5.
- [143] S. Kajiyama, T. Shoji, S. Okuda, Y. Izumi, E. I. Fukusaki, and A. Kobayashi. “A novel microsurgery method for intact plant tissue at the single cell level using ArF excimer laser microprojection”. *Biotechnology and Bioengineering* **93**:2 (Feb. 2006), 325–331.
- [144] C. S. Buer, K. T. Gahagan, G. A. Swartzlander, and P. J. Weathers. “Insertion of Microscopic Objects through Plant Cell Walls Using Laser Microsurgery”. *Biotechnology and Bioengineering* **60**:3 (1998), 348–355.
- [145] S. Kajiyama, F. Inoue, Y. Yoshikawa, T. Shoji, E. Fukusaki, and A. Kobayashi. “Novel plant transformation system by gene-coated gold particle introduction into specific cell using ArF excimer laser”. *Plant Biotechnology* **24**:3 (2007), 315–320.
- [146] S. Kajiyama, B. Joseph, F. Inoue, M. Shimamura, E. Fukusaki, K. Tomizawa, and A. Kobayashi. “Transient gene expression in guard cell chloroplasts of tobacco using ArF excimer laser microablation”. *Journal of Bioscience and Bioengineering* **106**:2 (Aug. 2008), 194–198.
- [147] H. Schinkel, P. Jacobs, S. Schillberg, and M. Wehner. “Infrared picosecond laser for perforation of single plant cells”. *Biotechnology and Bioengineering* **99**:1 (2008), 244–248.

- [148] T. B. Krasieva, C. F. Chapman, V. J. LaMorte, V. Venugopalan, M. W. Berns, and B. J. Tromberg. “Cell permeabilization and molecular transport by laser microirradiation”. In: *Cell permeabilization and molecular transport by laser microirradiation*. Ed. by D. L. Farkas, R. C. Leif, and B. J. Tromberg. Vol. 3260. Apr. 1998, 38–44.
- [149] U. K. Tirlapur and K. König. “Near-infrared femtosecond laser pulses as a novel non-invasive means for dye-permeation and 3D imaging of localised dye-coupling in the Arabidopsis root meristem”. *The Plant Journal* **20**:3 (Nov. 1999), 363–370.
- [150] C. M. Duckett, K. J. Oparka, D. A. M. Prior, L. Dolan, and K. Roberts. “Dye-coupling in the root epidermis of Arabidopsis is progressively reduced during development”. *Development* **120**:11 (1994), 3247–3255.
- [151] M. L. LeBlanc, T. R. Merritt, J. McMillan, J. H. Westwood, and G. A. Khodaparast. “Optoperforation of single, intact Arabidopsis cells for uptake of extracellular dye-conjugated dextran”. *Optics Express* **21**:12 (June 2013), 14662–14673.
- [152] S. C. Jeoung, M. S. Sidhu, and J. S. Yahng. “Application of Ultrafast Laser Optoperforation for Plant Pollen Walls and Endothelial Cell Membranes”. In: *Advances in Lasers and Electro Optics*. Ed. by N. C. Cartaxo and Adolfo. April. InTechOpen, 2010, 809–838.
- [153] Y. K. Baik, W. J. Jeong, Y. I. Park, K. S. Soh, and S. C. Jeoung. “Lilium Pollen Opto-perforation by ultrashort laser pulse”. In: *Pacific Rim Conference on Lasers and Electro-Optics, CLEO - Technical Digest*. 2007, 1–2.
- [154] J. A. Saunders and B. F. Matthew. “Pollen Electrotransformation in Tobacco”. In: *Methods in Molecular Biology*. Vol. 55. 1995, 81–88.

-
- [155] M. Wehner, P. Jacobs, D. Esser, H. Schinkel, and S. Schillberg. “Laser-mediated perforation of plant cells”. In: *Therapeutic Laser Applications and Laser-Tissue Interactions III*. Vol. 6632. 2007, 66321W–1–9.
- [156] W. Tang, D. A. Weidner, B. Y. Hu, R. J. Newton, and X. H. Hu. “Efficient delivery of small interfering RNA to plant cells by a nanosecond pulsed laser-induced stress wave for posttranscriptional gene silencing”. *Plant Science* **171**:3 (Sept. 2006), 375–381.
- [157] K. Awazu, T. Kinpara, and E. Tamiya. “IR-FEL-induced green fluorescence protein (GFP) gene transfer into plant cell”. *Nuclear Instruments and Methods in Physics Research A* **483**:1-2 (2002), 571–575.
- [158] M. Ferrando and W. E. L. Spiess. “Cellular response of plant tissue during the osmotic treatment with sucrose, maltose, and trehalose solutions”. *Journal of Food Engineering* **49**:2-3 (2001), 115–127.
- [159] G. Weber, M. Stanke, S. Monajembashi, and K. O. Greulich. “Microdissection of chromosomes of *Brassica napus* at 4000 x magnification with a UV laser microbeam and stable transformation of higher plants”. In: *ISPMB Congress Tucson*. 1991.
- [160] L. L. Wolfenbarger. “The Ecological Risks and Benefits of Genetically Engineered Plants”. *Science* **290**:5499 (Dec. 2000), 2088–2093.
- [161] N. M. Kerk, T. Ceserani, S. L. Tausta, I. M. Sussex, and T. M. Nelson. “Laser Capture Microdissection of Cells from Plant Tissues”. *Plant Physiology* **132**:1 (2003), 27–35.
- [162] R. Wiegand, G. Weber, K. Zimmermann, S. Monajembashi, J. Wolfrum, and K. O. Greulich. “Laser-induced fusion of mammalian cells and plant protoplasts”. *Journal of Cell Science* **88**:Pt 2 (Sept. 1987), 145–149.

- [163] K. C. Goodbody, C. J. Venverloo, and C. W. Lloyd. "Laser microsurgery demonstrates that cytoplasmic strands anchoring the nucleus across the vacuole of premitotic plant cells are under tension. Implications for division plane alignment". *Development* **113**:3 (1991), 931–939.
- [164] U. K. Tirlapur and K. König. "Femtosecond near-infrared laser pulses as a versatile non-invasive tool for intra-tissue nanoprocessing in plants without compromising viability". *The Plant Journal* **31**:3 (Aug. 2002), 365–374.
- [165] A. R. Taylor and C. Brownlee. "Localized Patch Clamping of Plasma Membrane of Polarized Plant Cell". *Plant Physiology* **99**:4 (1992), 1686–1688.
- [166] A. Kurkdjian, G. Leitz, P. Manigault, A. Harim, and K. O. Greulich. "Non-enzymatic access to the plasma membrane of Medicago root hairs by laser microsurgery". *Journal of Cell Science* **105**:1 (1993), 263–268.
- [167] A. H. De Boer, B. Van Duijn, P. Giesberg, L. Wegner, G. Obermeyer, K. Kohler, and K. W. Linz. "Laser microsurgery: a versatile tool in plant (electro) physiology". *Protoplasma* **178**:1-2 (Mar. 1994), 1–10.
- [168] F. Berger and C. Brownlee. "Physiology and development of protoplasts obtained from Fucus embryos using laser microsurgery". *Protoplasma* **186**:1-2 (1995), 63–71.
- [169] G. H. Henriksen, A. R. Taylor, C. Brownlee, and S. M. Assmann. "Laser microsurgery of higher plant cell walls permits patch-clamp access". *Plant Physiology* **110**:4 (Jan. 1996), 1063–1068.
- [170] G. H. Henriksen and S. M. Assmann. "Laser-assisted patch clamping: a methodology". *Pflügers Archiv: European Journal of Physiology* **433**:6 (Apr. 1997), 832–841.
- [171] C. A. Mitchell, S. Kalies, T. Čížmár, A. Heisterkamp, L. Torrance, A. G. Roberts, F. J. Gunn-Moore, and K. Dholakia. "Femtosecond Optoinjection of Intact To-

- bacco BY-2 Cells Using a Reconfigurable Photoporation Platform”. *PLoS ONE* **8**:11 (Jan. 2013), e79235.
- [172] A. P. Rudhall, M. Antkowiak, X. Tsampoula, M. Mazilu, N. K. Metzger, F. J. Gunn-Moore, and K. Dholakia. “Exploring the ultrashort pulse laser parameter space for membrane permeabilisation in mammalian cells”. *Scientific Reports* **2**:858 (Nov. 2012), 1–5.
- [173] A. E. Siegman. *Lasers*. University Science Books, 1986, 669.
- [174] J. Durnin and J. J. Miceli. “Diffraction-Free beams”. *Physical Review Letters* **58**:15 (1987), 1499–1501.
- [175] R. M. Herman and T. A. Wiggins. “Production and uses of diffractionless beams”. *Journal of the Optical Society of America A* **8**:6 (June 1991), 932.
- [176] J. Arlt, K. Dholakia, J. Sonesson, and E. M. Wright. “Optical dipole traps and atomic waveguides based on Bessel light beams”. *Physical Review A* **63**:6 (May 2001), 063602.
- [177] Z. Bouchal, J. Wagner, and M. Chlup. “Self-reconstruction of a distorted non-diffracting beam”. *Optics Communications* **151**:4-6 (1998), 207–211.
- [178] V. Garcés-Chávez, D. McGloin, H. Melville, W. Sibbett, and K. Dholakia. “Simultaneous micromanipulation in multiple planes using a self-reconstructing light beam”. *Nature* **419**:6903 (2002), 145–147.
- [179] F. O. Fahrbach, P. Simon, and A. Rohrbach. “Microscopy with self-reconstructing beams”. *Nature Photonics* **4**:11 (2010), 780–785.
- [180] C. Blatter, B. Grajciar, C. M. Eigenwillig, W. Wieser, B. R. Biedermann, R. Huber, and R. A. Leitgeb. “Extended focus high-speed swept source OCT with self-reconstructive illumination”. *Optics Express* **19**:13 (2011), 12141–12155.
- [181] A. E. Siegman. “How to (Maybe) Measure Laser Beam Quality”. In: *Optical Society of America Annual Meeting*. Vol. 17. October 1997. 1998, 184–199.

- [182] M. Mazilu, D. J. Stevenson, F. J. Gunn-Moore, and K. Dholakia. "Light beats the spread: "Non-diffracting" beams". *Laser & Photonics Reviews* **4**:4 (Sept. 2010), 529–547.
- [183] M. Antkowiak, M. L. Torres-Mapa, D. J. Stevenson, K. Dholakia, and F. J. Gunn-Moore. "Femtosecond optical transfection of individual mammalian cells". *Nature Protocols* **8**:6 (2013), 1216–1233.
- [184] O. Brzobohatý, T. Čižmár, and P. Zemánek. "High quality quasi-Bessel beam generated by round-tip axicon". *Optics Express* **16**:17 (Aug. 2008), 12688–12700.
- [185] R. Grunwald, U. Griebner, F. Tschirschwitz, E. T. Nibbering, T. Elsaesser, V. Kebbel, H. J. Hartmann, and W. Jüptner. "Generation of femtosecond Bessel beams with microaxicon arrays". *Optics Letters* **25**:13 (July 2000), 981–983.
- [186] S. Akturk, X. Gu, P. Bown, and R. Trebino. "Spatio-temporal couplings in ultrashort laser pulses". *Journal of Optics* **12**:9 (Sept. 2010), 093001.
- [187] P. Fischer, C. Brown, J. Morris, C. López-Mariscal, E. Wright, W. Sibbett, and K. Dholakia. "White light propagation invariant beams". *Optics Express* **13**:17 (Aug. 2005), 6657–6666.
- [188] F. Brandizzi, S. Irons, A. Kearns, and C. Hawes. "BY-2 cells: culture and transformation for live cell imaging". *Current Protocols in Cell Biology* (Aug. 2003), 1.7.1–16.
- [189] T. Nagata, Y. Nemoto, and S. Hasezawa. "Tobacco BY-2 Cell Line as the "HeLa" Cell in the Cell Biology of Higher Plants". In: *International Review of Cytology*. Ed. by K. W. Jeon and M. Friedlander. Vol. 132. Elsevier Inc., 1992, 1–30.
- [190] I. Takebe. "When I Encountered Tobacco BY-2 Cells!" In: *Biotechnology in Agriculture and Forestry*. Ed. by T. Nagata, S. Hasezawa, and D. Inzé. 53rd ed. Vol. 53. Heidelberg: Springer Berlin Heidelberg, 2004, 1–6.
- [191] D. N. Geelen and D. G. Inze. "A Bright Future for the Bright Yellow-2 Cell Culture". *Plant Physiology* **127**:4 (2001), 1375–1379.

- [192] C. A. Schneider, W. S. Rasband, and K. W. Eliceiri. “NIH Image to ImageJ: 25 years of image analysis”. *Nature Methods* **9**:7 (June 2012), 671–675.
- [193] J. Goudriaan. “A Family of Saturation Type Curves, Especially in Relation to Photosynthesis”. *Annals of Botany* **43**:6 (1979), 783–785.
- [194] F.-S. Wu and A. B. Cahoon. “Plasmolysis facilitates the accumulation of protein and DNA into extra-plasmalemma spaces of intact plant cells”. *Plant Science* **104**:2 (1995), 201–214.
- [195] U. K. Tirlapur and K. König. “Targeted transfection by femtosecond laser”. *Nature* **418**:6895 (July 2002), 290–291.
- [196] D. J. Stevenson, B. Agate, X. Tsampoula, P. Fischer, C. T. A. Brown, W. Sibbett, A. Riches, F. J. Gunn-Moore, and K. Dholakia. “Femtosecond optical transfection of cells: viability and efficiency”. *Optics Express* **14**:16 (Aug. 2006), 7125–7133.
- [197] C. M. Rounds, E. Lubeck, P. K. Hepler, and L. J. Winship. “Propidium iodide competes with Ca^{2+} to label pectin in pollen tubes and Arabidopsis root hairs”. *Plant Physiology* **157**:1 (Sept. 2011), 175–187.
- [198] W. Stiles. *Principles of Plant Physiology*. 2nd ed. New Dehli: Discovery Publishing House, 1994, 64.
- [199] K. A. Granath. “Solution properties of branched dextrans”. *Journal of Colloid Science* **13**:4 (1958), 308–328.
- [200] J. A. M. Smit, J. A. P. P. Van Dijk, M. G. Mennen, and M. Daoud. “Polymer size exponents of branched dextrans”. *Macromolecules* **25**:13 (June 1992), 3585–3590.
- [201] S. Okuda, H. Tsutsui, K. Shiina, S. Sprunck, H. Takeuchi, R. Yui, R. D. Kasahara, Y. Hamamura, A. Mizukami, D. Susaki, N. Kawano, T. Sakakibara, S. Namiki, K. Itoh, K. Otsuka, M. Matsuzaki, H. Nozaki, T. Kuroiwa, A. Nakano, M. M. Kanaoka, T. Dresselhaus, N. Sasaki, and T. Higashiyama. “Defensin-like

- polypeptide LUREs are pollen tube attractants secreted from synergid cells”. *Nature* **458**:7236 (Mar. 2009), 357–361.
- [202] J. Tukey. *Exploratory data analysis*. Addison-Wesley, 1977.
- [203] J. C. Carrington and D. D. Freed. “Cap-independent enhancement of translation by a plant potyvirus 5' nontranslated region”. *Journal of Virology* **64**:4 (1990), 1590–1597.
- [204] J. A. Lindbo. “TRBO: a high-efficiency tobacco mosaic virus RNA-based over-expression vector”. *Plant Physiology* **145**:4 (Dec. 2007), 1232–1240.
- [205] K. M. Wagstaff, J. Y. Fan, M. A. De Jesus, D. J. Tremethick, and D. A. Jans. “Efficient gene delivery using reconstituted chromatin enhanced for nuclear targeting”. *FASEB journal* **22**:7 (July 2008), 2232–2242.
- [206] J. R. Zupan, V. Citovsky, and P. Zambryski. “Agrobacterium VirE2 protein mediates nuclear uptake of single-stranded DNA in plant cells”. *Proceedings of the National Academy of Sciences of the United States of America* **93**:6 (Mar. 1996), 2392–2397.
- [207] S. Gopalakrishna, P. Singh, and N.-K. Singh. “Enhanced transformation of plant cells following co-bombardment of VirE2 protein of *Agrobacterium tumefaciens* with DNA substrate”. *Current Science* **85**:9 (2003), 1343–1347.
- [208] R. Hunold, R. Bronner, and G. Hahne. “Early events in microprojectile bombardment: cell viability and particle location”. *The Plant Journal* **5**:4 (Apr. 1994), 593–604.
- [209] H. Matsuoka, T. Komazaki, Y. Mukai, M. Shibusawa, H. Akane, A. Chaki, N. Uetake, and M. Saito. “High throughput easy microinjection with a single-cell manipulation supporting robot”. *Journal of Biotechnology* **116**:2 (Mar. 2005), 185–194.
- [210] T. Čižmár, M. Mazilu, and K. Dholakia. “In situ wavefront correction and its application to micromanipulation”. *Nature Photonics* **4**:6 (2010), 388–394.

- [211] O. Baron-Epel, P. K. Gharyal, and M. Schindler. “Pectins as mediators of wall porosity in soybean cells”. *Planta* **175**:3 (Sept. 1988), 389–395.
- [212] J. Summerton and D. Weller. “Morpholino antisense oligomers: Design, preparation and properties”. *Antisense & Nucleic Acid Drug Development* **7**:3 (1997), 187–195.
- [213] S. Kalies, D. Heinemann, M. Schomaker, H. M. Escobar, A. Heisterkamp, T. Ripken, and H. Meyer. “Plasmonic laser treatment for Morpholino oligomer delivery in antisense applications”. *Journal of Biophotonics* (2013), 1–9.
- [214] R. Paschotta. *Field Guide to Laser Pulse Generation*. Bellingham, WA: SPIE Press, 2008.
- [215] N. Ma, F. J. Gunn-Moore, and K. Dholakia. “Optical transfection using an endoscope-like system”. *Journal of Biomedical Optics* **16**:2 (Mar. 2011), 028002.
- [216] S. Tang, T. B. Krasieva, Z. Chen, G. Tempea, and B. J. Tromberg. “Effect of pulse duration on two-photon excited fluorescence and second harmonic generation in nonlinear optical microscopy”. *Journal of Biomedical Optics* **11**:2 (2006), 020501.
- [217] A. Uchugonova, M. Lessel, S. Nietzsche, C. Zeitz, K. Jacobs, C. Lemke, and K. König. “Nanosurgery of cells and chromosomes using near-infrared twelve-femtosecond laser pulses”. *Journal of Biomedical Optics* **17**:10 (Oct. 2012), 101502.
- [218] C. Rulliere. *Femtosecond Laser Pulses: Principles and Experiments*. Springer Science+Business Media, 2007.
- [219] J.-C. Diels and W. Rudolph. *Ultrashort Laser Pulse Phenomena*. Ed. by P. F. Liao and P. Kelley. 2nd ed. Academic Press, 2006.
- [220] A. Monmayrant, S. Weber, and B. Chatel. “A newcomer’s guide to ultrashort pulse shaping and characterization”. *Journal of Physics B* **43**:10 (2010), 103001.

- [221] M. Wollenhaupt, A. Assion, and T. Baumert. “Femtosecond Laser Pulses: Linear Properties, Manipulation, Generation and Measurement”. In: *Springer Handbook of Lasers and Optics*. Ed. by F. Trager. Springer Science+Business Media, 2007. Chap. Part C, 937–983.
- [222] C. Rulliere. *Femtosecond Laser Pulses*. 2nd ed. Springer New York, 2005.
- [223] A. Baltuska, Z. Wei, M. S. Pshenichnikov, and D. A. Wiersma. “Optical pulse compression to 5 fs at a 1-MHz repetition rate”. *Optics Letters* **22**:2 (Jan. 1997), 102–104.
- [224] R. Trebino, K. W. Delong, D. N. Fittinghoff, J. N. Sweetser, M. A. Krumbugel, B. A. Richman, and D. J. Kane. “Measuring ultrashort laser pulses in the time-frequency domain using frequency-resolved optical gating”. *Review of Scientific Instruments* **68**:9 (1997), 3277–3295.
- [225] A. M. Weiner, D. E. Leaird, J. S. Patel, and J. R. I. Wullert. “Programmable shaping of femtosecond optical pulses by use of 128-element liquid crystal phase modulator”. *IEEE Journal of Quantum Electronics* **28**:4 (1992), 908–920.
- [226] V. V. Lozovoy, I. Pastirk, and M. Dantus. “Multiphoton intrapulse interference. IV. Ultrashort laser pulse spectral phase characterization and compensation”. *Optics Letters* **29**:7 (Apr. 2004), 775–777.
- [227] A. Comin, R. Ciesielski, G. Piredda, K. Donkers, and A. Hartschuh. “Compression of ultrashort laser pulses via gated multiphoton intrapulse interference phase scans”. *Journal of the Optical Society of America B* **31**:5 (Apr. 2014), 1118–1125.
- [228] J. B. Guild, C. Xu, and W. W. Webb. “Measurement of group delay dispersion of high numerical aperture objective lenses using two-photon excited fluorescence”. *Applied Optics* **36**:1 (1997), 397–401.
- [229] Newport. *The Effect of Dispersion on Ultrashort Pulses*. June 2014. URL: www.newport.com.

- [230] F. Cannone, G. Chirico, G. Baldini, and A. Diaspro. “Measurement of the laser pulse width on the microscope objective plane by modulated autocorrelation method”. *Journal of Microscopy* **210**:2 (May 2003), 149–157.
- [231] B. Xu, J. M. Gunn, J. M. D. Cruz, V. V. Lozovoy, and M. Dantus. “Quantitative investigation of the multiphoton intrapulse interference phase scan method for simultaneous phase measurement and compensation of femtosecond laser pulses”. *Journal of the Optical Society of America B* **23**:4 (2006), 750–759.
- [232] N. Sultanova, S. Kasarova, and I. Nikolov. “Dispersion Properties of Optical Polymers”. In: *Proceedings of the International School and Conference on Photonics*. Vol. 116. 4. 2009, 585–587.
- [233] A. Roux, G. Koster, M. Lenz, B. Sorre, J.-B. Manneville, and P. Nassoy. “Membrane curvature controls dynamin polymerization”. *Proceedings of the National Academy of Sciences of the United States of America* **107**:9 (2010), 4141–4146.
- [234] X. Wei, B. J. Tromberg, and M. D. Cahalan. “Mapping the sensitivity of T cells with an optical trap: polarity and minimal number of receptors for Ca(2+) signaling”. *Proceedings of the National Academy of Sciences of the United States of America* **96**:15 (1999), 8471–8476.
- [235] B. J. Black and S. K. Mohanty. “Fiber-optic spanner”. *Optics Letters* **37**:24 (Dec. 2012), 5030–5032.
- [236] M. K. Kreysing, T. Kießling, A. Fritsch, C. Dietrich, J. R. Guck, and A. K. Josef. “The optical cell rotator”. *Optics Express* **16**:21 (2008), 16984–16992.
- [237] T. Kolb, S. Albert, M. Haug, and G. Whyte. “Dynamically reconfigurable fibre optical spanner”. *Lab on a Chip* **14**:6 (Mar. 2014), 1186–1190.
- [238] K. O. Greulich, G. Pilarczyk, A. Hoffmann, G. Meyer Zu Hörste, B. Schäfer, V. Uhl, and S. Monajembashi. “Micromanipulation by laser microbeam and optical tweezers: from plant cells to single molecules”. *Journal of Microscopy* **198**:3 (June 2000), 182–187.

- [239] S. Oddos, C. Dunsby, M. A. Purbhoo, A. Chauveau, D. M. Owen, M. A. A. Neil, D. M. Davis, and P. M. W. French. “High-speed high-resolution imaging of intercellular immune synapses using optical tweezers”. *Biophysical Journal* **95**:10 (Nov. 2008), L66–L68.
- [240] M. J. Lang, P. M. Fordyce, A. M. Engh, K. C. Neuman, and S. M. Block. “Simultaneous, coincident optical trapping and single-molecule fluorescence”. *Nature Methods* **1**:2 (2004), 1–7.
- [241] S. Ebrahimi, A.-R. Moradi, A. Anand, and B. Javidi. “Digital holographic microscopy with coupled optical fiber trap for cell measurement and manipulation”. *Optics Letters* **39**:10 (May 2014), 2916–2919.
- [242] E. Abbe. “Beiträge zur Theorie des Mikroskops und der mikroskopischen Wahrnehmung”. *Archiv für Mikroskopische Anatomie* **9**:1 (1873), 413–418.
- [243] R. Heintzmann and G. Ficz. “Breaking the resolution limit in light microscopy”. In: *Digital Microscopy*. Ed. by G. Sluder and D. Wolf. 4th. Vol. 114. Elsevier Inc., Jan. 2013, 525–544.
- [244] R. Hermann, P. Walther, and M. Müller. “Immunogold labeling in scanning electron microscopy”. *Histochemistry and Cell Biology* **106**:3 (Sept. 1996), 356–356.
- [245] M. G. L. Gustafsson, L. Shao, P. M. Carlton, C. J. R. Wang, I. N. Golubovskaya, W. Z. Cande, D. A. Agard, and J. W. Sedat. “Three-dimensional resolution doubling in wide-field fluorescence microscopy by structured illumination”. *Biophysical Journal* **94**:12 (June 2008), 4957–4970.
- [246] C. J. R. Sheppard. “Super-resolution in Confocal Imaging”. *Optik* **80**:2 (1988), 53–54.
- [247] M. G. L. Gustafsson. “Surpassing the lateral resolution limit by a factor of two using structured illumination microscopy”. *Journal of Microscopy* **198**:2 (May 2000), 82–87.

- [248] S. W. Hell and J. Wichmann. “Breaking the diffraction resolution limit by stimulated emission: stimulated-emission-depletion fluorescence microscopy”. *Optics Letters* **19**:11 (1994), 780–782.
- [249] A. Jost and R. Heintzmann. “Superresolution Multidimensional Imaging with Structured Illumination Microscopy”. In: *Annual Reviews of Materials Research*. Ed. by D. R. Clarke. Vol. 43. Palo Alto: Annual Reviews, 2013, 261–282.
- [250] E. Betzig, G. H. Patterson, R. Sougrat, O. W. Lindwasser, S. Olenych, J. S. Bonifacino, M. W. Davidson, J. Lippincott-schwartz, and H. F. Hess. “Imaging Intracellular Proteins at Nanometer Resolution”. *Science* **313**:5793 (2006), 1642–1645.
- [251] M. J. Rust, M. Bates, and X. Zhuang. “Imaging by stochastic optical reconstruction microscopy (STORM)”. *Nature Methods* **3**:10 (2006), 793–795.
- [252] W. Jung, W. Benalcazar, A. Ahmad, U. Sharma, H. Tu, and S. A. Boppart. “Numerical analysis of gradient index lens-based optical coherence tomography imaging probes”. *Journal of Biomedical Optics* **15**:6 (2010), 066027.
- [253] GRINtech. *High-NA Endomicroscopic Imaging Objective for Fluorescence Microscopy*. 2011.
- [254] C. L. Braun and S. N. Smirnov. “Why is water blue?” *Journal of Chemical Education* **70**:8 (Aug. 1993), 612.
- [255] J. B. Huppa and M. M. Davis. “T-cell-antigen recognition and the immunological synapse”. *Nature Reviews* **3**:12 (2003), 973–983.
- [256] N. B. Martín-Cófreces, J. Robles-Valero, J. Román Cabrero, M. Mittelbrunn, M. Gordón-Alonso, C.-H. Sung, B. Alarcón, J. Vázquez, and F. Sánchez-Madrid. “MTOC translocation modulates IS formation and controls sustained T cell signaling”. *The Journal of Cell Biology* **182**:5 (2008), 951–962.

- [257] M. Mittelbrunn and F. Sanchez-Madrid. “Intercellular communication: diverse structures for exchange of genetic information”. *Nature Reviews. Molecular Cell Biology* **13**:5 (2012), 328–335.
- [258] M. Mittelbrunn, C. Gutiérrez-Vázquez, C. Villarroya-Beltri, S. González, F. Sánchez-Cabo, M. A. González, A. Bernad, and F. Sánchez-Madrid. “Unidirectional transfer of microRNA-loaded exosomes from T cells to antigen-presenting cells”. *Nature Communications* **2**:282 (Jan. 2011), 1–10.
- [259] J. Huang, V. I. Zarnitsyna, B. Liu, L. J. Edwards, N. Jiang, B. D. Evavold, and C. Zhu. “The kinetics of two-dimensional TCR and pMHC interactions determine T-cell responsiveness”. *Nature* **464**:7290 (Apr. 2010), 932–6.
- [260] A. J. Crick, M. Theron, T. Tiffert, V. L. Lew, P. Cicuta, and J. C. Rayner. “Quantitation of malaria parasite-erythrocyte cell-cell interactions using optical tweezers”. *Biophysical journal* **107**:4 (Aug. 2014), 846–53.
- [261] A. C. N. Brown, S. Oddos, I. M. Dobbie, J.-M. Alakoskela, R. M. Parton, P. Eissmann, M. A. A. Neil, C. Dunsby, P. M. W. French, I. Davis, and D. M. Davis. “Remodelling of Cortical Actin Where Lytic Granules Dock at Natural Killer Cell Immune Synapses Revealed by Super-Resolution Microscopy”. *PLoS Biology* **9**:9 (2011), e1001152.
- [262] M. O. Lenz, H. G. Sinclair, A. Savell, J. H. Clegg, A. C. N. Brown, D. M. Davis, C. Dunsby, M. A. A. Neil, and P. M. W. French. “3-D stimulated emission depletion microscopy with programmable aberration correction”. *Journal of Biophotonics* **7**:1-2 (June 2014), 29–36.
- [263] C. Wülfing and M. M. Davis. “A Receptor/Cytoskeletal Movement Triggered by Costimulation During T Cell Activation”. *Science* **282**:5397 (Dec. 1998), 2266–2269.

- [264] S. Duchez, M. Rodrigues, F. Bertrand, and S. Valitutti. “Reciprocal Polarization of T and B Cells at the Immunological Synapse”. *Journal of Immunology* **187**:9 (2011), 4571–4580.
- [265] C. V. Irvin-Wilson, J. Y. Newburg, K. Kong, R. T. Javier, and S. J. Marriott. “High Throughput Method to Quantify Anterior-Posterior Polarity of T-Cells and Epithelial Cells”. *Viruses* **3**:12 (2011), 2396–2411.
- [266] T. C. Vogelmann. “Plant-tissue optics”. *Annual review of Plant Physiology and Plant Molecular Biology* **44**:1 (1993), 231–251.
- [267] S. L. Shaw and D. W. Ehrhardt. “Smaller, faster, brighter: advances in optical imaging of living plant cells”. *Annual Review of Plant Biology* **64**:1 (Jan. 2013), 351–375.
- [268] S. Chapman, K. J. Oparka, and A. G. Roberts. “New tools for in vivo fluorescence tagging”. *Current Opinion in Plant Biology* **8**:6 (Dec. 2005), 565–573.
- [269] D. Y. T. Liu, B. T. Kuhlmeier, P. M. C. Smith, D. A. Day, C. R. Faulkner, and R. L. Overall. “Reflection across plant cell boundaries in confocal laser scanning microscopy”. *Journal of Microscopy* **231**:2 (Aug. 2008), 349–357.
- [270] J. Fitzgibbon, K. Bell, E. King, and K. Oparka. “Super-resolution imaging of plasmodesmata using three-dimensional structured illumination microscopy”. *Plant Physiology* **153**:4 (Aug. 2010), 1453–1463.
- [271] K. Bell and K. Oparka. “Imaging plasmodesmata”. *Protoplasma* **248**:1 (Jan. 2011), 9–25.
- [272] O. Linnik, J. Liesche, J. Tilsner, and K. J. Oparka. “Unraveling the structure of viral replication complexes at super-resolution”. *Frontiers in Plant Science* **4**:6 (2013), 1–13.
- [273] J. Tilsner, O. Linnik, M. Louveaux, I. M. Roberts, S. N. Chapman, and K. J. Oparka. “Replication and trafficking of a plant virus are coupled at the entrances of plasmodesmata”. *The Journal of Cell Biology* **201**:7 (2013), 981–995.

- [274] D. Phillips, C. Nibau, J. Wnetrzak, and G. Jenkins. “High Resolution Analysis of Meiotic Chromosome Structure and Behaviour in Barley (*Hordeum vulgare* L.)” *PLoS ONE* **7**:6 (2012), e39539.
- [275] G. Komis, M. Mistrik, v. Olga, A. Doskočilova, M. Ovečka, P. Illés, J. Bartek, and v. Jozef. “Dynamics and Organization of Cortical Microtubules as Revealed by Superresolution Structured Illumination Microscopy”. *Plant Physiology* **165**:1 (2014), 129–148.
- [276] J. Liesche, I. Ziolkiewicz, and A. Schulz. “Super-resolution imaging with Pontamine Fast Scarlet 4BS enables direct visualization of cellulose orientation and cell connection architecture in onion epidermis cells”. *BMC Plant Biology* **13**:1 (2013), 226.
- [277] J Kleine-Vehn, K Wabnik, A Martinière, L. Łangowski, K Willig, S Naramoto, J Leitner, H Tanaka, S Jakobs, S Robert, C Luschnig, W Govaerts, S. W. Hell, J Runions, and J Friml. “Recycling, clustering, and endocytosis jointly maintain PIN auxin carrier polarity at the plasma membrane.” *Molecular Systems Biology* **7**:540 (Jan. 2011), 1–13.
- [278] P. Olesen. “The neck constriction in plasmodesmata”. *Planta* **144**:4 (1979), 349–358.
- [279] N. Malagnino, G. Pesce, A. Sasso, and E. Arimondo. “Measurements of trapping efficiency and stiffness in optical tweezers”. *Optics Communications* **214**:1-6 (Dec. 2003), 15–24.
- [280] S. K. Mohanty, K. S. Mohanty, and M. W. Berns. “Manipulation of mammalian cells using a single-fiber optical microbeam”. *Journal of Biomedical Optics* **13**:5 (2008), 054049.
- [281] C. Liberale, G. Cojoc, F. Bragheri, P. Minzioni, G. Perozziello, R. La Rocca, L. Ferrara, V. Rajamanickam, E Di Fabrizio, and I Cristiani. “Integrated microflu-

- idic device for single-cell trapping and spectroscopy”. *Scientific reports* **3**:1258 (Jan. 2013), 1–6.
- [282] M. Mahamdeh, C. P. Campos, and E. Schäffer. “Under-filling trapping objectives optimizes the use of the available laser power in optical tweezers”. *Optics Express* **19**:12 (2011), 11759–11768.
- [283] V. R. M. Rodrigues, A. Mondal, J. A. Dharmadhikari, S. Panigrahi, D. Mathur, and A. K. Dharmadhikari. “Enhancing the strength of an optical trap by truncation”. *PLoS ONE* **8**:4 (Jan. 2013), e61310.
- [284] A. J. Wright, R. A. Benson, R. W. Bowman, G. M. Gibson, M. J. Padgett, J. M. Girkin, J. Brewer, and P. Garside. “Investigating the interaction forces between T cells and antigen-presenting cells using an optical trapping system”. In: *Optical Trapping and Optical Manipulation VIII*. Vol. 8097. Sept. 2011, 80970I.
- [285] G. Volpe, G. P. Singh, and D. Petrov. “Optical tweezers with cylindrical vector beams produced by optical fibers”. In: *Optical Trapping and Micromanipulation*. Ed. by K. Dholakia and G. C. Spalding. Vol. 5514. Oct. 2004, 283–292.
- [286] J. Fitzgibbon, M. Beck, J. Zhou, C. Faulkner, S. Robatzek, and K. Oparka. “A developmental framework for complex plasmodesmata formation revealed by large-scale imaging of the Arabidopsis leaf epidermis”. *The Plant Cell* **25**:1 (Jan. 2013), 57–70.
- [287] M. A. Lauterbach, C. K. Ullal, V. Westphal, and S. W. Hell. “Dynamic imaging of colloidal-crystal nanostructures at 200 frames per second”. *Langmuir* **26**:18 (Sept. 2010), 14400–14404.
- [288] T. Čižmár, V. Kollárová, X. Tsampoula, F. J. Gunn-Moore, W. Sibbett, Z. Bouchal, and K. Dholakia. “Generation of multiple Bessel beams for a biophotonics workstation”. *Optics Express* **16**:18 (Oct. 2008), 14024–14035.

- [289] X. Tsampoula, M. Mazilu, T. Vettenburg, F. J. Gunn-Moore, and K. Dholakia. “Enhanced cell transfection using subwavelength focused optical eigenmode beams [Invited]”. *Photonics Research* **1**:1 (June 2013), 42–46.
- [290] T. Čižmár and K. Dholakia. “Tunable Bessel light modes: engineering the axial propagation”. *Optics Express* **17**:18 (2009), 15558–15570.
- [291] W. Yan, H. He, Y. Wang, M. Hu, and C. Wang. “Controllable generation of reactive oxygen species by femtosecond-laser irradiation”. *Applied Physics Letters* **104**:8 (Feb. 2014), 083703.
- [292] K. A. Walowicz, I. Pastirk, V. V. Lozovoy, and M. Dantus. “Multiphoton Intrapulse Interference. 1. Control of Multiphoton Processes in Condensed Phases”. *The Journal of Physical Chemistry A* **106**:41 (Oct. 2002), 9369–9373.
- [293] A. G. York, S. H. Parekh, D. D. Nogare, R. S. Fischer, K. Temprine, M. Mione, A. B. Chitnis, C. A. Combs, and H. Shroff. “Resolution doubling in live, multicellular organisms via multifocal structured illumination microscopy”. *Nature methods* **9**:7 (2012), 749–754.
- [294] M. Dal Maschio, F. Difato, R. Beltramo, A. Blau, F. Benfenati, and T. Fellin. “Simultaneous two-photon imaging and photo-stimulation with structured light illumination”. *Optics express* **18**:18 (Aug. 2010), 18720–31.
- [295] D. Dan, B. Yao, and M. Lei. “Structured illumination microscopy for super-resolution and optical sectioning”. *Chinese Science Bulletin* **59**:12 (2014), 1291–1307.
- [296] P. Kner, B. B. Chhun, E. R. Griffis, L. Winoto, and M. G. L. Gustafsson. “Super-resolution video microscopy of live cells by structured illumination”. *Nature Methods* **6**:5 (2009), 339–342.
- [297] M. A. A. Neil, R. Juskaitis, and T. Wilson. “Method of obtaining optical sectioning by using structured light in a conventional microscope”. *Optics Letters* **22**:24 (Dec. 1997), 1905–1907.

-
- [298] L. Shao, P. Kner, E. H. Rego, and M. G. L. Gustafsson. “Super-resolution 3D microscopy of live whole cells using structured illumination”. *Nature Methods* **8**:12 (Dec. 2011), 1044–1046.
- [299] L. H. Schaefer, D. Schuster, and J. Schaffer. “Structured illumination microscopy: artefact analysis and reduction utilizing a parameter optimization approach”. *Journal of Microscopy* **216**:2 (2004), 165–174.

A | Tissue culture

A.1 Plant cells

A.1.1 Liquid culture

Liquid medium was made by the addition of 4.3 g l^{-1} Murashige and Skoog powder (1x M & S, MP Biomedicals, USA) supplemented with 0.09 M sucrose (Sigma-Aldrich, UK), $1 \mu\text{M}$ 2,4-dichlorophenoxyacetic acid (MP Biomedicals, USA) and 25 nM KH_2PO_4 (Sigma-Aldrich Co., USA) to water and adjusting to 5.6 pH with 0.1 M KOH (Sigma-Aldrich Co., USA). The medium was autoclaved at 121°C for 15 minutes.

Tobacco BY-2 suspension cells (kindly provided by the James Hutton Institute) were cultured in 20 ml liquid medium in 50 ml conical flasks sealed with tin foil. Passaging was performed weekly at a 1 in 20 ratio. Liquid cultures were incubated at 25°C at 120 rpm on an orbital shaker (IKA Labortechnik, Germany). Liquid cultures were initiated by placing 2 mm callus (described below) into 20 ml liquid medium and pipetting to disperse.

Detailed BY-2 optical injection protocol is described in Section 5.2.

A.1.2 Solid culture

Solid medium was made by adding 1 % w/v Agargel (Sigma-Aldrich Co., USA) to liquid medium prior to autoclaving. The autoclaved solid medium was poured into 50 ml petri dishes and allowed to set. Solid culture was initiated from liquid culture by pipetting 1 ml liquid culture onto the solid plate and leaving to dry. Passaging of solid culture was performed monthly by excising approximately 2 mm of callus and transferring to a new solid plate. Passaging was performed in triplicate. Petri dishes were sealed with Nescofilm (Fisher Scientific, UK) and stored upside-down at room temperature.

A.1.3 Protoplast digest

5 ml of 2-5 day old BY-2 cells were collected by centrifugation or sedimentation and resuspended in 5 ml digestion mixture (500 mM mannitol, 10 mM MES, 2 % w/v cellulase, 0.25 % BSA (all Sigma-Aldrich Co., USA), 0.05 % pectolyase Y-23 (MP Biomedicals, USA), pH 5.5 with 0.1 M KOH). The digest was incubated at 25°C for approximately 3 hours on an orbital shaker, checking the protoplast fraction every hour. When 80 % or more cells were protoplasts, the protoplasts were washed three times in digestion solution without enzymes before being resuspended in protoplast medium (1x M & S medium, 0.4 M mannitol, 2.5 mM MES, 5 mM $\text{CaCl}_2 \cdot 2\text{H}_2\text{O}$) adjusted to pH 5.7 with 0.1 M KOH. Protoplasts were kept in a 50 ml falcon tube at a concentration of 5×10^4 cells/ml until required. Protoplast viability was checked using fluorescein diacetate (Sigma-Aldrich Co., USA) staining.

A.2 Mammalian cells

A.2.1 Cell culture

Chinese Hamster Ovary (CHO-K1) and Human Embryonic Kidney (HEK-293) cells were cultured in 5 ml MEM supplemented with 10 % Foetal Bovine Serum (Life Technologies, USA) and L-Glutamate, Penicillin and Streptomycin solution (Sigma-Aldrich Co., USA) in T25 flasks (Nuncleon, Denmark) at 37°C and 5 % CO₂. Passaging was performed three times weekly by bathing in 1 ml 0.25 % Trypsin-EDTA solution (Sigma-Aldrich Co., USA) for 5 minutes to detach the cells from the bottom of the flask before transferring a subculture to new medium.

A.2.2 Transfection protocol

Cells were prepared for photoporation by seeding detached cells onto 23 mm optical quality glass-bottomed dishes (World Precision Instruments, USA) in 2 ml MEM and incubated for ≥ 24 hours to allow cells to adhere to the bottom of the dish and grow to 50 % confluency. The cell monolayer was washed twice with 1 ml OptiMEM before the addition of 10 $\mu\text{g}\mu\text{l}^{-1}$ pCAG-GFP DNA plasmid in 300 μl OptiMEM. Cells were irradiated with three, approximately 1 μm axially separated, 40 ms laser doses. Approximately 50 cells per region of interest were irradiated. Afterwards, cells were washed twice with 1 ml MEM and incubated in 2 ml MEM for 2-3 days. Transfection was observed using a mercury arc lamp with a FITC filter.

The results from transfecting HEK cells is seen in Figure A.1. Uncorrected transfection efficiencies of up to 140 % were obtained. The corrected efficiency (calculated assuming a 24-hour doubling rate) of 9 ± 3 % is approximately half of that achieved for CHO cells in Praveen *et al.* [57]. The rate of spontaneous transfection (monitored in dishes prepared simultaneously with an irradiated dish) was quite high at 3 ± 2 %

compared to most studies, which typically see 1-2 cells per dish but, from experience, HEK cells tend to show higher rates of spontaneous transfection than the CHO cells used in these experiments. The rate of spontaneous transfection was usually high if the optical transfection efficiency was high. The average ratio of optical to spontaneous transfection per pair of dishes was 4 ± 1 , indicating the optical system was suitable to optically transfect mammalian cells, although possibly not fully optimised.

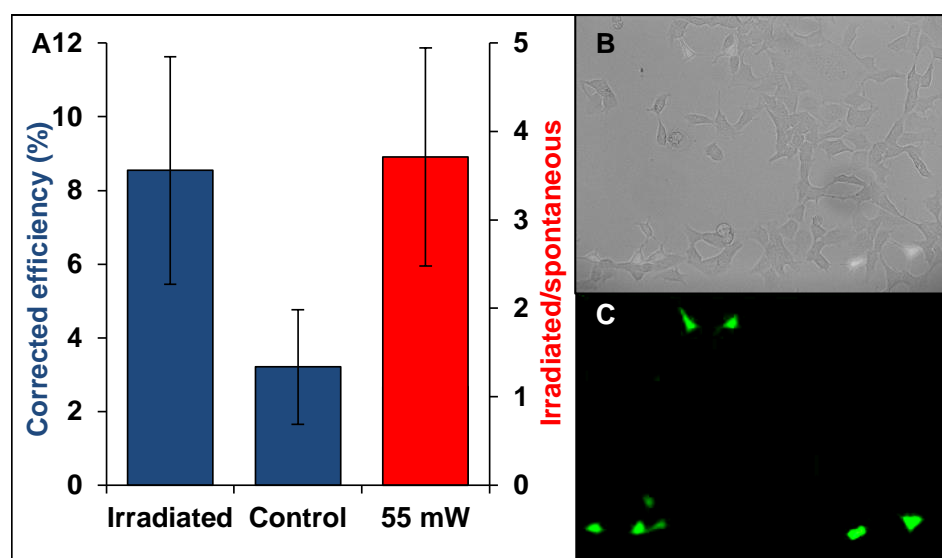


Figure A.1 – Mammalian cell transfection. (A) HEK cells were optically transfected using 55 mW and the efficiency of transfection (blue column) was determined 2-3 days later. The red column shows the ratio of optical to spontaneous transfection per irradiated/control pair. Data represents $n = 4$ irradiated dishes with approximately 50 cells irradiated per dish. Error bars denote the SEM. (B) and (C) show brightfield and epi-fluorescence images, respectively, of transfected cells.

B | The multiphoton intrapulse interference phase scan system

B.1 MIIPS optical set-up

A basic MIIPS optical system comprises an SLM bounded on either side by a grating and lens (Figure B.1). The first grating separates the pulse into its constituent wavelengths, which are collimated onto the SLM by a lens. Passing through the SLM, each pixel (corresponding to a single wavelength) applies a phase change to vary the spectral phase of the pulse. The pulse is then recombined with another lens and grating to form a pulse with total spectral phase $\phi_{out} = \phi_{in} + \phi_{SLM}$.

A commercial MIIPS system, such as the one used in this thesis, usually minimises dispersion and losses within the system by using curved mirrors rather than lenses. A double-pass through the SLM using an abutted mirror is also implemented rather than two gratings.

B.2 MIIPS theory

Multiphoton intrapulse interference is a process whereby the interference of multiple frequencies within a pulse can be affected by the phase of the pulse, this can focus the spectral energy on a particular frequency and control multiphoton processes [292].

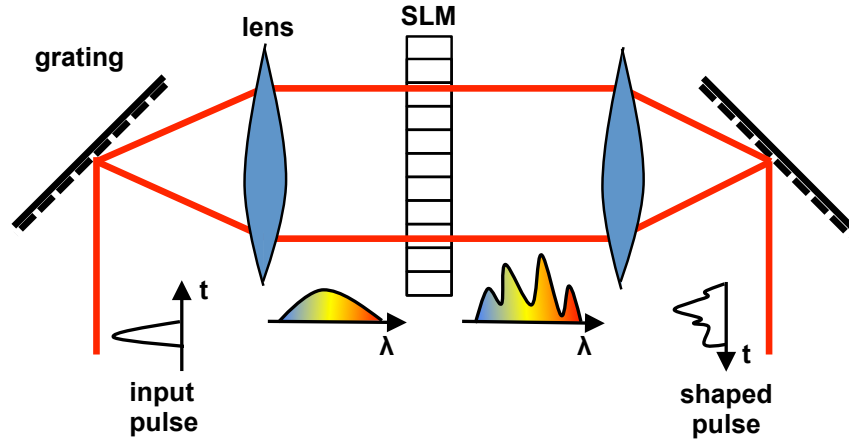


Figure B.1 – Schematic of a MIIPS pulse shaper. A spectrum of an input pulse is spatially separated using a grating. The lens then collimates the output and the SLM adds phase to different wavelengths. The spectrum is recombined with a lens and grating to form a shaped pulse with additional phase from the SLM.

MIIPS can find an unknown spectral phase of a pulse, $\phi(\omega)$, by scanning a reference phase, $f(\omega)$, across the SLM. The total phase, $\varphi(\omega)$, then changes as the reference pulse is scanned. The SHG signal produced by the pulse varies according to $\varphi(\omega)$ [226].

$$S^{(2)}(2\omega) = \left| \int |E(\omega + \Omega)| |E(\omega - \Omega)| \times \exp\{i[\varphi(\omega + \Omega) + \varphi(\omega - \Omega)]\} d\Omega \right|^2 \quad (\text{B.1})$$

Where Ω , the integration variable, is a detuning from the central frequency. This implies that SHG signal will be a maximum when $\varphi(\omega + \Omega) + \varphi(\omega - \Omega)$ is equal to zero. We can perform a Taylor expansion about ω to gain [231]:

$$\varphi(\omega + \Omega) + \varphi(\omega - \Omega) = 2\varphi(0) + \varphi''(\omega)\Omega^2 + \dots + \frac{2}{(2n!)}\varphi^{2n'}(\omega)\Omega^{2n} \quad (\text{B.2})$$

To the first approximation, the second derivatives of this equation are:

$$\varphi''(\omega) = \phi''(\omega) + f''(\omega) = 0 \quad (\text{B.3})$$

or

$$\phi''(\omega) = -f''(\omega) \quad (\text{B.4})$$

Where the second derivative of the reference function is known. The reference phase that is usually used is a sinusoidal function, which does not require the SLM to phase wrap (phase-wrapping occurs when the phase is outside $-\pi < \phi < \pi$).

A function $f(\omega) = \alpha \cos(\gamma\omega - \delta)$ is scanned by varying the phase δ [226]. A 2D MIIPS trace (Figure B.2) is formed of the SHG signal at different phases. The SHG signal is maximised when $\varphi(\omega) = 0$ and $\phi''(\omega) = -f''(\omega) = \alpha\gamma^2 \cos(\gamma\omega - \delta_{max})$ so $\phi(\omega)$ can be extracted by double integration. If δ_{max} is identified for each frequency, ω , then $\phi(\omega)$ is known for the whole spectrum. The MIIPS trace obtained can also quantitatively inform about phase distortions in the pulse. Transform-limited pulses, where $\delta_{max,TL} = \gamma\omega \pm \frac{\pi}{2}$, appear as parallel lines separated by π [226]. Chirped pulses have different separations and higher phase distortions manifest as non-parallel lines.

Using the SLM, the negative of the introduced phase distortions can then be applied to the spectral phase, cancelling out the phase distortions. The accuracy of the MIIPS increases as the phase distortions are minimised so a number of iterations are applied to achieve close-to transform-limited pulses (typically less than $\tau/\tau_{TL} < 1.03$).

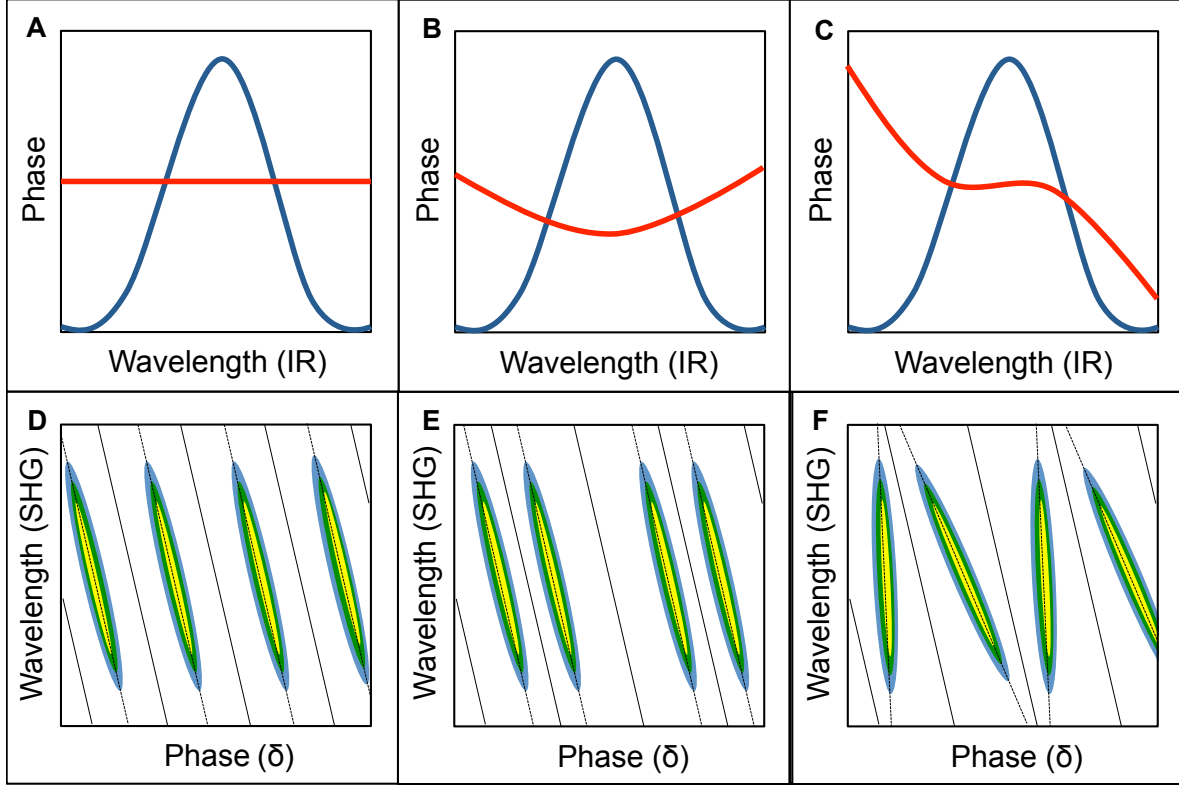


Figure B.2 – Spectral phase of applied distortions and corresponding MIIPS traces. A-C show an example IR spectrum (blue) and spectral phase (red) for different order distortions. A shows transform-limited pulses with zero phase. The MIIPS trace for TL pulses (D) show parallel lines (coloured contours) separated by π , the phase is varied from 0 to 4π . B shows the spectral phase for positive chirp and the MIIPS trace (E) has parallel lines with unequal separations. For third-order dispersion (C and F) the spectral phase is cubic and the lines in the MIIPS trace are no longer parallel. Solid black lines on MIIPS traces show the boundaries between which δ_{max} is determined and the dashed black lines show hypothetical values of δ_{max} . From this we can intuitively discern dispersion orders in a MIIPS trace.

C | Structured illumination microscopy

The phenomena of Moiré fringes has been well characterised for many years. When two spatial frequencies overlap, they produce a pattern with a third, lower, spatial frequency. The application to SR imaging runs thus - considering a sample containing spatial frequencies higher than the passband of the imaging objective, then applying an illumination that varies by a known spatial frequency creates Moiré fringes of a suitable spatial frequency to be easily observed using a camera. The unknown higher frequency data can then be computationally extracted [247].

An interesting consideration is the use of the term "structured illumination" to describe this sinusoidal illumination. Structured illumination is principally a generic term describing any illumination that has been shaped in any way but is often used to describe a specific type of illumination. This can lead to potential ambiguities when the term is used, for instance SIM [245] and MSIM (multifocal SIM) [293] are both super-resolution techniques but the former applies sinusoidal illumination rather than point-like illumination and thus can support the super-resolved spatial frequencies with much greater SNR than the latter. The former is therefore a more powerful SR technique, although more complex to execute. Structured illumination is also often referred to for non-SR microscopy and manipulation, such as in Dal Maschio *et al.* [294], where an SLM is used to only illuminate regions of interest in a field of view. In this thesis, structured illumination microscopy will refer to sinusoidal SIM only.

C.1 Principle of lateral resolution enhancement

The theory of imaging states that the observed image is a convolution of the sample emission, $E(r)$, and the point spread function, $H(r)$ [245].

$$D(r) = (E \otimes H)(r) \quad (\text{C.1})$$

The Fourier transform of this is then a simple multiplication following the convolution theorem:

$$\tilde{D}(k) = \tilde{E}(k)O(k) \quad (\text{C.2})$$

$O(k)$, the optical transfer function (OTF, the Fourier transform of the PSF) has finite support, outside of which it is zero. To observe beyond this, information outside the OTF must be brought into the observable region. If an object has a structure $S(r)$ then the sample emission is dependent on $S(r)$ and the illumination:

$$E(r) = S(r)I(r) \quad (\text{C.3})$$

$$\tilde{E}(k) = (\tilde{S} \otimes \tilde{I})(k) \quad (\text{C.4})$$

If a homogeneous illumination is applied then $\tilde{I}(k)$ is simply a delta function. If, however, $I(r)$ is spatially varying then observed regions of $\tilde{E}(k)$ are dependent on normally unobserved regions of $\tilde{S}(k)$ [245].

The application of a periodic pattern can extend the achievable resolution by a factor of two laterally. By applying an illumination of intensity [295]:

$$I(r) = I_0[1 + m\cos(2\pi k_0 r + \phi)] \quad (\text{C.5})$$

where k_0 is the spatial frequency and ϕ is the phase of the applied illumination pattern. I_0 and m are constants, the Fourier transform is:

$$\tilde{I}(k) = I_0[\delta(k) + \frac{m}{2}e^{i\phi}\delta(k - k_0) + \frac{m}{2}e^{-i\phi}\delta(k + k_0)] \quad (\text{C.6})$$

so the observed image becomes:

$$\tilde{D}(k) = I_0[\tilde{S}(k) + \frac{m}{2}e^{i\phi}\tilde{S}(k - k_0) + \frac{m}{2}e^{-i\phi}\tilde{S}(k + k_0)]O(k) \quad (\text{C.7})$$

There are now three frequencies in this equation, k , $k + k_0$ and $k - k_0$, all of which are within the OTF support. The first term is present under constant illumination whereas the extra two terms now provide more information to the image. Any single obtained image using this spatially varying illumination is a mixture of these three different components and therefore one image alone is not enough to extract all the necessary components. Instead, three different images are taken with the phase, ϕ , varied between each one to ensure all the necessary information is available to construct the SR image. The effective OTF is extended as visually described in Figure C.1. This, however, only extends in one direction so more images are taken with the grating applied at different angles to extend the effective OTF in all directions. Three different angles is usually enough to adequately extend the observable region, resulting in nine images in total required for one exposure: three phases for each of the three angles.

Physically, this sinusoidal grating is achieved by two beam interference [247]. A grating is used to diffract the light and the first orders are sent through either edge of the objective back aperture to create as high a spatial frequency as possible (better lateral resolution) on the sample plane. This grating is then physically rotated and moved to vary phase. Using an SLM to vary the pattern at the sample plane can speed up acquisition times [296].

C.1.1 Extension to 3D-SIM

The form of SIM described above is only capable of extending the observable Fourier space in the lateral region. The 3D OTF of a standard widefield microscope takes the shape of a torus, with a “missing cone” at the lateral origin, leading to a lack of accessible information in the axial direction and a significant reduction in the axial

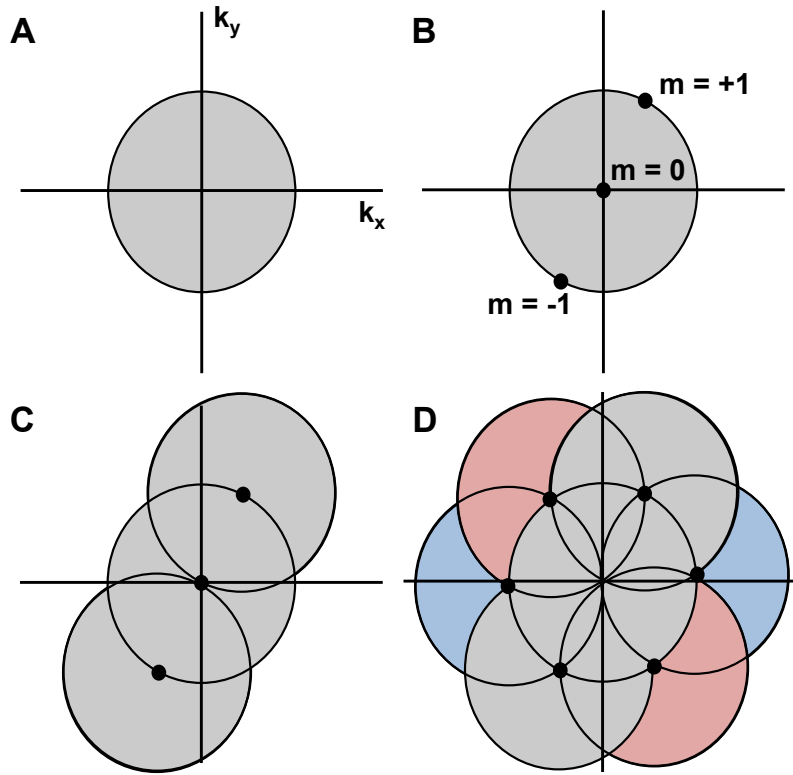


Figure C.1 – The lateral observable region in Fourier space (OTF support) for a standard widefield microscope is a circle (A). If a periodic grating illumination is applied this appears as three points in Fourier space (B). The distance of these points from the origin is dependent on the frequency of the grating applied. The smallest grating that can be applied is diffraction limited and therefore the points lie right on the edge of the original OTF (limiting the resolution enhancement to two). Convolution of these two patterns places circles with their origins at the points $m = \pm 1$, extending the observable region (C). Applying the grating at different angles extends this region in all directions (D). Image adapted from [247].

resolution compared to the lateral. If we use SIM to extend this torus laterally, we still have this “missing cone” effect [245].

One way to increase the optical sectioning is to apply a coarser grating, this now reduces the distance between the origin and the outside tori and overlaps the tori to fill

in the missing cone and increase the optical sectioning capability of the microscope. This technique greatly increases optical sectioning but at the expense of lateral resolution [297].

It is also possible to use a spatially-varying total internal reflection fluorescence (TIRF) illumination to force optical sectioning by only collecting light from the small section closest to the coverslip excited by the evanescent wave. Using TIRF, however, sacrifices depth because the working distance is negligible and so less applicable for large plant cells.

If an illumination pattern is employed that varies both laterally and axially, such as that created by three-beam interference at the sample plane, then both axial and lateral sectioning can occur at the same time [245]. The Fourier modes of the illumination produced by three-beam interference are at seven points around the torus; looking at a cross-section through the torus, the modes are at each vertex and at the top and bottom of each lobe. When the OTF is extended by convolving this illumination pattern, the observable region is extended axially as well. The presence of five lateral spatial components in each image, however, now requires five different phase images to obtain the full, super-resolution and axially sectioned, information from the sample, 15 images overall. This three-beam method, termed 3D-SIM, has also been extended to achieve a cell volume in 5 s using an SLM [298].

C.2 Capturing a SIM image

When working with any microscope, the imaging target, mounting preparation and imaging protocol must all be chosen carefully to achieve a meaningful image and working with the N-SIM is no different. While this will change from sample to sample, there are protocols that must always be followed when using the N-SIM to obtain high-quality images.

C.2.1 Choice of sample

To ensure an optimal SIM image, the decision of which sample to image, along with the choice of staining is critical. Whilst the lasers and filters used by the SIM mean that there is a wide range of standard fluorophores that can be used, unlike STED for example, the fluorophore needs to be tagged to the correct target. Linear SIM can achieve twice the diffraction-limited resolution, whilst this is better than a confocal or epi-fluorescence and more than enough for a lot of biological applications, it cannot achieve the resolution of STED or PALM, for example. The target for imaging, therefore, should possess some structure that can be resolved on these length scales e.g., SIM is not suitable to image two targets spaced 30 nm apart.

The N-SIM uses fixed gratings that are designed to work with a single objective. The N-SIM system used here possesses a grating suitable for use with a 100x TIRF objective, which grants the highest possible magnification for this system but restricts the field of view. Any target selected for imaging should occur on small enough length scales to be easily observed within a 30 x 30 μm space. It is possible to tile images together to increase the field of view but this increases the total exposure time.

Fast-moving specimens are unsuitable for SIM imaging because multiple exposures are required to obtain a single SIM image. The SIM can image up to 1 Hz but low fluorescence signal increases the required time for each exposure; when combined with multiple colours, it can take up to a few minutes to obtain a single slice through a sample. Objects that move between exposures induce artefacts in the image (seen in Figure ??).

C.2.2 Sample preparation and mounting

Samples were always mounted on a number 1.5 thickness coverslip, any change in coverslip thickness must be counteracted by changing the correction ring on the TIRF

objective. The coverslip could either be a glass-bottomed dish (for live-cell imaging) or cells sandwiched between a coverslip and microscope slide for fixed samples. Whichever sample type is used, the corresponding sample holder was used to ensure the correct mounting of the sample in the microscope. The N-SIM is highly sensitive to any source of aberrations (much like any SR microscope) so care was taken to ensure high-quality, flat coverslips are used. The coverslip also had to be clean, the presence of dirt, grease or old immersion oil can cause unwanted aberrations.

Rigid mounting of the sample in the microscope stage is crucial to minimise drift between exposures that would introduce artefacts into the final image. Clamps are used to fix the sample in place. To provide easy selection of suitable regions for imaging, immersion oil was placed on the 100x objective and initial imaging was performed with a 20x air objective to access a large field of view. Once a suitable section was chosen, imaging was performed after switching back to the 100x objective.

C.2.3 Setting up for a SIM exposure

Once the desired area for SIM imaging was selected, the imaging parameters were optimised in the N-SIM software prior to running the imaging protocol. The detection camera (EM-CCD, Andor) only operates in a linear regime up to a certain incident intensity, the camera exposure time and excitation laser powers are varied to maximise the emission intensity (to maximise the signal-to-noise ratio and reduce artefacts) whilst not breaking this linear limit. Increasing the laser power reduces the exposure time, reducing the overall acquisition time, but also causes more photobleaching. A compromise must be found between these two parameters based on the photobleaching resistance of the fluorophore being imaged and the required acquisition speed. These parameters could be set individually for each of the excitation lasers.

z -stacks and time series can also be captured using the N-SIM. z -stacks were obtained at intervals of 120 nm (or multiples thereof) for the SIM reconstruction algorithm

(Nyquist sampling for the theoretical achievable axial resolution). Information between stacks is estimated by interpolation. For multiple colour stacks, each slice should be captured in each colour before moving to the next z -position, performing the acquisition the other way round can increase drift between colour exposures.

Once all the necessary parameters have been set, the imaging could begin.

C.2.4 SIM exposure

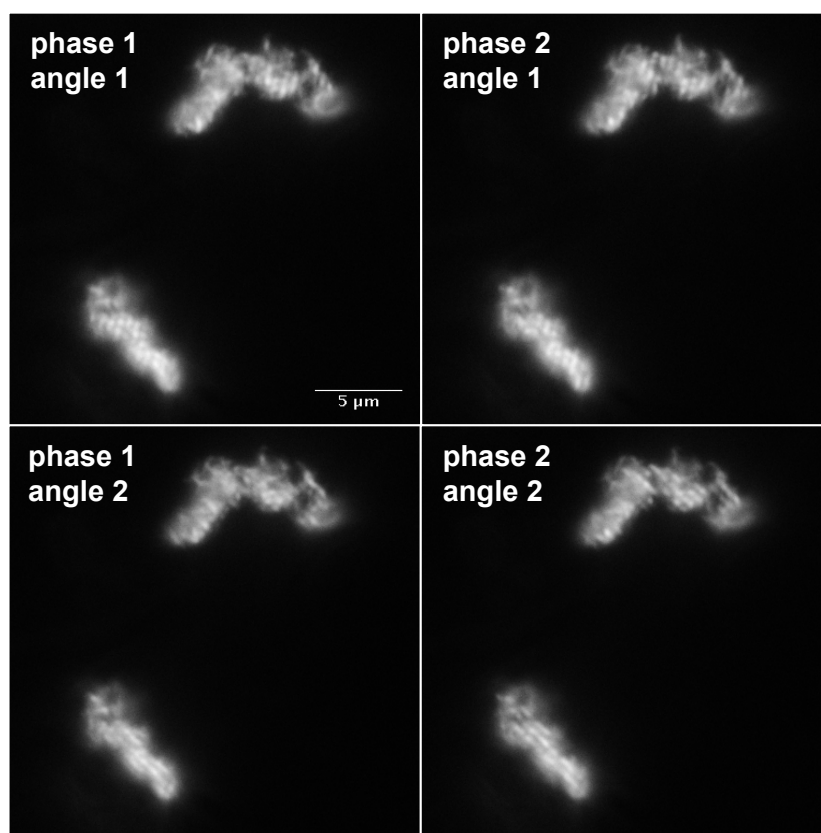


Figure C.2 – Selection of images from a full SIM exposure demonstrating the grating pattern applied to the sample. A full SIM exposure takes 15 images, three different angles (the top and bottom images show different grating angles being applied) and five different phases of the grating pattern (left and right images). Sample is an RFP labelled TGB1 protein aggregate within a tobacco epidermal cell from an epidermal peel.

During the imaging process, the SIM projects a grating pattern onto the sample, as seen in Figure C.2 and captures the resulting pattern (sample and grating) on the camera. During the 15 exposures, the angle of the grating (three different angles) and the phase of the grating pattern (five different phases) on the sample is varied. Figure C.2 shows a subset of the full 15 exposures, showing two different angles applied and two phases per angle, the change in phase is seen in the varying orthogonal positions of the “stripes” on the sample.

C.2.5 Image reconstruction

Once all the exposures have been collected, the SIM image was reconstructed from the multiple exposures. Image reconstruction is performed in Fourier space, with each Fourier mode extracted from each exposure and replaced to the correct point in Fourier space (from within the OTF to partially outside). Whilst the reconstruction within the N-SIM software automatically optimises the reconstruction parameters, there is the possibility to vary parameters prior to reconstruction to achieve the desired image. There are three parameters that can be varied within the software and Figure C.3 shows the effects of varying each parameter. For demonstration purposes, these have been varied widely to fully highlight the effect of changing each parameter, for obtaining images for research purposes, the parameters were usually kept as the automatic ones or tweaked slightly to improve the reconstructed image (mostly to reduce background noise).

Illumination modulation contrast - Varying this parameter by large amounts (A and B) does not affect the reconstructed image when compared to the other two parameters. The illumination modulation contrast is usually measured from the image but can also be input by the user. This is a factor that the OTF is multiplied by to account for the fact that measured (or calculated) OTF will display a different contrast to the current image (due to induced aberrations, scattering and absorption) [247].

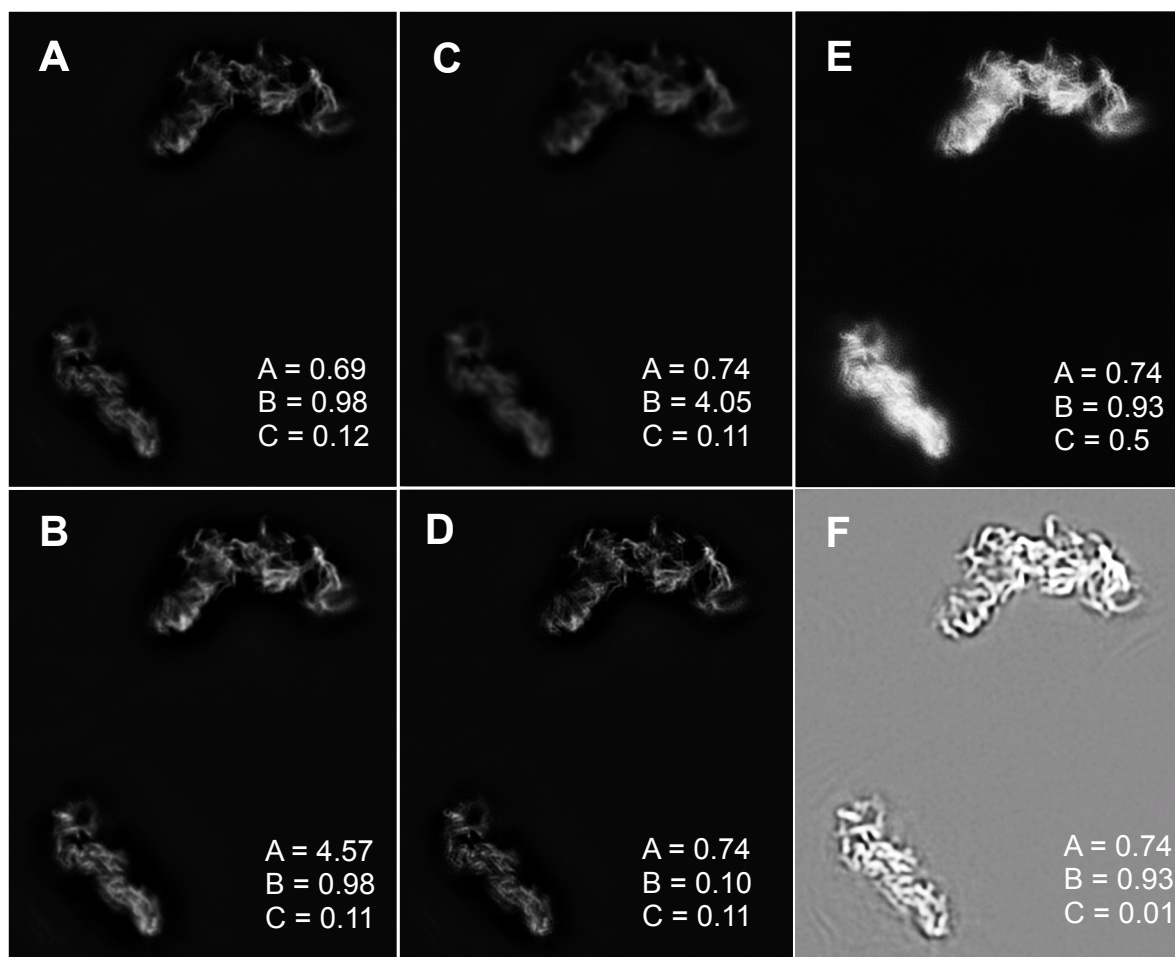


Figure C.3 – Reconstructed SIM images when the reconstruction parameters are varied. Each column of images displays the effect of changing one parameter. A = Illumination modulation contrast (images A and B), B = high resolution noise suppression (varied in images C and D) and C = out of focus blur suppression (images E and F). Reconstructions were performed from the full set of exposures for which a subset is displayed in Figure C.2. Sample is an RFP labelled TGB1 protein aggregate within a tobacco epidermal cell from an epidermal peel.

High resolution noise suppression - During the reconstruction, an apodizing filter (A) is applied that helps to decrease ringing artefacts [247]. Increasing the strength of the filter reduces high resolution noise but also removes high frequency information from the image in the process. This can be seen in Figures C.3C and D where a

high strength filter increases the "blur" in the image (C) and a low filter allows high frequency information in the image but also increases the effect of high resolution noise, appearing as a honeycomb effect within the aggregates.

Out-of-focus blur suppression - This removes low-frequency features and leads to greater optical sectioning. When this filter is very low (F), the constant (low-frequency) background that would usually be eliminated is visible.

Artefacts - Both movement and noise artefacts have already been discussed in Chapter 7. The third artefact (also present in Figure C.3) is induced by residual stripe pattern caused by changes in illumination and detection intensities during acquisition [299].

D | Python code for determining the centre of mass

```
#!/usr/bin/python
import cv2
import numpy as np
import matplotlib.pyplot as plt

sequence = [raw_input("Filename: ")] #Read in one or multiple
          filenames
borf = int(raw_input("Brightfield? (1 if true, 0 if false/fluorescent)
: "))

if borf == 1: #brightfield data processing
    for video in sequence:
        cap = cv2.VideoCapture(video)
        xCOM = []
        yCOM = []

        #Reading in all files in avi
        while(True):
            ret, img = cap.read()
            if (type(img) == type(None)):
                break
            #image processing
```

```
img = cv2.medianBlur(img,5)
cimg = cv2.cvtColor(img,cv2.COLOR_BGR2GRAY) #convert to 8
bit single channel
th2 = cv2.adaptiveThreshold(cimg,255,cv2.
    ADAPTIVE_THRESH_MEAN_C,cv2.THRESH_BINARY,11,2) #apply
    adaptive thresholding

kernel = np.ones((3,3),np.uint8)
erosion2 = cv2.dilate(th2,kernel,iterations = 1) #erosion
negative = 255 - erosion2 #inversion

h, w = img.shape[:2]
mask = np.zeros((h+2, w+2), np.uint8)
mask[:] = 0
central = (25,85) #set centre of circle for floodfill
cv2.floodFill(negative,mask,central, (255,255,255))

kernel = np.ones((12,12),np.uint8)
negative = cv2.morphologyEx(negative, cv2.MORPH_OPEN,
    kernel) #opening
#finding the CoM
row_totals = [sum(x) for x in negative]
mass = sum(row_totals)
x = []
for i in range(0,w):
    x.append(row_totals[i]*(i+1))
xC = sum(x)/float(mass)
xCOM.append(xC)

imgt = zip(*negative) #transpose matrix for y CoM
column_totals = [sum(x) for x in imgt]
y = []
for i in range(0,h):
    y.append(column_totals[i]*(i+1))
```

```

        yC = sum(y)/float(mass)
        yCOM.append(yC)

        if cv2.waitKey(1) & 0xFF == ord('q'):
            break

elif borf == 0: #fluorescent data processing
    print 'no'
    k = int(raw_input("Enter threshold value: "))
    for video in sequence:
        print video
        cap = cv2.VideoCapture(video)
        xCOM = []
        yCOM = []
        #Reading in all files in avi and processing
        while(True):
            ret, img = cap.read()
            if (type(img) == type(None)):
                break

            cimg = cv2.cvtColor(img,cv2.COLOR_BGR2GRAY)#convert to 8
                bit single channel
            ret,cimg = cv2.threshold(cimg,k,255,cv2.THRESH_BINARY) #
                apply user-determined thresholding
            h, w = img.shape[:2]
            #Find the COM
            column_totals1 = [sum(x) for x in imgt]
            x = []
            for i in range(0,w):
                x.append(column_totals1[i]*(i+1))
            xC1 = sum(x)/float(mass1)
            xCOM.append(xC1)

            imgt = zip(*cimg)
            row_totals1 = [sum(x) for x in cimg]

```



```
        mass1 = sum(row_totals1)
        y = []
        for i in range(0,h):
            y.append(row_totals1[i]*(i+1))
        yC1 = sum(y)/float(mass1)
        yCOM.append(yC1)

        if cv2.waitKey(1) & 0xFF == ord('q'):
            break
    else:
        print 'invalid command'

    cali = float("112e-9") #calibration px -> m

    xCOM[:] = [cali*(x - sum(xCOM)/float(len(xCOM))) for x in xCOM] #
        centering
    yCOM[:] = [cali*(x - sum(yCOM)/float(len(yCOM))) for x in yCOM]

    constant = float("1.38e-23")*293 #k(b)T
    conversion = float("1e6")

    ktxCOM = (constant/np.std(xCOM)**2)*conversion #finding trap stiffness
    ktyCOM = (constant/np.std(yCOM)**2)*conversion

    #Writing to file
    with open("test.txt", "a") as f:
        f.write('video:{}\n ktxCOM: {}\n ktyCOM: {}\n'.format(video,ktxCOM
            ,ktyCOM))

    #When everything done, release the capture
    cap.release()
    cv2.destroyAllWindows()
```